NONLINEAR OSCILLATIONS, NOISE AND CHAOS
IN
NEURAL DELAYED FEEDBACK

BY

André Longtin, M.Sc.
Department of Physics, McGill University

A thesis submitted to the Faculty of Graduate Studies and Research
in partial fulfillment of the requirements for the degree of
Doctor of Philosophy

Department of Physics
McGill University
Montréal, Canada
October 1989

à mes parents,
Paula et Jacques Longtin

"Do your own thing. Your reward will be doing it, your punishment having done it."

K.T. Pota

ABSTRACT

Bifurcations and complex oscillations in the human pupil light reflex (PLR) are studied. Autonomous pupil area oscillations are produced by substituting electronically controllable nonlinear feedback for the normal negative feedback of this reflex. A physiologically sound theoretical framework in which to study pupillary oscillations is developed. The model, framed as a delay-differential equation (DDE), agrees quantitatively with the simpler periodic behaviors and qualitatively with the complex behaviors. Much of the aperiodicity in the data can be ascribed to noise and transients rather than to chaos. The critical behavior of the PLR at oscillation onset is different with piecewise constant rather than smooth negative feedback. In the former, relative fluctuations in period are larger than those in amplitude, and *vice versa* in the latter. Properties of the time solutions and densities of a stochastic DDE are used to explain this experimental result. The Hopf bifurcation in this system is postponed by both additive and multiplicative colored noise. Theoretical insight into the behavior of stationary densities of DDE's and the origin of the postponement is given, and implications for analyzing bifurcations in neural delayed feedback systems are discussed.

RÉSUMÉ

Cette thèse porte sur les bifurcations et oscillations complexes dans le réflexe pupillaire (photomoteur) humain (RPH). Les oscillations autonomes de la pupille sont induites en substituant une rétroaction électronique à la rétroaction normale (négative) de ce réflexe. Une théorie des oscillations pupillaires est proposée. Le modèle, basé sur des données physiologiques, consiste en une équation différentielle à délai (EDD). Il reproduit quantitativement les comportements périodiques simples de la pupille, et qualitativement les comportements complexes. L'origine des oscillations apériodiques s'explique mieux dans l'hypothèse d'influences stochastiques au lieu de comportements chaotiques. Le comportement critique du RPH près du seuil d'instabilité s'avère différent pour les cas de rétroaction négative: 1) constante par parties et 2) différentiable. Dans le premier, les fluctuations relatives de la période dominent celles de l'amplitude, et *vice versa* dans le second. Les propriétés des solutions et des densités d'une EDD stochastique permettent d'expliquer cette observation. Le bruit coloré paramétrique ou additif retarde la bifurcation de Hopf dans le modèle. Le comportement des densités stationnaires des EDD ainsi que l'origine de ce retard sont étudiés afin d'élucider l'analyse des bifurcations dans les systèmes neuronaux à rétroaction retardée.

ACKNOWLEDGEMENTS

My thesis supervisor Michael Mackey deserves the lion's share of my gratitude. I have greatly benefited from his scientific versatility and mathematical rigor, and I especially appreciated his encouragement, friendship and humor. I am especially grateful for his letting me explore my own ideas. His open-mindedness and his general love of science have inspired me tremendously.

My co-supervisor John Milton also deserves a substantial share of my gratitude. His mind-boggling training as a physical chemist, biomathematician, physiologist, and last but not least, neurologist, makes him a truly amazing person to work with. Through his efforts, the pupillometer was loaned to the Montreal Neurological Institute. I have very fond memories of the experiments on Ward 2B of the Neuro. I greatly acknowledge his support and friendship, and his passion for plotting data and drawing figures.

I am particularly grateful to Michael and John for helping sort out my often jumbled results and for editing this thesis.

The experimental part of this thesis could not have been carried out without the collaboration of many people. First, I am very grateful towards Trevor Kirkham of the Department of Neuro-Ophthalmology at the Montreal Neurological Institute, for providing lab space and for many helpful discussions. His wit and good humor were always appreciated, and I am particularly thankful to him for sending us many interesting patients (whom I also thank for their time and for overcoming their fear of the experimental setup). Many thanks also to André Leduc and the Neuro-Electronics group for their technical help.

Further thanks go to Hamamatsu Photonics Corporation for lending us their prototype binocular infrared videopupillometer. The experiment would have proceeded much more slowly without it. I would also like to thank them for taking it back after six months, which forced us to make the best of the data we had, thus preventing us from repeating experiments whenever we had the least shadow of a doubt. I also thank the Japanese researchers at the MNI who tried (in vain) to translate the operating manual for the pupillometer. I also acknowledge the technical support of Gary Green of Hamamatsu. I thank Anne Beuter of UQAM for lending us her analog delay line for the duration of our experiments. I would also like to thank Jelte Bos of the Free University of Amsterdam for sharing his pupil data with us.

I extend my thanks to the other members of the Center for Nonlinear Dynamics in Physiology and Medicine : Leon Glass, Michael Guevara and Jacques Bélair and Anne Beuter. Their availability and openness to discussion, their good humor, their interest in this project and especially their critical comments have been a tremendous source of motivation and inspiration to me. I am also truly grateful to Christine Pamplin and Sandra James for their efficient and courteous secretarial work.

My colleagues and friends Marie-Claude Gagné, Alain Champagne and Sylvain Gravel deserve my special thanks for their continuing moral support. It was during a discussion with Sylvain that the idea for electronic pupil cycling emerged. I also thank all those who gave their pupils to science, and especially those whose pupils behaved as the theory predicted (Marie-Claude, Figure 3.4.1; Michel Laurence, Figures 3.2.2 and 3.2.6; and John Milton, most of the other experimental figures).

A very special thanks goes to Tara, for coping with my thesis hysteria and for all the encouragement she provided. I also thank my parents for their continuing moral support for all these years. Further, I wish to acknowledge all those who have made life at McGill so memorable, and especially : Antoine Saucier, Reinhart R^2 Richter, Ian Graham, Jacques Mainville, Robert Plamondon, Chris Roland, Ross Thompson, Ralf Bruening and Nick Provatas (my physics inmates), as well as Marc Courtemanche, Zeng Wanzhen, Ehud Isacoff, Sara McFarlane and Allan Mandelzys (in Physiology). I also thank the students who offered their help at various times in this project . Josée Morissette, Jérome Losson and Christian Cortis. And many thanks to Ian, Lou, David and the rest of the bunch at Café Santropol for keeping me sane and fed.

Finally I express my gratitude towards the Natural Sciences and Engineering Research Council of Canada (NSERC) for the financial support it has provided me during the first three years of this thesis, and also towards the J.W. McConnell Foundation for supporting me in the last year.

TABLE OF CONTENTS

LIST OF FIGURES

LIST OF TABLES

CONTRIBUTIONS TO ORIGINAL KNOWLEDGE

1. This thesis is the first extensive theoretical and experimental study of oscillations and bifurcations in a human neurological control system.
2. Pupillary oscillations are studied using nonlinear delay-differential equations (DDE's) and bifurcation theory (Section 2.2). A physiologically sound model accounts for the nonlinear gain of this reflex (Section 2.2.5) and explains why response asymmetry is enhanced by piecewise constant feedback (PCNF) but not by smooth negative feedback (SNF) (Sections 2.2.9 and 2.3.9).
3. For SNF, the model exhibits a supercritical Hopf bifurcation as gain or delay is increased (Section 2.3.6). A double oscillation in SNF reported by Stark[1] is shown not to correspond, as suggested, to a bifurcation to a 2-torus (Section 2.3.9).
4. The connection between nonlinear dynamics and transfer function analysis is established in the context of a specific neural delayed feedback system (Section 2.3). The model is shown to be compatible with earlier transfer function analyses.
5. The model for PCNF-induced oscillations can be used to separately assess the state of neural pathways for constriction and dilation (Section 3.2). Clinical implementation of PCNF provides a strong diagnostic tool for demyelinative optic neuropathy (a common symptom for multiple sclerosis) (Appendix B). Insight into the theory and measurement of retinal integration and adaptation is also given (Section 3.4.5).
6. Bifurcations and complex aperiodic behavior are induced in a neural control system clamped with external piecewise constant mixed feedback (PCMF) (Sections 3.3 and 3.4).
7. We analyze complex aperiodic behavior in the pupil light reflex in terms of a quantitative model (Sections 3.3 and 3.4). Noise is shown to limit observability of complex deterministic dynamics in such a system.
8. Multistability in a first order DDE with PCMF is demonstrated (Section 3.4).
9. A new integration method for DDE's is proposed. For equal integration time steps, the accuracy of the new method is close to that of a fourth order Runge-

Kutta method (Section 4.8), and decreases computation time by a factor of four.

10. Solutions and bifurcations of DDE's are studied from the density point of view (Section 4.3).
11. Analysis of a Hopf bifurcation in a noisy neural system is performed using amplitude and period distributions rather than the stationary probability density of model solutions (Section 5.3).
12. Critical behavior of the pupil light reflex at a Hopf bifurcation is studied using SNF. Numerical simulation of a DDE with additive and multiplicative Gaussian colored noise agrees with the observation that relative fluctuations in amplitude are larger than those in period (Section 5.3).
13. Critical behavior of the pupil light reflex at oscillation onset using PCNF is studied. The observation that relative fluctuations in period are larger than those in amplitude is explained theoretically using an adiabatic elimination technique in the model DDE (Section 5.3).
14. Noise-induced transitions at a Hopf bifurcation in a DDE with multiplicative and additive noise are discovered. The effect of noise amplitude and correlation time on the postponement of the bifurcation point are studied (Sections 5.3 and 5.4).
15. It is shown that hippus is not chaos in a negative feedback loop with delay (Section 2.2.8). From a study of critical behavior, hippus is found to behave very much like noise (Section 5.3).
16. Approximations to DDE's are studied via distributed delays. It is shown that precise time-localization of memory destabilizes delayed feedback systems (Section 4.4).
17. We verify numerically that the stationary density of the Fokker-Planck equation (in either the Ito or Stratonovich case) for a supercritical (Landau equation) and subcritical system converges to a Dirac delta function when it is not normalizable (Appendix A).
18. A connection between the Hopf bifurcation in a DDE and the first pitchfork (or "period doubling") bifurcation of the map obtained in the singular limit is derived (Section 4.6).

1. INTRODUCTION

> "For all men strive to grasp what they do not know, while none strive to grasp what they already know; and all strive to discredit what they do not excel in, while none strive to discredit what they do excel in. This is why there is chaos."
>
> Chuang-Tzu (369-286)

This thesis studies the periodic and aperiodic oscillations that arise in neural delayed feedback systems. Oscillations and fluctuations are the subject of nonlinear dynamics and statistical mechanics, while the study of neural feedback systems draws from the fields of neurophysiology, neurology, biomathematics and bioengineering. Hence this study brings together tools from many fields to achieve an understanding of how neural systems generate oscillations in a noisy environment.

In this introductory chapter, the concepts of neural system and delayed feedback are first defined and then examples of neural delayed feedback systems are given. Attention is then focussed on nonlinear dynamics, and especially on its recent popularity as a modelling tool for simple and complex oscillatory phenomena. Finally, nonlinear dynamics and neural delayed feedback systems are brought together to explore the properties of neural delayed feedback systems when their activity is oscillatory.

1.1 NEURAL SYSTEMS.

In a broad sense, the term neural system designates assemblies of neurons (nerve cells) of varying numbers, ranging from small circuits comprising two interconnected neurons to large scale neurological control systems or brain structures such as the hippocampus, the thalamus or the visual cortex. We define a neural system as an entity within the nervous system that accomplishes a specific function which can be assessed by the measurement of appropriate quantities called "neural correlates". Examples of neural correlates are the membrane potential of a neuron, which determines the rate of generation of action potentials (i.e. the rapid membrane depolarization-repolarization sequence which propagates as a wave of electro-chemical activity down the axon), or the mean firing rate of action potentials of a population of neurons

Depending on their precise configuration and function, neural systems can be viewed as input-output systems and/or autonomous systems Input-output neural systems generate an output response to an incoming stimulus, e.g the frequency at which a neural oscillator generates action potentials can be viewed as the response (output) to the stimulus intensity (input). Autonomous neural systems generate a pattern of activity or rhythm on their own (pacemaker cells belong to this class). If a system is spontaneously active but modifies its activity in response to a change in its environment (which is probably the case for almost all neural systems), then it can also be viewed as a hybrid between an autonomous and an input-output system.

In all neural systems, the concept of feedback is essential. By "feedback system" we mean a system whose output depends on both its input and output. The influence of the input on the output or of the output on itself is either instantaneous, or involves certain delays associated with the propagation of signals. This is particularly true in neural systems, in which the time required for action potential propagation and synaptic events is not negligible; in fact, the delay can be an important component of the dynamic behavior of the neural system. The simple case of two neurons interacting through their mutual connections can be viewed as a feedback configuration between two neural oscillators. For example, the first neuron can have an excitatory influence on the second neuron which in turn has an inhibitory influence on the first. This "recurrent inhibitory circuit" is ubiquitous in the nervous system and provides a simple example of delayed neural feedback (the delay being the time for neural activity to propagate around the loop). By extension, a single neuron that inhibits or excites itself by the collateral branches of its axon constitutes a delayed neural feedback system.

We have distinguished between autonomous and non-autonomous oscillations, where these terms are used in the same sense as in classical mechanics. Non-autonomous oscillations arise in a system which is forced by an externally imposed rhythm ; as a consequence its mathematical formulation explicitly contains the time variable. Autonomous systems contain time only implicitly through the dependence of the state variables on time. The existence of bounded autonomous oscillations in a system is a sign of nonlinearity, since linear systems can sustain finite amplitude oscillations only under periodic forcing or when their eigenvalues are purely imaginary. Thus the theory of bounded autonomous oscillations belongs to the realm of nonlinear dynamics.

1.2 NONLINEAR DYNAMICS.

There has been much focus in the last two decades on the ability of certain simple nonlinear systems to generate very complicated dynamical behaviour. Further, these systems undergo "bifurcations" as parameters in the equations governing their time evolution are altered. A bifurcation represents a change in the topology of the phase space of such a system, i.e. the vector space spanned by the degrees of freedom of the system in which the point in this space corresponding to the state of the system evolves in time. A topological change can be viewed as a qualitative change in the phase space trajectory. For example, the motion of a damped harmonic oscillator is a spiral into the origin of the phase space spanned by its position and velocity coordinates. This motion can be seen as the projection onto the phase space plane of the motion of a marble settling to the bottom of a bowl. This bowl can be viewed as a potential function which depends on the phase space coordinates. If the convexity of this bowl is controlled by some parameter, and if at a given value of this parameter the shape of the bowl goes from convex to concave (i.e. the topology has changed) the motion will no longer be directed toward the origin. This qualitative change is an example of a bifurcation Mathematically the motion in phase space is governed by a set of nonlinear coupled differential equations, and the bifurcations correspond to certain changes in the eigenvalues of the differential operators at fixed points (also called critical points), i.e. points in phase space where all time-derivatives are zero

Recently, simple mathematical models exhibiting bifurcations have enjoyed great popularity in many fields of science including physiology and medicine Their attractiveness lies both in their economy of representation, i.e. very few degrees of freedom and nonlinearities are needed to generate a variety of simple and complex behaviours, and their phase space motions of perplexing beauty The most intriguing of all is chaos, a special brand of phase space motion which never repeats itself, despite being governed by deterministic equations. This type of motion exhibits what is known as sensitivity to initial conditions This means that two identical chaotic experimental systems, prepared in what seems to be the same way will nevertheless follow different trajectories in phase space after a certain time. This is because it is not possible, due to finite experimental accuracy, to prepare two real physical systems in precisely the same way, and chaotic systems amplify errors exponentially while remaining in a bounded region of phase space.

The theory of nonlinear dynamics and chaos has been evolving since the time of Poincaré[2], who wrote about intrinsic randomness and sensitivity to initial conditions in relation to the three body problem The recent interest in nonlinear dynamics and chaos and their infiltration into many areas of science is largely due to the advent and availability of computational power since the 1960's. Further, since the pioneering work of Lotka[3], Volterra[4] and Raschevsky[5] in population and mathematical biology, and of van der Pol[6] in electrical engineering, the theory of dynamics has been actively evolving through its applications to complex nonlinear systems outside mainstream physics. These fields fostered new ideas and provided problems in which novel tools from the theory of dynamics could be tested, both theoretically and experimentally.

Probably what is most appealing about chaotic dynamics is the deterministic alternative it proposes to stochastic processes. Like a stochastic process, a chaotic system also generates "random" behaviour. Aperiodic behaviour once thought to be due to noise could now be due to chaos, which gives a new order to the phenomenon because chaos is deterministic. Many investigators in diverse fields have felt compelled to reinterpret noisy data in the face of this new paradigm. Since chaotic motion is in principle predictable, its intrinsic randomness has often been relegated to the rank of "pseudo-randomness". In fact chaotic systems are currently used as pseudo-random number generators (see e.g. Li and Yorke[7]).

For a given mathematical model, chaos is not "ubiquitous" ; when it occurs, it does so over a range of parameters Further, there are "bifurcation routes" leading to chaos (for a review see Schuster[8], Devaney[9]). Simply stated, the route refers to a precise sequence of bifurcations that occur as one or more parameters are varied, until chaotic motion sets in at a specific parameter value For example, in the period-doubling route to chaos (also known as the Feigenbaum scenario), the period of the solution to the equations of motion undergoes sequential doublings as a parameter varies, until the period is effectively infinite and the solution aperiodic. The route depends on the system, and different routes can exist for the same system, depending on the direction followed in parameter space. Further, different routes may lead to different kinds of chaotic motion. The properties of these different chaotic motions have been characterized using tools from various fields such as dynamical systems theory (Guckenheimer and Holmes[10], Devaney[9]), measure theory and information theory (Farmer[11], Farmer et al.[12]) and ergodic theory (Lasota and Mackey[13]).

The study of how experimental systems bifurcate and sustain chaotic motion is actively being pursued in many different fields (for a review, see Hao Bai-Lin[14], Cvitanović[15] and Holden[16]). The experimental demonstration that a system is chaotic depends on how well the dynamics of the system are understood The strongest demonstration involves showing that a sound theory quantitatively predicts the observed route or routes to chaos. It may be that the theory agrees only qualitatively with measurements, or that a phenomenological model shows agreement with the data. If the theory is not well understood or simply nonexistent, the experimental identification of a known route to chaos can be quite convincing.

In all these cases, the data analysis can be supplemented by one of several algorithms measuring, e.g., the rate of divergence of nearby trajectories (Lyapunov exponents), the fractal dimension of the attractors on which the systems are assumed to evolve or the rate of loss of information (Kolmogorov entropy) (see Schuster[8] or Mayer-Kress[17] for a review). Some algorithms are capable, at least in computer experiments, of assessing the relative proportion of noise and chaos in a time series[18]. Admittedly the weakest proof for the existence of chaos, it is often the only analysis one can implement, as in the case of electro-encephalographic data[19]. These algorithms must be used with caution, for it is not well understood what they are revealing about the data. In fact, they are designed to characterize steady-state behaviour on attractors (see Section 4.2). Real data, and especially physiological data, is subject to transients and nonstationarity, and often reflects phenomena occurring on many different time scales (for a review see Milton et al.[20]).

The identification of simple bifurcations is the gateway to understanding more complex dynamical behaviour, since they are the clear signature of nonlinearity in the system. It is important to realize however that, in the presence of noise, irregular oscillations can appear in the vicinity of bifurcation points, even far from the chaotic regime (see Chapter 5). In these cases, the noise is amplified at the bifurcation because the rate of decay of perturbations goes to zero, a phenomenon called "critical-slowing down". Further the parameter values at which bifurcations occur can be shifted by noise, and a bifurcation can appear where there was no bifurcation in the deterministic case. These effects are known as "noise-induced transitions"[21]. Noise can also induce chaotic behaviour[22] or enhance the emergence of coherent behaviour out of chaos (a phenomenon known as noise-induced order[23]). Hence, the analysis of nonlinear dynamical systems is complicated by noise. The influence of noise on simple bifurcations in neural systems is a major focus in this thesis.

1.3 NONLINEAR DYNAMICS AND NEURAL SYSTEMS.

Nonlinear dynamics and chaos have infiltrated the field of medicine, and of physiology in particular, since the work of Mackey and Glass[24,25] more than ten years ago. They associated qualitative changes in the dynamical behaviour of certain physiological variables with bifurcations in model equations governing the physiological dynamics. Examples of these variables are circulating blood cell numbers, neural firing rates, and the partial pressure of carbon dioxide in the blood. These authors went further to propose that these bifurcations could, in certain cases, be associated with the onset of a pathological state, which led to the concept of "dynamical disease". Since, these ideas have permeated physiological dynamics (reviews can be found in Glass and Mackey[26] and in Degn et al.[27]), and experimental evidence for biological chaos in simple cell systems *in vitro* has been given[28,29,30].

In this thesis, concepts from the two preceding sections are brought together to explore the deterministic and stochastic properties of neural delayed feedback systems when their activity is oscillatory. Specifically the thesis theoretically and experimentally addresses the following questions: 1) Can bifurcations and chaos realistically occur in large neural systems, and what are the difficulties involved in asserting such results?; 2) How easy is it to identify a bifurcation in the presence of high noise levels?; 3) Is it possible to obtain quantitative agreement between experiment and theory?; and 4) Can the analysis of bifurcations in the presence of noise shed light on system nonlinearities and on the origin and properties of the noise sources?

To understand what neural delayed feedback systems do and how they do it, one is faced with the problem of measurement. A system is needed whose physiology is well characterized, which can be non-invasively monitored and controlled, and as closely mimics the *in vivo* situation as possible in order for results to be relevant for intact neural systems.

The thesis focusses on the human pupil light reflex, a delayed neural feedback system which satisfies all these requirements and whose study has a history of at least 2000 years This involuntary reflex, with a response delay of ~ 300 msec, has been extensively studied in the bio-engineering literature as the paradigm of neurological control systems. It also exhibits a variety of interesting dynamical phenomena (reviewed in Sections 2.1 and 2.2) ranging from simple oscillations to ongoing aperiodic behaviour. In fact the pupil light reflex has all the properties required to address the questions formulated above.

1.4 ORGANIZATION OF THE THESIS.

The organization of the thesis is as follows. We first develop, in Chapter 2, a general theoretical framework in which to study pupillary oscillations. Our model, based on physiological and anatomical data, is framed in terms of a nonlinear delay-differential equation. From the large literature on this reflex, we choose only those aspects important for the generation of oscillations. One modelling criterion is to produce a representation that can make predictions in terms of realistic observables and allow for parameter estimation from experiment. This is in contrast to the wealth of models in the neural dynamics literature which, although interesting from a theoretical point of view, will be "immune" to experimental verification for many decades to come.

In Chapter 3, we investigate how complex dynamics can be sustained by the pupil light reflex. The experiment involves setting up autonomous oscillations in this reflex using external electronic feedback by modifying a technique developed by Stark and Sherman[31]. This study clarifies how a specific neural system generates complex deterministic motion in the presence of noise, and how a physiologically relevant model quantitatively predicts this behavior. The major conclusion is that bifurcations may be induced in this neural control system. However, the analysis of complex periodic motion is severely limited by noise.

As a consequence, Chapters 4 and 5 concentrate on simple deterministic behaviour in the presence of noise. In particular, noise-induced transitions (which belong to the broader class of nonequilibrium phase transitions) at the Hopf bifurcation in a prototypical delay-differential equation (DDE) are studied (see also Appendix A).

Chapter 4 develops our understanding of the dynamics of DDE's using theory and numerical simulation. Further, DDE's are studied from a new point of view, that of stationary densities in one variable.

Chapter 5 looks at the stochastic Hopf bifurcation in a first order DDE with : 1) smooth negative feedback; and 2) piecewise constant negative feedback (PCNF) These two types of feedback are experimentally important (see Section 3 2, and also Appendix B for a precise application of PCNF as a diagnostic tool for multiple sclerosis). A second set of experiments, done in collaboration with a group from the Medical Physics Department of the Free University in Amsterdam, is presented They involve inducing simple oscillations in the pupil light reflex using SNF and PCNF. The Amsterdam group provided the data for the SNF oscillations.

The deterministic and stochastic behaviour of the pupil area oscillation period and amplitude at oscillation onset are analyzed. The proper characterization of the noise is shown to be necessary to explain our observations. The interaction of the noise with the deterministic components is used to elucidate the properties of this reflex and the origins of the noise. This type of study may yield useful tools to diagnose neurological control systems since, for example, noise is thought to arise from the activity of other centers in the brain impinging on the pathways of the pupil light reflex. The activity in these centers is thus mirrored in some cryptic way in that of the pupil, and it may be deciphered using the appropriate analysis.

The common theme of the chapters is understanding noisy nonlinear oscillations in neural delayed feedback systems, and also in DDE's because of the importance of these in our models. However, each chapter relies on different tools to carry out different parts of the program. It is hoped that the reader will appreciate the presentation of the relevant introductory material at the beginning of each chapter, rather than be overloaded at the outset in this introductory chapter. Since most of the thesis is composed of manuscripts which are either accepted or submitted for publication, there is inevitably some overlap between the introductory remarks of the chapters and the introduction sections of the papers. Further, the introductory sections of the papers overlap to some extent, as the papers all share common elements of the same general research program.

The Faculty of Graduate Studies and Research of McGill University requires that the following text from the **GUIDELINES CONCERNING THESIS PREPARATION** be cited in full in the introductory sections of any thesis to which it applies. Appendix E details the contributions of the author to the manuscripts included in this thesis.

MANUSCRIPTS AND AUTHORSHIP.

The candidate has the option, subject to the approval of the Department, of including as part of the thesis the text, or duplicated published text (see below), of an original paper, or papers. In this case the thesis must still conform to all other requirements explained in **Guidelines Concerning Thesis Preparation**. Additional material (procedural and design data as well as descriptions of equipment) must be provided in sufficient detail (e.g. in appendices) to allow a clear and precise judgement to be made of the importance and originality of the research reported. The thesis should be more than a mere collection of manuscripts published or to be published. It must include a general abstract, a full introduction and literature review and a final overall conclusion. Connecting text which provide logical bridges between different manuscripts are usually desirable in the interests of cohesion.

It is acceptable for theses to include as chapters authentic copies of papers already published, provided these are duplicated clearly on regulation thesis stationery and bound as an integral part of the thesis. Photographs or other materials which do not duplicate well must be included in their original form In such instances, connecting texts are mandatory and supplementary explanatory material is almost always necessary.

The inclusion of manuscripts co-authored by the candidate and others is acceptable but the candidate is required to make an explicit statement on who contributed to such work and to what extent, and supervisors must attest to the accuracy of the claims, e.g. before the Oral Committee. Since the task of the Examiners is made more difficult in these cases, it is in the candidate's interest to make the responsabilities of authors perfectly clear. Candidates following this option must inform the Department before it submits the thesis for review.

CHAPTER 2

MODELLING AUTONOMOUS OSCILLATIONS IN THE HUMAN PUPIL LIGHT REFLEX.

STILL POOLS

[*Cypress*]

Cypress.
(Stagnant water.)

Poplar.
(Crystalline water.)

Willow.
(Deep water.)

Heart.
(Water of the pupil.)

Federico Garcia Lorca
First Songs, 1921

This chapter starts with a brief introduction to neurons and pupillary physiology. The core of the chapter comprises two papers. The first (Section 2.2), entitled "Modelling autonomous oscillations in the human pupil light reflex using nonlinear delay-differential equations", has been published in the *Bulletin of Mathematical Biology*. The title is self-explanatory. The second paper (Section 2.3), entitled "Insight into the transfer function, gain and oscillation onset for the pupil light reflex using nonlinear delay-differential equations", was published in *Biological Cybernetics*. It provides the connection between the approach of this thesis, based on nonlinear dynamics and bifurcation theory, and the control systems engineering approach which has permeated studies of pupillary dynamics for more than thirty years (see Stark[32] for a review). The conditions under which our model is compatible with previously derived transfer function analyses are determined. Particular attention is given to the onset of oscillation and to the asymmetry reflected in the speeds of constriction and dilation. Further, we modify an explanation given by Stark[1] for the origin of a double oscillation induced in the pupil light reflex using external electronic feedback. In these papers, the Hopf bifurcation is used as a tool to understand the onset of oscillation. The full Hopf bifurcation theorem is given in Section 5.1.

2.1 INTRODUCTION.

The pupil is the black hole in the middle of the colored part (iris) of the eyeball formed by the iris muscles. Light enters through the pupil and falls on the retina.

The autonomic (i.e. involuntary) nervous system uses the signal produced in the optic nerve to control the activity of the iris muscle and, as a consequence, pupil size. The major function of the pupil is to regulate the retinal light flux until the slower adaptation processes involving the retinal neurons set in, and to control the depth of field for visual acuity[33]. It is part of a "synkinetic triad" which refers to the three simultaneous events that occur when, for example, a subject changes his focussing distance from far to near: 1) the lens increases its curvature, thereby decreasing its focal length; 2) the eyes converge; and 3) the pupils constrict. This is why one must specify pupil *light* reflex, since the pupil also reacts, through the action of the autonomic nervous system, to non-visual stimuli and to focussing cues

The pupil light reflex has been studied for more than 2000 years (see Loewenfeld[34]). Differences in pupil size attracted the attention of early physiologists in the Roman empire. Plinius (23-79) and Galen (135-201) used specific plant extracts to dilate the pupil prior to cataract surgery. Centuries later, Rhazes (850-923) first recognized that the normal pupil contracts in light and dilates in the dark. Shortly thereafter, Ammar (c.a. 1000) assumed the iris to be a muscular organ. There has been a sustained interest in the pupillary system since the 1600's, as its role in the regulation of light and in the accommodation (focussing) reflex were discovered.

2.1.1 Neurons.

Before discussing the basic neural circuitry of the pupil light reflex, a brief summary of the general properties of neurons is in order.

The neuron is an excitable cell[35]. It requires a constant source of metabolic energy to move ions against electrochemical gradients in order to maintain a potential difference across its membrane ($\simeq -60$ mV, the inside being negative with respect to the outside). When the membrane is depolarized above a certain threshold ($\sim$ 40 mV), there is a sequence of ionic events which cause the membrane potential to rapidly depolarize to a positive value and then to repolarize to the original value. This sequence generates a potential change known as the action potential Although these events occur in the cell body (at the soma), they trigger a depolarization-repolarization wave that travels down a thin process extending out of the cell body called the "axon" (bundles of axons are called nerves).

A neuron communicates with other neurons at special junctions called "synapses"[33]. When the propagated action potential arrives at the end of the axon, it causes molecules known as "neurotransmitters" to be released from "synaptic boutons". The transmitter rapidly diffuses across the synaptic cleft (200-300 Å) from the presynaptic neuron to the postsynaptic neuron, where it binds to specific receptor molecules on the cell membrane. These receptors are generally located on the dendrites of the postsynaptic neuron, which are hairlike processes that channel information about external stimuli to the cell body. The transmitter binding causes ion channels to open and/or close in a variety of ways. These changes temporarily disrupt the ionic balance of the postsynaptic cell, generating postsynaptic potentials or PSP's. These potentials are either excitatory (EPSP's) or inhibitory (IPSP's), depending on the neurotransmitter and the receptor The PSP's propagate decrementially (as in cable conduction) down the dendritic tree to the cell body, in contrast to axonal wave propagation which is a regenerative process that maintains the action potential amplitude constant. The EPSP will depolarize the postsynaptic cell, while the IPSP hyperpolarizes it.

The balance of the excitatory and inhibitory influences at the soma at any given time determines the rate at which the neuron fires action potentials. In general the firing frequency is proportional to the amount of depolarization above the firing threshold. In simple terms, stimulus strength is encoded in the firing frequency. Action potential generation is an all-or-none process : if the stimulus is too small or inhibitory, no action potentials will result.

Neurons connecting to muscle cells are called motoneurons. They reside in " motor nuclei" or "motoneuron pools". Muscle cells are also excitable cells. Acetylcholine is the neurotransmmitter at the neuromuscular junction, i.e. at the synapse between a motoneuron and a muscle cell. The action potential in the muscle cell, triggered by the diffusion of acetylcholine, causes a sequence of chemical reactions and molecular movements leading to the contraction of the muscle cell. The strength of the contraction is generally proportional to the firing frequency of the motoneuron.

2.1.2 Circuitry of the pupil light reflex.

Figure 2.1.1 shows a schematic of the neural pathways mediating the pupil light reflex, while Figure 2.1.2 illustrates the pathways of the accommodation reflex which enable the eye to focus on a target[36]. These two reflexes have certain pathways in common. Note the mirror symmetry of the structures involved in both reflexes.

At the retina, photons are absorbed by certain molecules, which initiates a complex series of biochemical reactions leading to a change in membrane potential in the rod or cone cell[37]. This activity is relayed to other retinal neurons before reaching the retinal ganglion cells. The axons of these neurons join together to form the optic

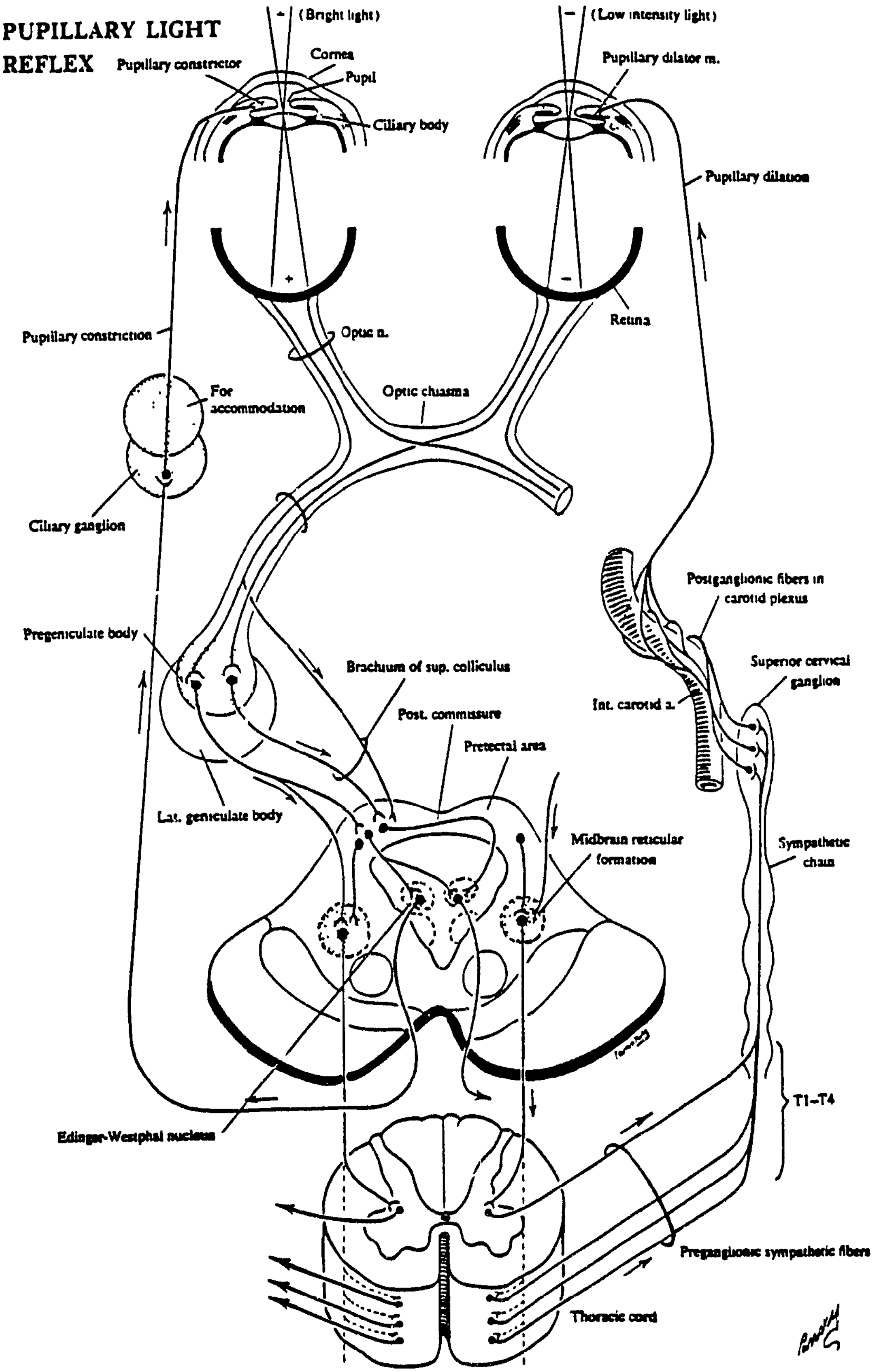

Figure 2.1.1 Schematic diagram of the neural pathways for the pupil light reflex. All structures are symmetric with respect to the midline, but for clarity, the parasympathetic pathway is drawn on the left and the sympathetic pathway on the right. All connections shown are excitatory. See text for explanation. (From Pansky and Allen[36], p.399)

ACCOMMODATION REFLEX

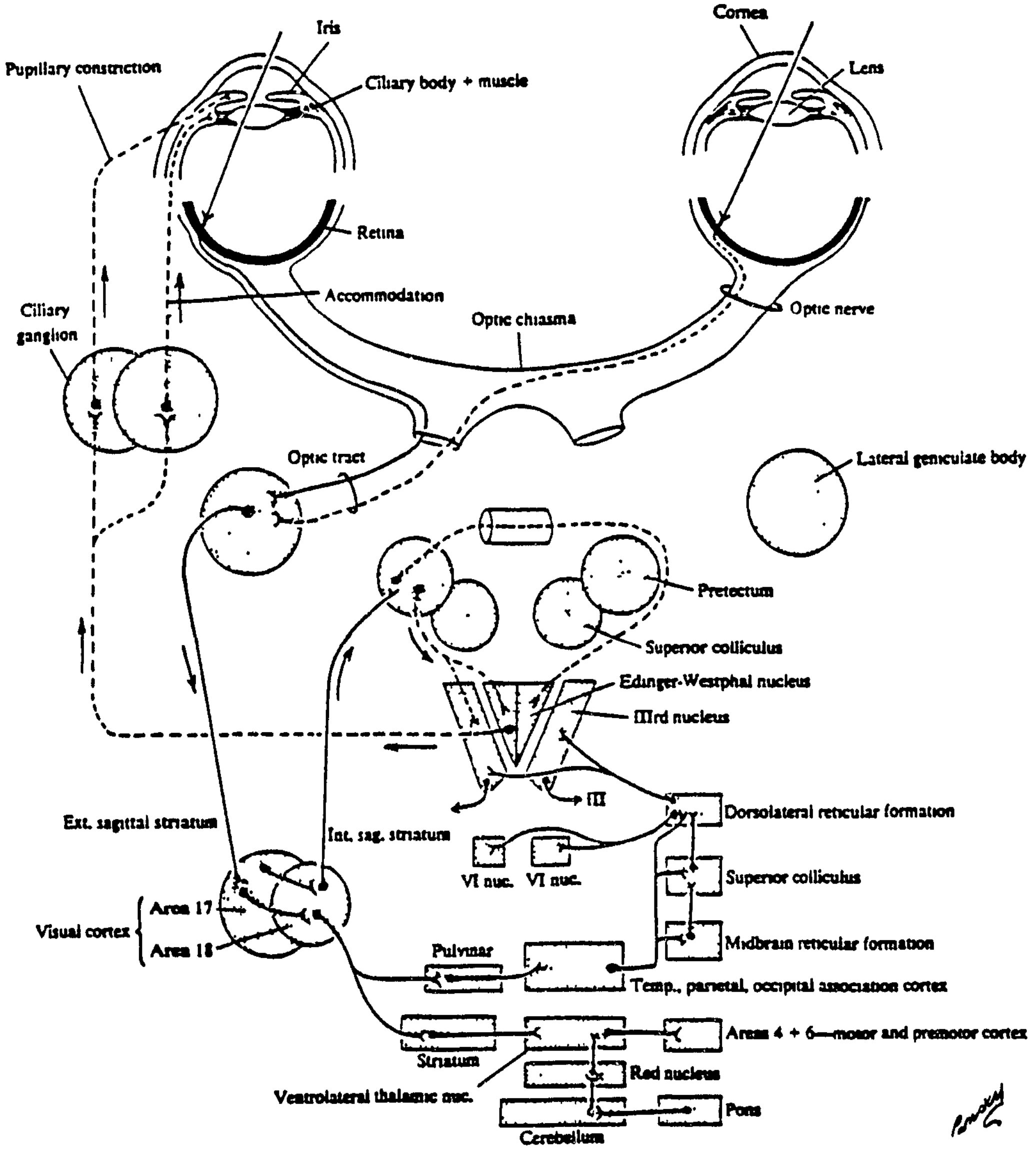

Figure 2.1.2 Schematic diagram of the neural pathways for the accommodation reflex. In contrast to the pupil light reflex, which is a brainstem reflex (Figure 2.1.1), the accommodation reflex involves the visual areas of the cortex. The final motor pathway of this reflex is the same as for the pupil light reflex. See text for explanation. (From Pansky and Allen[36], p.397)

nerve (the IInd nerve). Before reaching the lateral geniculate body (LGB), which is the way station where most optic nerve axons synapse on the way to the visual cortex, a small fraction of axons branch and these branches synapse in the pretectal nucleus (PTN) in the midbrain. Other axons synapse in the pregeniculate body, from which there is a projection to the pretectal area. It is not known whether there are retinal cells that are specific to the pupil light reflex. The connection between the optic nerve and the PTN belongs to the parasympathetic pathway, which is involved in constriction. Before discussing this pathway, we briefly describe the sympathetic pathway, which is responsible for dilation.

The afferent portion of the sympathetic pathway also begins at the retina. A fraction of the optic nerve axons synapse onto neurons in the pregeniculate body which in turn synapse in the midbrain reticular formation These neurons also receive input from the hypothalamus. The pathway then runs from the reticular formation to the spinal cord. It exits the spinal cord and goes up the cervical sympathetic trunk to synapse in the superior cervical ganglion From there, the path continues across the carotid plexus and finally reaches the radially arranged iris dilator muscle. This description is, however, complicated by the finding[38] that parasympathetic cells in the Edinger-Westphal nucleus of the cat cause the iris to dilate in response to focal electrical stimulation. Further, in response to an increase in retinal light flux, parasympathetic neurons in the rabbit have been shown to either increase or decrease their firing activity, i.e. these neurons are either ON units or OFF units[39]. The precise role of the sympathetic system and the physiology of dilation in general are still unclear.

The route of the parasympathetic pathway is known in more detail than the sympathetic pathway[37]. Each pretectal nucleus receives input from both retinas, because of the crossing at the optic chiasm. There is evidence of decussation at this level, meaning that the PTN's from both hemispheres communicate across the midline. There is stronger evidence that each PTN projects to the ipsilateral and contralateral Edinger-Westphal nucleus (EWN). The EWN is the motor nucleus that drives the circularly arranged iris sphincter muscle whose activation results in pupil constriction. Because each EWN receives activity from each retina, the pupil light reflex is consensual : stimulation of one retina causes both pupils to constrict.

The EWN is also the motor nucleus for the ciliary muscle, the component of the accommodation reflex that controls the curvature of the lens[37] (see Figure 2.1.2).

The pathway for the accommodation reflex goes from the optic nerve to the anterior occipital cortex, over to the superior colliculus and down to the EWN.

The axons of the EWN are part of the IIIrd nerve which synapses in the ciliary ganglion (CG). The axons of the ganglion cells innervate the sphincter muscle and the ciliary muscle. Although the accommodation and light reflexes both synapse in the EWN and in the CG, there is evidence that their pathways remain distinct throughout. However, the activity of the accommodation reflex certainly influences that of the pupil light reflex, because of the synkinetic triad. This most probably occurs in the EWN.

The activity in other regions of the brain is known to influence that of the pupil light reflex. Most of these influences are felt at the level of the EWN[40]. Spinoreticular and brainstem (Vth and VIIth N.) afferents have an excitatory effect on the EWN, causing the pupils to constrict. The sensorimotor and frontal cortices, the reticular activating system, other brainstem afferents as well as corticothalamo-hypothalamic and cortico-limbic pathways are known to inhibit the activity of the EWN (i.e. they cause pupil dilation) One of the most important influences on the EWN is the inhibitory effect of the reticular activating system (RAS) which controls alertness. When a subject falls asleep, activity in the RAS decreases, which means that the EWN is less inhibited. As a result, the pupil constricts In fact it has been observed[41,42] in the cat and the rabbit that in the absence of any inputs, the EWN settles into a steady state of high spontaneous random activity The external inputs serve to depress and modulate this activity. It has been suggested that the relaxation of the sphincter in pupil dilation is caused by such inhibitory inputs rather than by an increase in sympathetic outflow[43].

Other neuron populations in the pupil light reflex have been shown to exhibit high firing activity. For example, retinal ganglion cells of cats fire randomly, and a visual stimulus may temporarily increase or decrease the mean firing rate, but is rarely able to suppress it for more than a few seconds[44]. In rabbits, neurons in the ciliary ganglion receive tonic synaptic input which is not decreased by darkness or by acute section of the optic nerve[45]. The majority of these neurons increase their mean firing rate in response to retinal illumination; other cells, however, decrease their rate during illumination.

2.1.3 Hippus.

The pupil area undergoes temporal fluctuations ranging in magnitude from 0 to

20 %. This noisy pupil activity is normal and is called "hippus"[37]. It can be seen even under conditions of constant illumination. Hippus occurs in closed loop and in open-loop also (i.e. when the pupil can not control the retinal light flux)[16]. Because it occurs in open-loop, it does not reflect an instability in the feedback loop of the light reflex (see Section 2.3.8). Since hippus is perfectly synchronized in both pupils, its origin has to be at a point in the reflex arc common to both pupils The magnitude of the fluctuations depends on the value of pupil area, and is maximum at midrange area values. It has been shown that this area dependence of the magnitude of hippus is the same regardless of whether the area is controlled by the accommodation reflex (keeping the illumination constant) or by the light reflex (keeping the accommodation level constant)[47]. Based on these observations, it has been suggested that the inputs to the EWN which are external to the pupil light reflex pathways, as well as the intrinsic stochastic behaviour of the EWN itself, might be the source of hippus.

It has also been suggested that hippus simply mirrors the ongoing fluctuations in lens curvature that characterize the accommodation reflex[17]. This would not be surprising given the existence of the synkinetic triad, and that 3% of the ciliary nerve goes to the iris sphincter, while 97% goes to the ciliary muscle, making crosstalk between these two motor pathways not unlikely There has been a preliminary reporting of the synchronization of pupil and accommodation fluctuations in certain subjects, but not in others[48] Whether the pupil light reflex and the accomodation reflex are synchronized or not is unclear, and the precise origin of hippus is still unknown.

Apart from hippus, the pupil light reflex (PLR) exhibits a wide range of dynamical behaviours[32,19] (see Table 1 in Section 2 2) in response to different stimuli One of the most interesting effects is seen in narcoleptic patients at sleep onset in the dark[50]. As they become more drowsy, their mean pupil area decreases until, at midrange pupil areas, the irregular hippus gives way to a regular oscillation having a period of $\approx$ 5 seconds. This phenomenon has also been reported in normal subjects[51]. The origin is not known Hence, despite centuries of investigation, much is left to be understood about this reflex. The fundamental problem is that the anatomy and physiology are not well known because the experiments are extremely difficult to carry out. It is somewhat surprising that many anatomically distinct midbrain structures are contiguous, and that the EWN, which is only one of the nuclei in the so-called "oculomotor complex", is confined to a region the size of a pinhead.

2.2 MODELLING AUTONOMOUS OSCILLATIONS IN THE HUMAN PUPIL LIGHT REFLEX USING NONLINEAR DELAY-DIFFERENTIAL EQUATIONS.

Abstract.

Neurophysiological and anatomical observations are used to derive a nonlinear delay-differential equation for the pupil light reflex with negative feedback. As the gain or the time delay in the reflex is increased, a supercritical Hopf bifurcation occurs from a stable fixed point to a stable limit cycle oscillation in pupil area. A Hopf bifurcation analysis is used to determine the conditions for instability and the period and amplitude of these oscillations. The more complex waveforms typical of the occurrence of higher order bifurcations were not seen in numerical simulations of the model. This model provides a general framework to study the different types of dynamical behaviours which can be produced by the pupil light reflex, e.g. edge-light pupil cycling.

2.2.1 Introduction.

An intriging aspect of the nervous system in health and disease is the widespread occurrence of complex dynamical behaviours, e.g. tremors and the electrical activity of the cortex (see, for example, Mackey and Milton[54]; Milton et al.[20]). Recently there has been a great deal of speculation concerning the role of nonlinear neural control mechanisms in generating some of these dynamical behaviours[55,56,57] These proposals have been based on mathematical studies of physiologically realistic equations in which qualitative changes in dynamics ('bifurcations') occur as certain parameters are varied. The changes in dynamics produced by parameter variation range from stable equilibria to simple and complex periodic oscillations to aperiodic (chaotic in the current vernacular) fluctuations[14,26]. However, experimental verification of these predictions has been hindered by the paucity of suitable models in which it is possible to study the dynamics that arise by parameter variation.

A neural feedback control mechanism which is amenable to manipulation is the pupil light reflex. As shown in Table 2 1, this reflex exhibits a wide range of dynamical behaviours, which are typically monitored by changes in pupil area. For example, irregular variations in pupil area ('hippus') occur spontaneously, whereas regular oscillations ('pupil cycling') can be induced by focussing a small light beam at the pupillary margin[58,59]. The period[60,61] and regularity[62,63] of pupil cycling are

TABLE 2.1
Summary of Spontaneous Dynamical Behaviors Exhibited by the Pupil Light Reflex

Type of Dynamical Behavior	Description	Reference
Regular oscillations		
Simple waveforms	Edge-light pupil cycle time	Campbell and Whiteside (1950) Martyn and Ewing (1986) Miller and Thompson (1978) Stark and Cornsweet (1958) Stern (1944)
	Pupil cycling with external electronic feedback ("clamping")	
	(i) Continuous negative feedback	Reulen *et al.* (1988) Stark (1962)
	(ii) Piecewise constant negative feedback	Milton *et al.* (1988, 1989)
Complex waveforms	Hippus in narcoleptic patients	Yoss *et al.* (1970)
	Pupil cycling with external "mixed" and delayed feedback	Longtin and Milton (1988)
Irregular oscillations	Intermittent irregular pupil cycling in demyelinative optic neuropathy	Milton *et al.* (1988) Ukai *et al.* (1980)
Noise-like fluctuations	Hippus	Bouma and Baghuis (1971) Stark *et al.* (1958)

altered by pathology within the pupil light reflex pathways.

An important feature of this reflex is the ease by which it can be manipulated and monitored noninvasively. In particular, it is possible to 'clamp' this reflex[1,62,64,65]. Clamping refers to an experimental technique in which the feedback loop of the reflex is first "opened" by focussing a small beam of light on the center of the pupil in order to circumvent the shading effect of the iris on the retina (see Stark and Sherman[31]). The feedback loop is then reclosed with an electronically constructed 'area comparator' relating changes in pupil area to changes in light intensity. Thus a precisely specified feedback can be inserted into the reflex. In this manner Stark[1] verified that pupil area oscillations could occur once the gain became sufficiently large. The "linear" properties of the reflex determined the frequency of these oscillations, whereas their shape and amplitude depended on the "nonlinearities".

Recent studies have emphasized clamping the pupil light reflex with piecewise constant types of feedback[20,62,64] . the light is either on or off depending on the value of the pupil area relative to certain area thresholds. The main advantages of the use of piecewise constant feedback over smooth feedback are 1) the pupil area oscillations are much easier to control experimentally[62]; and 2) the properties of the oscillations are better understood analytically[20,64,66]. This approach has resulted in a new technique for detecting optic nerve pathology[62] and moreover allows certain nonlinearities of the reflex to be isolated for detailed study (this paper). From the general point of view of nonlinear dynamics, this experimental paradigm of neural control provides unique opportunities to verify theoretical predictions, to draw attention to unexplained phenomena, and to assess the role of superimposed random variations ("noise") in shaping the observed dynamics[20,64]. It can be anticipated that insights obtained from studies of the clamped pupil light reflex can be applied to other neural control mechanisms as well.

Despite the attractiveness of the study of the pupil light reflex as a nonlinear dynamical system, we know of no previous attempts to model it from this point of view. Indeed previous investigators have focussed on the modelling of, for example, the response of the pupil to transient and steady state oscillatory light inputs, and of various nonlinearities in the reflex arc[1,32,46,49,67]. Here we use neuro-physiological and anatomical considerations to derive a model for the pupil light reflex. A bifurcation analysis of the resulting nonlinear delay-differential equation is used to characterize its dynamical behaviours and to examine the influence of parameter variations on them. This model provides a general framework in which it is possible to study the different types of behaviours produced by the pupil light reflex.

2.2.2 The pupil light reflex.

The pupil light reflex pathway is represented schematically in Figure 2.2.1. Pupil size reflects a balance between constricting and dilating mechanisms[37]. Pupil constriction is caused by contraction of the circularly arranged pupillary constrictor muscle which is innervated by parasympathetic fibers The motor nucleus for this muscle is the Edinger-Westphal nucleus located in the oculomotor complex in the midbrain. There are two main neural mechanisms for pupil dilation[34] . 1) a mechanism which involves contraction of the radially arranged pupillary dilator muscle innervated by sympathetic fibers (traditionally referred to as "active" reflex dilation); and 2) a mechanism which operates by inhibition of the activity of the Edinger-Westphal nucleus (traditionally referred to as "passive" reflex dilation) Pupil cycling occurs even when the sympathetic supply to the iris is cut surgically[62] or blocked pharmacologically[60]. Thus during pupil cycling, dilation is primarily the result of 1) a decrease in the afferent activity and 2) increased inhibition of the activity of the Edinger-Westphal nucleus. The role of the sympathetic nervous system seems to be primarily one of determining the average pupil size

This reflex functions as a time-delayed negative feedback system[32,46]. The time delay, or pupil latency time, is ~ 200-500 msec[62,68]. This time delay is much longer than would be anticipated simply on the basis of neural conduction times The part of the reflex in which this delay originates is presently controversial : some authors favour an origin in the midbrain[38], others suggest that it arises at the level of the iris and its musculature[68,69].

2.2.3 Model. The variable controlled by the pupil light reflex is the retinal light level (flux)[46], ϕ (lumens), which is equal to the illuminance, I (lumens/mm^2), multiplied by the pupil area, A (mm^2)

$$\phi = IA. \tag{2.2.1}$$

The retinal light flux ϕ is transformed, after a time delay τ_r, into neural action potentials which travel along the optic nerve. We assume that it is the rate of these action potentials, i.e. $N(t)$ = number of action potentials per unit time, which is

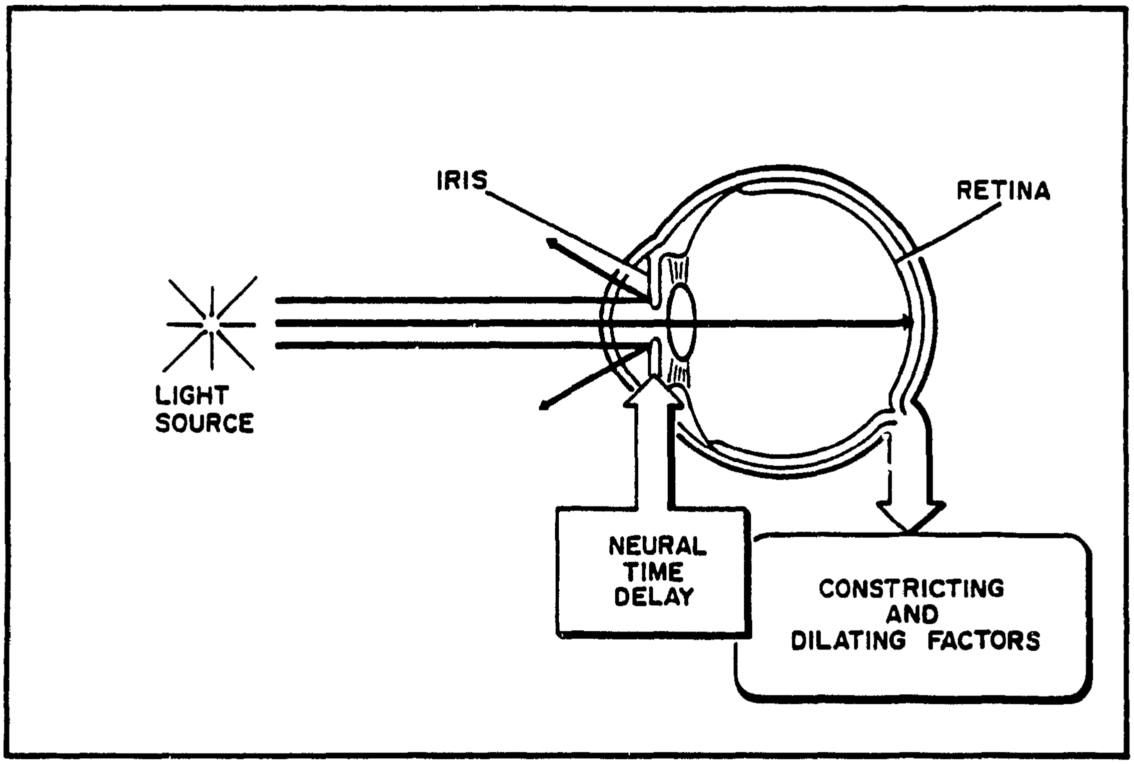

Figure 2.2.1 Simplified diagram of pupil light reflex. See text for explanation.

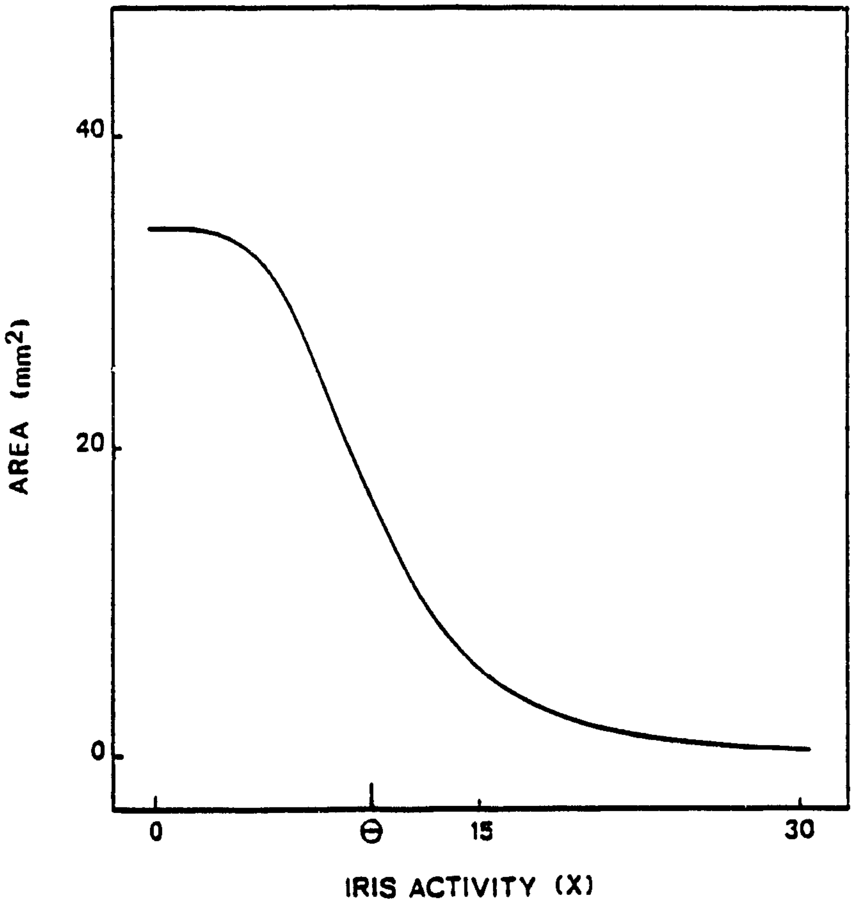

Figure 2.2.2 Plot of a Hill function (2.2.7) relating pupil area, A, to iris activity, x (solid line). Parameters are: $\Lambda = 30\ mm^2$, $\Lambda' = 0\ mm^2$, $\theta = 10\ mm^2$, $n = 4$.

important for reflex dynamics and that $N(t)$ is related to ϕ by

$$N(t) = \eta \ln \left[\frac{\phi(t - \tau_r)}{\bar{\phi}} \right] \tag{2.2.2}$$

where η is a rate constant, $\bar{\phi}$ is the threshold retinal light level (i.e. the light level below which there is no response), and the notation $\phi(t - \tau_r)$ indicates that this quantity depends on the retinal light flux at a time τ_r in the past. The logarithmic compression of light intensities at the retina has been discussed previously by Cornsweet[70] and is referred to as the Weber-Fechner law (see e.g. Webster[71]).

The afferent neural action potential rate, $N(t)$, gives rise to an efferent neural signal, $E(t)$, which is produced by the Edinger-Westphal nucleus after a time delay, τ_t. This efferent neural activity, also measured as the number of action potentials per unit time, exits the midbrain via parasympathetic fibers. We assume that

$$E(t) = \gamma' \ln \left[\frac{\phi(t - (\tau_r + \tau_t))}{\bar{\phi}} \right] \tag{2.2.3}$$

where γ' is a rate constant and τ_t is the midbrain time delay.

At the neuromuscular junction of the pupillary constrictor muscle, the neural action potentials result in the release of a chemical neurotransmitter (acetylcholine) which diffuses across the synaptic cleft, binds to specific receptors on the muscle membrane thus leading to the generation of muscle action potentials and initiating muscle contraction. These events require a time delay, τ_m. In this way the neural activity, $E(t)$, is transduced into tension in the constrictor muscle; this tension then produces a resulting pupil area. We first define a relationship between $E(t)$ and iris muscle activity, x, and then between x and pupil area, A.

The iris muscle activity, x, is determined by a number of factors which may include Ca^{++} concentration and diffusion, actin-myosin cross linking and the initial length and tension in the constrictor muscle. Since we are ultimately interested in pupil area, A, it is not necessary to exactly specify x. We take the relationship between $E(t)$ and x to be of the form[72]

$$\begin{aligned} E(t) &= M\left(x, \frac{dx}{dt}, \frac{d^2x}{dt^2}, \cdots\right) \\ &\simeq k \left(\frac{dx}{dt} + \alpha x \right) \end{aligned} \tag{2.2.4}$$

where α is a rate constant and k is a proportionality factor which depends on the definition and units of x used in the model. The justification for the first order approximation to $M(x, \frac{dx}{dt}, \frac{d^2x}{dt^2}, \cdots)$ is the success that the subsequent model has in predicting the experimentally observed oscillations in pupil area (see Longtin and Milton[64]; Milton et al.[20]).

By combining (2.2.3) and (2.2.4) we obtain the following nonlinear delay-differential equation

$$\frac{dx}{dt} + \alpha x = \gamma \ln \left[\frac{\phi(t-\tau)}{\bar{\phi}} \right] \tag{2.2.5}$$

where $\tau = \tau_r + \tau_t + \tau_m$ is the total time delay in the reflex arc and $\gamma \doteq \gamma'/k$.

Equation (2.2.5) is written in terms of muscle activity; however, experimentally it is pupil area that is more typically measured. In order to re-write (2.2.5) in terms of pupil area, A, it is necessary to have a function, $f(x)$, that relates muscle activity and pupil area, i.e.

$$A = f(x). \tag{2.2.6}$$

The function $f(x)$ must 1) meet the requirement that pupil area is positive and bounded by finite limits and 2) reflect the role played by elasto-mechanical properties of the iris in shaping pupil dynamics. In principle, $f(x)$ can be measured experimentally[73]. Here we consider one possible choice of $f(x)$ which satisfies the above requirements, i.e. the Hill function (Figure 2.2.2)

$$A = f(x) = \frac{\Lambda \theta^n}{\theta^n + x^n} + \Lambda' \tag{2.2.7}$$

where $\Lambda + \Lambda', \Lambda'$ are, respectively, the maximum and minimum pupil area ($\Lambda + \Lambda' > \Lambda' > 0$) and θ is the value of x for which pupil area is mid-range. A similar function, i.e. "S-shaped curve", has been proposed previously[53,74]. We show in Section 2.2.5 that this choice of $f(x)$ also reflects the nonlinear mechanical properties of the iris.

Using (2.2.7) we can re-write (2.2.5) in terms of pupil area, A, as

$$\begin{aligned} \frac{dg}{dA}\frac{dA}{dt} + \alpha g(A) &= \gamma \ln \left[\frac{\phi(t-\tau)}{\bar{I}\,\bar{A}} \right] \\ &= \gamma \ln \left[\frac{I(t-\tau)A(t-\tau)}{\bar{I}\,\bar{A}} \right] \end{aligned} \tag{2.2.8}$$

where $g(A) \equiv f^{-1}(A) = x$ (Figure 2.2.3), and we have made use of (2.2.1). Note that to solve (2.2.8) it is necessary to specify the initial functions $I(t)$ and $A(t)$ on the interval $t \in (-\tau, 0)$.

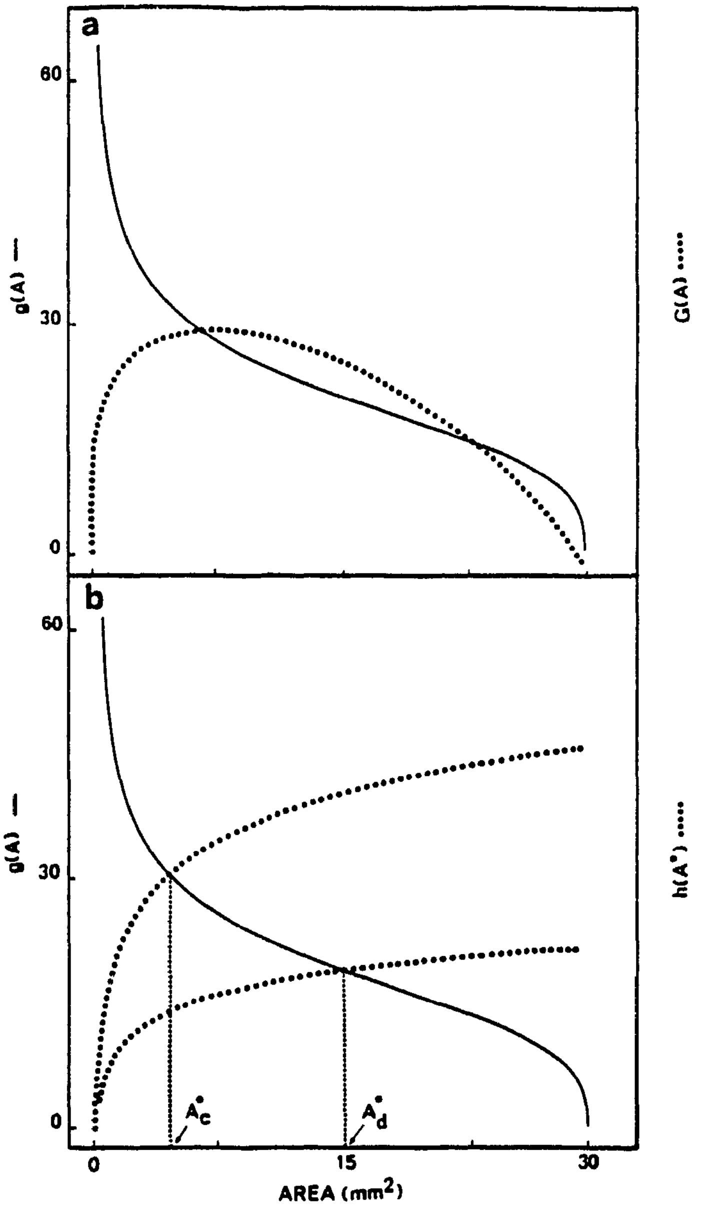

Figure 2.2.3 Plot of the inverse of the Hill function, $g(A)$, shown in Figure 2.2.2 (i.e. $x = f^{-1}(A) \equiv g(A)$) as a function of pupil area, A. In a) we compare $g(A)$ to the gain, G, which for $f(x)$ given by (2.2.7), can be written as

$$G(A) = -\frac{n\gamma A}{\alpha\Lambda\theta}\left[\frac{\Lambda}{A}-1\right]^{\frac{n-1}{n}}$$

where $\Lambda' = 0\ mm^2$. In b) we show a graphical method for determining the fixed points of (2.2.9) when $\alpha_c > \alpha_d$. The fixed point A^* is given by the intersection of $g(A)$ (solid line) and the right hand side of (2.2.9) which we have defined as $h(A)$ (dotted line). Parameter values have been arbitrarily set to $\Lambda = 30\ mm^2$, $\Lambda' = 0\ mm^2$, $n = 4$, $\gamma = 5\ sec^{-1}$, $I = 10\ lumens/mm^2$, $\overline{\phi} = 1\ lumen$.

2.2.4 Stability analysis.

We now investigate how spontaneous oscillations in pupil area may develop under conditions of constant light illumination. As will become clear, the method of analyzing (2.2.8) depends on the relative values of the pupillary rate constant for constriction (α_c) and dilation (α_d). In a few individuals, $\alpha_c \approx \alpha_d$ (see Lowenstein and Friedman[75]); however, in the majority $\alpha_c > \alpha_d$ [64,75]. We refer to these cases as, respectively, a symmetric and an asymmetric pupil light reflex.

2.2.4.1 Symmetric pupil light reflex ($\alpha_c = \alpha_d$).

The unique equilibrium pupil area, A^*, corresponding to an incident light illuminance, I^*, is defined by $dA/dt = 0$, and from (2.2.8) it is the solution of the equation (Figure 2.2.3 b)

$$\alpha g(A^*) = \gamma \ln \left[\frac{I^* A^*}{\bar{I}\,\bar{A}} \right] . \tag{2.2.9}$$

To determine the stability of this fixed point, it is necessary to linearize (2.2.8) about A^*. This is done in two steps. First, in (2.2.8), we expand $g(A)$ to first order around A^*, i.e.

$$g(A) \simeq g(A^*) + \beta(A - A^*) \tag{2.2.10}$$

where β is given by dA/dt evaluated at A^*. Substituting (2.2.10) into (2.2.8) we obtain

$$\beta \frac{dA}{dt} + \alpha g(A^*) + \alpha\beta(A - A^*) = \gamma \ln\{A(t-\tau)\} + \gamma \ln \left[\frac{I^*}{\bar{I}\,\bar{A}} \right] . \tag{2.2.11}$$

Next we define the displacement of $A(t)$ from equilibrium as $a(t) = A(t) - A^*$. For small amplitude oscillations, $a/A << 1$ and hence we can expand the first term on the right hand side of (2.2.11)

$$\begin{aligned} \gamma \ln[A(t-\tau)] &= \gamma \ln \left\{ A^* \left[\frac{a(t-\tau)}{A^*} + 1 \right] \right\} \\ &\simeq \gamma \ln A^* + \frac{\gamma}{A^*} a(t-\tau) . \end{aligned} \tag{2.2.11}$$

Combining (2.2.11) and (2.2.12) and using (2.2.9) we obtain

$$\frac{da}{dt} + \alpha a = \frac{\gamma}{\beta A^*} a(t-\tau) , \tag{2.2.13}$$

which in terms of pupil area, $A = a + A^*$, yields

$$\alpha^{-1} \frac{dA}{dt} + A = G \cdot [A(t-\tau) - A^*] + A^* \tag{2.2.14}$$

where we have defined the dimensionless quantity, G, as

$$G \equiv \frac{\gamma}{\alpha\beta A^{*}}\,. \tag{2.2.15}$$

Since $\beta < 0$, it follows that $G < 0$ which corresponds to negative feedback.

To examine the response of the pupil to small deviations in pupil area, A, from the equilibrium area A^{*} as described by (2.2.14), we make the usual ansatz that $A(t) \propto \exp(\lambda t)$. The characteristic equation is

$$\lambda + \alpha + B\exp^{-\lambda\tau} = 0 \tag{2.2.16}$$

where $\alpha > 0$ and $B \equiv -\alpha G > 0$. This quasi-polynomial has an infinite number of roots. We denote by $\lambda_1 = \sigma_1 \pm i\omega_1$ the root with the largest real part. The roots come in complex conjugate pairs since (2.2.16) is invariant under sign reversal of ω. We will focus only on the roots with positive frequency. It can be shown that (2.2.14) has a periodic solution when[76,77]

$$\omega_1\tau = \cos^{-1}(\frac{1}{G}) \tag{2.2.17}$$

where $|G| < 1$, $\omega_1^2 = \alpha^2(G^2 - 1)$ and the inverse cosine takes its value in the interval $[\frac{\pi}{2}, \pi]$. This is an implicit relation among the parameters of (2.2.14) that defines the condition $Re(\lambda_1) = \sigma_1 = 0$. The period, T, of this periodic solution is given by

$$T = \frac{2\pi}{\omega_1}, \qquad 2\tau < T < 4\tau\,. \tag{2.2.18}$$

Assume for now that the delay τ is the bifurcation parameter. Then, for α and B fixed, there will be a value of $\tau = \tau_o$ for which (2.2.17) will hold. By implicit differentiation of (2.2.16) with respect to τ, one obtains

$$\left.\frac{dRe(\lambda)}{d\tau}\right|_{\substack{\tau = \tau_o \\ \lambda = i\omega_1}} = \frac{\omega_1^2}{(1 + \alpha\tau_o)^2 + \omega_1^2\tau_o^2} > 0 \tag{2.2.19}$$

Hence $Re(\lambda_1) > 0$ for $\tau > \tau_o$ which corresponds to local instability of the fixed point $A = A^{*}$ when the delay is increased past the critical value τ_o. This also implies that in (2.2.17) the right hand side is greater than the left hand side. Hence periodic solutions occur in (2.2.14) for $\tau \geq \tau_o$. Similarly, if B is the bifurcation parameter, then keeping α and τ fixed, we obtain

$$\left.\frac{dRe(\lambda)}{dB}\right|_{\substack{B = B_o \\ \lambda = i\omega_1}} = \frac{\alpha + \alpha^2\tau}{B_o(1 + 2\alpha\tau + B_o^2\tau^2)} > 0 \qquad (2.2.20)$$

where B_o is the value of B satisfying (2.2.17). Thus periodic solutions occur in (2.2.14) for $B \geq B_o$.

In general, a Hopf bifurcation from a stable equilibrium point to a stable limit cycle may be either subcritical ("hard" excitation) or supercritical ("soft" excitation)[10]. Classifying the Hopf bifurcation for (2.2.14) is important since it allows a prediction of how the oscillation amplitude grows for values of τ (or B) beyond the point of oscillation onset, i.e. τ_o (or B_o).

The fate of the periodic solution that existed for the linearized system at $\tau = \tau_o$ (or $B = B_o$) is determined by the nonlinear terms that have been neglected in going from (2.2.8) to (2.2.13). A supercritical Hopf bifurcation will occur provided that certain nondegeneracy conditions are fulfilled by these nonlinear terms[78]. This means that as a complex conjugate pair of roots migrates across the imaginary axis (from left to right), the stable equilibrium becomes unstable and a stable limit cycle arises.

Verification of these nondegeneracy conditions is quite involved for functional differential equations such as (2.2.8). Instead, we have numerically verified (data not shown) that the bifurcation is supercritical by demonstrating that locally the amplitude of the oscillation grows as the square root of the distance (in parameter space) from the bifurcation point, i.e.

$$Amplitude \propto \sqrt{B - B_o} \quad (\text{or } \sqrt{\tau - \tau_o}). \qquad (2.2.21)$$

Further, the analytical computation of higher order corrections to the period (2.2.17) and amplitude (2.2.21) using the Hopf analysis for functional differential equations (of delay type here) is also quite involved and is not carried out here (see Stech[78]; Sirkus[79]).

Other bifurcations may occur as τ and B are increased further leading to other limit cycles, quasiperiodic motion and bounded aperiodic (chaotic) dynamics. This depends on the functional form of $g(A)$ in (2.2.8). For general $g(A)$, numerical integration is necessary to determine which type(s) of solution will be observed for a given choice of parameters and initial functions on $(-\tau, 0)$. For negative feedback, numerical calculations indicate that no other bifurcations occur after the Hopf bifurcation.

2.2.4.2 Asymmetric pupil light reflex ($\alpha_c > \alpha_d$).

In the derivation of our model, we have used the same dynamical variable x to describe constriction and dilation, even though each process involves different mechanisms which depend on different parameters[38,80,81,82,83]. The observation that $\alpha_c > \alpha_d$ introduces an asymmetry into our model of the pupil light reflex. To account for this we replace α in (2.2.8) by

$$\alpha' = \frac{1}{2}\left[\alpha_c + \alpha_d - (\alpha_c - \alpha_d) sgn\{\dot{A}\}\right], \qquad (2.2.22)$$

where $sgn\{\dot{A}\}$ equals $+1$ if $\dot{A} \equiv dA/dt > 0$ and -1 otherwise. The stability analysis requires first solving (2.2.9) for A^* with $\alpha = \alpha'$. Since α can have one of two values, (2.2.9) will not yield a unique A^* for a given $g(A^*)$. Indeed the graphical solution in Figure 2.2.3b indicates two fixed points A_c^* and A_d^* corresponding, respectively, to α_c and α_d. The analytical methods for determining the stability of such an equation in which the fixed point depends on the sign of the derivative of the state variable have not, to our knowledge, been developed. We therefore explored the behaviour of such an equation numerically.

Specifically, we simulated (2.2.8) with the asymmetry in α given by (2.2.22). We found that the solution depends on the initial condition (data not shown). The solution can go to one fixed point or the other, or oscillate around one fixed point, or the other. In addition for certain parameter values, we have an ill-defined problem: the initial value of α determines the fixed point and the sign of the derivative in the fourth order Runge Kutta algorithm. However, based on this sign, α' takes on the other value and the system attempts to converge to the other fixed point. The solution thus oscillates between the two fixed points with the value of the derivative changing at every integration time step.

2.2.5 Gain.

The parameter, G, can be formally identified to the gain, G_o, defined empirically from measurements of the response of the pupil to small amplitude sinusoidally modulated illumination[64]. Here we examine the dependence of G on the equilibrium pupil size, A^*.

It has been observed that the gain, G_o, attains its highest values at intermediate pupil sizes. This effect has been referred to as the "expansive range nonlinearity" and has been interpreted as a reflection of the nonlinear mechanical properties of the iris[53,74]. Figure 2.2.3 plots G as a function of A^*. In preparing this plot we have kept the parameters α and γ constant. Normally, A^* will depend on the value of α and γ (2.2.9), but we assumed that A^* is in fact varying independently of them, e.g. being set by the accommodation level of the lens[85]. As can be seen, the gain G will have its largest values for intermediate values of A^*. Furthermore, these observations indicate that the relevant nonlinear properties of the iris have been incorporated into the choice of the function $g(A)$ (see 2.2.7).

2.2.6 External piecewise constant negative feedback.

In previous studies[20,64] we found empirically that under conditions of imposed piecewise constant negative feedback, the oscillations in pupil area could be described by the equation

$$\alpha^{-1}\frac{dA}{dt} + A = \begin{cases} A_{off}, & \text{if } A_\tau < A_{ref} \\ A_{on}, & \text{if } A_\tau > A_{ref} \end{cases} \tag{2.2.23}$$

where the rate constant α differs for constriction (α_c) and dilation (α_d). When pupil area is greater than a threshold A_{ref}, pupil size decreases exponentially to lower asymptotic area (A_{on}), whereas when $A < A_{ref}$, pupil size increases exponentially to a higher asymptotic area (A_{off}). This equation describes "high gain" oscillations in pupil area since the gain is infinite when $A = A_{ref}$ (it is zero for all other values of A). The forcings, A_{on} and A_{off}, correspond physically to two different values of the flux (ϕ).

In the case of external piecewise constant negative feedback, the illumination is constructed electronically to be a Heaviside function of pupil area, $H(A)$, and hence

$$\phi(t) = \phi_b H\left[A(t) - A_{ref}\right] + \phi_{off}\ , \tag{2.2.24}$$

where

$$H\left[A(t) - A_{ref}\right] = \begin{cases} 1, & if\ A > A_{ref} \\ 0, & if\ A \leq A_{ref} \end{cases} \tag{2.2.25}$$

and where ϕ_{off} is the retinal light flux due to background illumination when the light beam is off and ϕ_b is the retinal light flux produced by the narrow light beam. Thus the retinal light level changes because the illuminance is switched on or off, while the area is constant and equal to the sectional area of the narrow light beam. Under these conditions it follows from (2.2.8) that the changes in pupil area are described by

$$\frac{dg}{dA}\frac{dA}{dt} + \alpha g(A) = \gamma \ln\left[\frac{\phi_{off}}{\bar{\phi}} + \frac{\phi_b}{\bar{\phi}} H(A_\tau - A_{ref})\right] \tag{2.2.26}$$

It is important to note that the right hand side of (2.2.26) is known. The unknown properties of our model for the pupil light reflex, i.e. $g(A)$ and $M(x, \frac{dx}{dt}, \cdots)$ (see 2.2.4) are confined to the left hand side of (2.2.26). Thus the advantage of studying the dynamics produced by the pupil light reflex clamped with piecewise constant negative feedback is that it directly permits evaluation of plausible choices for $g(A)$ and $M(x, \frac{dx}{dt}, \frac{d^2x}{dt^2}, \cdots)$.

To illustrate the above procedure let $M(x, \frac{dx}{dt}, \frac{d^2x}{dt^2}, \cdots)$ be given by (2.2.4) and take $g(A)$ as a linear function of A, i.e.

$$g(A) = g(A^*) + \beta(A - A^*), \tag{2.2.27}$$

where $\beta = dg/dA\ |_{A^*} < 0$ and $A^* \in [A_c^*, A_d^*]$ (Figure 2.2.3). A reasonable choice for A^* would be a mid-range value. Then (2.2.26) becomes

$$\alpha^{-1}\frac{dA}{dt} + A(t) = A_o + \frac{\gamma}{\alpha\beta}\ln\left[\frac{\phi_{off}}{\bar{\phi}} + \frac{\phi_b}{\bar{\phi}} H(A_\tau - A_{ref})\right]. \tag{2.2.28}$$

This equation is of the same form as (2.2.23) where

$$A_{off} = A_o + \frac{\gamma}{\alpha_d\beta}\ln\left[\frac{\phi_{off}}{\bar{\phi}}\right] \tag{2.2.29}$$

$$A_{on} = A_o + \frac{\gamma}{\alpha_c\beta}\ln\left[\frac{(\phi_{off} + \phi_b)}{\bar{\phi}}\right] \tag{2.2.30}$$

and the pupil area, A_o, is the maximal pupil area corresponding to zero iris muscular activity and is given by $g(A_o) = 0$ in (2.2.27)

$$A_o = A^* - \beta^{-1} g(A^*). \tag{2.2.31}$$

Since $\beta < 0$, it follows that $A_{off} > A_{ref} > A_{on}$ if $\alpha_c/\alpha_d < \ln[(\phi_{off} + \phi_b)/\bar{\phi}]/\ln[\phi_{off}/\bar{\phi}]$. This latter condition is satisfied for the symmetric case and for the asymmetric case holds provided that ϕ_b is large enough.

It should be noted that the behaviour of (2.2.23) cannot be determined using a Hopf bifurcation analysis since the feedback function is not differentiable. The solution of (2.2.23) (and 2.2.28) can be determined analytically[20,64,66]. Experimentally it is found that the period and amplitude of the observed pupil area oscillations agree to within 5-10 % of these predicted[20,64]. However, the predicted oscillations clearly have a slope discontinuity; this is not observed experimentally. We are presently evaluating alternative choices and $g(A)$ and $M(x, \frac{dx}{dt}, \frac{d^2x}{dt^2}, \cdots)$ in order to improve the agreement between theory and observation.

In principle, piecewise constant feedback can be used to evaluate M without the necessity of determining $g(A)$. The gain is proportional to the slope of the Hill function (2.2.7) and can be made infinitely steep by letting $n \to \infty$. Substituting (2.2.7) into (2.2.5) and taking the limit we obtain

$$\begin{aligned} \frac{dx}{dt} + \alpha x &= \lim_{n\to\infty} \gamma \ln \left[\frac{I}{\bar{\phi}} \left\{ \frac{\Lambda \theta^n}{\theta^n + x(t-\tau)^n} + \Lambda' \right\} \right] \\ &= \gamma \ln \left[\frac{I\Lambda}{\bar{\phi}} H(x(t-\tau) - x_{ref}) + \frac{\Lambda' I}{\bar{\phi}} \right] , \end{aligned} \tag{2.2.32}$$

where $I = I(t-\tau)$, $H(x(t-\tau) - x_{ref})$ is a Heaviside function, and we have identified x_{ref} with the limit as $n \to \infty$ of the inflection point of (2.2.7), i.e.

$$x_{ref} \equiv \lim_{n\to\infty} \left[\theta^{\frac{n-1}{n+1}} \right] = \theta \, . \tag{2.2.33}$$

Equation (2.2.32) takes the same form as (2.2.23) (i.e. the flux can take on two values). However, given the difficulties in measuring (and for that matter defining) x, this approach is presently not useful practically.

2.2.7 Illustrative example.

To illustrate the dynamical behaviours which can be produced by the class of equations we studied the following example

$$\frac{dA}{dt} + \alpha A = \frac{c\theta^n}{\theta^n + A(t-\tau)^n} \tag{2.2.34}$$

where c is a constant. This equation can be regarded to be a generalization of (2.2.23) for smooth negative feedback.

Figure 2.2.4 shows the solutions of (2.2.34) as the steepness of the Hill function is increased by increasing the parameter n. For small n there is a damped oscillation in pupil area (Figure 2.2.4a). For larger values of n, sustained regular oscillations in pupil area are obtained (Figure 2.2.4b-d). A supercritical Hopf bifurcation occurs between n equal to 3 and 10. Although the shape of these oscillations changes as n increases beyond 10, the more complex waveforms typical of the occurrence of higher order bifurcations are not seen.

2.2.8 Discussion.

We have used neuro-physiological and anatomical considerations to derive a nonlinear delay-differential equation describing the pupil light reflex. The main motivation behind this model was to develop a general framework to study the different types of dynamical behaviours produced by the pupil light reflex (Table 2.1) and, in particular, to examine the oscillations that occur under conditions of "high gain" negative feedback, e.g. edge-light or electronic pupil cycling[1,59,62,67].

Three observations lend support to our model for the pupil light reflex. First, the predicted period of the oscillations in pupil area from (2.2.18) (i.e. 600-1200 msec for a measured delay of $\sim$ 300 msec) agrees well with the observed period of edge-light pupil cycling (900 msec)[58,59,61,67]. Second, for the special case of external piecewise constant feedback, our model reduces to the same form as an empirical model known to have solutions which are in good agreement with experimental observations for a variety of feedback choices[20,64]. Moreover we have shown that this experimental design permits certain nonlinearities in the reflex to be isolated for more detailed study. Third, the dependence of the gain in our model on pupil size is consistent with the 'expansive range nonlinearity' studies by Usui and Stark[53,74]. Finally, in a separate study we have shown that our model is compatible with descriptions of the pupil light reflex based on experimentally measured transfer functions[84].

Oscillations in pupil area occur whenever the time delay and/or the gain become sufficiently large (2.2.17). The gain is related to three parameters: 1) the rate constant

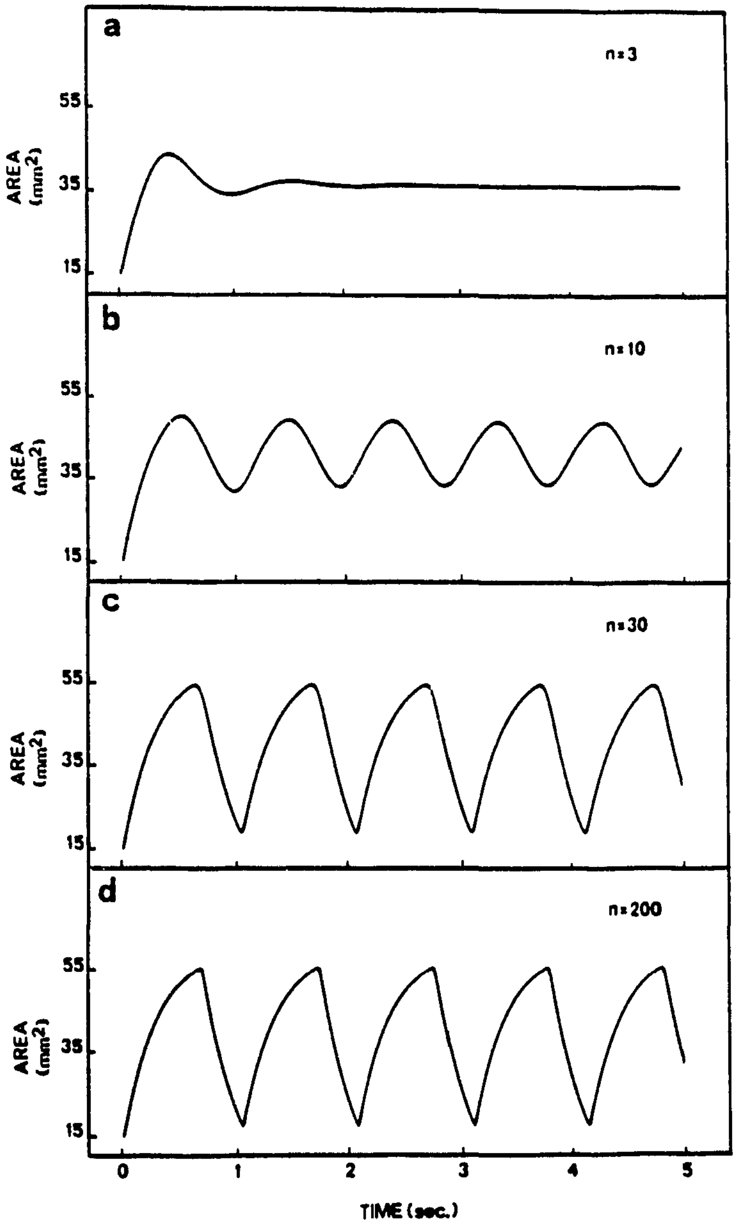

Figure 2.2.4 Solutions of (2.2.34) for increasing steepness of the feedback function. Value of n in the Hill function (right hand side of 2.2.34) has been indicated on each curve. In going from $n = 3$ to 10, the system has undergone a supercritical Hopf bifurcation. Initial condition for each simulation was $A(t) = 15\ mm^2$, $t \in (-\tau, 0)$. Parameter values were: $\tau = 300\ msec$; $\alpha = 3.21\ sec^{-1}$; $\theta = 50\ mm^2$; $c = 200\ mm^2$.

for the neural firing frequency (γ); 2) the steepness of the feedback function (β); and 3) the rate constant for pupillary movements (α). Stark[46] has used empirical observations to argue that constriction gain is decreased by retinal light adaptation and is inversely proportional to the constriction rate constant. These features come out very naturally in our model. The conditions for the onset of an oscillation as well as the period and amplitude of the oscillations should be sensitive to pathological alterations in any one of these three parameters. A variety of abnormalities in pupil area oscillations are indeed seen in patients with disease in the pupil light reflex pathways[60,61,62].

As the gain is increased beyond the point of oscillation onset the shape of the oscillation changes with little subsequent changes in its frequency (Figure 2.2.4). Near the bifurcation point, the oscillation amplitude is predicted to grow as the square root of these parameters beyond the point of instability onset. The more complex waveforms typically associated with the occurence of higher-order bifurcations, i.e period doubling bifurcations, or bifurcation from a limit cycle to a 2-torus, are not seen. This finding is consistent with previous studies of first order nonlinear delay-differential equations with negative feedback[60]; in particular, those which arise in the descriptions of the control of respiration[24,25], erythropoiesis[86] and the commodity price market[87]. Thus noise-like fluctuations in pupil area ('pupillary hippus ') cannot represent chaotic dynamics produced by a nonlinear negative feedback mechanism of the type we have considered here. However, we cannot exclude the possibility that hippus represents a chaotic process somewhere in the reflex arc or that it is simply due to noise injected, for example, at the level of the Edinger-Westphal nucleus[47,88].

One nonlinearity in the pupil light reflex that has received little attention in previous modelling studies is the response asymmetry of the pupil to the onset and offset of light. Although this asymmetry is most clearly manifested as a difference in the rates of pupil constriction and dilation[64], it is likely that it also occurs at the level of the output of the retina and midbrain as well. Neuro-physiological evidence for the presence of distinct light-ON and light-OFF responses in the reflex arc has been obtained for retinal ganglion cells[80,83] and for neuronal populations in the midbrain[38,81,82]. As the observations in Section 2.2.4.2 indicate the analysis of this situation certainly presents problems, except in the case of external piecewise constant feedback[20,64,89]. Previous modellers have also been concerned with the problem of reflex asymmetry[46,90]. For example, Stark[16] suggested that a steady state oscillation occurs when the constriction and dilation gains are equal. Thus, after a transient, there is no net increase or decrease in area in each oscillation period. In our model this would imply that $\gamma_c/\alpha_c = \gamma_d/\alpha_d$, where γ_c and γ_d are the neural firing frequencies (2.2.3) for, respectively, constriction and dilation. However, this assumption is not sufficient by itself to uniquely determine the steady state pupil area the system tends to (it likely will be a value between A_c' and A_d'). Determining whether the stabilization of the limit cycle occurs through this precise compensation or through another mechanism will require experimental investigations.

In our model we neglected the possibility that time-dependent processes occur in the response of the retina, e.g. adaptation[91]. It may be possible that by including these influences in (2.2.8), e.g. by making γ a function of time, that we will be able to obtain insights into pupil phenomena, such as pupillary escape[85]. In addition, it may be possible to account for some of the complex dynamical behaviours shown in Table 2.1, e.g. spontaneous periodic oscillations in sleepy narcoleptics[50], as more physiological information is incorporated into the choices of $f(x)$ (Equation 2.2.7) and γ.

We expect that models based on nonlinear dynamical systems approaches will come to play a greater role in the study of the properties of neural control mechanisms[20,54,84]. The advantage of these approaches is that the analysis is not restricted to the study of equilibria and their stability. By employing a combination of analytical and numerical techniques it should be possible to obtain insights into nature of the complex dynamical behaviours produced by the nervous system in health and disease.

2.2.9 Comment on asymmetry.

Section 2.2.6 of the preceding article develops the theory for oscillations in PCNF. This theory makes a number of interesting predictions, some of which will be explored in the subsequent chapters. In this section, we make a few remarks on a prediction of the model concerning response asymmetry.

Recall the condition for $A_{off} > A_{on}$

$$\frac{\alpha_c}{\alpha_d} < \frac{ln\left[\frac{\phi_{off}+\phi_b}{\bar{\phi}}\right]}{ln\left[\frac{\phi_{off}}{\bar{\phi}}\right]} \tag{2.2.35}$$

which we briefly mentioned after (2.2.31). Thus $A_{off} > A_{on}$ is equivalent to constriction being faster than dilation. We will see in Section 3.2 that the ratio on the left hand side of (2.2.35) is experimentally between 5 and 12, so inequality (2.2.35) will only be satisfied for sufficiently large values of ϕ_b, the light beam flux. At lower intensities, the inequality can no longer hold, unless the rate constants α_c and α_d change in a way that reduces their ratio.

This condition (2.2.35) is plausible when viewed from the perspective of Henneman's size principle[52]. Muscles are composed of motor units that differ in size, speed and tension threshold of operation (known as recruitment threshold). The size principle says that a small stimulus will recruit small motor units, which are slow and weak, while a stronger stimulus will recruit larger motor units and the response will be faster. Although the properties of smooth muscle (such as the iris muscles) are not known in as much detail, they appear similar to those of skeletal muscle, and the size principle probably holds for them as well[53]. Thus α_c will decrease at lower intensities, and inequality (2.2.35) can still be satisfied.

Our analysis in Sections 2.2.3 and 2.2.6 did not take into account the fact that the iris rate constants are functions of ϕ_b (probably because we use only one beam intensity in our experiments: see Section 3.2). More generally, for the PCNF case (2.2.28) should be replaced by

$$\alpha^{-1}[\phi_b, \dot{A}]\,\frac{dA}{dt} + A(t) = A_0 + \frac{\gamma}{\alpha[\phi_b, \dot{A}]\beta}\,ln\left\{\frac{\phi_{off}}{\bar{\phi}} + \frac{\phi_b}{\bar{\phi}}H\left[A_\tau - A_{ref}\right]\right\}, \tag{2.2.36}$$

while (2.2.8) for the SNF case should be

$$\frac{dg}{dA}\frac{dA}{dt} + g(A)\,\alpha[\phi_b, \dot{A}] = \gamma\, ln\left[\frac{I_T A_T}{\overline{\phi}}\right]. \tag{2.2.37}$$

In SNF, ϕ_b changes continuously: $\phi(t) = \phi^* + \Delta\phi(t)$, while in PCNF, ϕ_b changes abruptly. The fact that the motor units are recruited in a continuous fashion in SNF is probably responsible for the apparent symmetry of the waveforms, a point we address in the discussion of the following article (Section 2.3.9).

2.3 INSIGHT INTO THE TRANSFER FUNCTION, GAIN AND OSCILLATION ONSET USING NONLINEAR DELAY-DIFFERENTIAL EQUATIONS.

2.3.0 Transfer functions in brief.

Although interest in the pupil light reflex is centuries old, it is only recently that quantitative methods of investigation have been applied to its study. In fact, thirty years ago Stark and Sherman[31] were among the first to use Wiener's newly emerging theory of control and communication or "cybernetics"[92] in a specific biological context, namely that of the pupil light reflex. Over the years, Stark and several of his co-workers have demonstrated that concepts such as transfer functions, stability, nonlinearity and noise filtering were powerful modelling tools for this reflex.

Along with this theory of control came a precise experimental protocol and data analysis scheme[93]. For example, experiments involving responses to small amplitude sinusoidal light stimulation, step responses and impulse responses produced data that were analyzed using Bode plots, root locus plots and Nyquist diagrams. This "systems analysis" approach is aimed at a phenomenological description of the input-output characteristics of the system under study. It works only in parameter ranges where the dynamics are governed by linear differential equations, or equivalently where linear response theory applies. In this context, the output $y(t)$ of the system when the input is $x(t)$ is given by the convolution of the input with the system's Green function or "impulse response" $h(t)$:

$$y(t) = \int_{0^+}^{t} x(u)h(t-u)\,du \tag{2.3.0-1}$$

where causality requires that $h(t)$ be nonzero only for strictly positive arguments. The analysis is simplified by taking the Laplace transform of (2.3.0-1) :

$$H(s) = \frac{Y(s)}{X(s)} \tag{2.3.0-2}$$

where uppercase letters denote the Laplace transform of variables with the corresponding lower case letters and $s = \sigma + i\omega$ is the Laplace transform variable. The simplification follows from the fact that differential operators are replaced by functions of the Laplace variable s, hence converting differential equations into algebraic equations.* For example, if $y(0) = 0, y'(0) = 0, y^{(2)}(0) = 0, \ldots$ and $x(0) = X_0, x'(0) =$

---

* For linear differential-delay equations, $H(s)$ also includes transcendental functions see Section 4.1.

$0, x^{(2)}(0) = 0, \ldots$, the input-output relation

$$\left[a_n \frac{d^n}{dt^n} + a_{n-1} \frac{d^{n-1}}{dt^{n-1}} + \ldots + a_1 \frac{d}{dt} + a_0\right] y(t)$$
$$= \left[b_m \frac{d^m}{dt^m} + b_{m-1} \frac{d^{m-1}}{dt^{m-1}} + \ldots + b_1 \frac{d}{dt} + b_0\right] x(t) \quad (2.3.0\text{-}3)$$

becomes, in the Laplace domain,

$$H(s) = \left[\frac{b_m s^m + b_{m-1} s^{m-1} + \ldots + b_0}{a_n s^n + a_{n-1} s^{n-1} + \ldots + a_0}\right] \quad (2.3.0\text{-}4)$$

The function $H(s)$ is called the transfer function of the system. It contains all the information on steady state and transient behaviour of the system. The precise time-evolution of the system will however depend on the initial conditions.

We are dealing here not only with linear causal systems but also time-invariant ones, i.e. the coefficients in (2.3.0-3) are constants. The main property of these systems is that their steady-state response to an input sinusoid is also a sinusoid of the same frequency. However the ratio of output to input amplitude and the phase difference are given, respectively, by the modulus and the argument of the transfer function (in polar form) when $\sigma = 0$:

$$H(i\omega) = |H(i\omega)|\, e^{arg\{H(i\omega)\}} \quad (2.3.0\text{-}5)$$

This is a consequence of the fact that sinusoids, or more precisely the complex exponentials $e^{i\omega t}$, are eigenfunctions of the time derivative operator with eigenvalue $i\omega$.

While systems analysis can lead to quite complicated transfer functions, providing almost perfect fit to the experimentally observed response to a step in light intensity, one must remember that these functions represent black boxes. At best, each transfer function describes a different part of the physical system, but the precise relationship between its parameters and those of the system is often not clear Further, obtaining a transfer function that reproduces the observed responses is often achieved by using many parameters, and depending on how nonlinear the system is, a slight change in operating conditions might involve a whole new fit with completely different parameter values. Under such circumstances, it is justified to question the value of such models

The emphasis of linear systems analysis is on designing or producing a differential equation that reproduces the linear behaviours of systems in which an input and an output can be identified. This approach is strongly related with the design of stable control systems. However when phenomena like limit cycle oscillations, quasi-periodic motion and chaos are of interest, this systems theory approach is profitably supplemented by nonlinear dynamics.

Before continuing, it is important to draw attention to the tremendous body of knowledge that the theory of nonlinear control systems represents. It includes, for example, describing function theory[93] (also known as harmonic analysis), Volterra and Wiener kernel analysis or generalized transfer functions[94,95] and generalized Nyquist (Theodorchik) diagrams (see Minorsky[96]). This last approach is closely related to bifurcation theory since it deals with the basic problem of nonlinearity, i.e. the interdependence of frequency and amplitude, by calculating an amplitude-dependent transfer function

The realm of nonlinear phenomena that these theories address deals mostly with engineering type nonlinearities such as thresholds, saturations and static nonlinearities, and is thus somewhat different from that which we are interested in. Although some of these nonlinearities occur in the pupil light reflex, we prefer to include them in a theoretical framework more amenable to the phenomena we are interested in, namely autonomous (self-sustained) oscillations and their response to external perturbations. Hence, a theory that encompasses both autonomous and non-autonomous phenomena is needed, a condition satisfied by bifurcation theory.

Models in nonlinear dynamics can also be plagued by an overabundance of parameters, and modelers try to minimize their numbers. The emphasis is more on qualitatively explaining observed behaviour rather than on giving perfect fit, in the hope of gaining insight into the dynamical properties of the system, and ultimately into its nonlinearities It is from this knowledge of nonlinearities that one can proceed to the analysis of more complicated phase space motions and the influence of noise.

It is interesting that both nonlinear control systems theory and bifurcation theory are extensions of linear theory This is not always obvious because of the different language they use For example, the poles of a transfer function at which the residues are calculated (to invert the Laplace transform and obtain the time domain solution) are simply the eigenvalues of the linear operators governing the flow (i.e. the vector field) of the differential equation around fixed points

As a testimony to the thirty years of bio-engineering that have gone into the study of the pupil, next we present a paper that bridges the gap between bifurcation theory and control systems analysis in the context of a simple nonlinear phenomenon: pupillary oscillations. In particular, the model developed in the preceding article is shown to be compatible with earlier transfer function studies. Each approach is justified by its success in explaining a given body of experimental data. Oscillations have features that can be explained by linear theory and others that require nonlinear theory.

In this paper we define and make use of Nyquist's stability criterion. The proof of this theorem can be found in Nyquist's original paper[97]. The proof uses the argument theorem from complex variable theory to obtain a condition for the boundedness of the impulse response in the asymptotic time limit.

2.3 Insight into the transfer function, gain, and oscillation onset for the pupil light reflex using nonlinear delay-differential equations.

Abstract.

Analogies are drawn between a physiologically relevant nonlinear delay-differential equation (DDE) model for the pupil light reflex and servo control analytic approaches. This DDE is shown to be consistent with the measured open loop transfer function and hence physiological insight can be obtained into the gain of the reflex and its properties. A Hopf bifurcation analysis of the DDE shows that a limit cycle oscillation in pupil area occurs when the first mode of the characteristic equation becomes unstable Its period agrees well with experimental measurements. Beyond the point of instability onset, more modes become unstable corresponding to multiple encirclings of $(-1,0)$ on the Nyquist plot. These modes primarily influence the shape of the oscillation Techniques from dynamical systems theory, e.g. bifurcation analysis, can augment servo control analytic methods for the study of oscillations produced by nonlinear neural feedback mechanisms.

2.3.1 Introduction.

One of the most important mechanisms for regulating neural activity is feedback. An undeniable feature of human neural feedback mechanisms in health and disease is their propensity to generate oscillations and other complex dynamical behaviours, e.g. tremors and the electrical activity of the cortex[51]. The pupil light reflex is a human neural feedback mechanism in which it is possible to study the occurence of oscillations and their properties non-invasively[32]. It is well known that regular oscillations in pupil area occur under "high gain" conditions[1,46,59,62,67] and that the period of these oscillations can be estimated from the experimentally measured open-loop transfer function for this reflex[67] Moreover, it has been demonstrated that the 'linear' properties of this reflex determine the frequency of these oscillations, whereas the shape and amplitude depend on the 'nonlinearities' [1]

Interpretation of the above findings in a biological context requires that parameters such as the gain and open-loop transfer function be defined neuro-physiologically. Previous studies have examined the effect of the nonlinear characteristics of the iris musculature on the overall reflex gain and on pupillary phenomena such as hippus and the pupil size effect[32,74,98]. However, little attention has been given to identifying the physiological parameters which determine the linear and nonlinear properties of the high gain oscillations.

In a previous study we showed that the oscillations in pupil area which occur under conditions of external piecewise constant feedback were well described by the solutions of a nonlinear delay-differential equation[61]. Here we draw analogies between this delay-differential equation and servo control analytic theory. In this way we are able to obtain insight into the neuro-physiological properties of this reflex which determine the gain and open loop transfer function and which shape the high gain oscillations.

2.3.2 Background.

The changes in pupil area, A, which occur under conditions of imposed piecewise constant feedback can be described by[64,99]

$$\frac{dg}{dA}\frac{dA}{dt} + \alpha g(A) = F(A_\tau), \tag{2.3.1}$$

where α is the rate constant for pupillary movements, τ is the neural time delay, and $F(A_\tau)$ is a piecewise constant function of A_τ. The function $F(A_\tau)$ takes on one of two values depending on whether pupil area is greater than or less than a threshold. The notation A_τ denotes pupil area at a time τ in the past, i.e. $A_\tau = A(t-\tau)$. The feedback function, $g(A)$, relates changes in iris muscle activity, x, to changes in A and takes into account the inverse relationship between x and A. In our previous studies $g(A)$ was taken to be a linear function. Note that in order to solve (2.3.1) it is necessary to specify A_τ as an initial function on the interval $(-\tau, 0)$.

The right hand side of (2.3.1) is a forcing term that represents the changes in the retinal light flux, ϕ ($\phi = IA$, where I is the retinal illumination), due to changes in pupil area. For smooth negative feedback, (2.3.1) becomes[99]

$$\frac{dg}{dA}\frac{dA}{dt} + \alpha g(A) = \gamma \ln\left[\frac{\phi_\tau}{\hat{\phi}}\right] = \gamma \ln\left[\frac{I_\tau A_\tau}{\hat{I}\hat{A}}\right], \tag{2.3.2}$$

where we have taken into account the logarithmic compression of light intensities at the retina[70], γ is the rate constant for the neural firing frequency and $\hat{\phi}, \hat{I}, \hat{A}$ are the values of ϕ, I, A at threshold, i.e. the values below which there is no pupillary response.

Comparison of (2.3.2) to linear servo control theoretical descriptions of the pupil light reflex[1,32] requires linearization of (2.3.2) about the equilibrium pupil area, A^*, corresponding to an incident illumination of I^*. The value of A^* is obtained from (2.3.2) by setting $dA/dt = 0$ and is the solution of the equation

$$\alpha g(A^*) = \gamma \ln \left[\frac{I^* A^*}{\hat{I} \hat{A}} \right] \tag{2.3.3}$$

and linearization of (2.3.2) about A^* leads to

$$\alpha^{-1} \frac{dA}{dt} + A = G \cdot [A_\tau - A^*] + A^* , \tag{2.3.4}$$

where

$$G \equiv \frac{\gamma}{\alpha \beta A^*} \tag{2.3.5}$$

and $\beta \equiv dg/dA$ evaluated at A^*. When $\beta < 0$, it follows that $G < 0$ which corresponds to negative feedback.

2.3.3 Transfer function.

In this section we show that (2.3.4) can be derived from the experimentally measured closed loop transfer function for the pupil light reflex, $H(s)$

$$H(s) = \frac{P(s)}{1 + P(s)} , \tag{2.3.6}$$

where the open-loop transfer function is

$$P(s) = \frac{G_o \exp(-\tau s)}{(1 + ks)^3} \tag{2.3.7}$$

and where s is the Laplace variable and $\tau = 0.18$ *sec*. While the 18 db/octave roll-off of the Bode amplitude plot suggested that the transfer function had three poles, they could not be determined individually and were all set equal to 10 sec^{-1} by choosing the time constant $k = 0.1$ sec[46].

$G_o = 0.16$ is the dimensionless open-loop gain. The open loop gain is normally equal to the product of the forward gain and the feedback gain. The latter corresponds to the coefficient of $P(s)$ in the denominator of (2.3.7) and is unity here. We have called G_o in (2.3.7) the open-loop gain since it is numerically equal to the forward gain.

Based on small signal analysis, Stark[46] has argued that the open-loop gain should be expressed as

$$G_o \equiv \frac{I^* \Delta A}{A^* \Delta I} = \frac{\Delta A / A^*}{\Delta I / I^*} . \tag{2.3.8}$$

The numerator of (2.3.8) describes the change of flux due to pupil constriction in response to the change of flux due to the light increment in the denominator.* Since $I^*\Delta A < 0$ when $A^*\Delta I > 0$, G_o is negative. However, G_o has been defined to be positive[46] and the negative sign is taken into account in writing the closed-loop transfer function for negative feedback $H(s)$ (2.3.6).

In order to compare (2.3.4) to the formulation of (2.3.6), it is necessary to rewrite (2.3.6) in the time domain to obtain

$$k^3\frac{d^3\phi}{dt^3} + 3k^2\frac{d^2\phi}{dt^2} + 3k\frac{d\phi}{dt} + \phi(t) = G_o \cdot [F(t-\tau) - \phi(t-\tau)] , \tag{2.3.9}$$

where $\phi = I^*\Delta A$ is the retinal light flux change due to pupil area change, $F = A^*\Delta I$ reflects the flux change due to the light change and A^* is the equilibrium pupil area in an ambient light level I^*. The forcing variable F and the state variable ϕ have the same units.** The equilibrium retinal flux for a constant forcing F is $\phi = G_oF$ in open-loop, and is a factor $(1 + G_o)^{-1}$ smaller in closed-loop.

If we identify, to first order, ϕ with $I^*\Delta A$ and F with $A^*\Delta I$, then (2.3.9) becomes

$$\begin{aligned} k^3 I^*\frac{d^3(\Delta A)}{dt^3} + 3k^2 I^*\frac{d^2(\Delta A)}{dt^2} + 3kI^*\frac{d(\Delta A)}{dt} + I^*(\Delta A) \\ = \frac{I^*(\Delta A^*)}{A^*(\Delta I^*)}[A^*(\Delta I)_\tau - I^*(\Delta A)_\tau] . \end{aligned} \tag{2.3.10}$$

Note that ΔI^* and ΔA^* are simply numbers that determine the numerical value of G_o. Dividing by I^*, keeping only first order derivatives and defining $3k = \alpha^{-1}$, we obtain

$$\alpha^{-1}\frac{d(\Delta A)}{dt} + \Delta A = \frac{\Delta A^*}{A^*\Delta I^*}[A^*(\Delta I)_\tau - I^*(\Delta A)_\tau] . \tag{2.3.11}$$

Next, define $\Delta A = A - A^*$, then

$$\alpha^{-1}\frac{dA}{dt} + A = A^* - \frac{(\Delta A^*)I^*}{A^*(\Delta I^*)}A_\tau + \frac{\Delta A^*}{\Delta I^*}(\Delta I)_\tau + \frac{\Delta A^*}{\Delta I^*}I^* . \tag{2.3.12}$$

In obtaining (2.3.4), we assumed that everything was linearized about A^* which is the steady state response to I^*. In the transfer function approach, this means that

---

*Another way of seeing this is to write the total differential for the flux. Let $I = I^* + dI$, $A = A^* + dA$, then

$$d\phi \simeq \phi(I, A) - \phi(I^*, A^*) = I^*dA + A^*dI + O(dIdA)$$

From (2.3.8) we see that the open-loop gain appears as the ratio of the two first order terms.

**This can be made clearer by defining the gain as the relative area change over relative illuminance change and dividing (2.3.9) by the mean flux $\phi^* = I^*A^*$ to make all quantities dimensionless relative changes.

the input is constant and equal to I^*. Therefore $(\Delta I)_\tau = I_\tau - I^* = 0$. Thus if we identify G_o in eq. (8) with $-G$ in (2.3.5), (2.3.12) becomes

$$\alpha^{-1}\frac{dA}{dt} + A = A^* + \frac{\gamma}{\alpha\beta A^*}A_\tau - \frac{\gamma}{\alpha\beta} = G\cdot[A_\tau - A^*] + A^* \tag{2.3.13}$$

which is exactly (2.3.4).

2.3.4 Gain.

The observations in Section 2.3.3 indicate that the gain, G, defined by (2.3.5) and the gain, G_o, defined by (2.3.8) are related. The identification $G_o \rightarrow -G$ is reasonable in view of the way we defined the signs of these two gains. Further, both determine the magnitude of the influence of a delayed variable on the instantaneous time evolution of this variable. It thus makes sense to identify the forward gain (or open loop gain as we have seen) in control systems theory with the coefficient of A_τ in the delay-differential equation describing feedback operation.

An alternate way in which the association between G and G_o can be explored is to use the fixed point condition given by (2.2.3). Equation (2.2.3) simply states that I^* can be considered an explicit function of A^*

$$I^* = \frac{\bar{\phi}}{A^*}\exp[\alpha\gamma^{-1}g(A^*)]\,. \tag{2.3.14}$$

We can then compute

$$\frac{dI^*}{dA^*} = -\frac{I^*}{A^*} + g'(A^*)I^*\alpha\gamma^{-1} \tag{2.3.15}$$

$$\frac{A^*dI^*}{I^*dA^*} = -1 + A^*\alpha g'(A^*)\gamma^{-1}\,. \tag{2.3.16}$$

Provided we identify $g'(A^*)$ with β and the left hand side with $-1/G_o$ (we put a negative sign here because G_o is defined positive), we obtain

$$-\frac{1}{G_o} = -1 + \frac{1}{G} \quad or \quad G = \frac{G_o}{G_o - 1}\,. \tag{2.3.17}$$

This calculation is justified as long as we are not too far from equilibrium where the fixed point condition holds. This means that A^* should not vary too much, i.e. $dA^*/dI^* << 1$, implying that (2.3.17) holds only for $G_o << 1$. In this limit we do indeed recover our earlier relation: $G \approx -G_o - G_o^2 \approx -G_o$.

2.3.5 Pupil response to a step light input.

From the open loop transfer function given by (2.3.7), the predicted response of the pupil to a step light input, $U_3(t)$, is

$$U_3(t) = 1 - \exp(-\frac{t}{k})[1 + \frac{t}{k} + \frac{t^2}{k}], \tag{2.3.18}$$

where we have neglected the time delay which would simply shift the response. On the other hand, the observations in Section 3 suggest that under certain conditions it is possible to approximate $U_3(t)$ by a first-order response, $U_1(t)$, i.e.

$$U_3(t) \sim U_1(t) = 1 - \exp(-\frac{t}{\delta}), \tag{2.3.19}$$

where δ is a time constant to be determined. We can compute δ in a way that will minimize the square deviation of these two positive definite functions, i.e.

$$\frac{d}{d\delta} \int_0^\infty |U_1(t) - U_3(t)|^2 dt = 0 . \tag{2.3.20}$$

This problem leads, after a lengthy, but straight forward algebraic computation, to the problem of finding the roots of a fourth order polynomial in δ which can be solved numerically in terms of k. The physically meaningful root is $\delta = 0.311$ *sec* which is roughly equal to $3k$ since $k = 0.1$ *sec*.

As shown in Figure 2.3.1 the first order impulse function using the above value of δ agrees with the third order step response. Interestingly the value of $\delta = 0.311$ *sec* is roughly equal to $3k$, where $k = 0.1$ *sec* is the value determined by Stark[46]. Thus this value of δ can be regarded as the value of α^{-1} in (2.3.4). It should be noted that the slow onset of $U_3(t)$ may be at least partially incorporated into $U_1(t)$ as an additional contribution to the pure lag.

2.3.6 Conditions for oscillation onset.

In linear control systems theory, the onset of oscillation is studied using the Nyquist criterion. When the polar plot of the open loop transfer function (Nyquist plot: see Figure 2.3 2) encircles the $(-1,0)$ point in the complex plane, regenerative feedback occurs at a frequency for which $P(s) = -1$, corresponding to a pole in the closed-loop transfer function (see e.g. Pallu de la Barriere[100]). This criterion is also applicable when delays are present. Generally delays destabilize systems as do increases in gain. The presence of a delay causes a pure rotation of the polar plot,

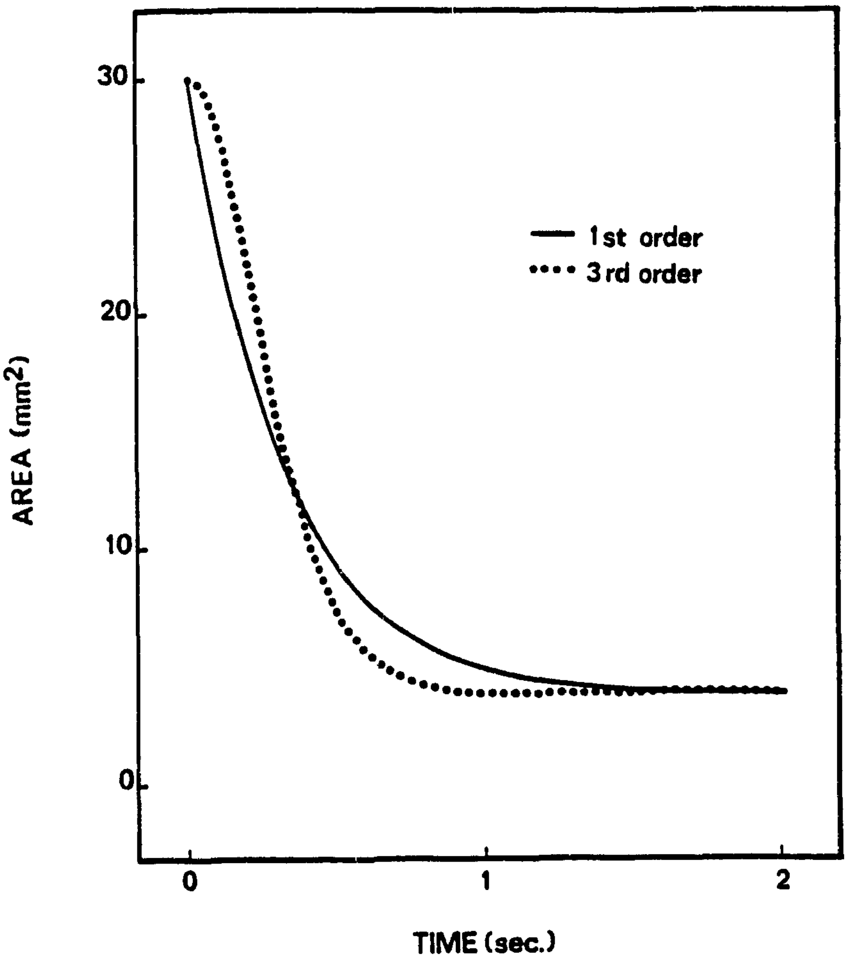

Figure 2.3.1 Comparison of open loop step responses for iris activity for a third order model (2.3.7) with k= 0.1 sec (dotted line) with a first order approximation with δ = 0.311 *sec* (solid line). We have neglected the time delay which would simply shift the responses. Ordinate is pupil area computed by subtracting iris activity from the maximal pupil area[46] and has been arbitrarily illustrated by plotting $A(t) = 30 - 25y(t)$.

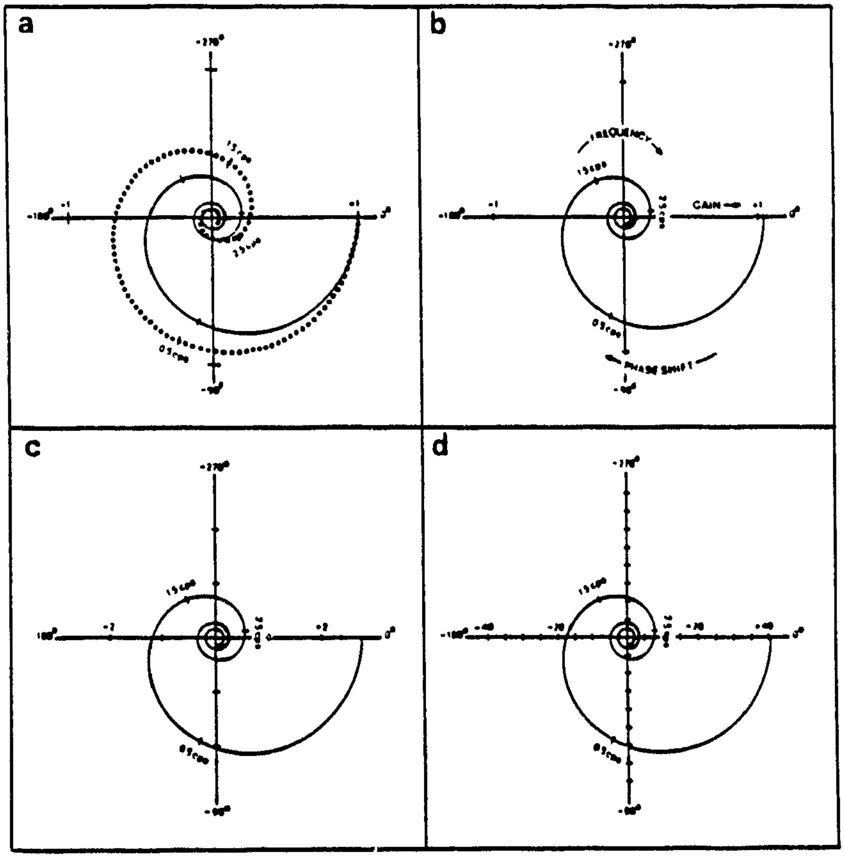

Figure 2.3.2 Polar plots of open loop transfer function (Nyquist plots) for the pupil light reflex. In a) we compare the third-order open-loop transfer function (dotted line; equation 2.3.7) with $k = 0.1$ *sec* and $\tau = 0.3$ *sec* to a first-order open-loop transfer function with the same delay and time constant $\delta = 0.311$ *sec* (solid line; equation 2.3.19). The gain has been set to one in both cases. In b)-d) we show the effect of increasing n on the Nyquist plots calculated by use of the characteristic equation for (2.3.25) (obtained by first linearizing (2.3.25)) for the same values of n shown in Figure 2.3.4. The gain in b)-d), which is proportional to n, is respectively, 3.36, 8.75, 130.3. There are seven encirclings of the $(-1, 0)$ point in d). The parameterization is only for positive frequencies (in cps).

which may lead to an encircling of the $(-1,0)$ point. That is why even a first order delay-differential equation can be made unstable by increasing the gain or the delay.

The conditions for instability and the frequency of the oscillation at the onset of instability can be directly determined from an analysis of (2.3.4). Define a small deviation in pupil area from A' as $a(t)$, i.e. $a(t) = A(t) - A'$. Then the characteristic equation can be obtained by substituting $a(t) \sim \exp(\lambda t)$ into (2.3.4) and is

$$\lambda + \alpha + B\exp(-\lambda\tau) = 0\,, \tag{2.3.21}$$

where λ is typically a complex eigenvalue and $B \equiv -\alpha G$. Equation (2.3.21) has an infinite number of roots which we denote as $\lambda_i, \overline{\lambda_i}$, where $\overline{\lambda_i}$ is the complex conjugate of λ_i. A conjugate pair of roots, $(\sigma_i + i\omega_i, \sigma_i - i\omega_i)$, characterize a mode. In Figure 2.3.3 we show the values of σ, ω for the two modes of (2.3.21) with the largest real parts as a function of B for $\alpha = 3.21\ sec^{-1}$ and $\tau = 300\ msec$. For simplicity only the root with positive frequency has been shown.

The problem of looking for pure imaginary roots of the characteristic equation is the same as that of determining the condition for regenerative feedback. At the point of onset of instability, the frequency of the oscillation will be determined by the mode with the largest real part, σ_1 [99]. Further, there is a supercritical Hopf bifurcation between a locally stable equilibrium and a locally stable periodic solution (limit cycle). The condition for the appearance of the limit cycle is

$$\omega_H\tau \geq \cos^{-1}\left(\frac{1}{G}\right)\,, \tag{2.3.22}$$

where ω_H is the values of ω_1 when $\sigma_1 = 0$, $|G| < 1$ and $\omega_H^2 = \alpha^2(G^2 - 1)$ and the inverse cosine takes its value in the interval $[\frac{\pi}{2}, \pi]$ [76,86].

Equality holds in (2.3.22) at the bifurcation point, where the period, T, is given exactly by

$$T = \frac{2\pi}{\omega_H}, \quad 2\tau < T < 4\tau\,. \tag{2.3.23}$$

Near the bifurcation point B_o (or τ_o) the period is given approximately by (2.3.23) and the amplitude of the oscillation is proportional to the square root of the distance (in parameter space) from the bifurcation point, i.e.

$$Amplitude \propto \sqrt{B - B_o} \quad (\ or\ \sqrt{\tau - \tau_o}\ )\,. \tag{2.3.24}$$

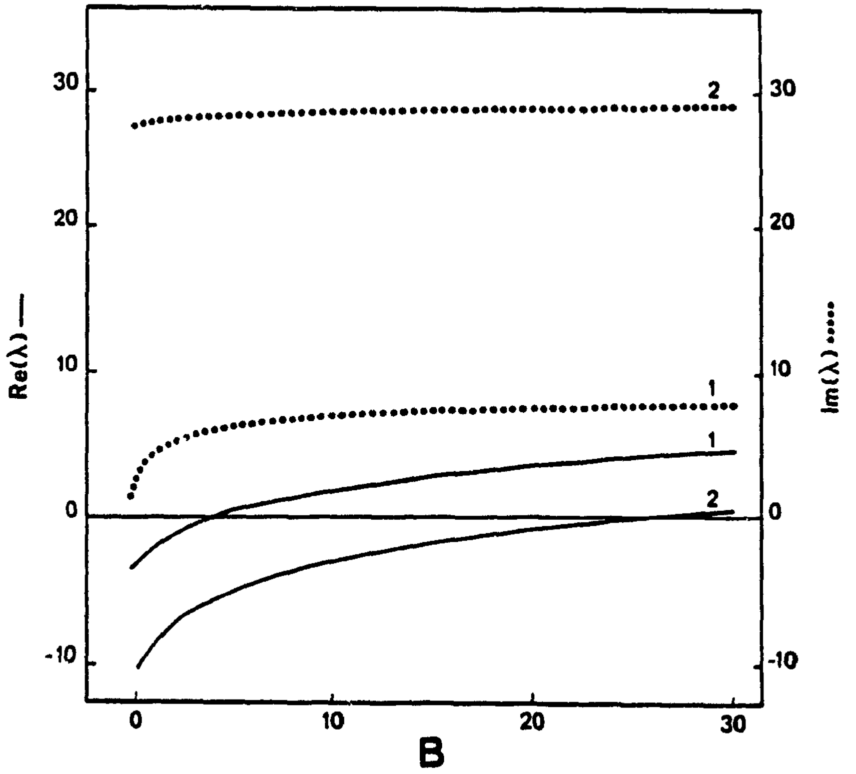

Figure 2.3.3 Plot of the real (solid line) and imaginary (dotted lines) parts of the first two roots of the characteristic equation (2.3.21) as a function of B. Parameter values were $\alpha = 3.21\ sec^{-1}$ and $\tau = 0.3\ sec$. Only the roots with positive frequency have been plotted.

For an average measured value of $\tau \sim 300\ msec$ [62], the period predicted by (2.3.23) is in good agreement with that predicted from the Nyquist plot and that measured experimentally

Equations (2.3.9) and (2.3.13) are of the same form. Thus, in the same way that (2.3.9) is associated with the third order open loop transfer function (2.3.7), it is possible to associate a first order open loop transfer function with (2.3.13), and hence to compute a Nyquist plot for (2.3.13). In Figure 2.3.2a we compare the Nyquist plot calculated from our first order model (solid line) to the third order open loop transfer function measured experimentally (dotted line; see (2.3.7)) but using the average time delay we have measured for the pupil light reflex ($0.3\ sec$) [62]. This time delay is longer that that estimated by Stark[46] from the Bode phase plot (i.e. $\tau = 0.18\ sec$), which is deduced from the phase of the transfer function at $4\ Hz$ and the fact that the third order pole should contribute 270^o at this frequency. Differences in τ of this magnitude can arise, for example, because of differences in retinal illumination used to measure the delay[68]. It may also arise because the third order step response (Figure 2.3.1) has a slow onset which may be included in our experimentally measured value of τ As can be seen the predicted high gain oscillation frequency for the first and third order model are similar (respectively, $1.2\ Hz$ and $0.8\ Hz$). Both of these frequencies are in good agreement with measurements of pupil cycling[62,64,67].

2.3.7 Gain dependence of oscillation frequency.

It should be noted that the condition for the appearance of undamped oscillatory solutions of (2.3.4), i.e. (2.3.22), will always be satisfied for sufficiently large τ and/or G. The effect of increasing G on the properties of the oscillations that occur can be studied by analysing how the roots of (2.3.21) depend on the parameter B (proportional to the gain G). In Figure 2.3.3, it is clear that when $\sigma_1 > 0$, $d\lambda_1/dB \simeq d\sigma_1/dB$ Hence the frequency varies only slightly with the gain This accounts for the accuracy of the period of the oscillation predicted by linear theory. Interestingly, the period of the first unstable mode in our first order approximation (Section 2.3.5) is $\sim 2\pi/6$ which is in good agreement with Stark and Cornsweet[67] and with our measured lower limit ($0.9 - 1.2\ sec$).

2.3.8 Beyond the point of instability onset.

As G increases in value, more linear modes become unstable as more root pairs cross the imaginary axis into the right hand complex plane. In order to determine the extent to which these additional modes contribute to the frequency and/or shape of the oscillations, we considered the following specific example[24,86]

$$\frac{dA}{dt} + \alpha A = \frac{c\theta^n}{\theta^n + A_\tau^n}, \tag{2.3.25}$$

where c and θ are constants. This equation, a generalization of (2.3.1), describes first order dynamics for the pupil light reflex operating with smooth external negative feedback[99]. The "gain", which is proportional to the slope of the Hill function evaluated at $A \approx \theta$, increases as n increases. As shown in Figure 2.3.4, regular oscillations in pupil area occur for sufficiently large n. A supercritical Hopf bifurcation occurs for n between 3 and 10. Although the shape of these oscillations change as a function of n, there is little change in the frequency (compare Figures 2.3.4b with 2.3.4c). In addition, the more complex waveforms characteristic of the occurrence of higher order bifurcations are not seen.

Figure 2.3.2b-d show the Nyquist plots for (2.3.25) as n is increased. As n increases in value, more linear modes become unstable, corresponding to multiple encirclements of $(-1, 0)$ on the Nyquist plot (for example, there are seven encirclings in Figure 2.3.2d). Numerical calculations demonstrated that as either n or τ is increased, the real parts of the eigenvalues increase monotonically, i.e. an unstable mode does not become stable again. Also, in the limit of very large delay, many modes tend to become unstable simultaneously. The modes that become unstable contribute to changing the shape of the oscillations (Figure 2.3.4). The observation that increasing the number of unstable modes in a system can affect mainly the shape, and not the frequency of the oscillation has been reported previously[101].

The above results on the migration of roots across the imaginary axis also hold for a third order system (data not shown). Indeed, we have numerically computed the loci of the first poles of $H(s)$ (2.3.6) for $\tau = 0.2$ *sec*, $k = 0.1$ *sec* and G_0 between 0.16 and 10. The lowest frequency roots cross at $\omega_1 = 6.3$ and $\omega_2 = 28.6$ corresponding, respectively, to frequencies of 1.0 Hz and 4.55 Hz. These values are very close to those calculated from the characteristic equation of our first order approximation (Figure 2.3.3).

2.3.9 Discussion.

We have shown that direct analogies can be drawn between a delay-differential equation model for the pupil light reflex and previous servo control analytical studies. Since this delay-differential equation can be derived on the basis of neuro-physiological

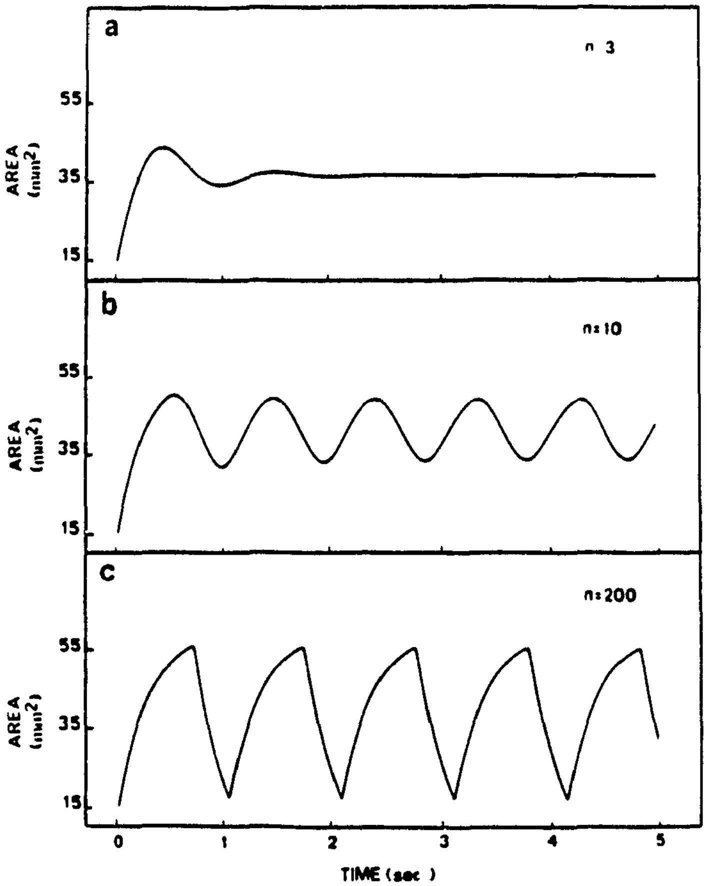

Figure 2.3.4 Solutions of (2.3.25) for increasing values of n. Initial condition for solution is: $A(t) = 15\ mm^2$, $t \in (-\tau, 0)$. Parameter values were: $\tau = 0.3\ sec$; $\alpha = 3.21\ mm^2$; $\theta = 50\ mm^2$; $c = 200\ mm^2$.

and anatomical considerations[99], this approach allows us to obtain insight into the properties of the reflex arc which determine, for example, its gain and transfer function. In particular, we are able to associate the gain, G_o, defined empirically by Stark[46] with three parameters (2.3.5): 1) the rate constant for the neural firing frequency (γ); 2) the steepness of the feedback function (β), and 3) the rate constant for pupillary movements (α). This association is further strengthened by the observation that both G [99] and G_o [74] attain their highest values at intermediate values of the steady state pupil area. This effect has been studied extensively and has been explained in terms of an 'expansive range nonlinearity' operating at the neuromuscular level and related to the nonlinear length-tension diagrams of the iris muscles

Oscillations in pupil area occur when the gain and/or delay become sufficiently large (2.3.22). The frequency of this oscillation predicted by linear servo control theory and a bifurcation analysis of (2.3.4) are both in good agreement with that measured experimentally, i.e ~ 1 Hz The appearance of this oscillation is associated with the migration of a root of the characteristic equation of (2.3.4), i.e. (2.3.21), with the largest real part (λ_1) across the imaginary axis into the right hand complex plane. As we have shown, the success of linear systems analysis in predicting this frequency is related to the relative insensitivity of the imaginary part of λ_1 to changes in the gain.

As the gain increases beyond the point of instability onset, more modes become unstable. In his 'clamped' pupil light reflex experiment, Stark[1] observed a double oscillation. It was suggested that the second mode to cross the imaginary axis results in a 0.2 Hz component superimposed on the basic 1 Hz rhythm. In the language of nonlinear dynamics, this suggests that a bifurcation from a limit cycle to a 2-torus has occurred. However, we have shown that for a first order delay equation this root alters the shape of the oscillation but has relatively little effect on its period Moreover, numerical simulations of the third order system indicate that the second mode would lie at a frequency of ~ 4.55 Hz and not at 0.2 Hz This observation indicates that the 0.2 Hz oscillation observed experimentally for the clamped pupil light reflex[1], in spontaneously recorded hippus[51] and in narcoleptics at sleep onset[50] cannot be attributed to simple nonlinear negative feedback mechanisms of the type we have considered here.

An important nonlinearity in the pupil light reflex is the response asymmetry of the reflex to the onset and offset of light[46,90] Although this asymmetry is most clearly manifested as a difference in the rates of pupil constriction and dilation[64,89], there is neuro-physiological evidence that this asymmetry also occurs at the level of the output of the retina and midbrain as well[80,82,83]. Because of this response asymmetry it is not possible to derive an impulse response in the classical sense from the pupil's response to a single light pulse.

The role played by reflex asymmetry in shaping pupil dynamics is most clearly shown in the case of external piecewise constant feedback since in this case the light is either on or off[64,89]. The transient behaviours of the pupil light reflex highlight the asymmetry. In Figure 2.3.3 we showed that ω_1 is not strongly dependent on the gain (through the related parameter B). We have found that this is also true if α in (2.3.21) is varied instead of B in either of two ways: first, be keeping B constant in the same range as that used in Figure 2.3 3 and second by recomputing B for every value of α since α determines A' and the parameter B contains $g'(A')$. Thus, if transients have died out, the waveforms should depend only on the imaginary part of the eigenvalues which vary only slightly with α. Asymmetry, which requires different values of α, would then be unnoticeable. This may explain the observation that transfer functions obtained under steady state conditions using low amplitude sinusoids predict so well the frequency of the high gain oscillations[67] Presumably there has been some kind of averaging of the asymmetric responses We expect that a transfer function based on transients (e.g one obtained by Fourier transforming the time derivative of the step response) may yield different results for light onset and offset.

Servo control analytical techniques, such as linear transfer functions, Volterra or Wiener kernel nonlinear response-fitting techniques, have been extensively used to provide descriptions of the response of the pupil to transient and steady state oscillatory light inputs and to identify nonlinearities in the reflex arc[46,49,74,98]. However, the description of the complex oscillatory phenomena produced by nonlinear neural control mechanisms (see, for example, Mackey and Milton[54]) requires that these techniques be augmented with methods from dynamical systems theory such as bifurcation analysis The analogies between the bifurcation analysis of a nonlinear ordinary differential equation and servo control analytic techniques have been made previously[102,103] Here we have given a concrete example to illustrate that these analogies can also be effectively made for nonlinear delay-differential equations.

CHAPTER 3
INDUCING NONLINEAR OSCILLATIONS IN THE HUMAN PUPIL LIGHT REFLEX

> "Richtiges Auffassen einer Sache und Miβverstehen der gleichen Sache schlieβen einander nicht vollständig aus."
> Franz Kafka

3.1 INTRODUCTORY REMARKS.

The physiological systems that have been studied from the point of view of nonlinear dynamics fall into two classes: externally forced oscillators and nonlinear feedback systems[26,27]. Experimental demonstration of bifurcations and chaos has been made in periodically forced neural oscillators such as mollusc neurons[30], as well as in embryonic chick heart cell aggregates [28] and Purkinge fibers[29]. Simple mathematical models involving one-dimensional maps and periodically forced Hodgkin-Huxley equations are in qualitative agreement with the observed behavior of these preparations. However, in these simple physiological systems (as in all physical systems), only a few bifurcations can be seen before aperiodic behavior sets in. Based on the models, it has often been concluded that the aperiodic time series represent a mixture of chaos and noise. Despite this, little effort has gone into characterizing the noise or determining whether an improvement in the models will yield better agreement between their predictions and the data. Also, a further question not resolved by these studies is whether the behavior of such isolated systems will be found in the intact *in vivo* systems.

While there exist experimental studies of forced oscillators from the nonlinear dynamics viewpoint, feedback systems have been relatively neglected because of the paucity of suitable experimental models. In this chapter, the following questions are addressed: 1) Can a human neural feedback system exhibit bifurcations from simple to complex deterministic motion? and if so, 2) How can these behaviors be analyzed in terms of a quantitative model? To answer these questions we have chosen to study oscillations in the human pupil light reflex.

The input to the pupil light reflex is the variation of retinal light flux (or "illuminance"), normally due to a change in light intensity. The output is also a variation in light flux, due to a change in pupil area following the neurological response. The input and output variations are normally of opposite sign, that is, they counteract each other. This describes closed-loop negative feedback operation. When the system is in open loop, the output response depends only on the input, rather than on the input and the output (at the same time or at an earlier time). Opening the loop leads to the interesting possibility of reclosing it using external feedback

This chapter describes experiments in which oscillations are induced in the pupil light reflex using external electronic feedback. This type of experiment is possible because the feedback loop can be easily and non-invasively opened using an optical method first described by Stark and Sherman[31]. It involves using a narrow ($< 1.2mm$ diam.) collimated light beam shone down the center of the pupil. Hence even under maximal pupil constriction, the iris can not shade the light beam The feedback loop is effectively opened using this "Maxwellian view" illumination. External electronically synthesized feedback[1,46,65] then allows an analog signal proportional to pupil area (as measured with a pupillometer) to control the intensity of the light source. The behavior of the resulting "clamped" neural control system can then be studied as the feedback parameters are varied.

Experimentally, it is relatively simple to convert pupil area variations into light intensity variations using a smooth (i e. differentiable) feedback function. It is very difficult, however, to control the mean light intensity because of uncontrollable drifts in the mean pupil area (e.g. due to hippus). Oscillations obtained under these conditions tend to be very unstable. This problem is circumvented to a great extent by using piecewise constant feedback in which the light intensity can take on only two values depending on the pupil area

In the following section we describe in detail the apparatus used to induce pupillary oscillations using piecewise constant negative (PCNF) and mixed (PCMF) feedback. An outline of Chapter 3 then follows.

3.1.1 Experimental methods.

Figure 3 2.1 in Section 3.2 shows a simplified schematic diagram of the experiment. Pupil area is measured using a binocular infrared videopupillometer (Hamamatsu Iriscorder Model C-2515, Hamamatsu City, Japan). The video cameras are infrared charge-coupled devices. The eyes are illuminated by an infrared light source (800 nm peak wavelength LED arrays) of adjustable intensity. Infrared illumination is used so as not to interfere with the visible light used to elicit the reflex. The 60 Hz sampling rate of the pupillometer is more than adequate given that the bandwidth of the PLR is about 2 Hz (3dB cutoff of open loop transfer function : see Stark[46]). The images are analyzed in real-time by a frame grabber that counts the number of pixels above a certain gray level set by the experimenter to discriminate between pupil and iris. The accuracy of area measurement is $0.01mm^2$ over a range of 0 to $150mm^2$ with a 1% linearity.

The output of the pupillometer is an analog voltage proportional to pupil area This signal is fed to the area comparator (Figure 3.2.1) which synthesizes the feedback. The schematic diagram of the area comparator and the driving circuit for the stimulus light are shown in Figure 3.1.1. The area comparator is simply composed of two voltage comparators and a logic gate The output of the circuit goes (TTL) high when the area signal is between the two adjustable thresholds T_1 and T_2, thus drives the light on. Otherwise, the subject sees the dark background illumination of the room The noisy fluctuations of the pupil area signal are band-limited by the sampling rate of the pupillometer. Thus the noise does not cause multiple triggerings as the area signal crosses the reference voltages of the comparators. For this reason we chose to use simple comparators rather than Schmidt triggers.

The stimulus light intensity provided by LED's (605 nm peak wavelength) was fixed at a value corresponding to a retinal illuminance of $\sim$ 375 trolands The light is collimated into a narrow beam the 1.2 mm beam waist is located at the pupil entrance (or "pupil plane") when the pupil is properly focused by the camera (the experimenter adjusts the focus using joysticks). Because of the divergence of the beam after entering the pupil, the subject sees large field illumination rather than a narrow spot. The subject focuses on a target (dim green asterisk) to keep the accommodation level (controlled by the lens curvature) constant, since pupil area varies with accommodation level (Section 2.1.2). The beam and target share the same optical axis as the cameras through the use of prisms.

In certain experiments, the digital signal from the area comparator was fed into an analog delay line which is a CMOS integrated circuit (EG&G Reticon 5208 "bucket brigade device" or BBD). This device produces delays which can vary from 4 milliseconds to 4 seconds by changing the sampling frequency f_s from 500 KHz to 500 Hz. The delay τ_{BBD} is given by $\tau_{BBD} = 2018/f_s$. The output of the BBD is processed by an 8-pole lowpass Bessel filter (Frequency Devices Model 902 LPF, Haverhill, MA, USA) to rid the signal of the sampling artifact.

The BBD can be inserted either between the pupillometer and the area comparator, or between the area comparator and the LED driver. However, the gain of the analog delay line is slightly dependent on the offset of the input signal. In view

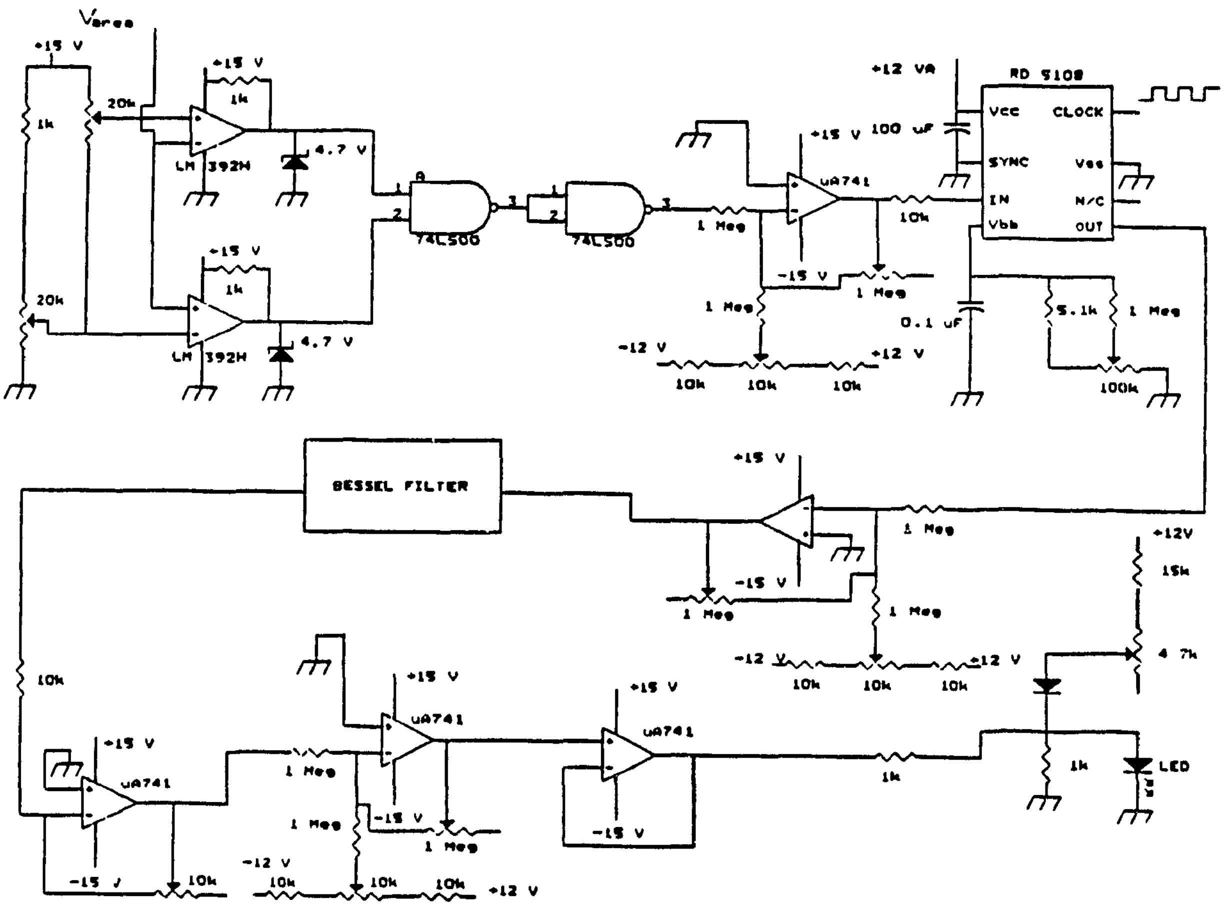

Figure 3.1.1 Circuitry for the external electronic feedback (or "area comparator") which was substituted to the normally occurring smooth negative feedback of the pupil light reflex. The input to the circuit is V_{area} (top left) which is the analog output of a videopupillometer. This voltage is proportional to pupil area. The first part of the circuit synthesizes the piecewise constant negative and mixed feedback (PCNF or PCMF). In certain experiments, an analog delay line was used to increase the delay. The output of this circuit is filtered by a Bessel 8-pole lowpass filter. The last stage of the area comparator is used to drive the stimulus light source. See text for details.

of the drifts in mean pupil area occurring during the experiments, we chose to put the BBD after the area comparator. By feeding the BBD a digital signal with constant offset (TTL 0-5 volts) from the area comparator rather than the signal from the pupillometer, the offset nonlinearity is effectively bypassed. This configuration has a drawback, since the subsequent Bessel filtering acts as a lowpass filter which will smooth out the abrupt transitions of the TTL signal. However, since the frequency of the TTL pulses will be low (0.5 - 20 Hz) due to the relatively slow pupil motion, a cutoff frequency of 200 Hz on the Bessel filter will produce a signal that still qualifies as digital on the time scale of the pupil response.

The video and image processing and the subsequent signal processing add a 25 msec delay to the normal physiological delay of this reflex ($\sim$ 300 msec). In certain experiments, an extra 75 msec delay was added when the TTL signal was sent to the light trigger input on the pupillometer rather than to the LED driver directly (see Figure 3.1.1). It is important that the timing and duration of the stimulus light pulses provided by the LED's are determined by the state of the system (pupil area) through the area comparator. This is very different from the case where non autonomous oscillations are produced by repetitive stimulation at a given frequency.

The left and right pupil areas and the stimulus light level were recorded on magnetic tape (Revox Model 110) and a polygraph chart recorder (Beckman Dynagraph Model 10000 BC). In all our experiments, the eye being stimulated is also the one being measured. The experiments were conducted on healthy males and females (ages 20-45) who were free from both ocular disease and disorders known to affect autonomic function. They were dark adapted for at least 15 minutes in a room lit only by a dim red light. During this dark adaptation, the retinal neurons increase their sensitivity and the pupils dilate. A measurement session could last up to an hour with many pauses of a few minutes, depending on the willingness and fatigue level of the subject. Because of blinking, typical records are limited to about 15-20 seconds for the mixed feedback experiments (Section 3.3 and 3.4) Blinking did not affect the negative feedback experiments, and cycling records lasting up to 120 seconds have been obtained.

3.1.2 Overview.

The outline of this chapter is as follows. Section 3.2 is an in-depth study of the simple oscillations obtained with PCNF. The section comprises the manuscript of a paper which has been accepted for publication in *Vision Research*. The modelling of visual physiology and the clinical implications of this paper make it suitable for *Vision Research*. Hence the mathematics and the nonlinear dynamics are reduced to their simplest expression.

We show that the physiologically sound model for PCNF oscillations (referred to as "pupil cycling") developed in Section 2.2.6 agrees very well with the experimental data. A key element in this analysis is an accurate method of estimating the model parameters from the data. Further the experiment and the theory suggest a technique to evaluate pupil constriction and dilation separately. Hence, it becomes possible to diagnose the state of the (different) neural pathways responsible for constriction and dilation. Also, by simplifying the feedback, it suggests ways to test for other specific nonlinearities.

The next two sections, 3.3 and 3.4, deal with the PCMF case. Chronologically, Section 3.3 was published first (in *Mathematical Biosciences*) as a preliminary study of the pupil light reflex clamped with PCMF. The model is completely *ad hoc*, and the parameter estimation scheme is based on responses to single pulses of light. Both the model and the estimation scheme are natural first steps towards the analysis of the results. The *ad hoc* model is shown to yield good quantitative agreement with the data for simple oscillations, and only qualitative agreement for the more complex behaviours. We ascribe the discrepancies to noise, and especially to multiplicative noise in the form of asymptote fluctuations (Section 2.2.6).

Subsequently the model was given a firmer footing (see Section 2.2), and a better parameter estimation scheme was devised (Section 3.2). Section 3.4 reinterprets the results of Section 3.3 for the PCMF case using the physiologically realistic model and the improved parameter estimation scheme. New results concerning multistability in the model equation are presented. The effect of additive and parametric noise on the observability of complex deterministic dynamics (and especially chaos) is discussed, along with physiologically relevant improvements to the model.

A more elaborate exposition of the model properties is given in Section 4.5 using the mathematical tools presented in Section 4.2.1, and the interested reader is encouraged to read these sections before proceeding to Sections 3.3 and 3.4.

3.2 EVALUATION OF PUPIL CONSTRICTION AND DILATION FROM CYCLING MEASUREMENTS.

Abstract.

Pupil cycling was produced using an electronic circuit so that the retina was illuminated in Maxwellian view only when pupil area exceeded an adjustable area threshold, A_{ref}. The maximum (A_{max}) and minimum (A_{min}) amplitude of the oscillations varied linearly with A_{ref}. These observations are described by a delay-differential equation. The A_{ref}-dependent changes in A_{max}, A_{min} were used, respectively, to quantitate dilation and constriction. A comparison of the predicted and observed period of pupil cycling suggests that the pupil latency times for light onset and offset are the same. Measurements of A_{max}, A_{min} provide a method for determining the average pupil light response.

3.2.1 Introduction.

Pupil constriction and dilation are typically evaluated from the changes in pupil area following a single light pulse. The accuracy of this method is limited by the effects of pupillary hippus and the intrinsic variability in the response of the pupil to identical light pulses[74]. Consequently, quantitative characterization of the pupil light response requires that a large number of pupil responses to individual light pulses be averaged (see, for example, Semmlow and Chen[49]; Sun et al.[103]; Usui and Stark[74]).

An alternative method for evaluating pupil movements involves inducing regular oscillations in pupil area ("pupil cycling") by either using a slit lamp to focus a narrow light beam at the pupillary margin[59,61] or by combining an infrared video-pupillometer with an electronic circuit which regulates retinal light flux as a function of pupil area[1,62,64,65]. Measurements of pupil cycling are important as a clinical test for detecting pathology within the pupil light reflex pathways. For example, a prolongation of the period of pupil cycling has been reported for a variety of afferent[61] and efferent[60] pupillary defects, whereas an intermittent irregularity in pupil cycling occurs in demyelinative optic neuropathies[62,63].

Here we show that measurements of the amplitude of pupil area oscillations reflect properties of the efferent arc of the pupil light reflex. This observation permits the development of a method for evaluating pupil movements from cycling measurements which offers a number of advantages over methods based on the pupil's response to single light pulses.

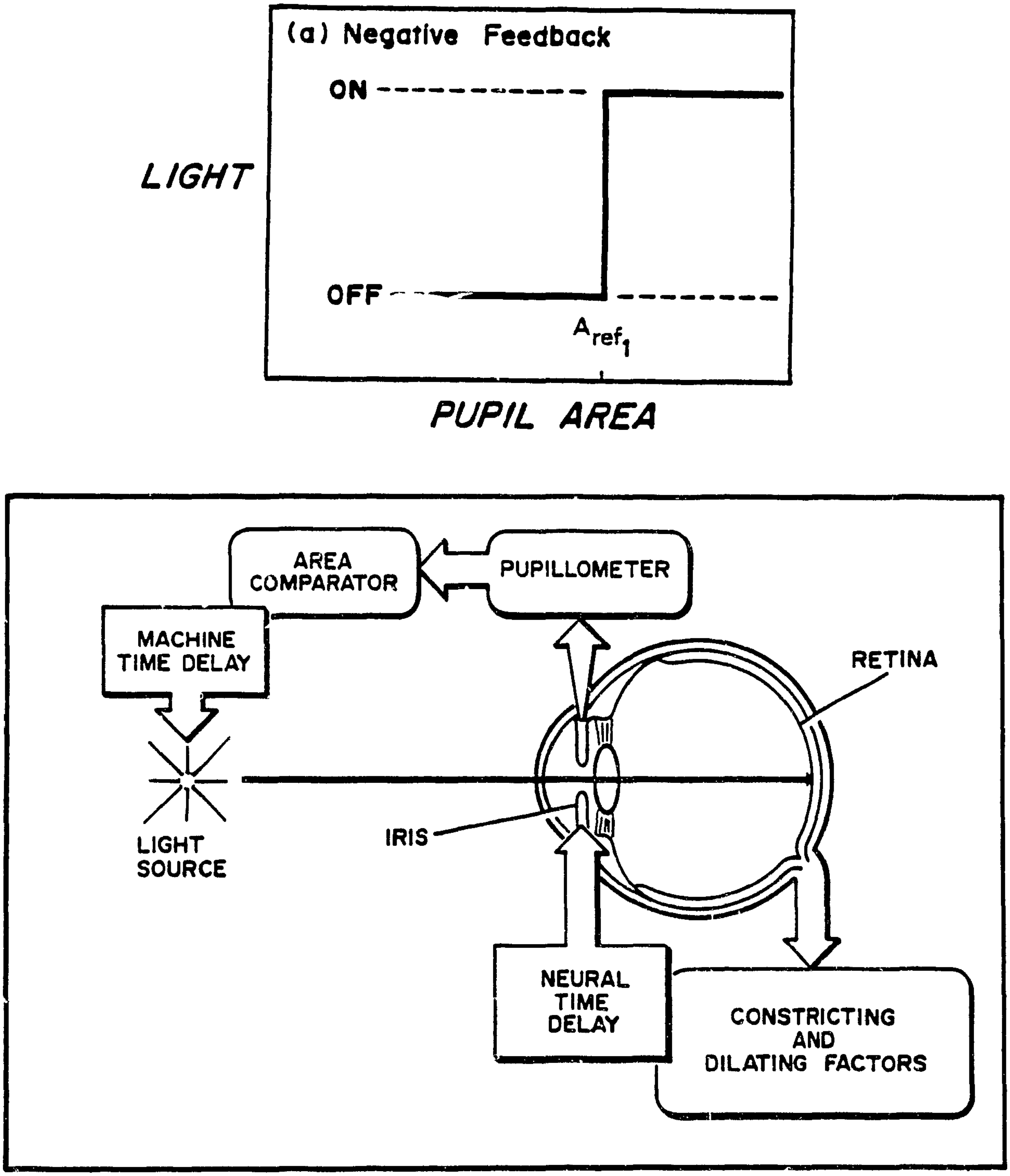

Figure 3.2.1 Schematic representation of the pupil light reflex with imposed external feedback. The area comparator used for pupil cycling compared the pupil area, A, to an adjustable area threshold, A_{ref}: when $A > A_{ref}$ the light was turned on and illuminated the retina in Maxwellian view, otherwise it was off. This area comparator corresponds to negative feedback since the pupil constricts when $A > A_{ref}$ (the light is on). It is piecewise constant negative feedback since the illumination can take on only one of two values, i.e. on or off.

3.2.2 Methods.

Subjects were healthy males and females ($n = 5$; ages 20-45 years) who were free from both ocular disease and disorders known to affect autonomic function. The experimental conditions and design of our experiment are the same as described previously[62,64]. A narrow light beam (diameter 1.2 mm; retinal illumination was 375-750 trolands; peak wavelength 605 nm) was focussed on the center of the pupil ('Maxwellian view') to "open" the feedback loop present in the pupil light reflex[31] When subjects were adapted for at least 15 minutes in a room lit only by a dim red light, the smallest pupil diameter was $\sim$ 4-5 mm. We used the measured pupil area to control the timing and duration of the light pulses falling on the retina by modifying the technique of environmental 'clamping' suggested by Stark[1] (Figure 3.2.1). This was accomplished by comparing the analog output of an infrared video-pupillometer (Hamamatsu Iriscorder C-2515) to an adjustable area threshold, A_{ref}, by using an electronic circuit (area comparator in Figure 3.2.1) The area comparator was constructed using standard voltage comparators (LM392H), operational amplifiers (LM741) and logic gates (74LS00) and was designed to simulate piecewise constant negative feedback (see legend to Figure 3.2.1). The retinal light intensity can take on only one of two values depending on whether the pupil area is greater than or less than A_{ref}. This area comparator is an idealization of the method of edge-light pupil cycling, where A_{ref} corresponds to the pupil area at which the positions of the slit lamp beam and the pupillary margin coincide. However, in our method the illumination is not at the pupillary margin, but is in Maxwellian view. The advantages of the electronic method of pupil cycling over that of edge-light pupil cycling are[62]. 1) the pupil area oscillations are easier to obtain and control experimentally; and 2) the oscillations can be studied over a range of pupil areas by varying A_{ref} (Figure 3.2.2).

The pupil images were analyzed by a frame grabber that counts the number of pixels above a gray level set by the experimenter to discriminate between pupil and iris. The sampling rate of the pupillometer was 60 Hz and the linearity is better than 1 % from 0 to 150 mm^2 with an accuracy of 0.01 mm^2 The bandwidth of the pupillometer is well beyond that of the pupil light reflex (about 5 Hz: see Stark[46]). Hence, for all practical purposes, the response time of the pupillometer can be neglected on the time scale of the phenomena we are considering in this study However, the following image and signal processing ($\sim$ 25 msec) and triggering of the light pulse

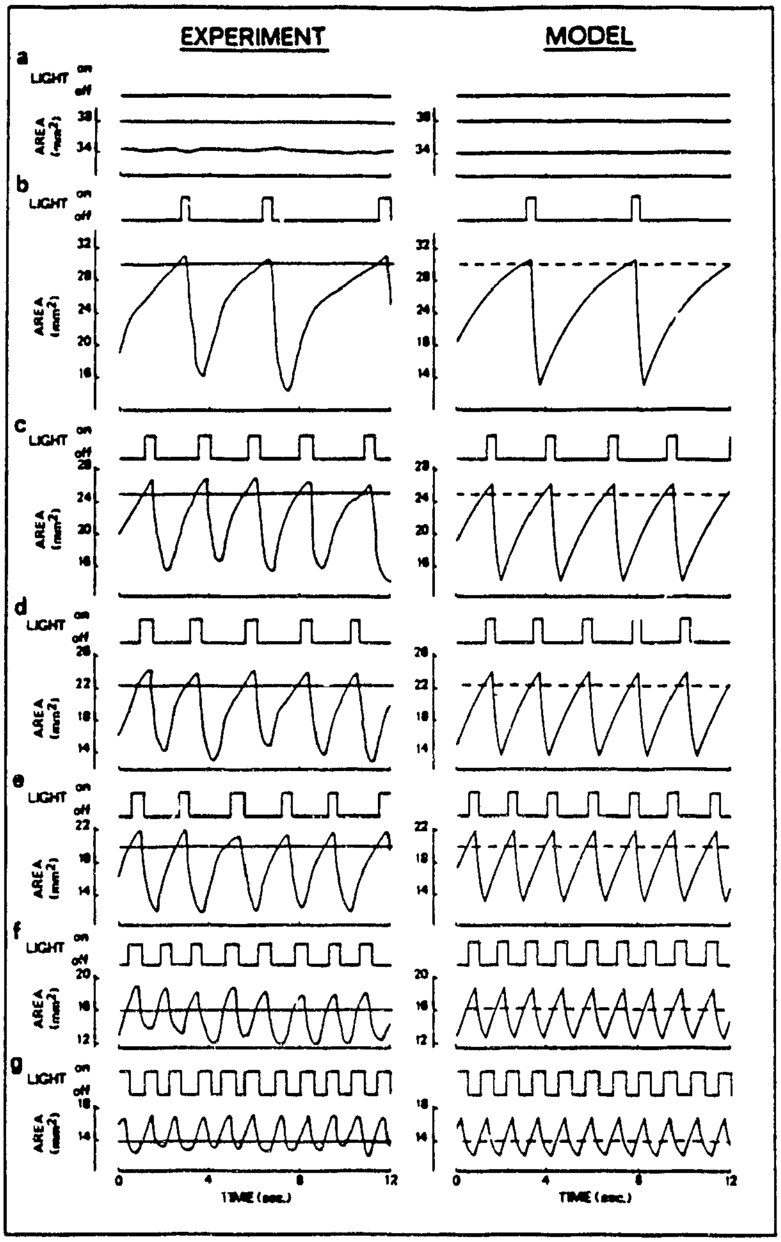

Figure 3.2.2 Pupil cycling with imposed piecewise constant negative feedback (Figure 3.2.1b) as a function of A_{ref} for subject A (ML) in Table 3.2 (left hand side). The value of A_{ref} is represented by the horizontal dotted line and was set at: a) 38.0 mm^2 , b) 30.1 mm^2, c) 25.0 mm^2, d) 22.5 mm^2, e) 20.1 mm^2, f) 16.2 mm^2 and g) 14.0 mm^2 . The left hand side of this figure shows the solutions of (3.2.1) for the values of the parameters given in Table 3.2.

(~ 75 msec) add a 100 msec pure delay ("machine delay") to the normal physiological delay of this reflex (~ 300 msec for the retinal illuminance used in this study[62]) The pupil latency time (delay) following light onset was evaluated as the time between the onset of the light stimulus and the onset of pupil constriction by using the computer supplied with the Hamamatsu Iriscorder C-2515. The determination of the pupil latency time following light offset is discussed in the RESULTS.

3.2.3 Results.

Pupil Area Oscillations

Figure 3.2.2 shows pupil area as a function of time for a normal subject (subject A in Tables 3.1 and 3.2) when the area threshold, A_{ref}, is set at various levels. When A_{ref} is larger than the initial pupil area, A_i, regular oscillations in pupil area do not occur (Figure 3 2.2a). Repetitive constrictions and dilations in pupil area occur when $A_{ref} < A_i$. The light is turned on ~ 100 msec after pupil area exceeds A_{ref}. This delay represents the machine delay. The onset of constriction occurs ~ 300 msec after the light is turned on. This delay is the pupil latency time to light onset. Once pupil area constricts to a value less than A_{ref}, the light is turned off after the machine delay. The pupil continues to constrict for the duration of another latency (latency time for light offset), after which it begins to dilate. The process repeats and gives rise to cycling.

In the discussion which follows we use the notation τ_c, τ_d to refer to the sum of the machine delay and pupil latency time for, respectively, light onset and light offset

The period and amplitude of the pupil area oscillations shown in Figure 3 2 2 depend on the choice of A_{ref} relative to A_i. As A_{ref} is brought closer to A_i, the amplitude and period of the pupil area oscillations increase. In addition, the fraction of time that the light is on during each cycle in pupil area decreases (~ 0.5 when $A_{ref} = 14.2$ mm^2 versus ~ 0.1 for $A_{ref} = 30.1$ mm^2) As shown in Figure 3.2.3, the maximum amplitude, A_{max}, and minimum amplitude, A_{min}, of the pupil area oscillations vary linearly as a function of A_{ref}. In contrast, there is a nonlinear relationship between the average period of the pupil area oscillations and A_{ref} (Figure 3.2.4).

TABLE 3.1

PARAMETERS FOR PUPIL CONSTRICTION AND DILATION FROM PUPIL CYCLING MEASUREMENTS

Subject	τ^a (msec)	α_c (sec^{-1})	α_d (sec^{-1})	A_{on} (mm^2)	A_{off} (mm^2)
A	380	4.46	0.42	11.8	34.0
B	385	3.11	0.74	15.7	34.5
C	411	3.88	0.27	15.5	34.2
D	400	4.69	0.36	26.3	52.4
E	305^b	5.19	0.46	16.4	39.5

TABLE 3.2

PARAMETERS FOR PUPIL CONSTRICTION AND DILATION MEASURED FROM SINGLE LIGHT PULSE PUPILLARY RESPONSES

Subject	τ^a (msec)	α_c (sec^{-1})	α_d (sec^{-1})	A_{on} (mm^2)	A_{off} (mm^2)
A	380	2.50	0.48	10.0	34.4
B	385	2.50	0.84	15.2	33.6
C	411	3.33	0.50	15.8	34.8
D	400	3.84	0.63	25.2	51.1
E	305^b	4.87	0.55	14.0	35.5

a) Total time delay = neural time delay + machine time delay

b) Machine time delay was 100 msec for all subjects, except subject E for whom it was 25 msec.

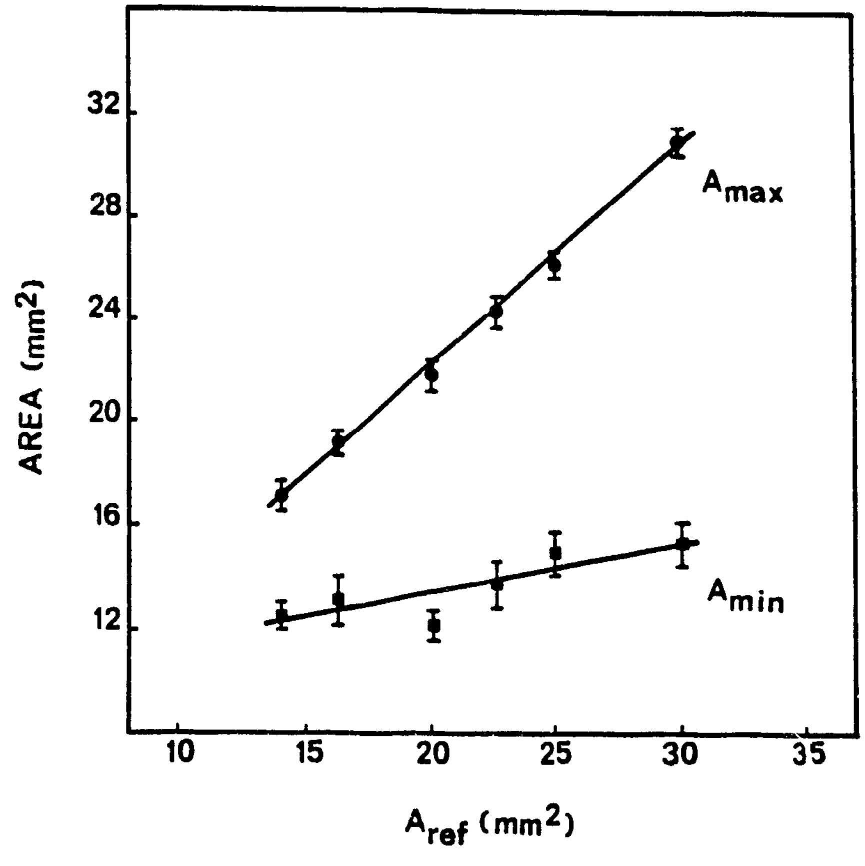

Figure 3.2.3 Plots of A_{max} and A_{min} as a function of the area threshold, A_{ref}, for subject A (Tables 3.1 and 3.2 and Figure 3.2.2). Data has been represented as the mean ± 1 SD and is for a range of 12-18 consecutive cycles. Solid lines were determined from a linear regression analysis.

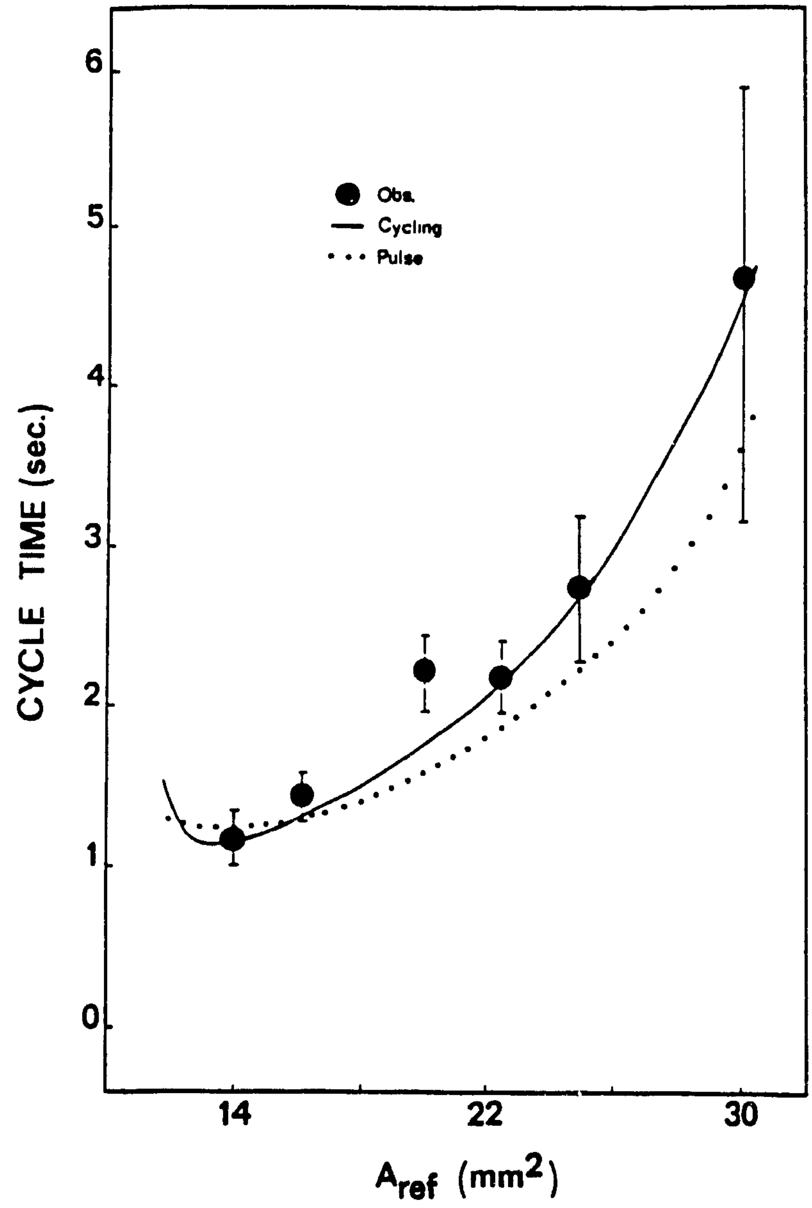

Figure 3.2.4 Comparison of the observed period, T, of pupil cycling as a function of A_{ref} for subject A (Figures 3.2.2 and 3.2.3) to that predicted by (3.2.4). Data has been represented as the mean ± 1 SD and is for a range of 12-18 consecutive cycles. The solid line is the value of T predicted from (3.2.4) when $\tau_c = \tau_d$. In all calculations, τ_c =380 msec.

First-Order Model

Background

The pupil light reflex may be viewed as a delayed negative feedback neural control mechanism which regulates the retinal light flux (equal to the light intensity multiplied by the pupil area) by changing the pupil area. The delay arises because of the pupil latency time(s). Pupil cycling occurs when, for example, the gain of the feedback loop is increased[67,84,99] Self-generated oscillations of this type are referred to as autonomous oscillations. It is important to distinguish autonomous pupil cycling (Figure 3.2.2) from experiments in which oscillations in pupil area occur in response to an independent external light pulse generator ("forced" oscillations) (see, for example, Sun et al.[104]).

The description of autonomous oscillations in pupil area requires the use of a nonlinear delay-differential equation[64,84,99]. The nonlinearities arise, for example, because of the logarithmic compression of light intensities at the retina (Weber-Fechner law). For physiologically relevant choices of the feedback function these equations cannot be solved analytically[99]. However, under the experimental conditions described in Figure 3.2.1 the feedback function (area comparator) is of a very simple type and the oscillations in pupil area, A, can be described by[20,64,99]

$$\alpha^{-1}\frac{dA}{dt} + A = \begin{cases} A_{on}, & \text{if } A_{\tau} > A_{ref} \\ A_{off}, & \text{if } A_{\tau} < A_{ref} \end{cases} \qquad (3.2.1)$$

where A_{τ} is the pupil area at a time τ in the past, i.e. $A_{\tau} = A(t - \tau)$. Equations of the form of (3.2.1) are of particular interest for the study of oscillations in feedback mechanisms because it is possible to obtain a great deal of mathematical insight into their properties[66] (see also Appendix I).

Equation (3.2.1) is a first-order model for pupil cycling since both constriction and dilation are described by single exponential processes. However, the rate constant for pupil movements differs for constriction (α_c) and dilation (α_d) Figure 3.2.5 shows a typical solution of (3.2.1). When the light is on, pupil size decreases exponentially to a lower asymptotic area (A_{on}), whereas when the light is off, pupil size increases exponentially towards a higher asymptotic area (A_{off}).

Parameter estimation

In order to compare the first order model for pupil cycling given by (3.2.1) to the experimental observations in Figures 3.2.2-4 it is necessary to estimate seven para

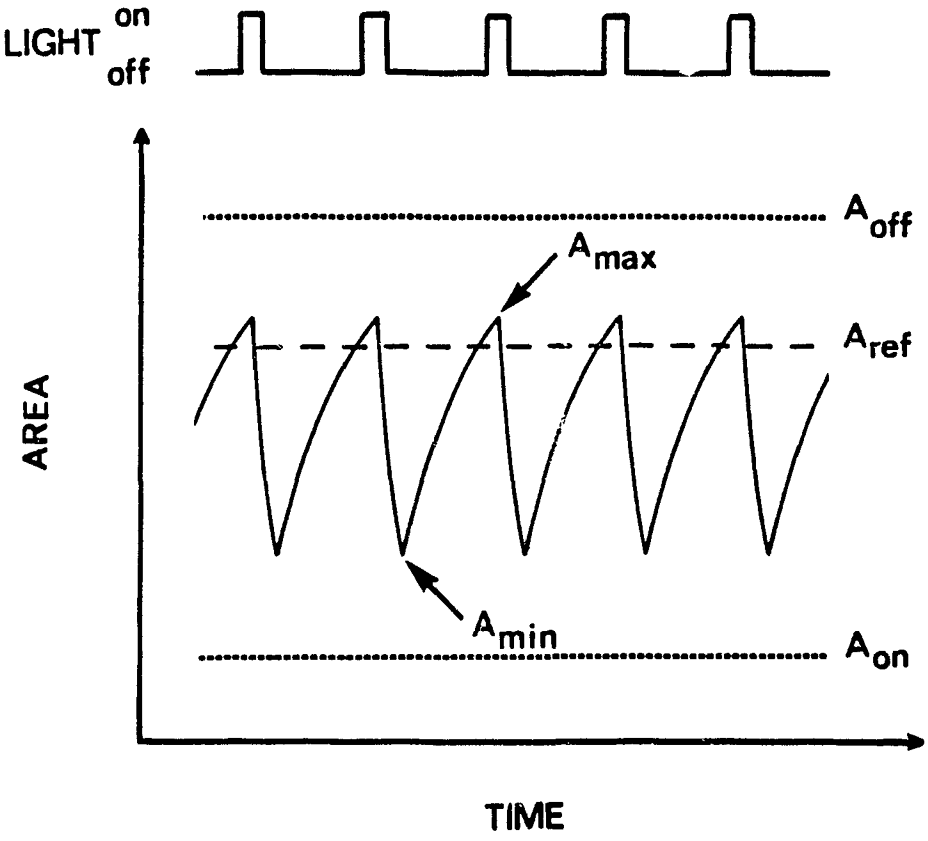

Figure 3.2.5 Detailed representation of a typical solution of (3.2.1) when $A_{ref} < A_i$. See text for details.

meters: $\alpha_c, \alpha_d, A_{on}, A_{off}, A_{ref}, \tau_c$ and τ_d. The value of A_{ref} is set by a potentiometer. In our previous study[64] we assumed that τ_c τ_d and estimated the values of $\alpha_c, \alpha_d, A_{on}$ and A_{off} from the changes in pupil area that occur following a 0.5 second light pulse as shown in Figures 3.2.6a and 3.2.6b. The area asymptote, A_{off}, is taken as the initial pupil area and A_{on} is the minimum pupil area following a longer (2 second) light pulse of the same illuminance. The values of $\alpha_c, \alpha_d, A_{on}$ and A_{off} determined in this manner for five normal subjects are listed in Table 3.1.

Here we show that the parameters $\alpha_c, \alpha_d, A_{on}$ and A_{off} can be estimated directly from pupil cycling measurements. This result follows from the fact that (3.2.1) can be solved analytically (Appendix I). The solution indicates that a plot of A_{min} versus A_{ref} will be linear (Figure 3.2.3) and specifically that

$$A_{min} = a + bA_{ref} \tag{3.2.2}$$

where

$$a = A_{on}(1 - b) \tag{3.2.3a}$$

and

$$b = \exp(-\alpha_c \tau_c) \tag{3.2.3b}$$

Since the value of τ_c can be determined experimentally (see Methods), the slope of this plot yields α_c and the intercept A_{on}. An expression equivalent to those given by (3.2.2) and (3.2.3) is found for A_{max} except that α_c, τ_c and A_{on} are replaced, respectively, by α_d, τ_d and A_{off} Thus the intercept of a plot of A_{max} versus A_{ref} can be used to determine A_{off}. However, since τ_d is not known, the slope of this plot does not permit the value of α_d to be determined uniquely

Table 3.2 summarizes the values of $\alpha_c, \alpha_d, A_{on}$ and A_{off} determined from cycling measurements for the same five subjects in Table 3.1 under the assumption that $\tau_c = \tau_d$. In comparing the results in Tables 3.1 and 3.2 it is important to realize that the results in Table 3.1 are determined from the response to a single light pulse at a single initial pupil area, whereas for cycling these parameters represent, in some sense, an averaging over 50-70 single pulse determinations covering a range of initial pupil areas (i.e. 10 light pulses per area threshold, times 5-7 area thresholds) The values of A_{on} and A_{off} obtained by the two methods are in good agreement; however, the values of α_c and α_d differ. The differences in α_d cannot simply be attributed to the uncertainty in τ_d since an increase in τ_d would decrease the value of α_d even further (see (3.2.3b)).

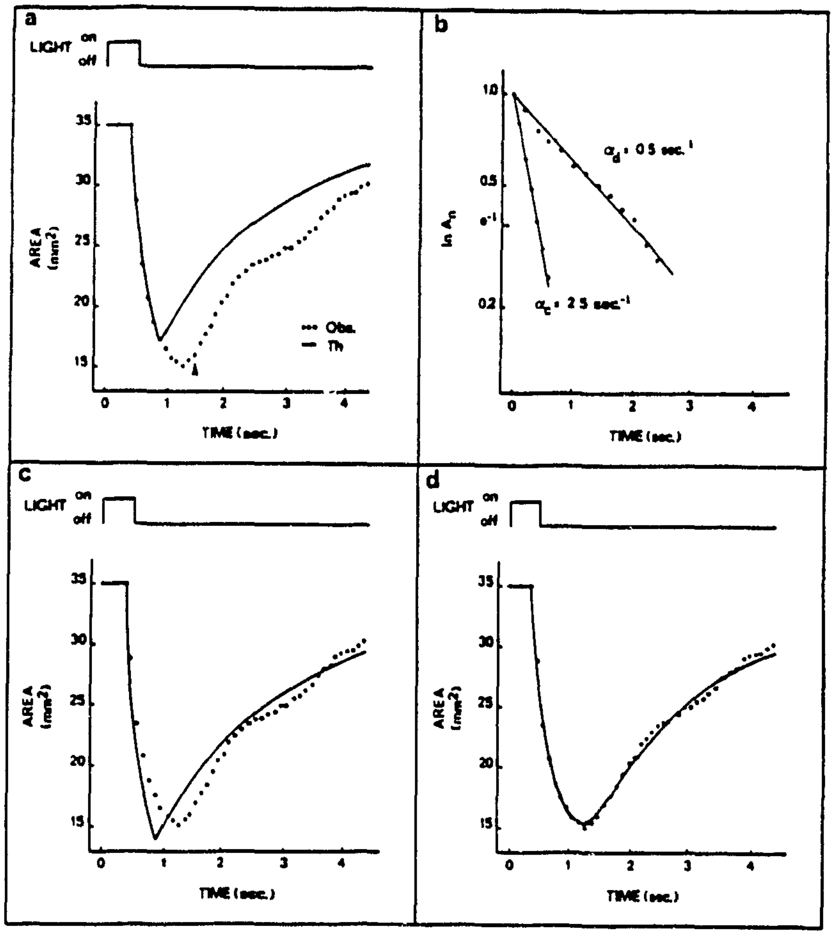

Figure 3.2.6 Pupil area as a function of time, A_t, following a single 0.5 second light pulse for subject A (dotted line). In a) the observed pupillary response is compared to that predicted by (3.2.1) when the parameters are estimated by the single pulse method (solid line, subject A in Table 3.1, see text for details). The semi-log plots for the determination of α_c, α_d are shown in b) where A_n is the normalized pupil area, i.e. $A_n = |A_t - A_{on,off}| / |A_i - A_{on,off}|$. For pupil constriction the initial value of A_t was taken as the onset of constriction and for dilation the initial value of A_t was arbitrarily chosen as the point indicated by " ▲ ". In c) the observed pupillary response is compared to that predicted by (3.2.1) when the parameters are estimated from cycling measurements (solid line, subject A in Table 3.2). In d) the observed pupil response is compared to an empirical model in which constriction is described by a single exponential process and dilation by two exponentials (i.e. equation (3.2.5)). Details of the parameter estimation for the predicted solution in d) are given in Appendix II.

Figures 3.2.6a and 3.2.6c compare the changes in pupil area that occur following a 0.5 second light pulse to those predicted from (3.2.1) when the parameters $\alpha_c, \alpha_d, A_{on}$ and A_{off} have been estimated, respectively, from single pulse measurements (Figures 3.2.6b, Table 3.1) and pupil cycling measurements (Figure 3.2.3, Table 3.2). Pupil cycling measurements yield parameters which provide a better description of the pupillary time course when $\tau_c = \tau_d$. Similar results were obtained for all subjects studied. In the discussion which follows we consider only those solutions of (3.2.1) in which the parameters have been estimated from cycling measurements.

Period of pupil area oscillations

The period of pupil cycling, T, predicted by (3.2.1) is (Appendix I)

$$T = \tau_c + \tau_d + \alpha_c^{-1} \ln \left[\frac{A_{max} - A_{on}}{A_{ref} - A_{on}} \right] + \alpha_d^{-1} \ln \left[\frac{A_{min} - A_{off}}{A_{ref} - A_{off}} \right] \qquad (3.2.4)$$

In Figure 3.2.4 we show the period (T) of pupil cycling (solid line) calculated from (3.2.4) when $\tau_c = \tau_d$. The discrepancy between the predicted and observed average period of pupil cycling is typically less than 5-10 %.

It should be noted that (3.2.4) predicts that the period of pupil cycling is not a monotone increasing function of A_{ref}, but passes through a minimum. We were unable to verify this experimentally. With decreases in A_{ref} below 14 mm^2, pupil area would undergo 2-3 cycles with increasing A_{min} until the cycling stopped with the light on and $A_{min} > A_{ref}$. It is not clear whether this phenomenon arose because of a type of pupillary escape[85,98,105] or represents changes in A_{on} due to retinal adaptation[64].

Light offset latency time (τ_d)

Equation (3.2.4) in combination with (3.2.2) and (3.2.3) can also be used to calculate the period (T) of pupil cycling when the latency times for light onset and offset are not the same (i.e. $\tau_c \neq \tau_d$). In Figure 3.2.4 we show the period (T) of pupil cycling calculated from (3.2.4) for two values of $\tau_d > \tau_c$ (and hence of α_d; see (3.2.3b)) (dotted lines). As can be seen the best agreement between the predicted and observed periods of pupil cycling occurs when $\tau_c = \tau_d$.

Amplitude of pupil area oscillations

The fact that the values of $\alpha_c, \alpha_d, A_{on}$ and A_{off} are determined from the data in Figure 3.2.3 guarantees that the solutions of (3.2.1) will have the same average amplitude as observed for pupil cycling (Figure 3.2.2).

Shape of pupil area oscillations

One way to compare the shape of the predicted and observed pupil area oscillations is to plot pupil area as a function of time (Figure 3.2.2). However, the limitations of this method for comparing the shape of oscillations are immediately apparent. The observed pupil area oscillations show small cycle to cycle variations in period and amplitude due to noisy inputs into the pupil light reflex which have not been incorporated into (3.2.1). Thus one cannot easily compare theory with observation by, for example, superimposing the predicted and observed time series.

A much better method for comparing the shape of predicted oscillations to those observed experimentally involves the construction of a "phase plane diagram". A phase plane diagram is a convenient way of graphing pupil area changes as a function of time since for an oscillation a closed loop trajectory will be obtained. For (3.2.1) a phase plane diagram can be constructed by plotting $A(t)$ versus $A(t-\tau)$. The advantage of constructing a phase plane diagram is that the overall average shape of the oscillation can be assessed and compared to theory even in the presence of noisy perturbations.

Figure 3.2.7 compares the measured phase plane diagrams for different values of A_{ref} to those predicted by (3.2.1). As plotted the trajectories are traversed in a counter-clockwise direction and the orientation is as follows : the upper right-hand corner corresponds to the change from dilation to constriction and the lower left-hand corner to the change from constriction to dilation. As A_{ref} is changed, the predicted shape of the closed trajectories changes from triangular (Figure 3.2.7a) to roughly quadrilateral (Figure 3.2.7d). Overall there is surprisingly good agreement between the experimentally measured and predicted phase plane trajectories. However, on closer inspection it can be seen that the best agreement between (3.2.1) and observation occurs for the latter stages of dilation and the earlier stages of constriction.

Alternative Models for Pupil Cycling

The preceding results demonstrate that the period and amplitude of pupil area oscillations can be predicted from a model (3.2.1) in which both constriction and dilation are described by single exponentials and in which the latency times for light onset and offset are the same (Figures 3.2.2-4). However, the shape of the predicted oscillations is not exactly the same as that observed (Figure 3.2.7).

We found that a much better fit to the changes in pupil area following a single light pulse was obtained when dilation was represented by a sum of two exponentials

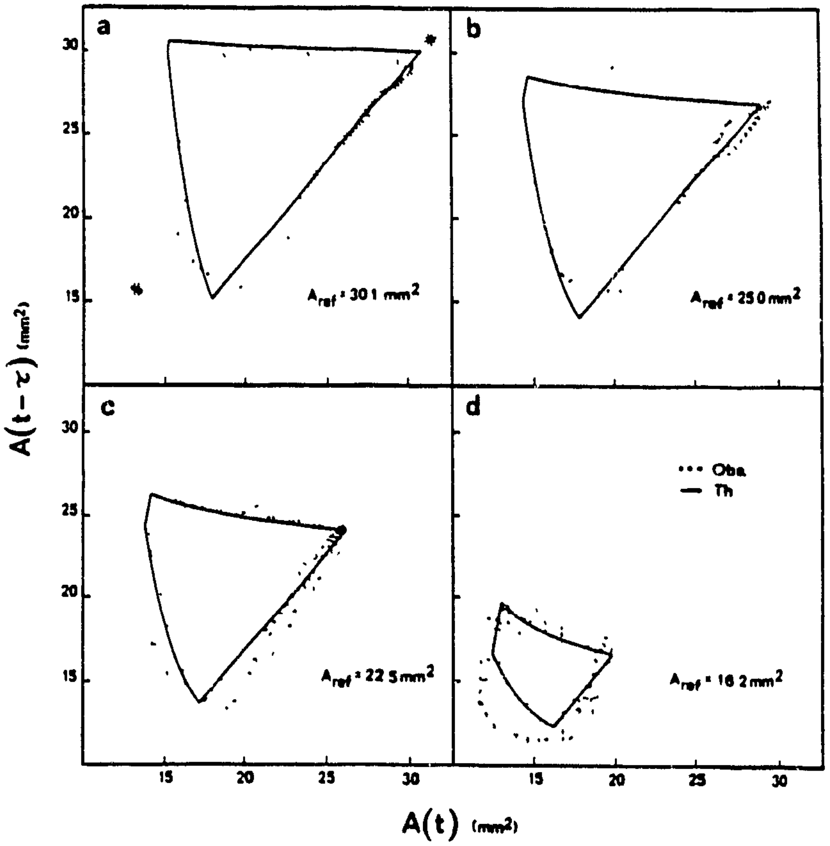

Figure 3.2.7 Phase plane diagrams for pupil cycling as a function of A_{ref} for subject A (Figures 3.2.2 to 3.2.4). The data was digitized at a frequency of 20 Hz. Solid lines are those predicted by (3.2.1) for parameters estimated from the data in Fig. 2 (subject A in Table 3.2). A_{ref} was set at: a) 30.1 mm^2, b) 25.0 mm^2, c) 22.5 mm^2, and d) 16.2 mm^2. The change of constriction to dilation is indicated by the '#' in a) and the change from dilation to constriction by the '$*$'.

(compare Figure 3.2.6d with Figures 3.2.6a,b,c). This fit was obtained with $\tau_c = \tau_d$ (Appendix II). In view of these observations, an alternative model for pupil area oscillations becomes

$$\left.\begin{aligned} \alpha^{-1}\frac{dA}{dt} + A = A_{on} \qquad & \text{if } A_r > A_{ref} \\ \frac{d^2A}{dt^2} + \delta\frac{dA}{dt} + \omega^2 A = A_{off} \qquad & \text{if } A_r < A_{ref} \end{aligned}\right\} \tag{3.2.5}$$

where δ, ω are constants to be determined. In contrast to the expressions derived from (3.2.1), it is not possible to obtain simple mathematical expressions for A_{max} and T. Thus we cannot presently estimate the three pupillary rate constants and area asymptotes from cycling data in a way more practical than fitting the time course of the pupil area changes following a single light pulse using a nonlinear regression analysis.

Preliminary computer simulations of (3.2.5) indicate that the shape of the pupil area oscillations closely resemble that of the observed oscillations (data not shown). However, given the difficulties in estimating the required parameters, it is not yet possible to assess the agreement between model and data with certainty.

3.2.4 Discussion.

Our observations emphasize the importance of measurements of the amplitude, rather than the period, of pupil area oscillations for obtaining quantitative descriptions of pupillary constriction and dilation. In particular, when pupil area oscillations are produced under conditions of piecewise constant negative feedback (Figure 3.2.1), it is found that the minimum (A_{min}) and maximum (A_{max}) amplitude vary linearly with A_{ref}. The A_{ref}-dependent changes in A_{min} depend only on factors which influence pupil constriction (see, for example, (3.2.2)), whereas changes in A_{max} are related only to changes in the factors which influence pupil dilation. This follows from the response assymmetry of the pupil to light onset and offset[84,99]. Thus pupil constriction and dilation can be quantitated in terms of the slopes and intercepts of straight line plots. This technique should facilitate the evaluation of efferent pupillary defects.

Quantitative evaluation of pupil responses from measurements of pupil area oscillations produced under conditions of piecewise constant negative feedback offers a number of advantages over measurements following single light pulses and edge-light pupil cycling. By cycling the pupil, the effects of hippus are minimized since high frequency noise is reduced by the self-filtering action of the resonance peak of the autonomous oscillations which acts as a narrow-bandpass filter[1]. Second, generating a plot of A_{min} (or A_{max}) versus A_{ref} is in some sense equivalent to averaging 50-70 single light pulses covering a range of initial pupil areas. These measurements are not time consuming: the experiment in Figure 3.2.2 took less than 5 minutes to complete. Obtaining an averaged pupil response is important in view of the intrinsic variability of the pupil's response to light pulses[74]. Finally, measurements of amplitude show less variability than those of period (compare standard deviations for A_{min}, A_{max} in Figure 3.2.3 to those of period in Figure 3.2.4, especially at the higher values of A_{ref}).

The infrared pupillometer chosen for this type of study must meet two requirements. First, its response time must be sufficiently faster than the pupil responses (20-60 Hz is adequate for most purposes). Second, since the differences between, for example, A_{max} and A_{ref} can be quite small (Figure 3.2.3), it is important that the pupillometer be able to measure pupil area accurately. The 0.01 mm^2 resolution of the pupillometer used in this study appears to be adequate for most purposes. The necessary area comparator (Figure 3.2.1) can be easily installed in both video-type[62,64,106] and reflectance-type[1,65] pupillometers.

The observation that A_{min} (or A_{max}) varies linearly with A_{ref} can be explained by a mathematical model for pupil cycling (3.2.1) in which both pupil constriction and dilation occur as single exponential processes but with different rate constants. This model also correctly predicts the period of the pupil area oscillations. However, measurements of the period of the oscillations as a function of A_{ref} are not sufficient to identify the individual role of the constricting and dilating mechanisms of the pupil light reflex (3.2.4). This observation emphasizes the importance of amplitude over period measurements for evaluating the properties of the efferent pathways of the pupil light reflex.

It is generally held that the pupil latency time for light offset (τ_d) is either equal to or longer than the latency time for light onset (τ_c) (see, for example, Löwenstein and Friedman[75]). However, direct measurement of τ_d is difficult since the onset of dilation following light offset cannot readily be determined by visual inspection. The problem is that pupil area may initially continue to decrease after the onset of dilation because of the effects of the mechanical properties of the iris and its musculature which prevent sudden changes in the sign of the velocity. Thus determination of τ_d from the pupil response to a light pulse requires reference to a mathematical model. On the other hand, it is unlikely that τ_d can be measured directly from the pupil response to a dark pulse. The response of the pupil to either a light or dark pulse is in the same direction ("unidirectional rate sensitivity") (see Clynes[90]). Thus it is unclear whether measurement of a latency to a dark pulse would correspond to the τ_d relevant for pupil cycling measurements. From the standpoint of a first-order model for pupil cycling (3.2.1), the best agreement between the predicted and observed period of the pupil area oscillations occurs when τ_c and τ_d are approximately the same. When the alternative, more complex model for the pupil response to light (3.2.5) was used, the observed pupillary response could also be modelled with $\tau_c = \tau_d$. These observations do not prove conclusively that $\tau_c = \tau_d$, but they are certainly highly suggestive.

The shape of the observed oscillations in pupil area is only approximately described by (3.2.1). It is possible that by increasing the number of exponentials which describe constriction and/or dilation a better description of the shape of the oscillations can be obtained. In this way insights can be gained into the properties of the efferent properties of the pupil light reflex. For example, we found that a better agreement between the predicted and observed shape of the pupil response to a single light pulse is obtained when dilation is modelled as the sum of two exponentials. The main limitation of this type of approach are the difficulties associated with estimating the required number of parameters from the experimental data.

Our observations do not allow us to identify the neurophysiological mechanisms responsible for pupil dilation during pupil cycling. The role of sympathetic efferents is uncertain given the observations that pupil cycling can be elicited in human subjects even when the sympathetic supply to the pupil is cut surgically[62] or blocked pharmacologically[60].

A parasympathetic mechanism producing pupil dilation involves active inhibition of the Edinger-Westphal nucleus[34]. Experiments will be required to determine the relative roles of the sympathetic and parasympathetic mechanisms for producing pupil dilation during pupil cycling.

Studies of the pupil light reflex "clamped" with external electronic feedback have been used previously to determine the influence of the 'linear' and 'nonlinear' properties of the reflex in determining the period and shape of the oscillations[1]. Here we have shown that this technique can also be used as a practical method for evaluating the average pupil constriction and dilation. From the more general point of view of the study of oscillations (i.e. nonlinear dynamics), this experimental paradigm of neural control also provides unique opportunities to verify theoretical predictions, to draw attention to unexplained phenomena, and to assess the role of superimposed random variations ("noise") in shaping the observed dynamics[20,64,99]. It can be anticipated that by continuing to exploit this experimental model it will be possible to gain insights into the properties of this reflex by, for example, clever design of the area comparator. Some of these insights may also be applicable to other neural control mechanisms as well.

Appendix I: Solution of Equation (3.2.1)

The oscillations in pupil area produced by (3.2.1) (Figure 3.2.5) are referred to as limit cycles. Assume that the motion described by (3.2.1) has settled onto the limit cycle oscillation. Then we can write the solution as

$$A(t) = \begin{cases} A_{on} + [A(t_o) - A_{on}][\exp(-\alpha_c(t - t_o))], & \text{if } A(s - \tau) > A_{ref} \\ A_{off} + [A(t_o) - A_{off}][\exp(-\alpha_d(t - t_o))], & \text{if } A(s - \tau) \leq A_{ref} \end{cases} \tag{I.1}$$

where $s \in (t_o, t)$. Let A_{max} (A_{min}) denote the maximal (minimal) area reached by the oscillations (Figure 3.2.5). Then

$$A_{ref} = A_{max} \exp(-\alpha_c t_1) + A_{on}[1 - \exp(-\alpha_c t_1)] \tag{I.2a}$$

$$A_{ref} = A_{min} \exp(-\alpha_d t_2) + A_{off}[1 - \exp(-\alpha_d t_2)] \tag{I.2b}$$

from which we can easily obtain

$$t_1 = \alpha_c^{-1} \ln \left[\frac{A_{max} - A_{on}}{A_{ref} - A_{on}} \right] \tag{I.3a}$$

$$t_2 = \alpha_d^{-1} \ln \left[\frac{A_{min} - A_{off}}{A_{ref} - A_{off}} \right] \tag{I.3b}$$

The period, T, is equal to $\tau_c + \tau_d + t_1 + t_2$. The values of A_{min} and A_{max} ((3.2.2) and (3.2.3) in text) can be determined from (I.1) by choosing $A(t_o) = A_{ref}$.

It was found both analytically and numerically that these limit cycle solutions of (3.2.1) are very stable. In fact, the transients leading to the limit cycle behaviour decay very quickly.

Appendix II: Parameter estimation for Equation (3.2.5)

In order to fit (3.2.5) to the response of the pupil to a single light pulse (Figure 3.2.6) we imposed four constraints (see program SPF12ORD in Appendix C, with the substitution $\alpha_d \rightarrow \mu_d$) : 1) the transition from constriction to dilation occurs at time $t_c + T_p$ where t_c is the time of constriction onset ($\sim$ 300 msec after light pulse falls on retina) and T_p is the light pulse duration (500 msec); 2) the pupil area is continuous at time $t = T_p$; 3) the area velocity is continuous at time $t = T_p$; and 4) the initial pupil area is fixed.

If we let $t_c = 0$ and denote pupil area by $A(t)$, we have:

$$A(t) = \begin{cases} A_c(t) = A(0) + B[\exp(-\alpha_c t) - 1] & 0 < t < T_p \\ A_d(t) = C\exp[-\mu_d(t - T_p)] + D\exp[-\beta_d(t - T_p)] + E & t > T_p \end{cases} \tag{II.1}$$

where δ in (3.2.5) corresponds to $-\mu_d - \beta_d$ and ω^2 to $\mu_d\beta_d$. The constraints 2) and 3) are used to express parameters D and E as a function of the parameter set to be determined by nonlinear regression: $\{B, C, \alpha_c, \mu_d, \beta_d\}$. For the data in Figure 3.2.6 our fit produces $A = 21.81mm^2$, $C = 10.14mm^2$, $\alpha_c = 3.44$ sec^{-1}, $\mu_d = 2.83$ sec^{-1} and $\beta_d = 0.58$ sec^{-1} with a χ^2 value of 10.62 ± 0.54. Note that the values of β_d and α_c have not changed significantly from those of, respectively, α_d and α_c determined for the first order model (Tables 3.1 and 3.2).

3.3 COMPLEX OSCILLATIONS IN THE HUMAN PUPIL LIGHT REFLEX WITH "MIXED" AND DELAYED FEEDBACK.

Abstract.

Simple periodic as well as more complex behaviors are shown to occur in the human pupil light reflex with piecewise constant mixed and delayed feedback. The output of an infrared videopupillometer, an analog voltage proportional to pupil area, is processed by an electronic comparator which synthesizes the piecewise constant feedback. The system is described by a nonlinear delay differential equation which has been previously shown analytically to exhibit periodic and aperiodic behavior. After parameter estimation from the data, it is found that the observed simple periodic behaviors correlate well with the model behaviors. Although more complex behavior can be observed for parameter values which gave complicated dynamics in the model, there is not a one-to-one correspondence between the observed and predicted results. The effect of uncontrollable fluctuations in the parameters on the observability of complex dynamics in this system is discussed.

3.3.1 Introduction.

The control of a physiological variable x is often given by an equation of the form

$$\begin{aligned} \frac{dx}{dt} \equiv \dot{x} &= \text{production - destruction} \\ &= g\big(x(t-\tau)\big) - \alpha x \,, \end{aligned} \tag{3.3.1}$$

where $g\big(x(t-\tau)\big)$ is a nonlinear function of $x(t-\tau)$ and α is a positive constant[24,25,54,57,107,108]. The time delay, τ, is an essential feature of these control systems and arises, for example, as the time required for a cell to mature, or the time required for a nerve impulse to travel along an axon and across a synapse, or the time for hormonal signals to travel from their site of production to target organs by diffusion and/or passage through the circulation.

For many physiological control systems, $g\big(x(t-\tau)\big)$ is a "humped" function of $x(t-\tau)$, i.e., maximal production occurs at some intermediate value of $x(t-\tau)$, and thus the control system displays both positive and negative feedback characteristics[57,66,107,117]. Analytic and computer simulation studies have shown that for various choices of "humped" $g\big(x(t-\tau)\big)$, (3.3.1) can exhibit a rich variety of periodic and aperiodic ("chaotic") dynamics[24,25,66,107]. Moreover, it has been shown that for biologically appropriate choices of $g(t - \tau)$ including estimation of the relevant parameters from published data, there is qualitative agreement between the observed and predicted dynamics[24,25].

We are not aware of a previous report of an experimental study of the dynamics seen in a physiological control system with delayed mixed feedback The control of pupil area by the light reflex has been extensively studied as an example of a neurological control system[1,31,32,46,111] and from an experimental point of view, this system offers the advantages that it is readily accessible and can be monitored and manipulated by noninvasive techniques. Here we study a hybrid experimental system for the control of the human pupil light reflex which incorporates piecewise constant delayed and mixed feedback (Figures 3.3.1 and 3.3.2). For Equation (3 3 1) with this kind of feedback, it has been possible to analytically prove the existence of stable equilibria, of stable and unstable limit cycles, and of infinitely many periodic solutions and uncountably many aperiodic, mixing solutions for defined regions in parameter space[66,114]. With the simple form of the delayed mixed feedback we have chosen, it is possible to compute the solutions exactly and thus to compare the observed and predicted dynamics for different parameter sets. Moreover we are able to quantify the intrinsic variability of certain parameters and thereby address the issue of the observability of complex dynamics in this system.

3.3.2 Methods.

Subjects were healthy males and females (n=10; ages 20-45 years) who were free from both ocular disease and disorders known to affect autonomic function. All measurements were performed in subjects who had been dark adapted for at least 15 minutes in a room lit only by a dim red light. During pupillary measurements, the subjects were instructed to refrain from blinking as much as possible and to fix their gaze on the target appearing on the viewing screen (a dim green asterisk); some subjects performed mental tasks (e.g. multiplication tables) to minimize spontaneous fluctuations in pupil area ("hippus")[51].

Measurements of pupil area were made with an infrared videopupillometer (Hamamatsu Binocular Iriscorder C2515)[106]. The video cameras (Figure 3.3 2) are of the charge-coupled device (CCD) type, and their output is analyzed by a frame grabber which counts the number of pixels above a slice level ("gray level") adjusted by the experimenter to discriminate between pupil and iris. The output of the frame grabber is an analog voltage proportional to the pupil area (sampling rate 60 Hz). Light

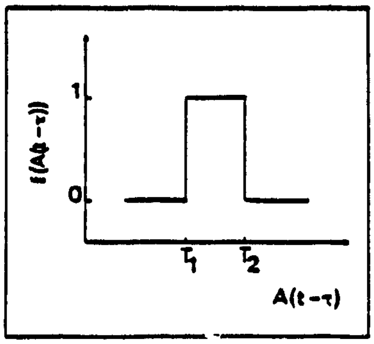

Figure 3.3.1 Piecewise constant delayed feedback nonlinearity used in this study. The function is defined in (3.3.2). T_1 and T_2 are, respectively, the lower and higher thresholds which are set by the investigator.

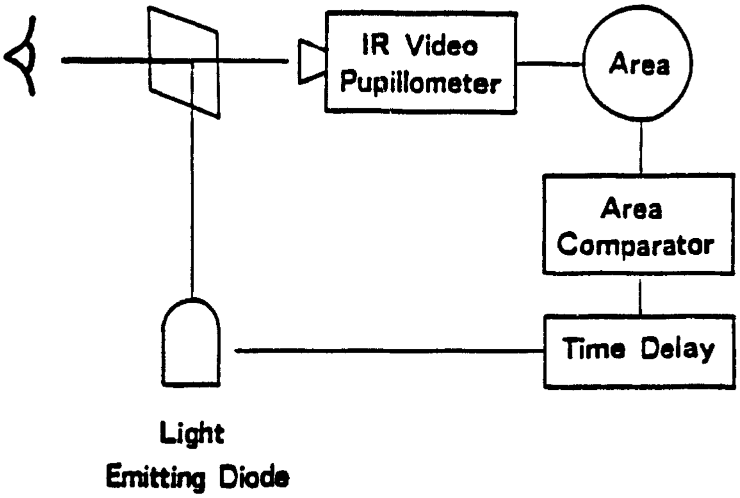

Figure 3.3.2 Schematic of the instrumentation used for investigating the pupil light reflex with delayed mixed feedback. The area comparator described in "Methods" utilizes operational-amplifier circuitry. Although the Hamamatsu Iriscorder C-2515 is a binocular apparatus, we used it only in the monocular mode, as this was more convenient in that only one camera had to be focussed and aligned.

sources were light emitting diodes (peak wavelength of 605 nm). All experiments were done under "open-loop" conditions[31] by focussing a 1.2mm beam of light on the center of the pupil (initial diameter 5-7 mm). Under these conditions the iris does not alter the beam of light falling on the retina.

The variable x in (3.3.1) can be identified with the area of the iris, which is regulated by the autonomic nervous system (parasympathetic and sympathetic), and the function $f(x(t-\tau))$ can be identified with the feedback of the iris on the light flux to the retina. Since the pupillometer measures pupil area and not iris area, (3.3.1) has to be rewritten to take account of the inverse relationship between iris size x and pupil size A. Defining A_0 to be the maximal size of iris plus pupil and $\beta f(A(t-\tau)) \equiv g(A_0 - A(t-\tau))$, we can write $A(t) \approx A_0 - x(t)$, and (3.3.1) becomes

$$\dot{A} + \alpha A = -\beta f(A(t-\tau)) - I + \alpha A_0 , \tag{3.3.2}$$

where β is the intensity of the light pulse, and α is the reciprocal of the time constant for pupillary movements and is different for constriction (α_c) and dilation (α_d). In going from (3.3.1) to (3.3.2) we have added a forcing term I to represent the background illumination of the retina. It is important to note that with the choice of $f(A(t-\tau))$ shown in Figure 3.3.1, (3.3.2) can be solved exactly, without resorting to numerical integration methods, the initial condition being specified by a function defined on the interval $(-\tau, 0)$.

In our experiments the measured pupil area is used to control the timing and duration of light pulses falling on the retina by modifying a technique originally developed by Stark[1]. The control system for the pupil area, given by (3.3.2), was constructed by opening the feedback loop and inserting the piecewise constant feedback function (Figure 3.3.1) in the following way. The analog output proportional to the pupil area, A, was compared to the two adjustable thresholds T_1 and T_2 using operational-amplifier circuitry. The output logic level goes HIGH when $T_1 < A < T_2$ and LOW otherwise. The HIGH level drives the light on, and illuminates the retina in open-loop. This circuitry is included in Figure 3.3.2 as the box labeled "Area Comparator". In our experiments, the pupil being stimulated was also the one being measured.

The solution of (3.3.2) requires the specification of seven parameters : the time delay; the time constants for constriction and dilation, t_c and t_d; the asymptotic values the pupil area tends to when the light is ON and OFF, A_{on} and A_{off}; and the lower and upper thresholds, T_1 and T_2. The value of A_0 does not affect the qualitative behavior of (3.3.2) and was taken to be $100mm^2$. Of the remaining parameters, T_1 and T_2 are fixed by the investigator , and the others are estimated experimentally. The neural time delay for the response of the pupil to light was determined as the time between the onset of the light pulse and the onset of the pupillary constriction, using a computer program incorporated in the Iriscorder C2515. This neural time delay was assumed to be the same as the time between the cessation of the light pulse and the onset of dilation. The time required for the signal from the video camera to reach the light emitting diode contributed an additional 100 msec delay. The time delay τ in (3.3.2) is equal to the neural time delay plus the machine delay. The time constants t_c and t_d were measured as the e^{-1} times for a pupil receiving a single 0.5 sec light pulse (Figure 3.3.3). The values of the asymptotes are given by

$$A_{on} = \frac{\alpha_c A_0 - I - \beta}{\alpha_c} \tag{3.3.3}$$

and

$$A_{off} = \frac{\alpha_d A_0 - I}{\alpha_d} \, . \tag{3.3.4}$$

The asymptotes were measured as follows. Let A_a be the area at some time when the pupil is constricting; then

$$A_a = A + A_{on} \, , \tag{3.3.5}$$

where A is a pupil area to be determined. At time $t_c = \alpha_c^{-1}$ later, the pupil area is A_b and we can write

$$A_b = e^{-1} A + A_{on} \, . \tag{3.3.6}$$

By combining (3.3.5) and (3.3.6),

$$A = \frac{A_a - A_b}{0.632} \, , \tag{3.3.7}$$

and A_{on} can be calculated from (3.3.5). The value of A_{off} can be evaluated in a similar manner when the pupil is dilating.

3.3.3 Results.

Figure 3.3.3 (insert) shows the change in pupil diameter as a function of time following a single 0.5 sec light pulse. After a delay of 292 ± 10 msec (mean $\pm SD$ for 10 subjects), the pupil undergoes a rapid constriction followed by a slower dilation. The time courses for constriction and dilation are reasonably well fitted by a single

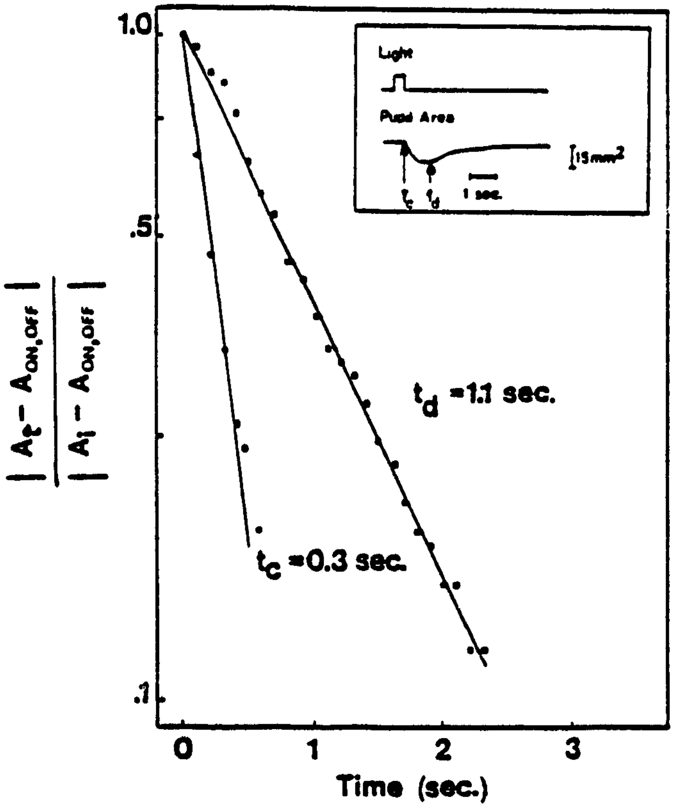

Figure 3.3.3 Plot of the logarithm of the change in pupil area A_t as a function of time following a single 0.5 second light pulse. The changes in pupil area have been normalized to the total change in pupil area that occurs for constriction and dilation respectively. For pupillary constriction the initial value of A_t was measured at the onset of constriction $t = t_c$ (see insert), and the asymptote, A_{on}, was the minimum area obtained with a 2 second light pulse. For pupillary dilation the initial value of A_t was measured at the onset of dilation $t = t_d$. In principle, A_{off} is equal to the initial pupil area (as is true for the example given in the insertion), but typically, following a 0.5 second light pulse the pupil the pupil did not dilate back to its initial value, suggesting that some adaptation had occurred. In these cases, A_{off} was reestimated from the time course of the dilation.

exponential decay : $t_c = 0.4 \pm 0.1$ seconds for 5 subjects. These observations suggest that for the hybrid system incorporating the choice of $f(A(t-\tau))$ shown in Figure 3.3.1, (3.3.2) will provide a good description of the response of the pupil to light.

CASE 1 : $A_{on} < T_1 < A_{off} < T_2$.

Figure 3.3.4 shows the behavior of the pupil area when the lower threshold T_1 is chosen to be between the asymptotes and also the upper threshold T_2 is greater than the upper asymptote A_{off}. Under these conditions, pupil area undergoes repetitive constrictions and dilations, the light being turned on whenever the pupil area A is greater than T_1. The period of these oscillations is the time between successive pupillary constrictions and is a function of the values of A_{on}, A_{off}, the time constants, and the total time delay τ (the intrinsic neural time plus that of the elecronic feedback). The mean period of pupil cycling can be varied from 1 to 8 seconds by changing T_1 and τ (data not shown). We have found that the observed mean period over this range agrees with that predicted by (3.3.2) to within 20% (typically better than 10%)[89].

CASE 2 · $A_{on} < T_1 < T_2 < A_{off}$.

Figure 3.3.5 gives a representative bifurcation diagram for the calculated solution of (3.3.2) over the parameter space spanned by (T_1, T_2). Our computer simulations indicate that for the delay present in the system (380-450 msec), most regions of this subspace correspond to stable periodic behavior; however, in a narrow band (labeled C in Figure 3.3 5) solutions of different periodicities are in close proximity and aperiodic ("chaotic") solutions occur. For simplicity we have represented the dynamics by the number of light pulses per periodic cycle. Although the solutions within each region have the same qualitative features, i.e. number of light pulses per period, they do not necessarily have the same period. The region labeled 0 corresponds to solutions where the pupil area dilates asymptotically to A_{off}. The region labeled 1 corresponds to results of the type shown in Figure 3.3.4, i.e. one light pulse per cycle.

Next to region 1 is a region labeled 2, corresponding to two light pulses per cycle. Figure 3.3 6 compares the observed and predicted dynamics for a choice of T_1 and T_2 within this region. For solutions of this type a smaller pupillary constriction-dilation change occurs in the trough of the larger one. As for the dynamics observed in region 1, there is good agreement between theory and experiment. It should be noted that the transition 1 → 2 corresponds to a bifurcation in (3.3.2), but that it is not a period-doubling bifurcation, since little change in period occurs. There is also another region in which there are two light pulses per cycle, labeled as $\overline{2}$. Solutions

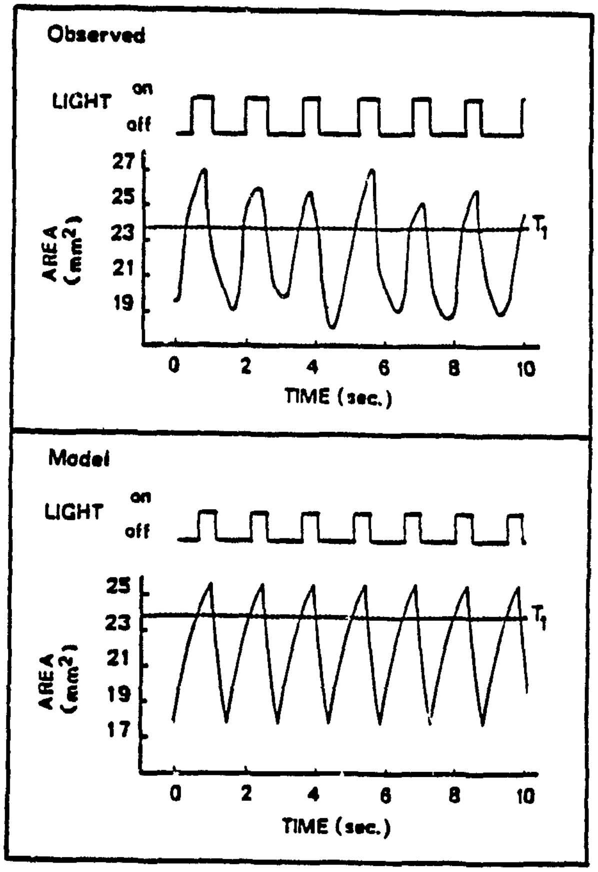

Figure 3.3.4 Example of pupil cycling in a one-threshold experiment (case 1). Simple periodic behavior (referred to as type 1 in Figure 3.3.5) is initiated at the left by lowering T_1 to the level indicated. Above the data, we have shown the sequence of light pulses seen by the retina. In the experiment (top graph) the light turns on (off) 100 msec after the pupil area crosses the threshold area T_1. This time delay represents the machine delay. The model solution was obtained by using the following parameters : $\tau = 0.385 sec$, $\alpha_c = 2.50 sec^{-1}$, $\alpha_d = 1.25 sec^{-1}$, $A_{on} = 14.2 mm^2$, $A_{off} = 28.7 mm^2$, $T_1 = 23.8 mm^2$, $T_2 = 70.0 mm^2$. The value of A_{on}, A_{off} represent the average of the values obtained for each cycle (see Figure 3.3.8). Initial pupil area is $34 mm^2$.

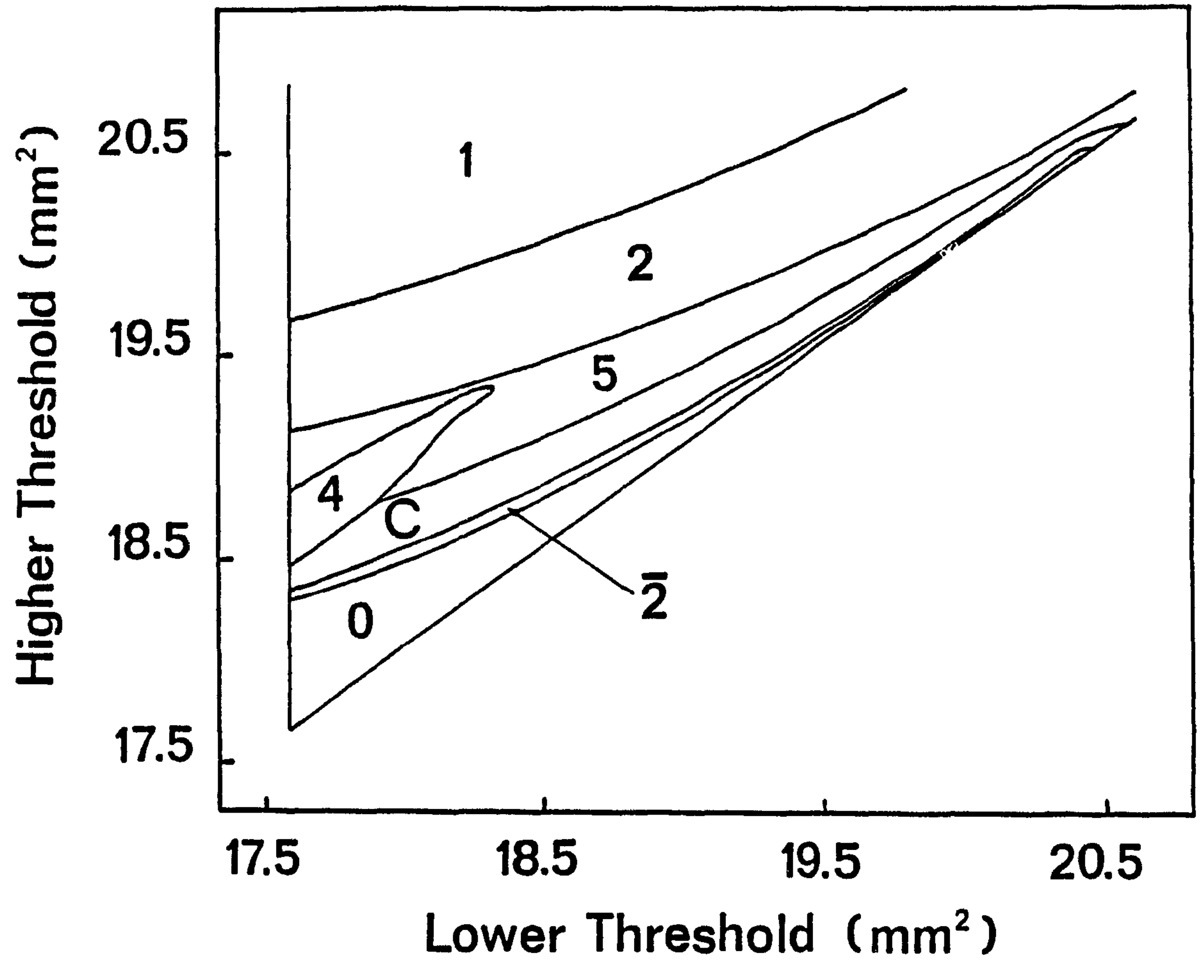

Figure 3.3.5 Dynamic picture in a region of parameter space spanned by the thresholds T_1 and T_2 (note that $T_1 < T_2$). The numbers labeling the different regions correspond to the number of light pulses per period in the exact solutions of (3.3.2). Only the low-periodicity regions are indicated. All of the more complicated solutions belong to the region marked C. Note that the solution in the narrow region marked $\bar{2}$ is qualitatively different from the one marked 2. Parameter values are $\tau = 0.425 sec$, $\alpha_c = 4.00 sec^{-1}$, $\alpha_d = 1.429 sec^{-1}$, $A_{on} = 15.0 mm^2$, $A_{off} = 22.0 mm^2$.

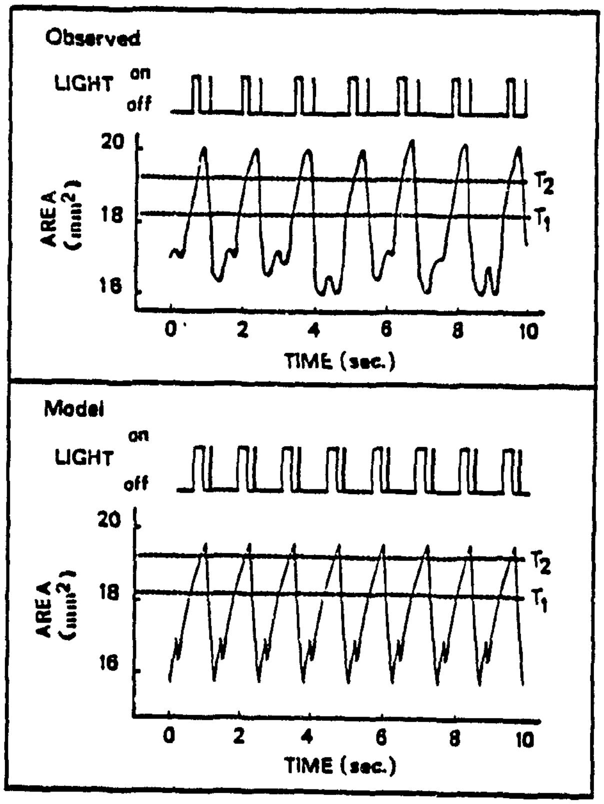

Figure 3.3.6 Example of a solution characteristic of region 2, in which the retina sees a double pulse of light in each cycle. The model prediction is given in the lower half of the figure. Parameter values are $\tau = 0.425sec$, $\alpha_c = 4.00sec^{-1}$, $\alpha_d = 1.429sec^{-1}$, $T_1 = 18.2mm^2$, $T_2 = 19.2mm^2$, $A_{on} = 13.8mm^2$, $A_{off} = 21.3mm^2$. The averaged values of the asymptotes were determined as in Figure 3.3.4.

in this region have the smaller pupillary constriction-dilation change occurring on the peak of the larger one. We have not observed solutions of this type.

Close to region 2 there are smaller regions containing more complex dynamics, i.e. regions 4,5 and C. The period varies continuously in each of these regions. The boundary between regions 2 and 5 corresponds to a period-doubling bifurcation, but the boundary between regions 4 and 5 does not. Additional period doublings have been shown to occur in region C.

In Figure 3.3.7 we show the observed oscillations in pupil area in an experiment in which the lower threshold T_1 was held constant and the upper threshold T_2 was adjusted to a value which produces a region 5 solution of (3.3.2). With this choice of T_1 and T_2 more complex oscillations are obtained than were observed in region 2 (compare Figures 3.3.6 and 3 3.7b). Figure 3.3.7c shows the solution of (3.3.2) for the parameters estimated from the data in Figure 3.3.7b. Although there is not a one-to-one correspondence between the observed and predicted oscillations, there are nonetheless some similarities. The region 5 solution shows a recurring pattern of a large pupil dilation-constriction, followed by a smaller one, then another larger one followed by two smaller ones. A similar pattern in the successive amplitudes is seen during the first 7 seconds of the observed oscillation (Figure 3.3.7b). The period of this recurrence in the successive amplitudes of the observed oscillations over the first seven seconds is $\approx 3.6 sec$, which is ≈ 2.2 times the period of the corresponding region 1 oscillation shown in Figure 3.3.7a. This observation offers support for the possibility that the observed oscillation is, at least transiently, in a region of parameter space associated with a period doubling, i.e. region 5, or more complex.

We next explore the solutions of (3.3.2) in the neighborhood of the region 5 solution shown in Figure 3.3.7c to see if better agreement with the observed oscillation could be obtained. Figure 3.3.7d shows a solution of (3.3.2) which is closer to the observed oscillation over the first 7 seconds. This solution was obtained by increasing the parameter A_{off} by only 5%. The period of this solution is ≈ 2.1 times that of the corresponding region 1 solution (i.e. the solution with the same T_1). These observations emphasize the sensitivity of the solutions of (3.3.2) to small fluctuations in the control parameters.

Even more complicated oscillations are observed when the thresholds are chosen to give solutions in region C (data not shown).

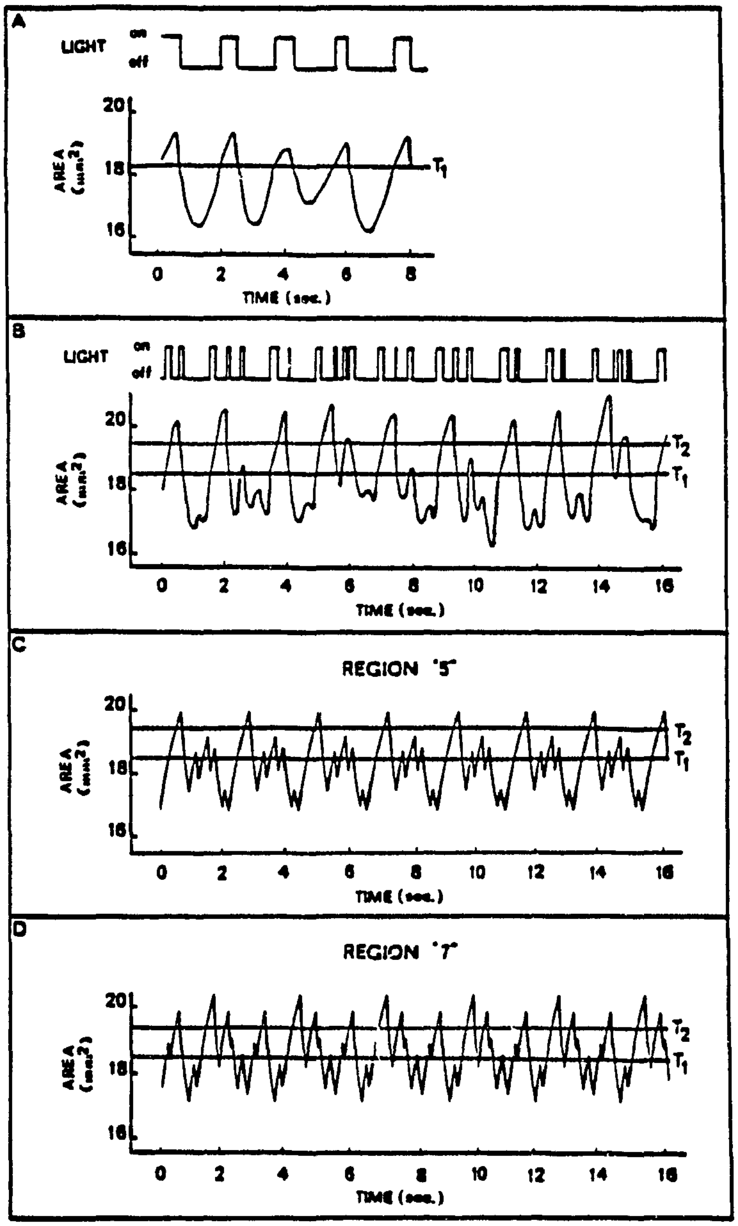

Figure 3.3.7 Experimentally observed pupil oscillations near a period-doubling bifurcation. (a) shows the pupil oscillation obtained when $T_1 = 18.5mm^2$ and $T_2 = 40mm^2$, and (b) shows the oscillation obtained when T_2 is lowered to $19.5mm^2$ and T_1 is held constant. (c) shows the solution of (3.3.2) for the parameters estimated from (b): $\tau = 0.425sec$, $\alpha_c = 4.0sec^{-1}$, $\alpha_d = 1.429sec^{-1}$, $A_{on} = 16.0mm^2$, $A_{off} = 22.0mm^2$. (d) shows a solution of (3.3.2) using the same parameters as used for (c) except that A_{off} was increased to $23.05mm^2$.

3.3.4 "Noise" and observability.

It is possible that the lack of agreement between the solutions of (3.3.2) and the observed complex oscillations (compare Figure 3.3.7b and c) may have arisen because of uncontrollable fluctuations in certain of the control parameters describing the pupil's response to light (compare Figure 3.3.7c and d). Here we examine this possibility.

We assumed that the only parameters that changed in our experiments were the values of the asymptotes (see Methods and Discussion). Support for this assumption is given in Figure 3.3.8. In Figure 3.3.8b we plot the values of the asymptotes as a function of the ith cycle for the data shown in Figure 3.3.4, and in Figure 3.3.8a we compare the measured period for each cycle with the period predicted from (3.3.2) using the corresponding values of the asymptotes. In this manner, it can be seen that the variations in period are largely accounted for by the variations in the asymptotes.

Figure 3.3.9 shows a region of parameter space spanned by (A_{on},A_{off}) in which T_1 and T_2 are fixed at the values used to obtain the type 2 oscillations shown in Figure 3.3.6 and the oscillations in Figure 3.3.7. In this parameter space, we have plotted the measured values for the asymptotes for each successive cycle for these oscillations - respectively, area a and area b It is clear that our ability to observe oscillations which ressemble the type 2 solutions of (3.3.2) is due to the fact that the variations in the asymptotes are not large enough to go outside region 2 in parameter space. On the other hand, it is not surprising that we were not able to obtain agreement between our model and the observations in Figure 3.3.7b, since the fluctuations in the values of the asymptotes overlap several regions in this parameter space. Presumably the experimentally observed oscillations shown in Figure 3.3.7b represent a mixture of solutions from adjacent regions in parameter space and transients.

3.3.5 Discussion.

We have studied the dynamics of a hybrid system for the control of the human pupil light reflex possessing mixed delayed feedback, and compared the observed with the predicted dynamics. The piecewise constant delayed mixed feedback function shown in Figure 3.3.1 was chosen because it has the advantage of being well characterized analytically[66,114], all the relevant parameters can be directly estimated from the experimental data, and the corresponding solutions of the model can be computed exactly. It must be emphasized that the solutions of this model (i.e. the solutions of (3.3.2)) are solutions of an autonomous delay differential equation and not the

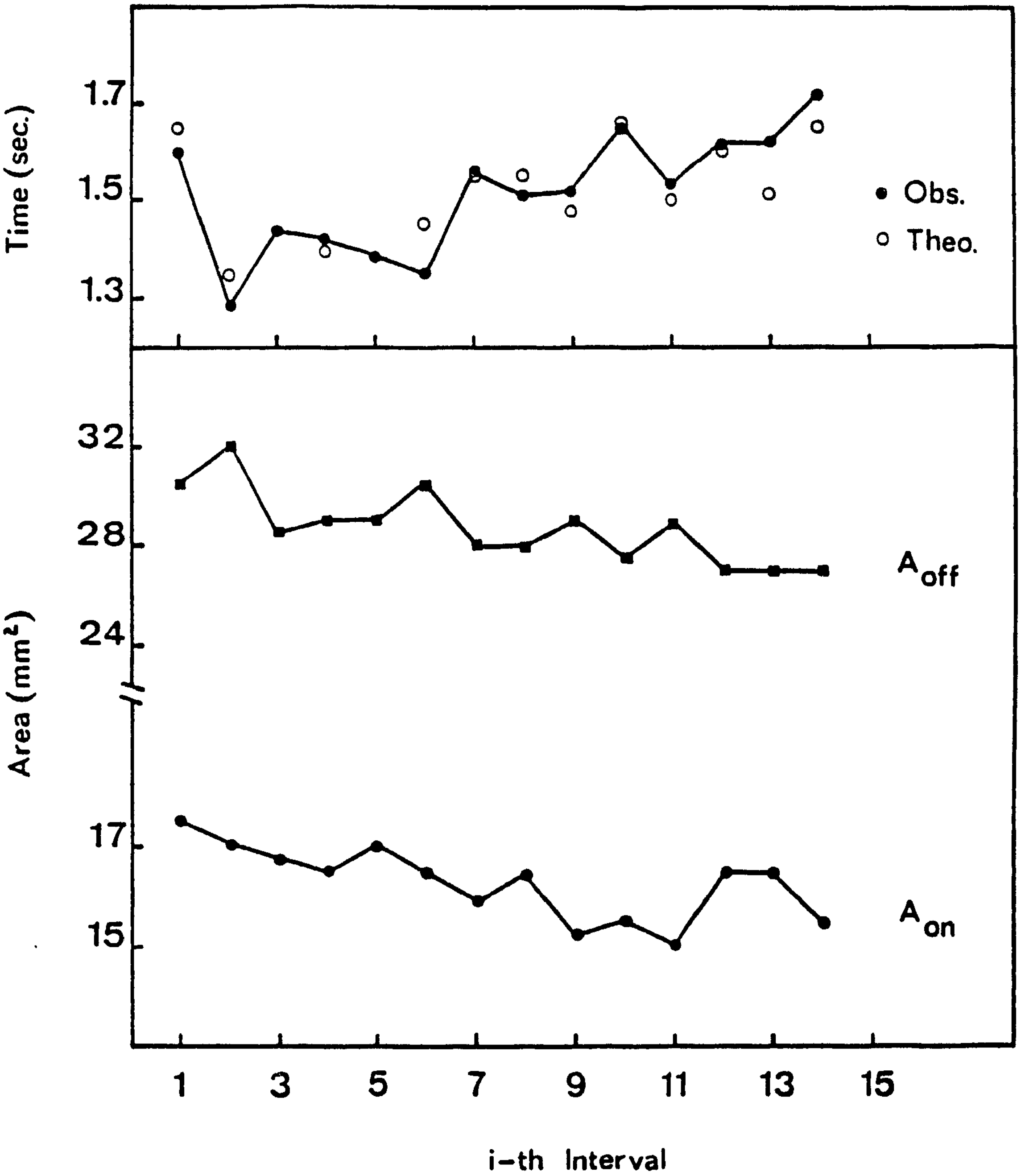

Figure 3.3.8 (a) Comparison of the measured (●) and predicted (○) cycle times for the data given in Figure 3.3.4. (b) The predicted cycle times have been calculated from (3.3.2) using the appropriate values of the asymptotes and represent the steady-state period. The estimated error in the asymptotes was $0.5mm^2$.

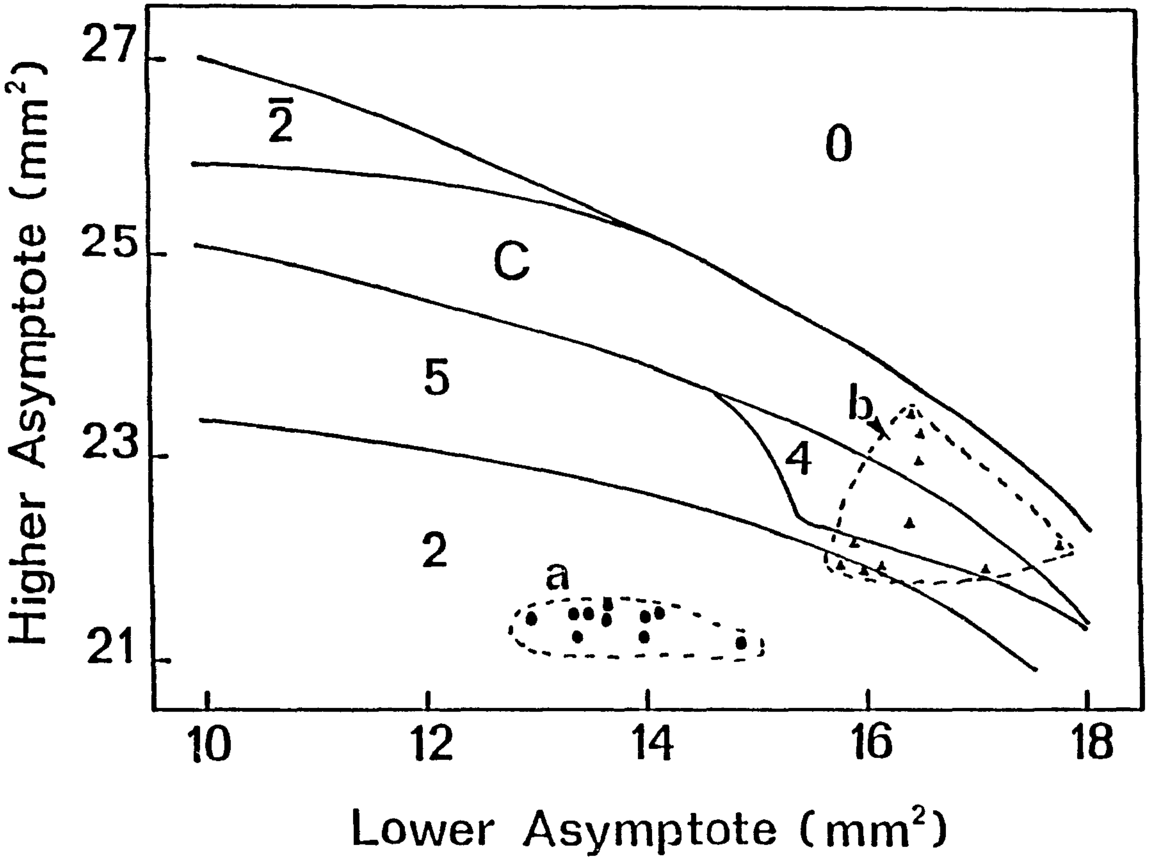

Figure 3.3.9 Dynamical picture in a region of parameter space spanned by the asymptotes A_{on} and A_{off}. The labeling is the same as in Figure 3.3.5. Parameter values are $\tau = 0.425 sec$, $\alpha_c = 4.00 sec^{-1}$, $\alpha_d = 1.429 sec^{-1}$. The values of the asymptotes in the region labeled *a* (•) were measured for the oscillation shown in Figure 3.3.6, and those in the region labeled *b* (▲) have been measured for the oscillations shown in Figure 3.3.7b. The dynamic pictures for *a* and *b* were sufficiently close to warrant the use of the same diagram to display the variability of the asymptotes. The estimated error in measuring the asymptotes was $0.5 mm^2$.

response to external periodic forcing.

We observed a rich variety of dynamics, including no oscillation (region 0), simple limit-cycle oscillations (regions 1 and 2), and more complex oscillations (Figure 3.3.7b). There was quantitative agreement between the observed oscillations and those predicted by (3.3.2) in region 1, and good qualitative agreement with the model in region 2. The model also correctly predicted the parameter ranges over which more complicated dynamics are observed experimentally.

However, for the more complex oscillations there is not good agreement between the observed pupillary dynamics and those predicted by (3.3.2). We suggest that these discrepancies arise because of unmodeled fluctuations in certain of the parameters which describe the pupil's response to light. As the oscillations become more and more complicated in the model, the corresponding regions in parameter space become smaller and smaller (see Figures 3.3.5 and 3.3.9). Eventually the region in parameter space occupied by the variability of these parameters becomes large relative to the size of the region over which a particular type of oscillation occurs. This is reflected experimentally by a solution which combines the dynamics observed in neighboring regions of parameter space as well as transients (solutions of (3.3.2) often show long transients before settling on a periodic cycle). Although in other physiological[28] and physical[110,112,113,116] systems it has been possible to observe more bifurcations than we observe here, the inherent noise in the system eventually prevents the observation of the predicted dynamics[109,115].

There are five parameters in (3.3.2) which can undergo changes in our experiments: the time delay (τ), the rate constants for constriction and dilation (α_c, α_d), and the asymptotes (A_{on}, A_{off}). We assume that the only parameters which changed in our experiments were the values of the asymptotes. The main rationale for this assumption is the observation that it permitted good agreement between experiment and theory for the region 1 and 2 solutions with all values of the parameters being measured from the data (Figures 3.3.4 and 3.3.6). In contrast, when we assumed that the only parameters which changed were the values of the rate constants, there was no agreement between the model and any of the observed oscillations. Finally, computations showed that the observed variations in the intrinsic neural delay (±30 msec) were not large enough to significantly influence the predicted dynamics. Although these observations do not eliminate the possibility that these latter parameters have also changed during our experiments, they do suggest that the most significant changes in the parameters affecting the dynamical behavior of our system occur in the asymptotes.

There are a number of factors which contribute to the changes in the values of the asymptotes. A major influence is the adaptation of the retina to the average light level (ambient light plus the repetitive light pulses during pupil cycling)[1,46]. As the pupil cycle time is decreased from 7 to 1 seconds, the fraction of time that the light is on increases from 0.01 to 0.4 (data not shown). Thus under conditions of more rapid cycling the pupil will tend to be smaller (since the average light level is greater). In addition, there are other retinal factors such as photoreceptor bleaching, as well as the influence of neural systems on the pupil light reflex such as the ascending reticular activating system (occurring in particular at the level of the Edinger-Westphal nucleus), the accommodation reflex, and the resting activity of the optic nerve[37].

It is possible that by constructing a model incorporating all of the influences on the values of the asymptotes, it might be possible to predict the observed dynamics in more detail. In particular, extension of our model to at least a second-order delay differential equation would be required to eliminate the slope discontinuities present in (3.3.2). However, besides rendering the exact computation of orbits and estimation of relevant parameters more difficult, we expect that as the predicted dynamics become more complex, the region in parameter space over which they are observed will become narrower until the remaining "unmodeled" noise becomes larger than these regions, thus rendering the dynamics unobservable. Although it is clear that such an approach would narrow the region in this extended parameter space over which unmodeled parameter variability occurs, it remains to be seen whether this narrowing would be great enough to allow observation of the more complex predicted dynamics.

"Noisy" variations are characteristically seen in physiological data. The fact that (3.3.1) can admit very complicated dynamics suggests the possibility that some of this noise may be of deterministic origin[24,25,54,66] However, it is clear that in any real physical or biological system there will also be some degree of stochasticity, for example in the form of thermal noise, and that deterministic chaos, if present at all, will be superposed on this background signal. In our system, complicated "noisy" solutions are observed even for parameter choices which do not correspond to chaotic solutions of (3.3.2). We feel that these noisy behaviors reflect a combination of different types of solutions in adjacent regions of parameter space and transients resulting from the perturbations introduced by the noisy parameters.

3.4 REMARKS ON NOISE AND UNMODELLED PHENOMENA.

This section begins with a reinterpretation of the analysis of the PCMF-induced oscillations in the last section. The parameter estimation scheme developed in Section 3.2 is shown to yield model solutions that are in better agreement with the data than those for which the parameters are obtained from the single pulse method (Section 3.3). Further, the reestimated asymptote fluctuations allow a better quantitative assessment of the observability of the more complex model solutions. The limitations of experimental accuracy are then discussed. Results on multistability in the model equation follow, and the question of whether we have observed noise or chaos is addressed. Finally, extensions of the model which include temporal integration at the retina, adaptation and damping of the iris muscles are examined.

3.4.1 PCMF revisited.

In Section 3.3, the observed pupillary oscillations were compared to the solutions of an *ad hoc* model, and the parameters were obtained from a single pulse response measured just before the PCMF experiments. Subsequently, the more physiologically sound model of Sections 2.2 (2.2.6 in particular) and 3.2 (Appendix I) was developed, along with a parameter estimation scheme that requires information from many pulse responses (i.e. many cycles). The parameters obtained using this scheme were shown to provide a better fit of the single pulse response (Figure 3.2.6).

In view of this, the next logical step is to reinterpret our PCMF data using parameters estimated from the method in Section 3.2, to see if better agreement between experiment and theory can be obtained. The estimation scheme of Section 3.2 will now be referred to as the C1D1 method (meaning that both Constriction and Dilation obey a first order differential equation), while the method used in Section 3.3 will be referred to as the SPR method (i.e. based on the Single Pulse Response).

Figure 3.4.1 shows pupillary oscillations induced using PCNF (Figure 3.4.1a). The data is obtained from a different subject than in Figure 3.2 2. The parameters are estimated using the C1D1 method, i.e. from the plots in Figure 3.4 1b. Notice again the very good agreement between the waveforms, periods and light pulse durations predicted by the model and those seen experimentally. In Figure 3.4.1g, the delay was increased using the analog delay line (see Section 3.1.1). This was done to demonstrate that the model, combined with the C1D1 parameter estimation scheme, provides good agreement with the data even when one parameter (the delay) is well out of the normal physiological range.

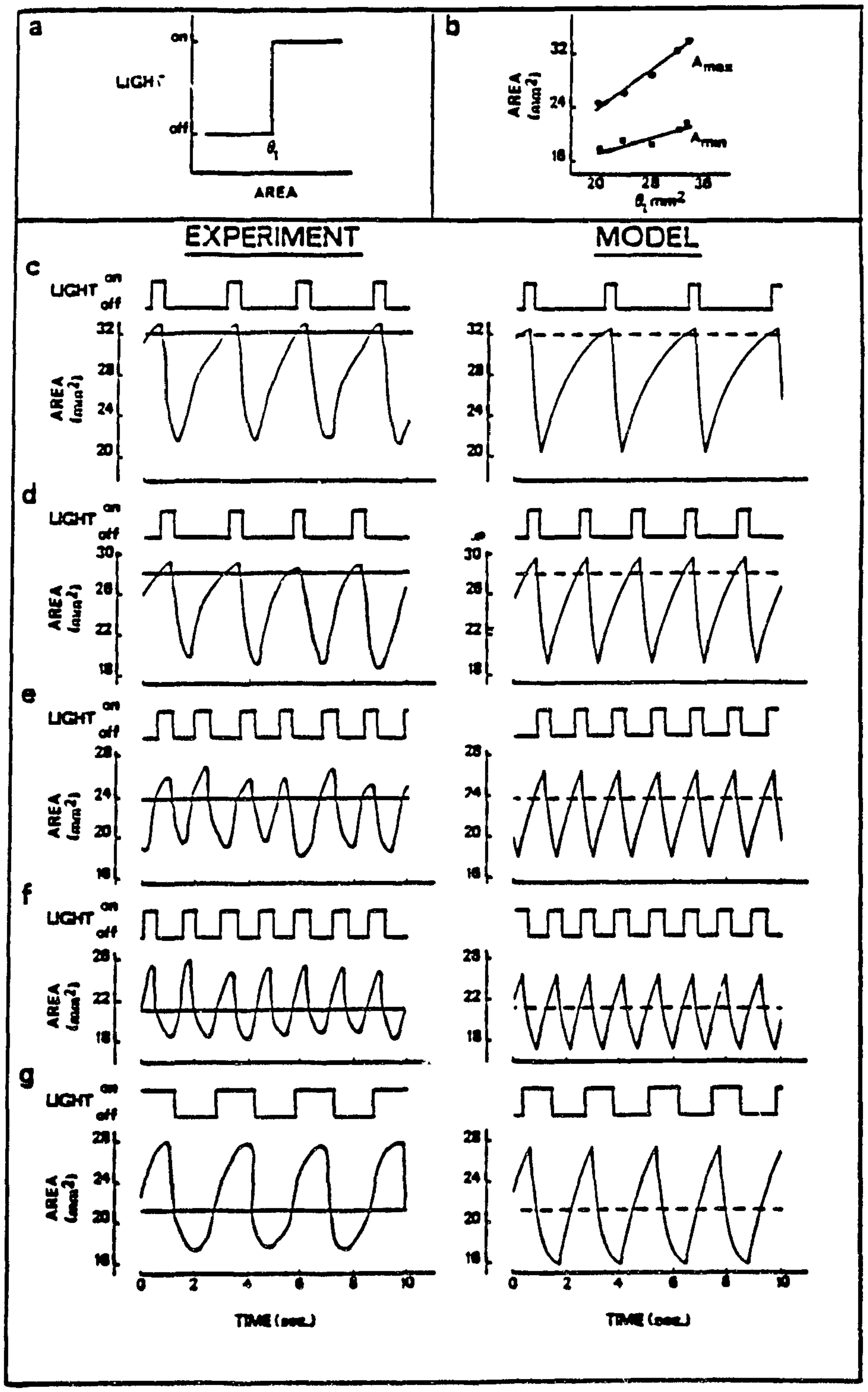

Figure 3.4.1 Comparison of the changes in pupil area that occur as a function of time with imposed negative feedback to those predicted by (3.4.1) (subject MC). The piecewise constant negative feedback is shown in (a). The pupil latency time was $285msec$. In (c-f), the machine delay was $100msec$ (for a total delay $\tau = 385msec$) and in (g) the machine delay was increased to $579msec$ ($\tau = 864msec$). The area threshold, θ_1, was set at : (c) $32mm^2$, (d) $28.1mm^2$, (e) $23.8mm^2$, and $21.4mm^2$ in (f) and (g). The values of α_c, A_{on}, α_d and A_{off} used to calculate the solutions of (3.4.1) were calculated from plots of A_{min}, A_{max} vs. θ_1 shown in (b) (details can be found in Section 3.2.3) and were $\alpha_c = 3.11sec^{-1}$, $\alpha_d = 0.74sec^{-1}$, $A_{on} = 15.7mm^2$ and $A_{off} = 34.5mm^2$. In (b) the values of A_{min} and A_{max} represent values averaged over a minimum of ten consecutive cycles.

Figure 3.4.2 shows pupillary oscillations over a range of threshold values for the PCMF case (Figure 3.4.2b). To find the parameters for this PCMF case, a PCNF experiment as in Figure 3.4.1 is first carried out. The parameters are obtained from the usual plot in Figure 3.4.2b. These parameters are then used directly in the model

$$\alpha^{-1}\frac{dA}{dt} + A = \begin{cases} A_{on}, & \text{if } \theta_1 < A_\tau < \theta_2 \\ A_{off}, & \text{if } A_\tau < \theta_1 \text{ or } A_\tau > \theta_2\,, \end{cases} \tag{3.4.1}$$

where the asymptotes are expressed in terms of physiological parameters in (2.2.29) and (2.2.30).

The model solutions obtained for these parameters are shown in Figure 3.4.2 to the right of the observed oscillations. They are in agreement with the data, even in Figure 3.4.2e. However, as in Section 3.3.3, the fine structure of the model solutions is not seen in the data. Rather, the observed oscillations appear as lowpass filtered versions of the model solutions

Figure 3.4.3 compares the performance of the C1D1 and SPR parameter estimation schemes in modelling the PCMF data (we have already seen that the C1D1 method is superior for fitting the single pulse response). While both methods give good agreement for the simpler behaviors, the C1D1 gives better qualitative agreement with the data in Figures 3.4.3c and d. This is particularly obvious in Figure 3.4.3d, where the SPR method predicts an equilibrium solution $A(t) = A_{off}$ while the C1D1 method predicts a complex limit cycle with 14 pulses per period.

Our model of PCNF-induced oscillations in Section 2.2.6 shows that the asymptotes are functions of all the other physiological parameters, including the rate constants. Hence, if any of these parameters fluctuates (e.g. because of hippus), the asymptotes will also fluctuate. The model thus provides justification for the approach in Section 3.3.4, in which the asymptotes were assumed to fluctuate. Also, the assumption that the rate constants undergo the most important changes does not yield satisfactory results (Section 3.3.5).

Figure 3.4.4 illustrates the bifurcation diagrams of (3.4.1) in the subspace of parameter space spanned by A_{on} and A_{off} (all other parameters are kept constant). The boxes represent asymptote variability. The size of the boxes was determined from PCNF oscillations in the same way as for Figures 3.3.8 and 3.3.9, i.e. by estimating the asymptote values at each cycle using the rate constants as in Equation (3.3.7). However, the rate constants were provided by the C1D1 method rather than the SPR method. This asymptote variability was assumed to be independent of the threshold

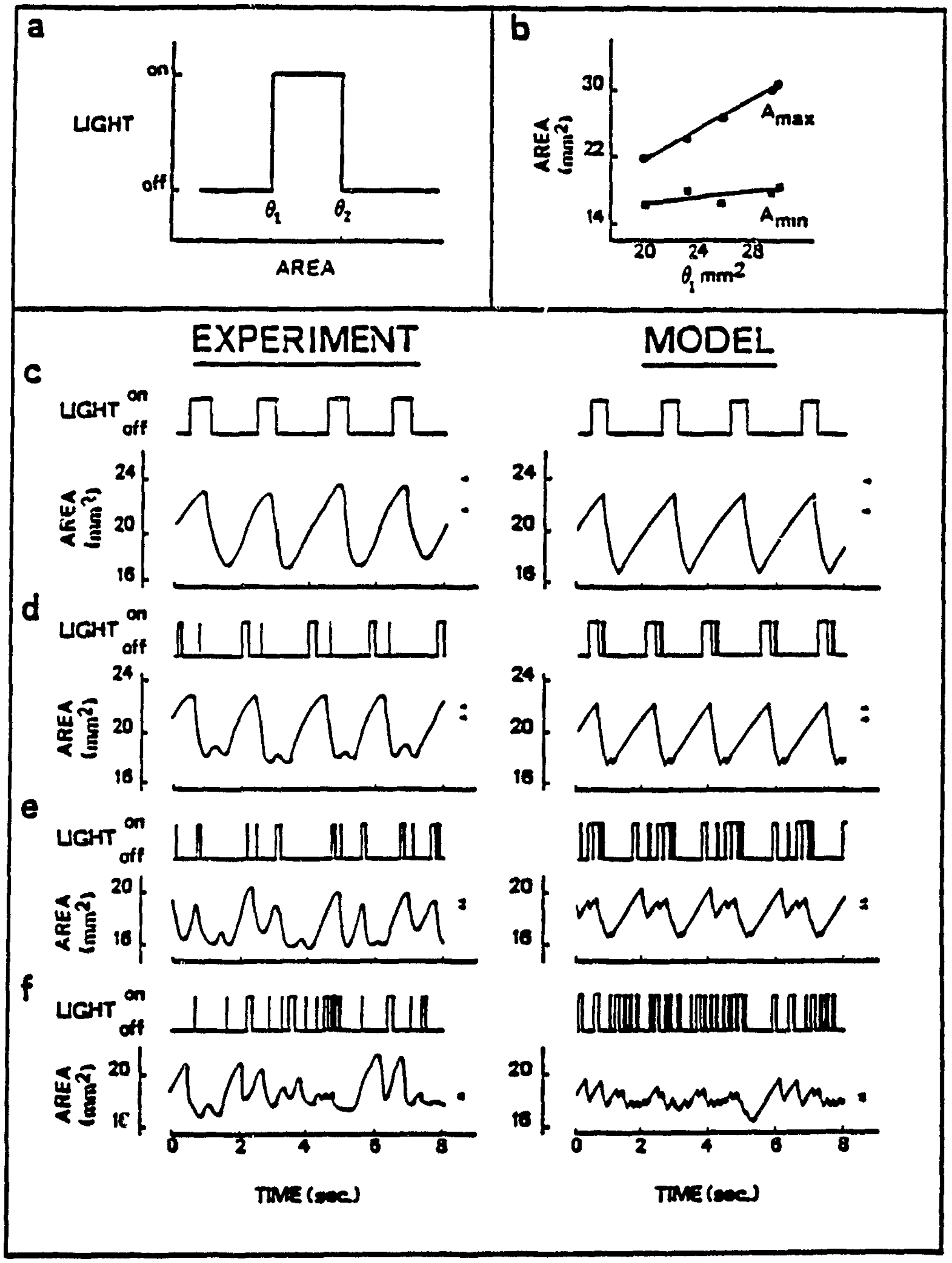

Figure 3.4.2 Comparison of the changes in pupil area that occur as a function of time with imposed mixed feedback to those predicted by (3.4.1) (subject JM). The piecewise constant mixed feedback is shown in (a). The parameters $\alpha_c = 3.88sec^{-1}$, $\alpha_d = 0.265sec^{-1}$, $A_{on} = 15.5mm^2$ and $A_{off} = 34.2mm^2$ were measured from the plots in (b) obtained in a preliminary experiment with piecewise constant negative feedback (as in Figure 3.4.2). The delay was $\tau = 411msec$. The upper (θ_2) and lower (θ_1) area thresholds are indicated by the arrows at the right sides of the time series and were respectively : (c) $21.5mm^2, 24.5mm^2$; (d) $21mm^2, 22mm^2$; (e) $18.9mm^2, 19.5mm^2$; and (f) $17.95mm^2, 18.5mm^2$.

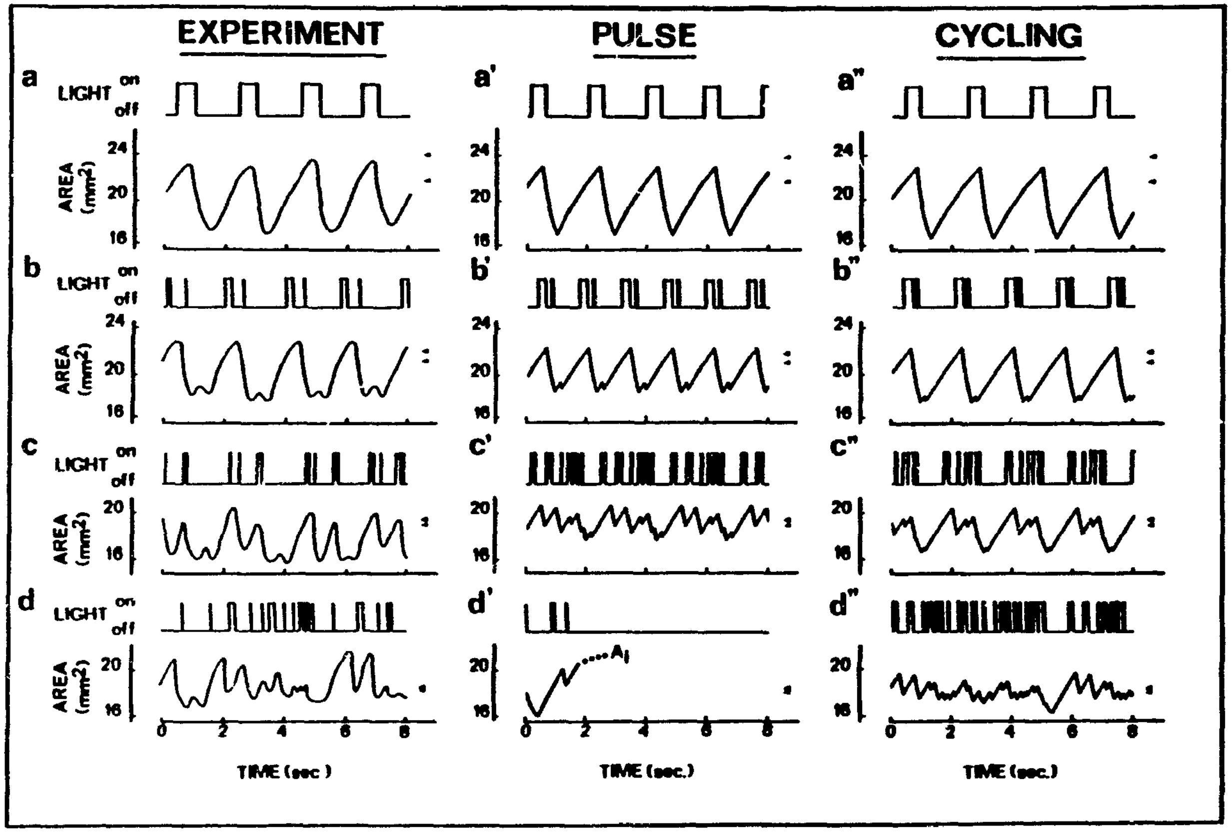

Figure 3.4.3 Comparison of the changes that occur as a function of time with imposed piecewise constant mixed feedback (Figure 3.4.1) to those predicted by (3.4.1) when the parameters are estimated from either the response of the pupil to a single light pulse (a'-d') (Section 3.3.2) or from cycling measurements (a"-d") (Section 3.2.3). The upper (θ_2) and lower (θ_1) area thresholds are indicated by the " " at the right hand sides of the figure and are respectively : a,a',a") 21.5 mm^2, 24.5 mm^2 ; b,b',b") 21.0 mm^2, 22.0 mm^2 ; c,c',c") 18.9 mm^2, 19.5 mm^2 ; and d,d',d") 17.95 mm^2, 18.5 mm^2. The cycling method is seen to give better agreement over the range of threshold values investigated.

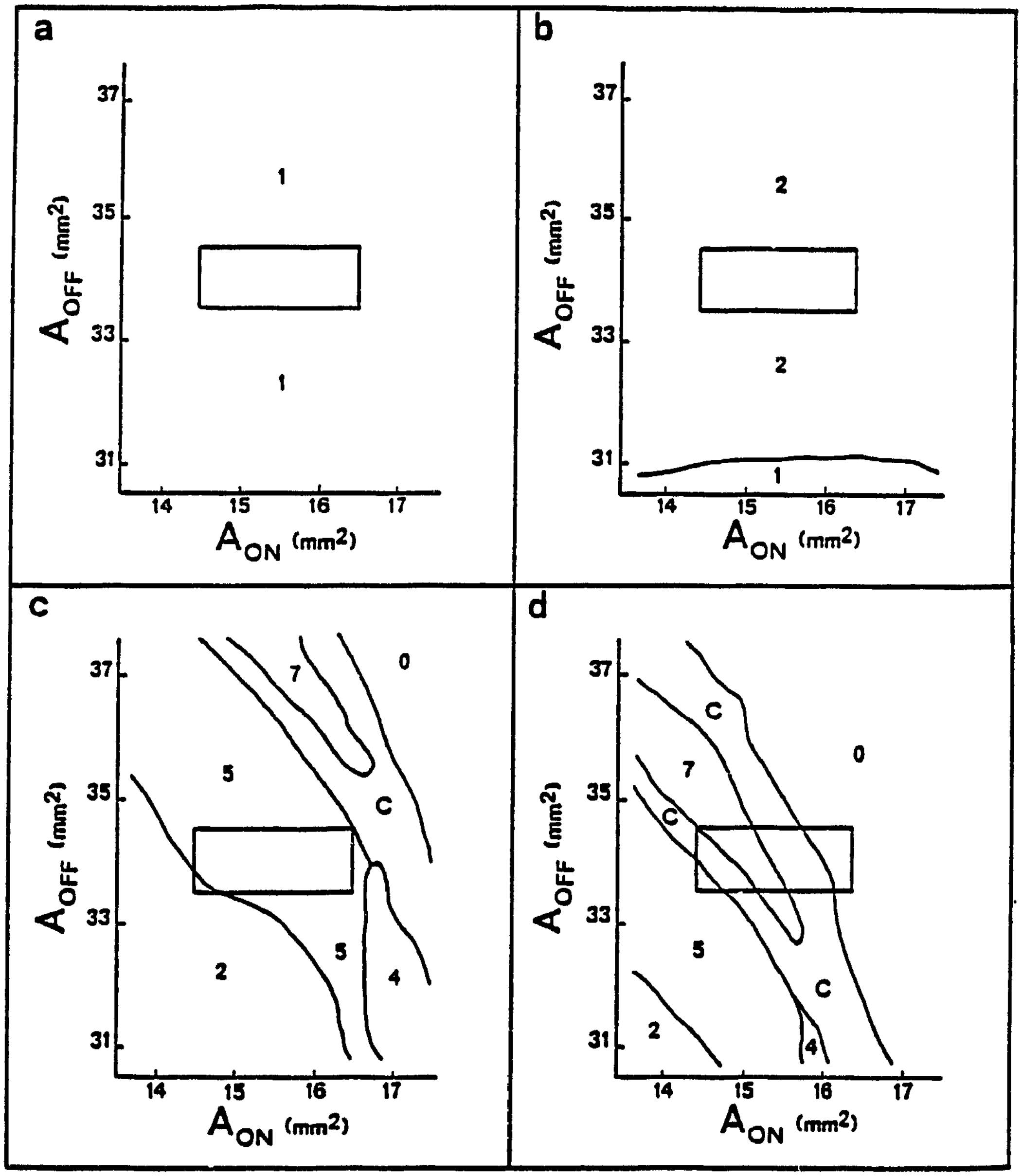

Figure 3.4.4 The (A_{on}, A_{off})-parameter space for Equation (3.4.1) for the values of the area thresholds θ_1, θ_2 in Figure (3.4.2) (a,b,c and d correspond, respectively, to Figure 3.4.2 c,d,e and f). In constructing these parameter spaces the values of α_c, α_d and τ have been fixed and we have classified the periodic solutions of (3.4.1) by the number of light pulses per period as in Figures 3.3.5 and 3.3.9. The region "C" contains very complex periodic solutions in close proximity, as well as unstable mixing solutions. The parameter fluctuations were measured in the same way as for Figures 3.3.8 and 3.3.9, i.e. using the values of α_c and α_d and (3.3.7) on each successive cycle of the negative feedback oscillations. The rectangular boxes enclose these measured values of A_{on} and A_{off}, and are assumed to all be the same size (i.e. the size is independent of the thresholds).

settings, and thus all the boxes are the same size. The center of each box is the same in all panels of Figure 3.4.4, and corresponds to the values of A_{on} and A_{off} obtained from the C1D1 method (Figure 3.4.2b).

Figure 3.4.4 shows that the asymptote fluctuations do not affect the observability of the period 1 and 2 solutions. In fact, our analysis even predicts that the period 5 solutions (Figure 3.4.4c) should be observable, which is the case. Finally, from Figure 3.4.4d, the asymptote fluctuations are shown to overlap regions of parameter space corresponding to qualitatively different solutions. This implies again that the observed behavior might be aperiodic. However, our model solution has features in common with the data in Figure 3.4.2f. This might be a consequence of the long correlation time of the noise (i.e. to its slow variation - see Section 5.2.2), which can maintain the asymptotes in one of the regions of parameter space long enough for the corresponding behavior to be observed.

Overall, the C1D1 parameter estimation method performs better than the SPR method. It is based on a model which not only characterizes the pupil light reflex by five parameters (the rate constants, the asymptotes and the delay), but also estimates these from averages over many single pulse responses occurring under cycling conditions. Our analysis of PCMF oscillations using (3.4.1) and the C1D1 estimation scheme is probably optimal without resorting to higher order models. Experimentally, the fine structure of the model solutions is generally not seen, which is an indication that our model overestimates the bandwidth of the pupil light reflex.

3.4.2 Limitations of experimental accuracy.

The preceding analysis indicates that much of the irregularity in the oscillations observed in mixed feedback can probably be ascribed to hippus and other noise sources which influence the deterministic oscillations. However, there are other factors that might contribute to discrepancies between experiment and theory, but to a lesser extent. One factor concerns fluctuations in pupil area that arise due to fluctuations in the accommodation reflex. In fact, it is very difficult for a subject to fixate on a target for long periods of time (i.e. for 20 seconds or more); further, these accommodation fluctuations often occur unconsciously.

A second factor is that the measurement of pupil area itself has certain accuracy limitations. Although the $0.01mm^2$ precision and 1% linearity are sufficient for our purpose, eye movements will affect infrared illumination and hence the gray level discrimination between iris and pupil. These movements, though minimized by fixing the gaze on the target, are unavoidable and the resulting area value will be slightly inaccurate. Further, when the pupil is small, eye movements might perturb the illumination in Maxwellian view. This results in a partially closed feedback loop and the "clamping" is no longer perfect. We believe this effect to be minimal since pupil diameter rarely goes below $4mm$ and the beam waist at the pupil is $1.2mm$. Finally, there is a $16msec$ uncertainty in the signal processing delay, due to the sampling time of the pupillometer.

3.4.3 Multistability.

All the properties of the C1D1 model discussed to this point and in Section 4.5 have been obtained for initial functions which are either constant or have a single crossing of the threshold θ_1 on the interval $(-1,0)$. Multistability of equilibrium solutions has been shown for the latter type of initial function (Section 4.5). In this section it is shown that the limit cycle solutions of the C1D1 model are also not always globally attracting when the initial conditions are of the latter type. Thus, with different initial functions, solutions may evolve towards different eventual asymptotic behaviors.

Solutions corresponding to two slightly different initial functions having a single threshold crossing on the interval $(-1,0)$ are plotted in Figure 3.4.5. The crossing times differ by 0.001. The limit cycle solution in Figure 3.4.5a has 6 pulses of light per period, while that in Figure 3.4.5b,c has 38 pulses per period. More precisely, the interval $(-1,0)$ was found to be partitioned into two sets I1 and I2 of subintervals. The initial functions having their crossing time in the set I1 were attracted toward the period 6 solution, while the others with crossing time in I2 converged toward the period 38 solution. This type of multistability was found for many different parameter sets corresponding to complicated limit cycles. However, for this class of initial functions, multistability was not found for simpler limit cycles (e.g. with 1,2,4,5,7 pulses per period). It is possible that multistability of the type shown here (i.e. bistability) or of a more complicated type is quite common in differential-delay equations, especially when the initial functions are more complex.

3.4.4 Noise or Chaos?

The fact that certain parameters fluctuate randomly leads to a system in which transients are more often observed than steady-state motion on an attractor. This is particularly true if the parameters fluctuate over regions of parameter space where qualitatively different motions are in close proximity, as is usually the case for complex

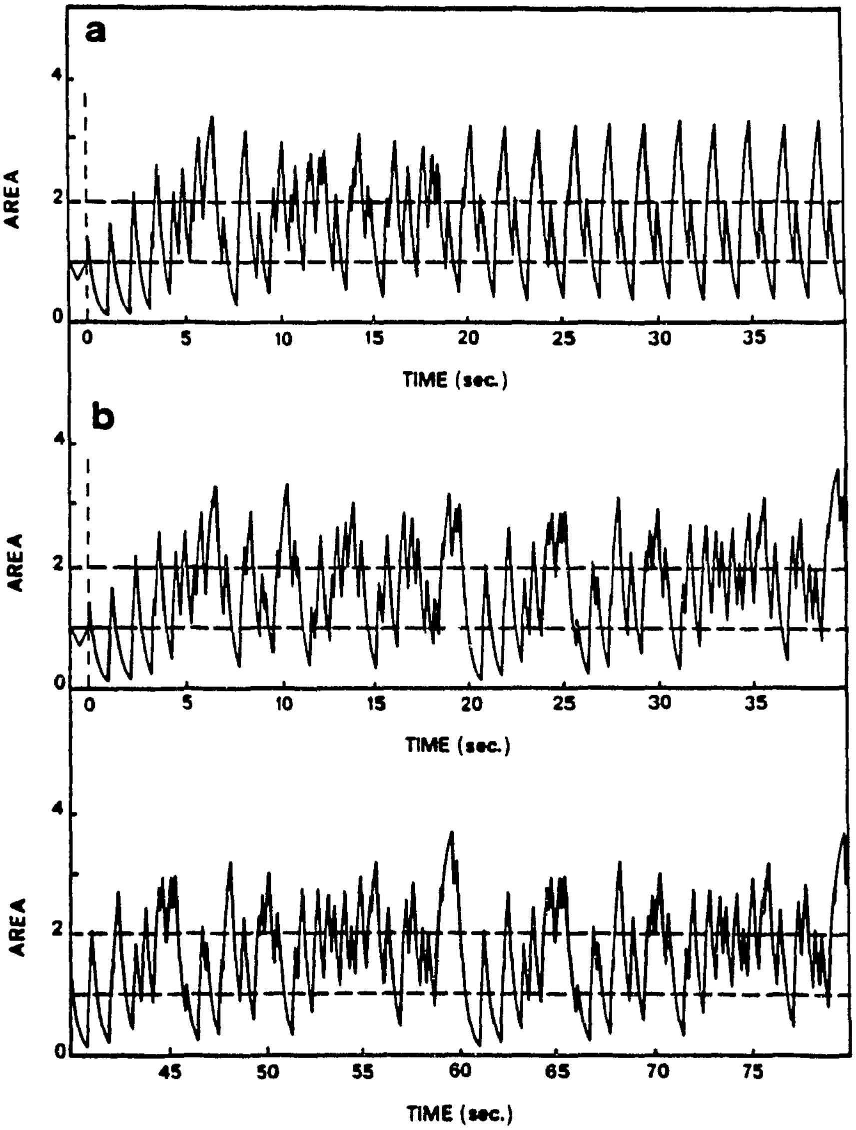

Figure 3.4.5 Illustration of multistability in Equation (3.4.1). The initial function is between the two thresholds for $t \in (-1, -1+w)$ and less than the lower threshold θ_1 for $t \in (-1+w, 0)$, and $x(0) = \theta_1$. In (a) the threshold crossing occurs at $w = 0.055$ and the solution is attracted to a period-6 (3.65 *sec*) limit cycle (i.e. the solution enters the region bounded by the two thresholds 6 times per period). In (b), $w = 0.056$ and the solution is attracted to a different limit cycle of period 38 (20.14 *sec*).

periodic and chaotic motion. In fact, for a given noise correlation time, the system location in parameter space spends more time in the large regions corresponding to simple periodic motion and hence these behaviors are easily identifiable in a time series.

Our current level of understanding of our model DDE for PCMF (see Section 4.5 for more details) does not allow us to say with certainty whether or not we have observed chaos in the pupil light reflex clamped with PCMF. The chaotic solutions for which there exist proofs of existence (for certain parameters: see Section 4.5) are not stable. Likewise, the mixing solutions known to exist in the case where the system is asymptotically stable (Section 4.2.1 and 4.5) are unstable because the slope of the map used in the proof is everywhere greater than one. In computer experiments as in real physical systems, only stable behaviors can be observed. The presence of the unstable solutions can nevertheless complicate phase space motion, especially far from attractors (where transients occur). In fact, although all our simulations of (3.4.1) converged to limit cycle solutions, the transients were extremely long for certain parameter sets (sometimes up to 1000 delays).

Further, certain more complex limit cycles (and possibly all limit cycles) are not globally asymptotically stable, according to the results of Section 3.4.4. Hence, if different initial conditions converge to different solutions in the absence of noise, then it is possible for additive noise to perturb the system from one basin of attraction to another in phase space. Our picture of a system being perturbed from one behavior to another by parametric fluctuations (because the phase space topology is fluctuating), and undergoing transients associated with the different solutions (see Sections 3.3.5 and 3.4.1), will be further complicated by additive noise. The transients may also be complicated by noise amplification at bifurcation points (at which no solution is stable) (see Section 5.2). However, in Section 5.3 it is shown that this effect should occur for smooth feedback and be negligible for piecewise constant feedback. In fact, a detailed analysis of the simpler PCNF case in Section 5.3 reveals that noise causes the period to fluctuate much more than the amplitude in the vicinity of the bifurcation point corresponding to oscillation onset. These period fluctuations are also expected to occur near bifurcations between more complex types of behaviors as seen in the PCMF case.

3.4.5 Noise, damping, temporal integration and retinal adaptation.

In this section, we investigate how to include damping, temporal integration and retinal adaptation into the model developed in Section 2.2. The motivations for doing this are: 1) to obtain a model equation that is at least second order in time to account for the smooth waveforms seen experimentally in PCNF and PCMF; and 2) to see whether the model suggests ways of estimating new parameters characterizing these phenomena. The modelling of noise is also discussed.

Modelling the iris muscles using second order differential equations.

The onset of constriction is always very rapid. Hence, despite the presence of the dilator muscle and of visco-elastic forces, the constriction of the sphincter predominates and is well approximated by a first order process On the other hand, the dilation phase has a slower onset, and in many instances appears to involve two or more exponentials (see e.g. Figure 3.2.2b). This reflects the fact that the dilation phase is the result of many competing influences, such as dilator activation (after a delay greater than 300$msec$), active inhibition of the Edinger-Westphal nucleus and passive relaxation of the sphincter muscle. After-discharge, which describes the ongoing neural activity after the stimulus has stopped, may also occur in the afferent part of the parasympathetic pathway (e.g. at the retina). This would also delay the onset of dilation[33].

In Figure 3.2.6, the single pulse response was shown to be more accurately fit by a model that accounts for the fact that the iris muscle cannot change its velocity instantaneously. This model assumed that constriction involved one exponential, while dilation involved two (i.e. it is a C1D2 fit), and that the function and slope were everywhere continuous. On the other hand, fits of the single pulse response using a C2D2 model have been found to be very unreliable (see Appendix C). Thus, as a first approach towards a higher order model for pupillary oscillations, we will look at C1D2 type models.

To properly model the observed pupillary oscillations, and especially the PCMF-induced oscillations, it is important to fit a segment of the data that is representative of the oscillation. The isolated single pulse response is different from the pulse response that occurs during pupil cycling. In fact, the asymptotes obtained for the isolated pulse tend to be higher, because the average illumination is lower than during pupil cycling. Thus, this isolated response was not considered representative of the cycling data. Instead, we have chosen to directly fit a single pulse response in a pupil cycling record.

Time $t = 0$ is chosen unambiguously as the time at which the area signal crosses the threshold downwards. The value of the upper asymptote is chosen to be the one obtained using the C1D1 method (i.e. from Figure 3.4.2b). Figure 3.4.6a shows the C1D2 fit (SPFC1D2 in Appendix C) to the first pulse response in Figure 3.4.2c. Comparison with similar fits for the other cycles in Figure 3.4.2c shows that the parameter α_d from 1.68 to 17.0, while α_c varies between 6.36 and 10.18, β_d between 0.36 and 0.93 and A between 3.96 and 5.13. The pulses have different amplitudes because the time spent above threshold varies, presumably because of hippus.

The parameter values from this C1D2 fit were then used to numerically integrate the differential equations (3.2.5) corresponding to this C1D2 model in the PCNF configuration. The result is shown in Figure 3.4.6b. The period of ≈ 2 seconds agrees with the mean period of pupil cycling in Figure 3.4.2c. As expected, the derivative is continuous in the transition from constriction to dilation, and discontinuous for the opposite transition. The overall shape of the waveform agrees with that observed experimentally.

The obvious next step is to numerically integrate the same model but with PCMF rather than PCNF. We have found (data not shown) that for equal threshold values, the model solutions were significantly different from the data. For example, the period 2 type solution was not seen for the same threshold values, although it was seen for other threshold values. Further simulations also revealed that threshold values which produced complex limit cycles were difficult to locate. The introduction of a second dilatory component seems to have limited the bandwidth of the model.

The inclusion of higher order dynamics in our model yields simple solutions that are in better agreement with the data, at the expense of losing agreement for the more complex solutions. There is a lot of uncertainty and arbitrariness in the ways to extend our model. It is not very clear what insights into pupillary dynamics will be gained by pursuing this type of fitting.

Additive and Multiplicative noise.

As mentioned in Section 3.4.1, the asymptotes corresponding to the equilibrium solutions of (3.4.1) are given by (2.2.29) and (2.2.30), and they are functions of all the other physiological parameters. This suggests that fluctuations in any of these parameters will also induce fluctuations in the asymptotes. Some parameters are more likely to fluctuate than others. For example, α, A_0 and β are related to properties of

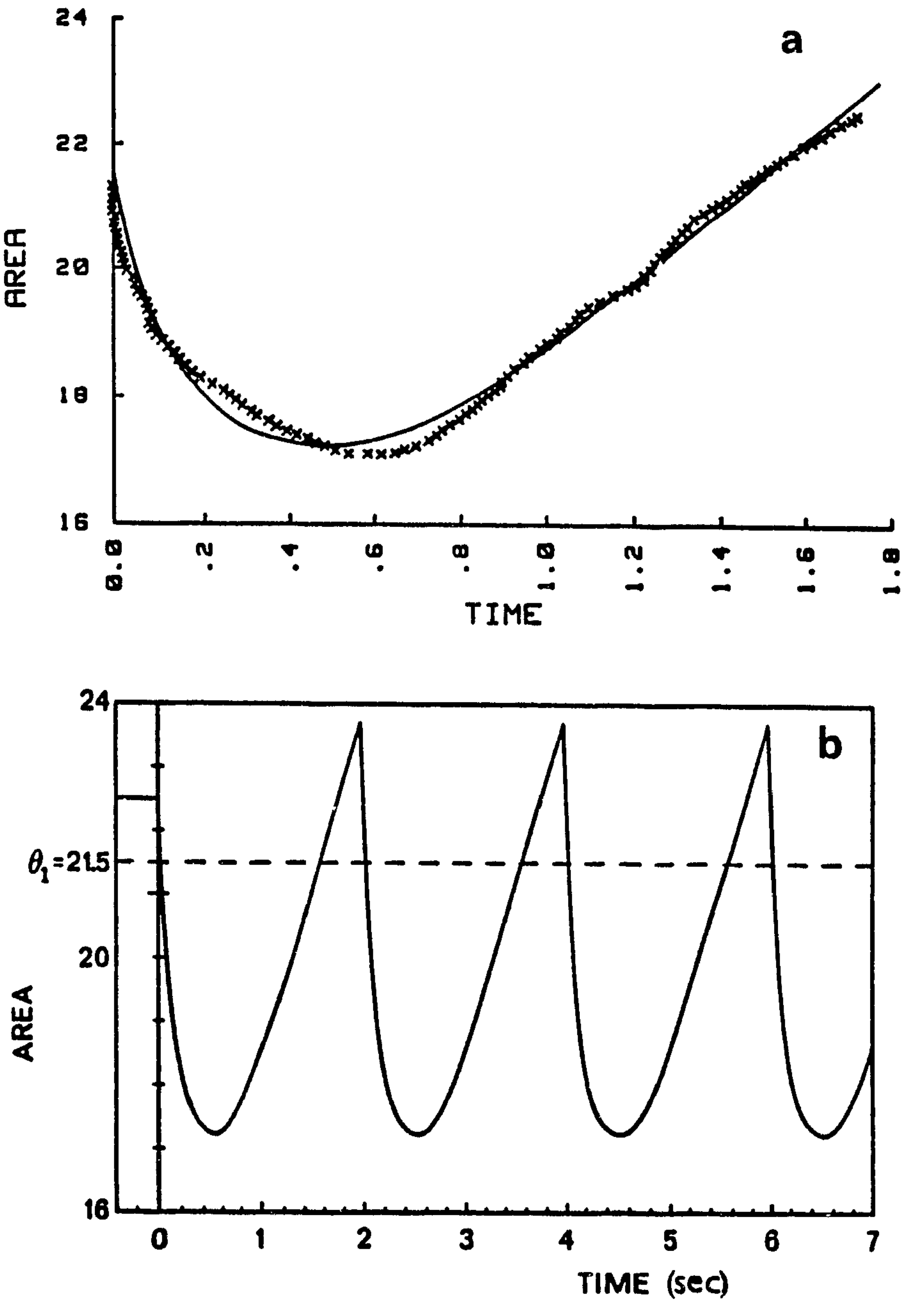

Figure 3.4.6 a) Fit of the first pulse response in the cycling data shown in Figure 3.4.2c. The constriction is fitted by one exponential, and dilation by two exponentials (program SPFC1D2 in Appendix C). Because the point of constriction onset is slightly ambiguous (although not as ambiguous as the point of dilation onset), $t = 0$ was chosen to correspond to the downward crossing of the threshold θ_1. The fitting function assumes that constriction occurs from time $t = 0$ to time $t = 0.411$ (the delay), after which dilation occurs. Because of the continuity constraint on the function and its derivative at time $t = 0.411$, the area still decreases for a hundred milliseconds or more before the actual dilation is observed. A_{off} was set to the value (34.2) determined by the C1D1 method (Table 3.1, subject C). The fit yields the parameters $A = 4.39$, $\alpha_c = 7.90$, $\alpha_d = 1.68$ and $\beta_d = 0.58$. The χ^2 is 6.92 ± 0.25. The fit was repeated for many sets of initial guesses and was found to be very robust. In b), the solution of the C1D2 model using the parameters from the fit in a) in the program C1D2SOL (Appendix C and D) is shown. The first cycle corresponds to a).

the iris muscles; their variations are minimal since pupillary fluctuations are synchronized in both pupils (Section 2.1.3).

The root-mean-square amplitude of hippus has been shown to depend on pupil area[47]. This suggests a multiplicative noise model (see also Section 5.2). It has also been shown that the amplitude of hippus closely parallels the deterministic gain of the reflex[74]. Additive Gaussian noise, injected at the level of the Edinger-Westphal nucleus and filtered by the nonlinearities of the neuromuscular system, has been shown to reproduce the multiplicative characteristic of hippus[74]. In our model, this corresponds to multiplicative noise on γ, i.e. $\gamma = \bar{\gamma} + \sigma\xi(t)$, where $\bar{\gamma}$ is the mean value, σ is the noise intensity and $\xi(t)$ is a stochastic process.

The real situation is probably more complicated than this. The stochastic activity of neurons within the reflex arc itself, as opposed to the activity of other neurons which modulates parameters such as γ, may be viewed as additive noise when its amplitude is independent of the state of the system. High spontaneous activity of Edinger-Westphal neurons has been reported, even in the absence of any synaptic input (see Section 2.1.2). Hence, it is reasonable that the neural output E of the midbrain (Section 2.2.3) will look like :

$$E(t) = \bar{\gamma} ln[\frac{\phi(t-\tau_r-\tau_t)}{\phi}] + \sigma_1\xi_1(t)\, ln[\frac{\phi(t-\tau_r-\tau_t)}{\phi}] + \sigma_2\xi_2(t) \qquad (3.4.2)$$

The output consists of a term proportional to the logarithm of the light flux, a term proportional to the product of the logarithm of light flux and the multiplicative noise intensity σ_1, and another term simply proportional to the additive noise intensity σ_2. By substituting this expression for $E(t)$ into (2.2.4) or (2.2.8), the model for pupillary oscillations becomes a stochastic DDE with additive and multiplicative noise.

Temporal integration and adaptation at the retina.

In response to a light pulse, the activity in the optic nerve does not increase instantaneously but rather builds up with a time constant on the order of 50-100 msec[46]. This "temporal integration" at the retina will affect pupil area dynamics, so Equation (2.2.2) should read:

$$\Delta\frac{dN(t)}{dt} + N(t) = \eta ln[\frac{\phi(t-\tau_r)}{\bar{\phi}}] \qquad (3.4.3)$$

The steady state output of the optic nerve will be proportional to the logarithm of the light flux and inversely proportional to the time constant of neural activity decay (Δ).

Using the results of Section 2.2.3, the dynamics of the pupil are now described by two coupled ODE's, (3.4.3) and

$$k\frac{dg(A)}{dA}\frac{dA}{dt} + k\alpha g(A) = \gamma' N(t - \tau_t - \tau_m) \tag{3.4.4}$$

Equations (3.4.3) and (3.4.4) can be combined into a second order differential equation for pupil area :

$$k\frac{dg(A)}{dA}\{\frac{d^2A}{dt^2} + (\alpha + \Delta^{-1})\frac{dA}{dt}\} + \frac{k\alpha}{\Delta}g(A) = \frac{\gamma'\eta}{\Delta}\,ln\,[\frac{\phi(t-\tau)}{\bar{\phi}}] \tag{3.4.5}$$

If $g(A)$ is linearized, i.e. $g(A) \simeq g(A^*) + \beta(A - A^*)$, the model for PCNF-induced oscillations becomes

$$\begin{aligned}\frac{d^2A}{dt^2} + (\alpha + \Delta^{-1})\frac{dA}{dt} + \frac{\alpha}{\Delta}A(t)& \\ = \frac{\alpha A_o}{\Delta} + \frac{\gamma'}{k\beta\Delta}\,ln&\left[\frac{\phi_{off}}{\bar{\phi}} + \frac{\phi_b}{\bar{\phi}}H\big(A(t-\tau) - A_{ref}\big)\right]\end{aligned} \tag{3.4.6}$$

It appears from (3.4.6) that temporal integration at the retina does not change the value of the asymptotes, since Δ disappears when all time derivatives are zero and $\gamma'/k \equiv \gamma$ as in (2.2.29) and (2.2.30). Further, it is now possible to include second order effects by simply including the proper retinal time constant into our model. All the other parameters can be estimated as usual from the C1D1 cycling model.

This model was investigated numerically for a range of values of Δ between 0.01 and 1 seconds (data not shown). It was found that smooth oscillations could be obtained, and for the PCNF case the period agreed with the experimentally measured value (Figure 3.4.2a) when $\Delta = 0.05$ seconds. However, the transition from dilation to constriction was more abrupt than that from constriction to dilation, which is opposite to what is experimentally observed in PCNF. This behavior is probably due to the response asymmetry, which modifies the damping and natural frequency. It is possible that the value of Δ should also depend on whether the light is on or off Further the value of Δ at time t should depend on the light intensity at a time $t \quad \tau_r$ where τ_r is the retinal delay.

In response to constant stimulation (e.g. provided by the average light level), neural activity in the afferent pathway of sensory systems usually exhibits an abrupt increase at stimulus onset, followed by a decrease in this activity[33,46]. This means that the activity is proportional to the time derivative of the stimulus intensity. The rate of activity decrease is called the adaptation rate. Different adaptation processes operating on different time scales are known to exist in the visual system[118]. Some processes occur at the retina, others higher up in the afferent arc. The model presented in Section 2.2 neglects the high and low frequency characteristics of the pupil light reflex associated with adaptation.

A more complete model for pupillary oscillations would include temporal integration and adaptation in the afferent arc, additive and multiplicative noise injected at the midbrain, as well as a second order differential equation for the muscle inertia and damping (we still neglect the sympathetic pathway as well as the intensity dependence of the iris rate constants seen in Section 2.2.9):

$$\frac{dg(A)}{dA}\frac{d^2A}{dt^2}+\delta\frac{dg(A)}{dA}\frac{dA}{dt}+\omega^2 g(A)=K\,E(t-\tau_m) \tag{3.4.7}$$

$$\Omega\frac{dE(t)}{dt}+E(t)=\rho\frac{dN(t-\tau_t)}{dt}+\left[\frac{\gamma'}{\eta}+\frac{\sigma_1\xi_1(t)}{\eta}\right]N(t-\tau_t)+\sigma_2\xi_2(t) \tag{3.4.8}$$

$$\Delta\frac{dN(t)}{dt}+N(t)=\eta ln\left[\frac{I(t-\tau_r)A(t-\tau_r)}{\bar{\phi}}\right] \tag{3.4.9}$$

Eq.(3.4.8) is a simple model for linear adaptation[46]. Again the retina imperfectly integrates the activity in the optic nerve. The output of the midbrain is proportional to the steady state activity in the optic nerve $N(t)$ (tonic response) and to the time derivative of this activity (phasic response). The bandwidth of the pupil light reflex will depend sensitively on this phasic response.

3.4.6 Summary of Chapter 3.

The results of this chapter show that simple oscillatory activity can be sustained by the different neuronal populations comprising the pupil light reflex arc. This behaviour can be modelled by a simple DDE for the pupil light reflex. However, the analysis of complex deterministic oscillations in this neural delayed system is severely limited by the high noise levels. The question of whether or not we have observed chaos is still open. Our approach has been to characterize the noise and improve our simple model to obtain better agreement with data. Hence we have relied on the stringent test of quantitative agreement between experiment and theory (see Section 1.2) to determine whether the origin of the observed aperiodic behaviour was deterministic or stochastic As Noyes[109] has pointed out, aperiodicity can be a consequence of many phenomena other than chaos which deserve just as much consideration. It is often hard to abandon such an elegant explanation for aperiodicity as chaos, especially when it is generated by a simple deterministic equation with a small number of measurable parameters.

CHAPTER 4
INVARIANT DENSITIES FOR DELAY-DIFFERENTIAL EQUATIONS

> "Nothing puzzles me more than time and space; and yet nothing troubles me less, as I never think about them."
> Charles Lamb

4.1 INTRODUCTION.

This chapter continues the study of delay-differential equations (DDE's) from the point of view of densities constructed from time series. This lays the groundwork for Chapter 5 in which we study the onset of oscillatory motion in the pupil light reflex. In these last two chapters (except for Section 4.5), the focus is no longer on complex deterministic motion in a neural control system (obtained using PCMF) but rather on simple periodic motion. The emphasis is on understanding the deterministic and stochastic behaviour of neural delayed feedback systems (such as the pupil light reflex) at oscillation onset.

This shift in focus comes from the demonstration in Chapter 3 of the difficulty in analyzing complex deterministic motion in the presence of noise. Irregular aperiodic behaviour is observed in the pupil light reflex even though a deterministic model predicts simple periodic limit cycle motion (Section 3.2). This observation is not especially surprising, since it has been made in all experimental systems where routes to chaos have been studied. It suggests that the effect of noise deserves more attention than it has previously received, and that an analysis of the origin and properties of noise might provide deeper insight into the dynamics of neural systems.

There are two reasons why we are interested in densities for delay-differential equations. The first is related to the properties of dissipative dynamical systems, and the second is related to noise.

The dynamical systems we are interested in, i.e. nonlinear DDE's, are dissipative, as opposed to conservative. An important property of dissipative dynamical systems is that Liouville's theorem does not hold, which means that phase space volume (or Lebesgue measure : see Section 4.2) is not preserved as the system evolves in time. In the asymptotic long time limit after transients have died out, phase space trajectories of such systems approach an invariant set (Section 4.2), called the attractor (assuming a stable attractor exists), which can be characterized by a density. A trivial example of an attracting invariant set for a dissipative dynamical system is the stable equilibrium point of a damped harmonic oscillator.

The existence of an attractor allows us to study dynamical properties of the system using the attractor. For example, if the dynamical system has the property of ergodicity, time averages can be written as phase space averages using the invariant density of the measure associated with the attractor (see Section 4.2). This invariant density is of great importance. The value of the density at given point on the attractor is a measure of the fraction of the time the system spends in a neighborhood of this point. For example, in the microcanonical ensemble where the energy and the number of particles is constant, the invariant density is the uniform density (the density of the Lebesgue measure) on the invariant set (energy surface) Hence, for the microcanonical ensemble, the uniform density implies that the system explores the invariant set uniformly.*

The other reason for studying invariant densities is noise. The presence of noise makes the statistical properties of individual trajectories characterized by probability distributions important, and further motivates the study of the dynamics of DDE's from the evolution of densities. In fact, we will see in Chapter 5 that densities are essential when studying bifurcations in the presence of noise since it is the extrema of these densities (often different from those in the deterministic case) that undergo bifurcations.

In this chapter, the concepts of attractor, density, ergodicity and chaos will be formally presented. They will be applied to the study of deterministic and stochastic DDE's. Section 4.2 introduces the mathematical tools for the study of invariant densities of discrete and continuous time dynamical systems with and without noise. In Section 4.3, we calculate densities for the Mackey-Glass equation and their behaviour at bifurcation points. Section 4.4 looks at an approximation of DDE's via coupled ODE's when there is a distribution of delays rather than a single fixed delay. In Section 4.5, we review the known properties (obtained using the tools of Section 4.2) of the first order DDE with PCMF encountered in Chapter 3 Section 4.6 examines the singular perturbation limit in which the DDE becomes a discrete time map Section 4.7 deals with this same limit but in continuous time. The resulting continuous time difference equation provides insight into the dynamics of DDE's. Finally, Section 4.8 presents a new numerical integration method for DDE's based on observations made

---

*In this example from statistical mechanics, the phase space motion is however not attracting: it is always confined to the energy surface in Sections 4.6 and 4.7.

4.2 INVARIANT DENSITIES FOR DISCRETE AND CONTINUOUS TIME SYSTEMS.

4.2.1 Deterministic dynamical systems.

The evolution of a one-dimensional discrete time dynamical system is described by a mapping:

$$x_{i+1} = S(x_i)\,. \tag{4.2.1}$$

The domain and range of the mapping have to be specified along with the functional form of $S(x)$. A well-studied example is the logistic (also called quadratic) map $S : [0,1] \rightarrow [0,1]$ defined by:

$$x_{n+1} = rx_n(1 - x_n)\,. \tag{4.2.2}$$

Starting with an initial condition x_0, a trajectory is obtained by iterating the map. In the asymptotic long time limit the trajectory will trace out the attractor corresponding to the particular value of the parameter r. By constructing a histogram of the iterates, after allowing enough time for the transients to die out, an invariant density on this attractor can be numerically constructed.

An alternate way of obtaining an invariant density is by starting with an initial density $f_0(x)$ supported on some subset of the domain of the map. One can then iterate this density under the action of S to obtain $f_1(x), f_2(x), \ldots$ in the same way that single points are iterated. This corresponds to simultaneously iterating an infinite number of points and hence to following an infinite number of trajectories at once. The initial density specifies the weight associated with each initial condition. If the dynamical system (4.2.1) is ergodic (see 4.2.13), this density point of view is completely equivalent to the time series point of view.

The mapping $S(x)$ is said to be nonsingular if the measure[*] μ on the phase space X of the variable x satisfies $\mu(S^{-1}(A)) = 0$ for all subsets A of phase space such that $\mu(A) = 0$. If $S(x)$ is nonsingular, an expression for the operator P that transforms a density $f_n(x)$ into a new density $f_{n+1}(x) = Pf_n(x)$ after one iteration of the map can

---

[*] A real-valued function μ defined on a phase space X is a measure if : a) $\mu(\emptyset) = 0$ where $\emptyset$ is the null set; b) $\mu(A) \geq 0$ for all subsets A of X; and c) $\mu(\cup_k A_k) = \sum_k \mu(A_k)$ if $\{A_k\}$ is a finite or infinite sequence of pairwise disjoint subsets of X, that is, $A_i \cap A_j = \emptyset$ for $i \neq j$.

be obtained (see Lasota and Mackey[13]). The fraction of the density Pf contained in some set A is given by

$$\int_A P\,f(s)\,ds\,. \tag{4.2.3}$$

The points in A contributing to Pf had their origin in the counterimage of the set A under the action of the map S, given by $S^{-1}(A) = \{y : S(y) \in A\}$. Since the fraction of the density Pf in A must equal the fraction of the original density in $S^{-1}(A)$, we have[*]

$$\int_A P\,f(s)\,ds = \int_{S^{-1}(A)} f(s)\,ds\,. \tag{4.2.4}$$

The operator P, called the Frobenius-Perron operator, is unique by the Radon-Nikodym theorem[13].

An explicit form for this operator, when $A = [a, x]$, is

$$f_{n+1}(x) \equiv Pf_n(x) = \frac{d}{dx} \int_{S^{-1}([a,x])} f_n(s)\,ds\,. \tag{4.2.5}$$

It can also be written as :

$$f_{n+1}(x) \equiv Pf_n(x) = \int_a^b \delta(S(y) - x) f_n(y)\,dy \tag{4.2.6}$$

where δ is the Dirac delta function and the integration extends over the domain of the map $[a, b]$.

The usual Lebesgue measure of a set of points A is denoted by $\mu_L(A)$, and the density of the Lebesgue measure is the uniform density, i.e. $f(x) = 1$ for all x. Hence we write $\mu_L(dx) = dx$. To a general density $f(x)$ is associated an $f-$measure which, for an arbitrary subset A of the total phase space X, is defined by

$$\mu_f(A) = \int_A f(x)\,dx\,. \tag{4.2.7}$$

The f-measure is said to be absolutely continuous with respect to the measure μ, which is the Lebesgue measure dx in the case of (4.2.7). A set A is said to be invariant under S if $S^{-1}(A) = A$. Also, $S(x)$ is measure preserving if

$$\mu(S^{-1}(A)) = \mu(A) \tag{4.2.8}$$

---

[*] The set of densities is defined by $D = \{f \in L^1 : f \geq 0, \| f \| = 1\}$. The desired operator P is a Markov operator, i.e. a linear operator satisfying a) $Pf \geq 0$ and b) $\| Pf \| = \| f \|$ so that P maps densities into densities.

for all subsets A. We will say alternately that the measure μ is invariant under S if S is measure preserving. It can be shown that a measure μ_f is invariant under S if and only if f is a fixed point of the Frobenius-Perron operator P, i.e. a density that satisfies

$$Pf_*(x) = f_*(x)\,. \tag{4.2.9}$$

We then call f_* the invariant density for the map S.

For the logistic map (4.2.2) with $r = 4$, the Frobenius-Perron operator takes the form

$$Pf(x) = \frac{1}{4\sqrt{1-x}}\{f(\tfrac{1}{2} - \tfrac{1}{2}\sqrt{1-x}) + f(\tfrac{1}{2} + \tfrac{1}{2}\sqrt{1-x})\}\,. \tag{4.2.10}$$

It is easily verified that the nonuniform density

$$f_*(x) = \frac{1}{\pi\sqrt{x(1-x)}} \tag{4.2.11}$$

satisfies $Pf_* = f_*$. Hence, the measure

$$\mu_{f_*}(A) = \frac{1}{\pi}\int_A \frac{dx}{\sqrt{x(1-x)}} \tag{4.2.12}$$

is invariant under $S(x) = 4x(1-x)$.

In general, given the Frobenius-Perron operator P, it is difficult to solve (4.2.9) for f_*. Although numerically it takes the same time to compute the invariant density to a given resolution by iterating a single point than by iterating an initial density, there is one striking feature of the latter method: densities converge very rapidly (within a few iterations) to the invariant density. Further, complicated motion along single trajectories in phase space may correspond to simple behaviour for the densities. For example, when the trajectory is chaotic (i.e. when $r = 4$) in the logistic map (4.2.2), the density converges rapidly and uniformly to the smooth density given by (4.2.11).

The existence of an absolutely continuous invariant measure does not necessarily imply any particularly interesting or erratic behavior. The behavior is more interesting if the Frobenius-Perron operator has a unique fixed point f_*, so there is a unique absolutely continuous invariant measure. In this case the map $S(x)$ is ergodic, meaning that every set invariant under S is trivial, i.e.

$$S^{-1}(A) = A \text{ implies } \mu(A) = 0 \text{ or } \mu(X - A) = 0 \tag{4.2.13}$$

for all A in the total phase space X. Ergodic systems may not produce very irregular solutions. In fact, two arbitrarily close initial conditions may yield arbitrarily close trajectories for all time.

Nearby trajectories will diverge if the map has the added property of mixing, which is a mild kind of chaotic behavior. If A and B are subsets of X with measure $\mu(X) = 1$, then for all A, B a mixing transformation satisfies :

$$\lim_{n\to\infty} \mu(A \cap S^{-n}(B)) = \mu(A)\mu(B) . \tag{4.2.14}$$

A stronger type of chaotic motion will occur if, besides ergodicity and mixing, the system has the added property of exactness.* A measure-preserving transformation $S(x)$ is said to be exact if

$$\lim_{n\to\infty} \mu(S^n(A)) = 1 \tag{4.2.15}$$

for every subset A such that $\mu(A) > 0$. This means that a set of initial conditions of nonzero measure will have spread and completely filled the phase space.

In general, it is very difficult to prove that a map is mixing or exact using these definitions. Equivalent criteria have been derived[13] for classifying various degrees of irregular behavior. They concern the convergence properties of iterates $P^n f$ of the Frobenius-Perron operator corresponding to these transformations, rather than the behavior of sequences of sets. Simply stated, $S(x)$ is ergodic, mixing or exact if and only if the sequence $\{P^n f\}$ is, respectively, Cesaro, weakly or strongly convergent to 1, i.e. the uniform density, for all initial (normalized) densities. The precise definitions of these terms and the proofs of these results can be found in Lasota and Mackey[13] (p.63 et seq.).

It can be shown[13] that a one-dimensional map $S(x)$ is exact if its Frobenius-Perron operator has the property of asymptotic stability, i.e. there is a unique density $f_* \in L^1$ such that $Pf_* = f_*$ and

$$\lim_{n\to\infty} \|P^n f - f_*\| = 0 \text{ for every density } f \in D . \tag{4.2.16}$$

The map $S(x) : I \longrightarrow I$, where $I = [a_0, a_r]$ is a compact interval of the real line, is asymptotically stable if :

i) there is a partition $a_0 < a_1 < a_2 < \ldots < a_r$ of I such that for each integer 1,2,...r the restriction of S to the interval $[a_{i-1}, a_i)$ is twice continuously differentiable;

---

*In the hierarchy *ergodicity* ⟶ *mixing* ⟶ *exactness*, each property implies those to its left, but the reciprocal is not necessarily true (see Ref. 13, p.73).

ii) $S([a_{i-1}, a_i)) = [a_0, a_r)$, i.e. S is surjective (or onto) on each subinterval;

iii) there is a constant $\lambda > 1$ such that $|\frac{dS(x)}{dx}| \geq \lambda$ whenever $x \neq a_i$ for $i = 1, 2, ..., r$;

iv) there is a constant $c < \infty$ such that $|\frac{d^2S(x)}{dx^2}| < c[\frac{dS(x)}{dx}]^2$ whenever $x \neq a_i$ for $i = 1, 2, ..., r$.

Condition (iii) on the slope of S is important because it implies that all solutions will be unstable.* Hence if the Frobenius-Perron operator is asymptotically stable, the behavior of the solutions is much more complicated than if it were simply ergodic.

The Frobenius-Perron operator associated with the map S is "asymptotically periodic" rather than "asymptotically stable" if condition (ii) above is not satisfied. In this case, an invariant measure always exists. However, the iterates of an arbitrary initial density f_0 cycle periodically (after a transitory period) between a finite number of densities. Further, each density comprises a certain number of functions supported on disjoint intervals, and these functions permute cyclically among themselves. The case where the period is 1 (i.e. no change from one iterate to the other) corresponds to asymptotic stability. A detailed account of the properties of asymptotic periodicity is given in Lasota and Mackey[13 119].

CONTINUOUS TIME DYNAMICAL SYSTEMS

The evolution of an d-dimensional continuous time dynamical system $x(t)$ is governed by the d-dimensional vector field generated by

$$\frac{d\vec{x}}{dt} = B(\vec{x}). \tag{4.2.17}$$

Each component B_i of B is a scalar function of the coordinates x_i. The flow of densities is governed by a continuous semigroup of Frobenius-Perron operators

$$f(x,t) = P_t f(x,0) \equiv P_t I(x) = \int_{R^d} \Gamma(x,y;t) I(y)\, dy \tag{4.2.18}$$

where $I(x)$ is the initial density and the kernel $\Gamma(x,y;t)$ is called the fundamental solution or the Green's function of the system. The density $f(x,t) = P_t f(x,0)$ satisfies the partial differential equation (PDE)

$$\frac{\partial f(x,t)}{\partial t} = -\sum_{i=1}^{d} \frac{\partial}{\partial x_i}[B_i f(x,t)] \tag{4.2.19}$$

---

*The trajectory of a discrete time dynamical system is stable (i.e. attracting) if the product of the slopes of $S(x)$ evaluated at all the points on the trajectory is less than 1 in absolute value[8].

which is known as the generalized Liouville equation. The invariant density f_* is found by solving the PDE obtained by setting $\frac{\partial f(x,t)}{\partial t} = 0$ in (4.2.19). As in the discrete time case, the Frobenius-Perron operator can be either ergodic, mixing or exact[13].

4.2.2 Stochastically perturbed dynamical systems.

Noise can directly perturb the trajectories of a discrete time dynamical system. In this case we say that the noise is "additive":

$$x_{n+1} = S(x_n) + \xi_n \,. \tag{4.2.20}$$

Noise can also perturb the dynamics by modifying one of the parameters of $S(x)$, in which case one has "multiplicative" or "parametric" noise:

$$x_{n+1} = S(x_n, \xi_n) \,. \tag{4.2.21}$$

From the point of view of statistical mechanics, it is the average influence of the noise on the deterministic system that is of interest. Hence in defining any function r one should only consider an ensemble average, i.e. an average over the different sequences of random numbers $\{\xi_i\}, i \in N$ generated by the same probability density $g(\xi)$:

$$\langle r \rangle = \int_{-\infty}^{\infty} r(\xi) g(\xi)\, d\xi \tag{4.2.22}$$

If we consider only one trajectory evolving from the initial condition x_0, then the probability density of x at the nth iterate, is $f_n(x) = \delta(x - x_n)$, where $x_n = S^n(x_0)$. This result holds for a particular realization of the stochastic process. Since x_n is a function of all the perturbations ξ_i, $i = 1, 2, ..., n$, we can calculate the density of x_n as an average of $\delta(x - x_n)$ over all possible realizations of the ξ_i's. Generalizing (4.2.22), we write

$$\tilde{f}_n(x) = \int_{R^n} \prod_{i=1}^{n} g(\xi_i) d\xi_i \delta(x - x_n) \,. \tag{4.2.23}$$

This average probability for x_n is a path integral for noise (see e.g. Feigenbaum and Hasslacher[120]). It can be shown[13,121] that the iteration of densities under the action of the map (4.2.20) satisfies

$$\tilde{f}_{n+1}(x) = \int_R \tilde{f}_n(y) g(x - S(y))\, dy \,. \tag{4.2.24}$$

for the additive noise case. Note that the argument of g is simply ξ from (4.2.20). For multiplicative noise, the iteration of densities would also satisfy (4.2.24) but with the proper expression for ξ from (4.2.21). Comparison with (4.2.6) shows that the delta function has been replaced by the density of the noise, and the domain of integration is no longer that of the map but rather that of the noise. Further, the Frobenius-Perron operator is replaced by the more general Markov operator[13] (4.2.24).

In the stochastically perturbed continuous time case, the dynamics obey the generalized Langevin equation[13,21]

$$\frac{d\vec{x}}{dt} = B(\vec{x}) + Z(\vec{x})\xi(t) \tag{4.2.25}$$

where ξ is a vector of stochastic variables and Z is a matrix whose components Z_{ij} are scalar functions of the x_i's. The flow of densities is governed by the Fokker-Planck equation

$$\frac{\partial f(x,t)}{\partial t} = -\sum_{i=1}^{d} \frac{\partial}{\partial x_i}[B_i f(x,t)] + \frac{1}{2} \sum_{i,j=1}^{d} \frac{\partial^2}{\partial x_i \partial x_j}[a_{ij} f(x,t)] \tag{4.2.26}$$

where

$$a_{ij}(x) = \sum_{k=1}^{d} Z_{ik}(x) Z_{jk}(x) . \tag{4.2.27}$$

Comparison with (4.2.19) shows that the diffusion term, i.e. the second term on the right hand side of (4.2.26), is due to the stochastic perturbation.

4.3 SOLUTIONS AND BIFURCATIONS OF DDE's FROM THE DENSITY POINT OF VIEW.

In this section, our investigation of the properties of DDE's begins with the study of a solvable first order linear DDE. It is then shown how a density can in general be calculated from the explicit time-dependent solution of a differential equation in the asymptotic time limit. The problem of obtaining the explicit time-dependent solution of a nonlinear DDE (especially in the presence of noise), as well as the problem of interpreting the density obtained from the solution of an infinite dimensional DDE are discussed. This leads us to our numerical approach to the study of densities for DDE's.

4.3.1 Linear delay-differential equations.

DDE's are functional differential equations. They are infinite dimensional because their solution requires the specification of an initial function on $[-\tau, 0]$, which corresponds to an infinite number of initial conditions. The few techniques available for their study are mathematically involved (see Hale[122]; Mohammed[123]), since they describe flows in a functional space (such as a Banach space) rather than in the usual phase space for ODE's.

The situation is much simpler for linear DDE's, which may arise from the linearization of nonlinear DDE's such as our model for pupillary oscillations in Section 2.2.3 :

$$\frac{dx}{dt} = -\alpha x(t) + \beta x(t-\tau) . \tag{4.3.1}$$

A closed form solution can be found for this first order linear DDE. Its Laplace transform can be written :

$$X(s) = \left\{ \beta\, e^{-s\tau} \int_{-\tau}^{0} e^{-su} x(u)\, du \; + \; x(0) \right\} \cdot [s + \alpha - \beta e^{-s\tau}]^{-1} . \tag{4.3.2}$$

$(s + \alpha - \beta e^{-s\tau})$ is a meromorphic function since it has an infinite number of conjugate pairs of isolated poles. Using the Mittag-Leffler theorem (see e.g. Saaty[124]), we can form the expansion

$$[s + \alpha - \beta e^{-s\tau}]^{-1} = \sum_{k=-\infty}^{\infty} \frac{c_k}{s - s_k} = \sum_{k=-\infty}^{\infty} \frac{1}{(s - s_k)(1 + \tau s_k + \alpha\tau)} \tag{4.3.3}$$

where c_k is the residue of the left hand side at s_k and is obtained using l'Hopital's rule. The inverse Laplace transform yields

$$x(t) = \frac{1}{2\pi i} \int_{c-i\infty}^{c+i\infty} e^{st} X(S)\, ds = \sum_{k=-\infty}^{\infty} \gamma_k\, e^{s_k t} \tag{4.3.4}$$

where

$$\gamma_k \equiv c_k x(0) \; + \; \beta\, c_k\, e^{-s_k \tau} \int_{-\tau}^{0} x(u) e^{-s_k u}\, du .$$

The solution involves an infinite number of integrals over the initial function. Further, different initial functions will yield the same solution if all the integrals corresponding to the different s_k's have the same value. The zero solution, neutrally stable oscillations (when there are pure imaginary eigenvalues) and unbounded solutions are the only possible asymptotic solutions for this and every other linear differential delay equation.

Given the difficulties involved in obtaining analytical solutions for nonlinear DDE's, linear stability analysis and eigenfunction expansions of the solution are among the few tools available for their study.

4.3.2 Calculating a density from the solution.

Given the explicit solution $x(t)$ of a differential equation, it is straightforward to determine the density $f(x)$ corresponding to the degree of freedom x. Let A be a set of points in the domain of the time variable t, and assume that the uniform (Lebesgue) measure is the invariant measure for this variable. The case where a solution $x(t)$ is obtained by numerical integration of a differential equation with a fixed time step, or where a solution is uniformly sampled in time, are illustrations of a uniform measure on time. The measure of the set A is then simply $\mu_L(A)$. Likewise, assume the measure μ_f is associated with the variable x, where $f(x)$ is a density to be determined. The explicit time-dependent solution $x(t)$ can be seen as a mapping from the time domain to the x-domain. The set A is then transformed into the set $B = x(A)$. It follows that

$$\int_B f(x)\,dx = \int_A dt\,. \tag{4.3.5}$$

Since the set A is arbitrary, the density $f(x)$ is given by

$$f(x) = \frac{1}{dx/dt}\,. \tag{4.3.6}$$

In the case where the solution is periodic, the density can be constructed from a single period of the solution. From (4.3.6) it is obvious that $f(x)$ is singular whenever $\dot{x} = 0$. Since (4.3.6) involves the vector field $f(\vec{x})$ ($= \frac{dx}{dt}$, as in (4.2.17)), one might think that the density can be obtained directly from the differential equation without having to integrate it. However, the vector field gives the value of the derivative at any point in the field, including those where transients occur, while we are interested only by the support of the density, i.e. the attractor.

As an example of how a density is obtained from the solution, let

$$x(t) = A\sin(\omega t) = \alpha\sqrt{k-k_0}\,\sin(\omega t)\,, \tag{4.3.7}$$

which approximates the solution of a DDE close to the Hopf bifurcation point $k = k_0$. The normalized density on the x-axis is

$$f_k(x) = \frac{1}{\pi A\,\cos[\arcsin(\frac{x}{A})]}\,, \tag{4.3.8}$$

which is singular at $x = \pm A$. Also,

$$\lim_{k\to k_0}\int_{-\sqrt{k-k_0}}^{\sqrt{k-k_0}} f_k(x)\,dx = 1 \tag{4.3.9}$$

and thus

$$\lim_{k \to k_0} f_k(x) = \delta(x) \tag{4.3.10}$$

which is the density (or rather distribution since it is no longer L^1) of the equilibrium solution (for $k < k_0$).

4.3.3 Numerical computation of invariant densities.

While the theory of invariant densities for ODE's and maps is well developed, to our knowledge it is nonexistent for DDE's. In fact it is not clear what kind of measure to use in the infinite-dimensional phase space in which the solutions of DDE's evolve. The bold approach which assumes that a generalized Liouville equation can be defined for a DDE leads to the extremely difficult problem of solving a PDE with retarded argument. It is possible that the application to DDE's of measure-theoretical techniques developed for the study of PDE's[13] may prove more fruitful.

In this and the next chapter, we examine the densities constructed from the trajectory of the state variable obtained by numerical integration of DDE's. It is not clear whether these densities represent "invariant densities" for DDE's. However, it is clear that for constant initial functions they numerically converge to an invariant form with or without noise, and that they have features in common with invariant densities for maps and ODE's. We make the tacit assumption that invariant densities for the DDE's of interest exist and are globally stable (attracting) for the class of constant initial functions. With this proviso, henceforth these numerically generated densities will be referred to as "invariant densities".

The densities shown in Figure (4.3.1) were obtained from the numerical integration of the Mackey-Glass equation[24] :

$$\frac{dx}{dt} = -\alpha x(t) + \frac{\lambda \theta^n x(t-\tau)}{\theta^n + x^n(t-\tau)} \tag{4.3.11}$$

after allowing sufficient time for the transients to decay. The interval $(0.5, 1.5)$ (centered about the fixed point $x^* = 1$) was divided into 500 bins. A fourth order Runge-Kutta algorithm (see Appendix D) was used, and the initial function was a constant.

The densities appear to be continuous with very narrow peaks corresponding to the zero-slope points of the solution. The amplitude of the very narrow peaks in the density is irrelevant, as it is determined by the precise boundaries of the bins, and would be infinite if the bins were infinitely narrow (see Section 4.3.2). The value of

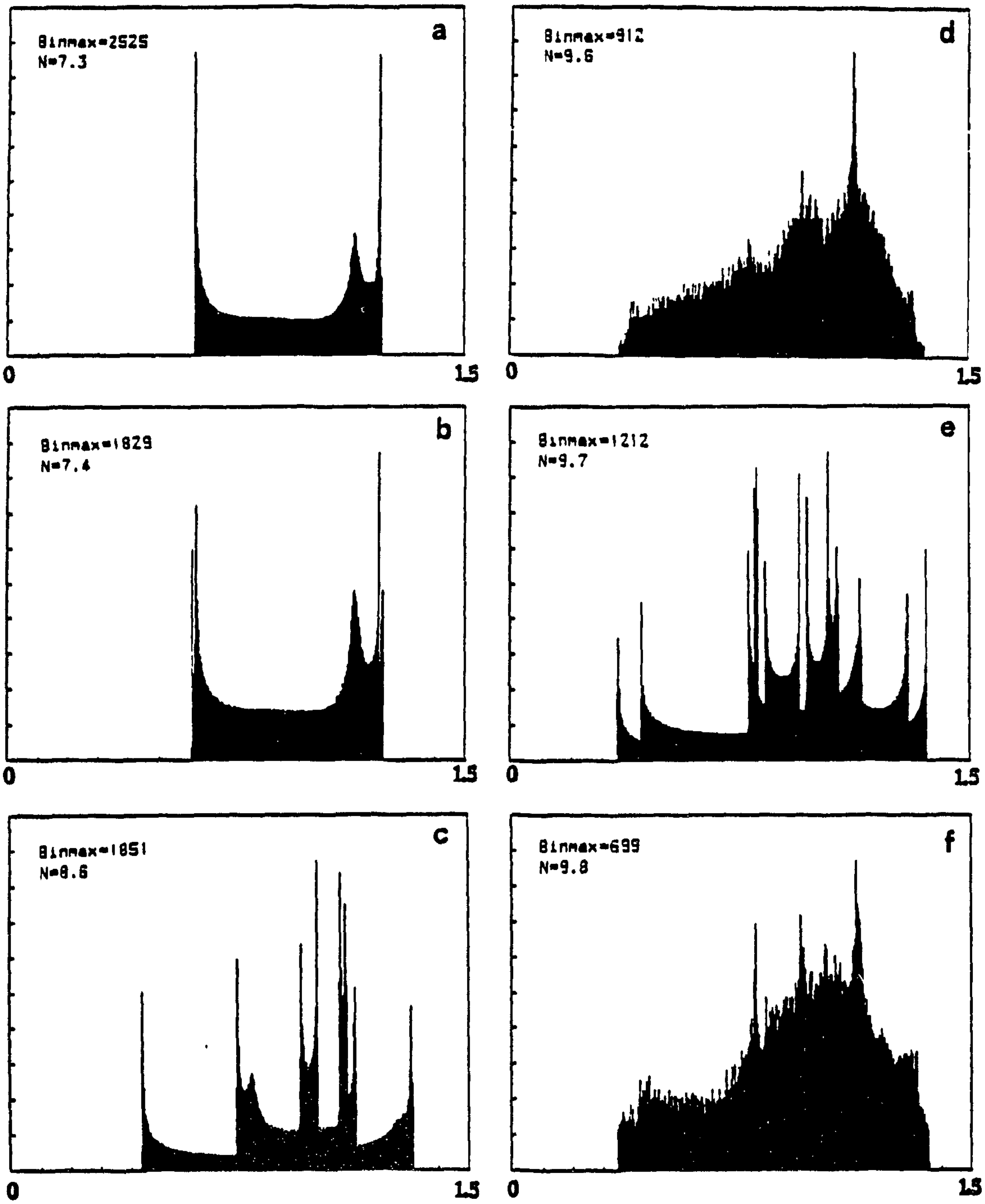

Figure 4.3.1 Numerically computed densities corresponding to solutions of the Mackey-Glass equation (4.3.11). The densities are constructed by partitioning the x-interval $(0, 1.5)$ into 500 bins. The parameter values are $\tau = 2$, $\lambda = 2$, $\theta = 1$ and $\alpha = 1$. The integration time step for the fourth order Runge-Kutta method with linear interpolation for the delay is $\tau/40$. (4.3.11) is integrated starting from a constant initial function for 1000 delays, which are discarded as transients. The density is obtained from the solution for the next 2000 delays. The ordinate scale goes from 0 to BINMAX, which is 1.1 times the value of the highest peak in the histogram. A period doubling bifurcation occurs as n goes from 7.3 to 7.4 (compare a,b). Also, a periodic window emerges out of chaos as n goes from 9.6 to 9.7 (d,e).

the bifurcation parameter n in (4.3.11) increases from Figure 4.3.1a to 4.3.1f. Figure 4.3.1a corresponds to a nearly sinusoidal solution for a parameter value between that at which a Hopf bifurcation ($n = 5.04$) and the first period-doubling bifurcation ($n = 7.36$) occur. As the Hopf bifurcation is approached, the small peak between the two larger peaks disappears (data not shown) and the shape of the density is approximated by (4.3.8). A period-doubling bifurcation has occurred between 4.3.1a and 4.3.1b. As a consequence of this period-doubling, the solution has two more zero-slope points during one period, observed as a splitting in the narrow peak structure of the density. Figure 4.3.1c illustrates the invariant density of a complicated periodic orbit.

The invariant density for a chaotic solution is seen in Figure 4.3.1d. In the chaotic regime, the density looks like that for periodic motion with superimposed noise. Further, narrow peaks are now broadened and there are no longer any sharp cusps. In Figure 4.3.1e, it is seen that upon further increase of the parameter n in (4.3.11), the chaotic type of solution gives way to a periodic solution. This "periodic window" is once again replaced by chaotic motion as n is increased further.

4.4 DISTRIBUTED DELAYS: APPROXIMATING THE DDE WITH COUPLED ODE's.

In this section, the approximation of DDE's by ODE's is considered. Then, the concept of "distributed delay system" is defined and an example is given. It is shown how such systems can be equivalent to DDE's, and the degree to which they approximate the behavior of a DDE at a Hopf bifurcation.

4.4.1 Approximating the DDE by an ODE.

It is straightforward to rescale Equation (4.3.11) as

$$\frac{dx}{dt} = -x(t) + f\big(x(t - \alpha\tau)\big)\,, \tag{4.4.1}$$

where f corresponds to the second term on the right hand side of (4.3.11). In the limit $\alpha\tau \ll 1$ where (4.4.1) (or (4.3.13)) behaves like an ODE, it is possible to expand the nonlinear delayed feedback in powers of $(\alpha\tau)$. Thus

$$x(t - \alpha\tau) \approx x(t) - (\alpha\tau)\dot{x}(t) + \frac{(\alpha\tau)^2}{2}\ddot{x}(t) - \dots. \tag{4.4.2}$$

Further, f can be expanded around a solution x_0 which is, for example, a fixed point, or the limit cycle solution $x_0(t) = x^* + A\,sin(\omega t)$:

$$f\big(x(t-\alpha\tau)\big) \approx f(x_0) + [x(t-\alpha\tau) - x_0]\left.\frac{df}{dx}\right|_{x_0} + \tfrac{1}{2}[x(t-\alpha\tau) - x_0]^2\left.\frac{d^2f}{dx^2}\right|_{x_0} + \dots \tag{4.4.3}$$

Hence, the DDE (4.4.1) is approximated by

$$\begin{aligned}\frac{dx}{dt} + x(t) &\approx \alpha^{-1} f(x_0)\\ &\quad + \alpha^{-1} \left.\frac{df}{dx}\right|_{x_0} \left\{x(t) - x_0 - (\alpha\tau)\dot{x}(t) + \frac{(\alpha\tau)^2}{2}\ddot{x}(t)\right\}\\ &\quad + \tfrac{1}{2\alpha} \left.\frac{d^2 f}{dx^2}\right|_{x_0} \left\{x(t) - x_0 - (\alpha\tau)\dot{x}(t) + \frac{(\alpha\tau)^2}{2}\ddot{x}(t)\right\}^2 + \dots\end{aligned} \tag{4.4.4}$$

The limit $\alpha\tau \ll 1$ can be achieved by letting α and/or τ go to zero. However, when α goes to zero, the right hand side of (4.4.4) diverges due to the α^{-1} terms. If $\alpha\tau \to 0$ because the delay goes to zero, the expansion will converge (see Mallet-Paret and Nussbaum[125]). Approximating the DDE by an ODE in the above manner will only work when the delay is small. For the pupil, the value of $\alpha\tau$ is between 0.2 and 1, and the delay is certainly not negligible. Thus this approximation is inappropriate for our problem and will not be pursued any further.

4.4.2 Distributed delays.

Up to now, the focus has been on systems whose time evolution depends not only on their present state but also on the value of some state variable at a precise time in the past. More generally, one can consider systems whose memory extends over the whole past. The extent to which values in the past affect their present evolution is determined by a kernel $K(t)$:

$$\frac{dx}{dt} = f(x(t), z(t)) \qquad \text{where} \qquad z(t) = \int_{-\infty}^{t} K(t-u)x(u)\,du \tag{4.4.5}$$

The fixed delay case we have considered thus far corresponds to choosing a Dirac delta function for the kernel.

As a specific example of a system with distributed delay, consider the transmission of electrical activity along the optic nerve. This nerve consists in a bundle of axons emanating from the cell bodies of specific neurons in the retina (the ganglion cells). These axons are not all identical, because their axon diameters are distributed according to a certain probability density. Axon diameter determines the propagation speed of the nerve impulse. For myelinated axons, the velocity is proportional to the square root of the diameter of the axon, while it is proportional to the diameter for demyelinated axons. Thus, even if all ganglion cells fire simultaneously, the action potentials will arrive at the postsynaptic neuron population after different propagation delays, hence the origin of distributed delays in nerve conduction. Often the spread in conduction times is small enough to warrant the use of a single fixed delay.

4.4.3 Transforming a DDE into coupled ODE's.

Under certain conditions, a DDE is equivalent to an infinite set of ODE's. This can be shown using the following approach[126-128]. Assume the kernel in (4.4.5) is normalized and has the form of a gamma distribution

$$G_a^m(q) = \frac{a_{m+1}}{m!} q^m e^{-aq}, \qquad a, m \geq 0 \tag{4.4.6}$$

where m is an integer. This kernel has a maximum at $q = \frac{m}{a}$ so the average delay is given by

$$\overline{\tau} = \frac{\int_0^\infty q G_a^m(q)\, dq}{\int_0^\infty G_a^m(q)\, dq} = \frac{m+1}{a}. \tag{4.4.7}$$

The important property of this kernel is

$$\lim_{\substack{m,a \to \infty \\ \overline{\tau}\ \text{const}}} G_a^m(q) = \delta(q - \overline{\tau}) \tag{4.4.8}$$

so that in this limit

$$z(t) = x(t - \overline{\tau}). \tag{4.4.9}$$

We now define

$$\begin{aligned} y_0(t) &\equiv x(t) \\ y_i(t) &\equiv \int_{-\infty}^{t} x(u) G_a^{i-1}(t-u)\, du \qquad i = 1, \dots, m+1 \end{aligned} \tag{4.4.10}$$

The equations satisfied by the $y_i(t)$'s are obtained by computing $\frac{dy_i}{dt}$ (using Leibniz's rule) and using the recursive relation

$$\frac{dG_a^p(t-u)}{dt} = a\left\{G_a^{p-1}(t-u) - G_a^p(t-u)\right\} \tag{4.4.11}$$

The result is

$$\begin{aligned} \frac{dy_0}{dt} &= f(y_0, y_{m+1}) \\ \frac{dy_i}{dt} &= a(y_{i-1} - y_i) \qquad i = 1, 2, \dots, m+1 \end{aligned} \tag{4.4.12}$$

where the first equation follows from $y_{m+1}(t) = z(t)$. Hence (4.4.5) is strictly equivalent to the system of equations (4.4.12), which is an $(m+2)$-dimensional system of ODE's, all of which are linear except for the first one which contains f. If the limit in (4.4.8) is taken, the original system (4.4.5) becomes a DDE, and it is equivalent to an infinite set of linear ODE's plus one nonlinear ODE.

In the limit $m \to \infty$, the initial condition for both the integro-differential equation (4.4.5) (a function on $(-\infty, 0])$ and the system (4.4.12) is infinite-dimensional. However, for finite m, the initial condition for (4.4.5) is still infinite dimensional, while that for (4.4.12) is a point in an $(m+2)$-dimensional phase space. This "dimension reduction" which occurs in the transformation from the distributed delay system to the finite-dimensional set of ODE's is, however, only apparent.

Let $I(t)$, $t \in (-\infty, 0]$ be the initial condition of (4.4.5). Then the initial conditions $y_i(0)$ of (4.4.12) are constants given by

$$y_i(0) = \int_{-\infty}^{0} I(u) G_a^{i-1}(-u)\, du\,. \tag{4.4.13}$$

Further, if $I(u)$ equals a constant C, then $y_i(0) = C$ for all i because the kernels are normalized. What this means is that although the initial condition is infinite dimensional, the solution depends only on a finite number of constants given by the integrals in (4.4.13). This becomes more apparent when the problem is formulated in terms of the $(m+2)$ coupled ODE's.

4.4.4 Approximating the behavior of a DDE at a Hopf bifurcation.

In Section 5.3, the Hopf bifurcation in DDE's is studied in relation to experiments on the onset of pupillary oscillations. In Section 5.2, it is shown that the Hopf bifurcation analysis for DDE's is mathematically involved. Hence, any approach that can give analytical insight into this bifurcation is welcome. The approximation of a DDE by ODE's studied in this section can yield such insight. Here, we address the question of how many ODE's are needed to obtain a reasonable approximation to the behaviour of the DDE at a Hopf bifurcation.

If a small number suffices, we might improve our understanding of the dynamics of DDE's using the analytical tools to deal with ODE's. In turn, these analytical tools would open the door to the study of the influence of noise on DDE's, a topic about which very little is known.

We give the beginning of an answer to this question by investigating the Hopf bifurcation in the set of ODE's equivalent to the Mackey-Glass equation :

$$\frac{dx}{dt} = -\alpha x(t) + \frac{\lambda \theta^n x(t-\tau)}{\theta^n + x^n(t-\tau)} \equiv F\big(x(t), x(t-\tau)\big) \tag{4.4.14}$$

In particular, we want to know how many ODE's are needed for close agreement between the values n_0 at which the bifurcation occurs in the DDE and in the system of ODE's. We first proceed to the Hopf analysis of the $m+2$-dimensional system. After linearizing the set of ODE's (4.4.12) around its fixed point

$$y_0^* = y_1^* = ... = y_{m+1}^* = \theta\left[\frac{\lambda}{\alpha} - 1\right]^{1/n} \qquad (4.4.15)$$

we can compute the characteristic equation for the linearized flow

$$(\alpha + \lambda)(a + \lambda)^{m+1} = \beta a^{m+1} \qquad (4.4.16)$$

where $\beta = \alpha - n\alpha + \dfrac{n\alpha^2}{\lambda}$. Setting $\lambda = i\omega$, (4.4.16) becomes

$$(\alpha + i\omega) \sum_{j=0}^{m+1} C_j^{m+1} a^{m+1-j} (i\omega)^j = \beta a^{m+1} \qquad (4.4.17)$$

where $C_a^b = \dfrac{b!}{a!(b-a)!}$ are the binomial coefficients. For given values of m, a, θ, α and λ, we must find the values of ω and β which satisfy the real and imaginary parts of (4.4.17). From this value of β, the value of n in (4.4.14) can be deduced.

We have computed the values of ω and β which satisfy (4.4.17) for the parameter values : $\theta = 1$; $\alpha = 1$; $\lambda = 2$; $\tau = 2$ for which the fixed point of (4.4.14) satisfies $x^* = 1$. As m is increased, the ratio $\bar{\tau} = \frac{m+1}{a}$ is kept equal to 2, the value of the delay in the Mackey-Glass equation. This implies that a in fact depends on the value of m, so in (4.4.17) we have $a = a(m)$. Figure (4.4.1) plots, as a function of m, the value of n (corresponding to the values of ω and β which satisfy (4.4.17)) at which the Hopf bifurcation occurs. We find that as $m \to \infty$, the value of n converges to the value for the DDE ($n_0 = 5.04$). Also, the fewer ODE's one uses for the approximation of the DDE, the steeper the feedback function (the steepness is proportional to n) has to be in order to destabilize the fixed point.

A system that undergoes a Hopf bifurcation when the slope of its feedback function is steep is considered to be more stable than one in which the bifurcation occurs for a small slope. Our result implies that as the memory function G in (4.4.6) becomes more localized in the past (as $m \to \infty$), the system loses stability. This suggests that the nervous system might use distributed delays to avoid regenerative oscillations in negative feedback loops. On the other hand, it may use "localized

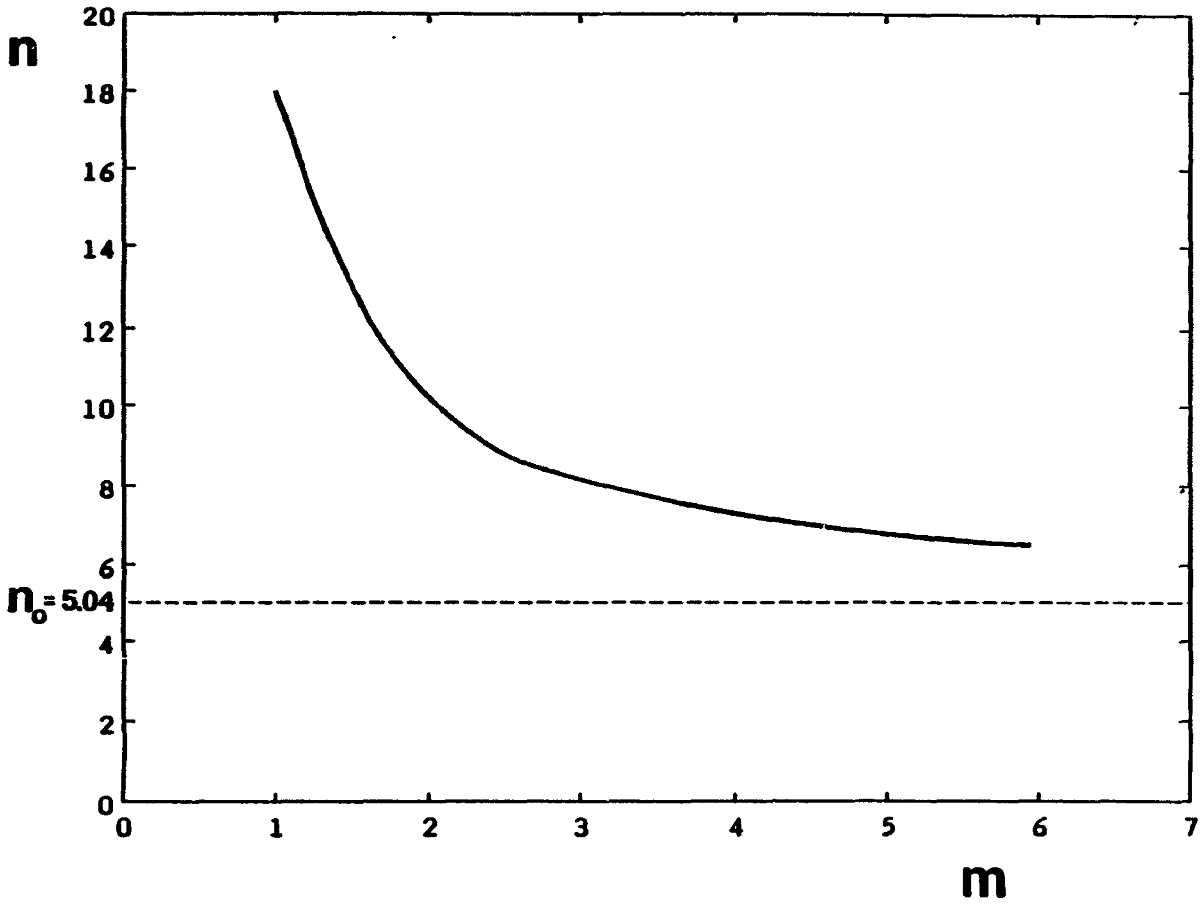

Figure 4.4.1 Value of n at which a Hopf bifurcation occurs in the set of coupled ODE's (4.4.12) used to approximate (4.4.14) versus the number m of equations used in the approximation. m corresponds to the order of the memory kernel (4.4.6). As m increases, the memory function becomes more localized, and the value of n converges to that for which the delay-differential equation (4.4.14) undergoes a Hopf bifurcation (5.04).

memory functions" corresponding e.g. to the kernels (4.4.6) with a high m value to maintain oscillatory behavior.

A simple calculation shows that the 2-dimensional system corresponding to $m = 0$ does not have a Hopf bifurcation. At least a 3-dimensional system of ODE's modelling distributed delays is needed to produce oscillatory behavior (one dimension more than the minimum of two required for the occurrence of a Hopf bifurcation in ODE's). A similar result has been reported by Marriott and Vallée^{129}, who have approximated the DDE using a N-dimensional ODE modelling a system with N independent components with identical response times.

The study of DDE's using distributed delays gives us insight into how a system loses stability as memory is progressively shifted to a precise time in the past. It would be interesting to see whether this result still holds when there is a nonzero minimal delay, which is more relevant physiologically than distributed delays alone. In fact, in the nonzero minimal delay case, it can be shown that the DDE reduces to one nonlinear DDE and $(m+1)$ linear ODE's. The approach of this section has also shown that the space of initial functions for DDE's, although infinite-dimensional, is partitioned into subsets which yield the same solution. In fact, in the $m \to \infty$ case corresponding to the DDE, the solution is shown to depend on an infinite number of integrals of the initial function over the kernels, and many initial functions will yield the same value for these integrals

4.5 MAPS AND INVARIANT DENSITIES FOR A DDE WITH PCMF.

4.5.1 Introductory remarks.

We now give a specific application of the concepts of Section 4.2 to the analysis of the dynamical properties of a delay-differential equation. The equation is the first order DDE with piecewise constant mixed feedback (PCMF) encountered in Sections 3.3 and 3.4 :

$$\alpha^{-1}\frac{dx}{dt} + x(t) = f(x_\tau) \qquad \text{where } f = \begin{cases} c & \theta_1 < x_\tau < \theta_2 \\ d & x_\tau < \theta_1 \text{ or } x_\tau > \theta_2 \,, \end{cases} \tag{4.5.1}$$

where the state variable is denoted by x instead of A. The structure of this equation is identical to that used for pupil area dynamics; its solutions are simply inverted and shifted by a constant. This is because an increase in the forcing (light intensity) in the pupil equation causes the area to decrease, due to the increase in the activity to the iris sphincter muscle.

When the feedback function f is a single-humped smooth (rather than piecewise constant) nonlinear function (4.5.1) becomes the paradigm of systems exhibiting "mixed feedback", i.e. a combination of positive and negative feedback (see an der Heiden and Mackey[66] and references therein). This equation has received much attention in physiological dynamics, and especially in blood cell population dynamics, where it is known as the Mackey-Glass equation (see (4.3.11)). It also arises in nonlinear optics, where it serves as a model for optical bistability and is known as the Ikeda equation[130]. In this latter case, the function f can be multi-humped.

Piecewise linear and piecewise constant systems such as (4.5.1) have also received considerable attention in the mathematics literature[66,114,131,132]. Besides being interesting in their own right, they often serve as approximations to, or idealizations of, systems with smooth nonlinearities. In fact, analytical insight into the dynamics of smooth feedback systems becomes possible if f is assumed to be constant over major sections of its domain. Under certain conditions this assumption allows us, as we will show, to study an infinite-dimensional DDE in terms of a one-dimensional discrete time map.

In this section, the most important properties of (4.5.1) are reviewed and new findings from our own simulations are presented. Equation (4.5.1) is one of the few continuous time dynamical systems for which there are analytical proofs of existence of chaotic motion. The proofs for the analytical results in this section are very tedious and can be found in the references[66 114]. The properties presented here have been proved for the more general case where the feedback function has three levels (in the context of PCMF-induced pupillary oscillations in Section 3.3, this would correspond to different OFF-state illuminations on each side of the ON-state). Further, these properties hold when certain smoothing conditions are applied to remove the discontinuities in f (Walther[131]).

4.5.2 Analysis of PCMF using crossing time maps.

The analysis summarized in this section shows that successive differences in threshold crossing times obey a one-dimensional map which, for different parameter sets, either: 1) satisfies the Li and Yorke conditions[133] for chaotic motion; or 2) has an asymptotically stable Frobenius-Perron operator associated with it ; or 3) has an asymptotically periodic Frobenius-Perron operator associated with it (definitions of these terms are found in Section 4.2).

The first step in the analysis is to scale time in units of the delay, as in (4.3.13):

$$\frac{dx}{dt} = -\alpha\tau x(t) + \tau f[x(t-1)]\,. \tag{4.5.2}$$

where f now denotes the nonlinear function on the right hand side of (4.5.1). It is also possible to rescale the amplitude of x so that the lower threshold satisfies $\theta_1 = 1$.

At any given time, the function f is equal to a constant. Hence, (4.3.13) is a first order linear inhomogeneous differential equation. If x_τ is between the two thresholds, $\theta_1 < x_\tau < \theta_2$, then $x(t)$ will consists of an exponential increasing towards an upper asymptotic value $\frac{f}{\alpha} = \frac{c}{\alpha}$. If x_τ is outside the region between the two thresholds, i.e $x_\tau > \theta_2$ or $x_\tau < \theta_1$, the solution will be an exponential decreasing towards a lower asymptotic value $\frac{d}{\alpha}$. The solution of (4.5.2) is thus given by a continuous function made up of a sequence of increasing and decreasing exponentials, as shown in Figure 4.5.1. Further, since the derivative in (4.5.2) has a finite discontinuity (due to the piecewise constant nature of f), the solution $x(t)$ will be continuous (a consequence of the smoothing action of the integration) However, $x(t)$ will not be differentiable at the connecting points between increasing and decreasing exponentials.

The complexity of the solution in the interval $(t, t+1)$ depends on the number of times the solution crossed the thresholds during the interval $(t-1, t)$, as the system has no memory beyond one delay. Since at any given time the solution consists of a single exponential, it is possible to analytically determine the threshold crossing times. Such would not be the case if the homogeneous part of (4.5.2) were second order or higher. The key property of (4.5.2) lies in the fact that its solutions can be constructed from a knowledge of the crossing times t_i with the thresholds θ_1 and θ_2. In fact, the extrema or "turning points" of the solution occur at times $t_i + 1$, i.e. the crossing time plus one delay. We will show that the crossing times are uniquely determined by the the thresholds crossings of the initial function, and give an example where a map relating successive crossing time differences can be derived Before proceeding, results concerning the simpler behaviors of (4.5.2) are presented[66].

Let $\theta_1 = 0$ and $\theta_2 = b$, which corresponds to the negative feedback case. If the upper asymptote $\gamma = \frac{c}{\alpha}$ satisfies $\gamma < \theta_2$, then γ is a globally asymptotically stable stationary solution of (4.5.2). However, if $\gamma > b$, (4.5.2) has an asymptotically orbitally stable periodic solution of period larger than 2 which attracts all orbits corresponding to monotone initial conditions. This periodic solution is simply the piecewise constant negative feedback solution encountered in Sections 2.2.6 and 3.2.

Now let $\theta_1 = 1$ and $\theta_2 = b = \infty$. This corresponds to a positive feedback configuration. If $\gamma < 1$, then the origin is a globally asymptotically stable stationary solution of (4.5.2). But if $\gamma > 1$, then the constant solutions γ and 0 are only locally asymptotically stable. In fact, if the initial condition $\phi(t), t \in [-1,0]$ satisfies $0 \leq \phi(t) < 1$, the solution will be attracted towards the origin. Likewise, if $\phi(t) > 1$, the solution will converge to γ. The threshold θ_1 acts as a repellor.

What happens if the initial condition oscillates about θ_1 ? An der Heiden and Mackey[66] have shown that there exists an unstable periodic solution which separates the domains of attraction of the two constant solutions γ and 0. This solution has exactly one minimum per period. The unstable periodic orbit is at the origin of the more complicated dynamics exhibited by (4.5.2).

REDUCTION OF THE DYNAMICS TO A ONE-DIMENSIONAL MAP

Assume that the feedback is positive. Consider the set I of initial functions ϕ defined as follows (see Figure 4.5.1a,b): $\phi \in I$ if there is some $w \in [0,1]$ such that $\phi(t) > 1$ for all $t \in [-1,-1+w)$, and $\phi(t) < 1$ for all $t \in (-1+w, 0)$ with $\phi(0) = 1$. A map $V : I \rightarrow [0,1]$ is induced by $V(\phi) = w$. It follows that

$$x(t) = \gamma - (\gamma - 1)e^{-\alpha t} \qquad \text{for all} \quad t \in [0, w]\,, \tag{4.5.3}$$

$$x(t) = x(w)e^{-\alpha(t-w)} \qquad \text{for all} \quad t \in [w, 1]\,. \tag{4.5.4}$$

The solution on $[0,1]$ is uniquely determined by w. Hence, the solution for all time depends only on w. Depending on the value of w, it is seen from Figure 4.5.1a,b that $x(1)$ can be either smaller or larger than $\theta_1 = 1$. Figure 4.5.1a illustrates the limiting case $w = w_1$ where the increasing solution starting at $x(1)$ does not reach the threshold; the solution simply decreases towards the locally stable origin. Likewise, Figure 4.5.1b shows the other limiting case $w = w_2$ where $x(1) > 1$, in which the solution increases towards γ.

Between these two limiting cases, i.e. for $w \in [w_1, w_2]$, the dynamics of positive feedback can be analyzed as follows. Let t_1 be the crossing time in the interval $[w,1]$ at which $x(t_1) = 1$. Also, let $t_2 \in [1, 1+t_1]$ be the next crossing time where $x(t_2) = 1$ (in this case the solution is increasing when it crosses). The point of the analysis is to find an interval in which the solution belongs to the same class I of initial functions. This interval can then serve as an initial condition, and the process repeats. It is seen in Figure 4.5.2a that $(t_2 - 1, t_2)$ is such an interval, and this new initial condition is

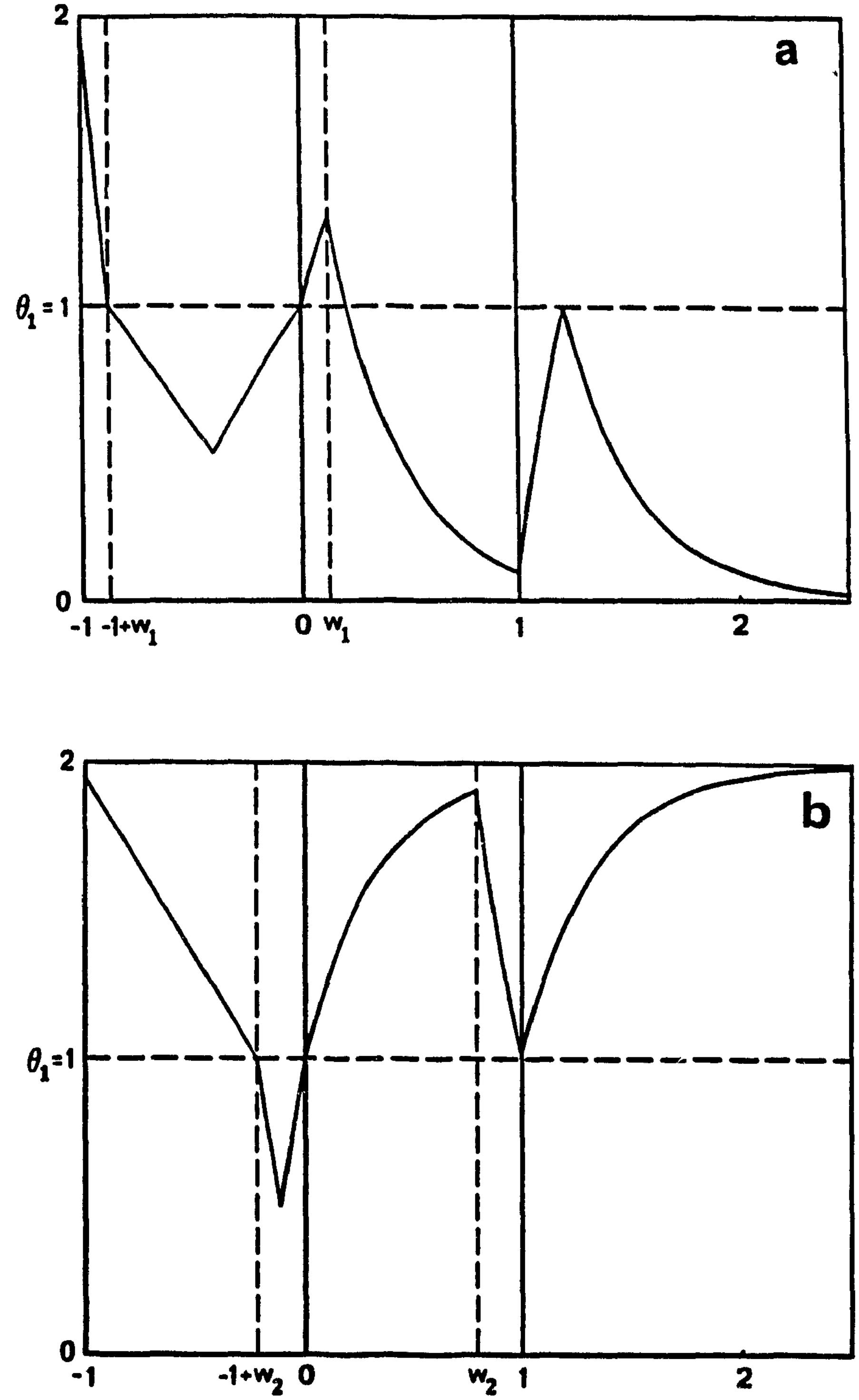

Figure 4.5.1 a) Time solution of (4.5.1) for an initial condition defined by the crossing time $(-1+w_1)$. The solution is repelled from the unstable limit cycle to the origin. b) Time solution of (4.5.1) for an initial condition defined by the crossing time $(-1+w_2)$. The solution is repelled from the unstable limit cycle to the upper locally stable fixed point $\gamma = 2$. The parameters of (4.5.1) are $\alpha = 3$, $\tau = 1$, $\theta_1 = 1$, $\theta_2 = 2.9$, $\gamma = \frac{c}{\alpha} = 2$, $w_1 = 0.123$ and $w_2 = 0.79$.

denoted ψ_w. The crossing time for this initial condition is simply

$$V(\psi_w) = 1 - \left(t_2(w) - t_1(w)\right) . \tag{4.5.5}$$

A continuous map $F : [w_1, w_2] \to [0,1]$ can then be defined by $F(w) = V(\psi_w)$. Denoting by $0 < \tau_1 < \tau_2 < \ldots$ the times at which $x(\tau_i) = 1$, the mapping can be written more generally as

$$\tau_{2i} - \tau_{2i-1} = \tilde{F}(\tau_{2i-2} - \tau_{2i-3}) \tag{4.5.6}$$

By determining the expressions for $t_1(w)$ and $t_2(w)$, an analytical form for $F(w)$ is obtained[66]. $F(w)$ is plotted in Figure 4.5.2b for $w \in [w_1, w_2]$. The slope of $F(w)$ is greater than one on this interval, which implies that the fixed point is unstable.

It is possible to analyze the more complex behavior that arises when the upper threshold b is smaller than the upper asymptotic value γ. The resulting solution is shown in Figure 4.5.2a. The solution oscillates a few times around to lower threshold before drifting upward because of the presence of the unstable periodic orbit centered on θ_1. The solution exits the hump (i.e. increases past b) and subsequently decreases towards the origin. But then the same initial condition repeats, so the cycle repeats. This behavior can again be analyzed in terms of a map $\tilde{F}(w)$. In fact, in the interval (w_1, w_2), the map is simply $F(w)$.

We now see that any aperiodic behavior of F will be reflected in the random occurrence of crossing times. $\tilde{F}(w)$ is plotted in Figure 4.5.2b. While initial conditions corresponding to $w \in [0, w_1]$ still yield solutions that converge to zero, those for which $w \subset [w_2, 1]$ now yield periodic solutions of spiral type as in Figure 4.5.2a. This is due to the nonzero constant portion of $\tilde{F}(w)$ on $(w_2, 1]$ which reinjects the orbit near the unstable fixed point.

The parameter b determines the (constant) value of the map on $(w_2, 1]$. For a certain value of b, the orbit is reinjected into the unstable fixed point w_p. This case corresponds to a homoclinic orbit[10], at which the stable and unstable manifolds of the fixed point intersect. At this homoclinic point the solution oscillates an infinite number of times around the lower threshold, so the period is infinite. At this point we have spiral type chaos.

an der Heiden and Mackey[66] have built more complicated maps from $\tilde{F}(w)$ in order to characterize more complicated motion. Further they have shown that, under certain conditions, the Li and Yorke criteria[133] for chaotic motion in one-dimensional

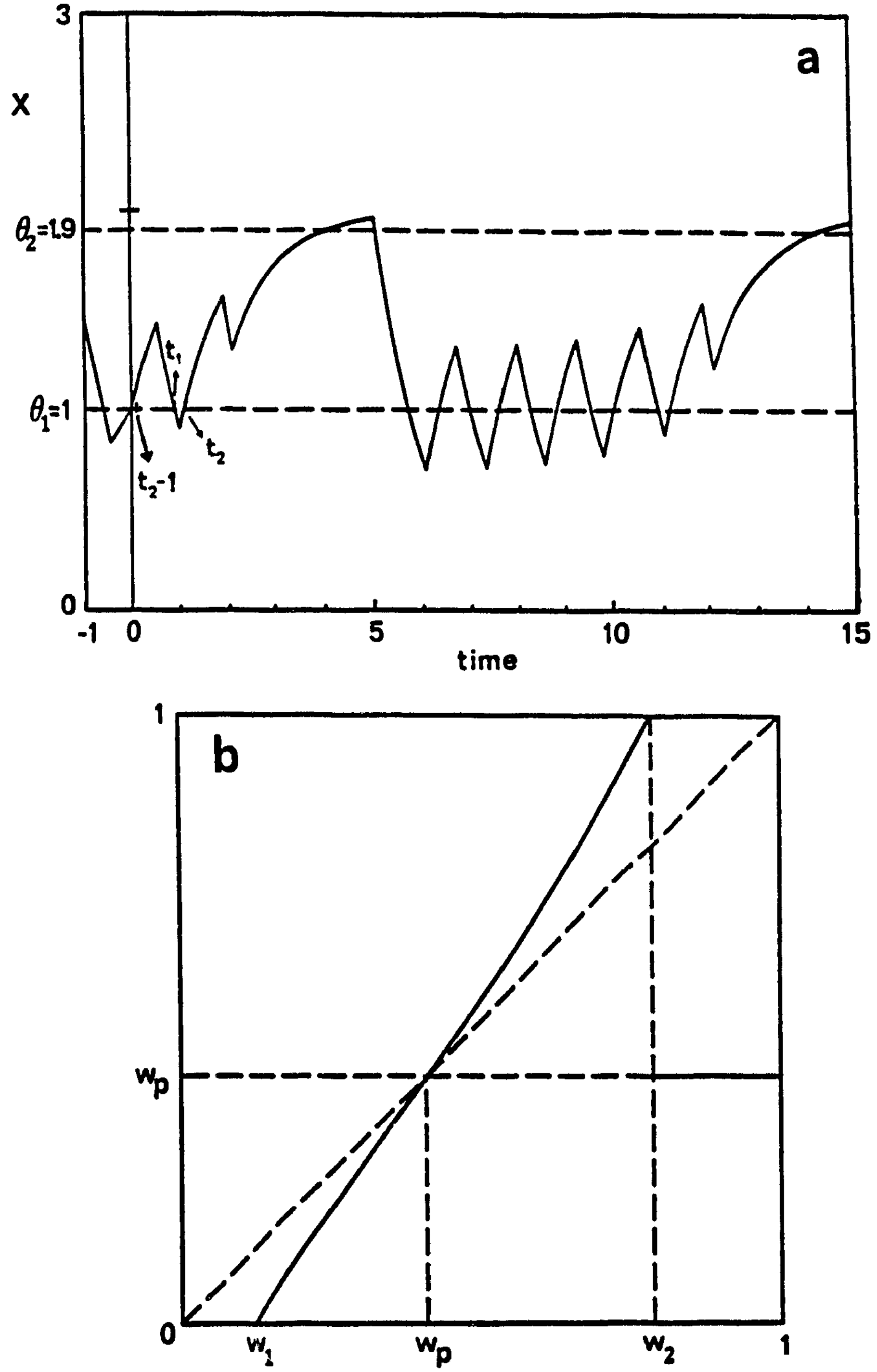

Figure 4.5.2 a) Spiral type solutions to (4.5.1). The solutions oscillates a certain number of times around θ_1, is slowly repelled upwards from the unstable limit cycle about θ_1, increases past θ_2 then decays back towards θ_1 and the cycle repeats. The quantities t_1 and t_2 are defined in the text. This behavior of (4.5.1) occurs for $w \in (w_1, w_2)$ in Figure 4.5.1 and is governed by the map shown in 4.5.2b. For initial conditions $w < w_1$, the solution eventually goes to zero. For $w > w_p$, the spiral type limit cycle solutions are obtained. There is a value of the upper threshold $\theta_2 = b$, at which the constant part to the right of w_2 equals w_p. At this point a homoclinic orbit ensues and the solution has infinite period. Parameter values in a) are $\alpha = 1$, $\gamma = 2$, $\tau = 1$, $\theta_1 = 1$, $\theta_2 = 1.9$ and $w = 0.55$. In b), $\alpha = 3$, $\gamma = 2$, $\theta_1 = 1$, $\theta_2 = 5.8$, $w_1 = 0.124$, $w_2 = 0.735$ and $w_p = 0.406$.

maps are satisfied by one such map. This implies the existence of infinitely many different periodic orbits and of infinitely many aperiodic orbits. However, as an der Heiden[114] pointed out, all of these solutions may turn out to be unstable (the result stated above is about existence, not stability), and all solutions will be eventually attracted to periodic orbits. This implies that the aperiodic solutions will not be observable in physical or computer experiments. This behavior is indeed observed in the numerical integration of (4.5.2) (see Appendix D). However, the transients of the periodic solutions can be very long, even for constant initial conditions.

an der Heiden[114] extended the analysis to show that the behavior of solutions corresponding to a very broad class of initial conditions can be studied from the density point of view. This approach is based on the use of the Frobenius-Perron operator for a map G derived from $\tilde{F}$ in (4.5.6) (see Section 4.2). For certain parameter sets, an der Heiden (1985) has shown that the Frobenius-Perron operator associated with G is asymptotically periodic[13] (see Section 4.2.1). Although it has been shown that a unique invariant measure is associated with G, which implies that G is at least ergodic, the motion is more complicated than ergodic motion because the slope of G is everywhere greater than one (in absolute value), which implies that all orbits are unstable.

Finally an der Heiden[114] has shown that for certain parameters G is asymptotically stable, i.e. it is exact with respect to a measure which is itself absolutely continuous with respect to Lebesgue measure (Section 4.1). This is our working definition of "chaotic motion". This result implies that the map for the differences in successive crossing times τ_i is mixing, and thus the times τ_i occur randomly. But here, as above, the trajectories are unstable and thus not observable numerically. They can be responsible, however, for making transients very long and irregular (see Section 3.4).

It should be noted that the solutions of (4.5.2) obtained on the computer correspond in fact to the exact analytical solutions. Our computer algorithm (see Appendix D) keeps track of all the crossing times using their analytical forms. As a consequence, a solution is considered to be periodic when it goes through the same values with an accuracy of one part in 10^{11} (the Hewlett Packard 9816 computer used for these computations has 12 bit precision).

4.5.3 Other properties of PCMF revealed by simulation.

Many of the dynamical behaviors of (4.5.2) have yet to be explained using one-dimensional maps as in the preceding section. The mixed feedback case comprises all the behaviors of the negative and positive feedback case, and shows a variety of simple and complex limit cycles. The complexity arises becauses of the unstable periodic orbit for positive feedback.

We have found that the solutions of (4.5.2) can undego period doubling sequences as certain parameters are varied (not shown). These sequences are apparently always truncated (i.e. a solution of unrelated period) when only one parameter is varied at a time. Period triplings and period halving have also been observed. A wealth of other dynamical behaviors is expected to occur for more complicated initial functions. Examples of bifurcation diagrams for (4.5.2) were shown in Figures 3.3.5 and 3.3.9. Finally, recall from Section 3.4.3 that (4.5.2) can, for certain parameter sets, exhibit multistability. In fact, for these parameters, the different limit cycle solutions are only locally stable. The structure of the basin boundaries (in function space) of (4.5.2) is not known and is currently being investigated (Losson et al., in prep.).

4.6 SINGULAR PERTURBATION LIMIT: DDE BECOMES A MAP.

In this section, we investigate the conditions under which the dynamics of first order DDE's are similar to those of a one-dimensional map. Such similarities would enable us to analyze the dynamics of DDE's using the powerful mathematical tools that have been developed for maps (see Section 4.2).

The DDE of interest is again (4.3.13)

$$\frac{dx}{dt} = -\alpha\tau x(t) + \tau f\big(x(t-1)\big)\,. \tag{4.3.13}$$

The limit where $\alpha\tau \longrightarrow \infty$ is called the singular perturbation limit. In this limit, the differential term acts as a perturbation on the difference equation that results when this term is not present* :

$$x(t) = \alpha^{-1} f\big(x(t-1)\big) \tag{4.6.1}$$

Denoting $x_n \equiv x(n\tau)$, (4.6.1) can be written as a discrete time map:

$$x_{n+1} = \alpha^{-1} f(x_n) \tag{4.6.2}$$

The dynamical behaviors of this map, such as period-doubling bifurcations and chaotic motion, are also found in the DDE. In fact, the DDE exhibits a much broader range

---

*In the case where $\alpha\tau \longrightarrow \infty$ because $\alpha \longrightarrow \infty$, the ratio $\frac{f}{\alpha}$ must be kept constant in taking the limit.

of dynamical behaviors than the map obtained in the singular limit. In general, there is no continuous transition between the dynamical structures of the map (periodic orbits, their stability properties, bifurcation points) and those of the DDE, no matter how large the parameter $\alpha\tau$ [125].

Examples of invariant densities for this map are shown in Figure 4.6.1. The parameters are the same as those of the Mackey-Glass equation for which the densities are shown in Figure 4.3.1. It is seen that while the density for the DDE is characteristic of a simple limit cycle, which undergoes a period doubling bifurcation between $n = 7.3$ and $n = 7.4$, the density for the map (4.6.2) shows a density with many peaks.

For discrete time systems, the density corresponding to a periodic solution is supported on a set of measure zero containing the points of the periodic orbit. The densities in Figure 4.6.1a,b,d are characteristic of chaotic motion, and the peaks correspond to trajectories of values near the maximum of the map, which are very stable (the orbit of the maximum itself is called the superstable orbit, because the product of the slopes of the map along this trajectory equals zero)[22]. These peaks thus have a different origin than those for the DDE, which correspond to zero-slope regions of the solution. Such regions would correspond to peaks for the map if the map were undergoing periodic rather than chaotic motion Thus, for equal parameter values, the densities for the DDE and the map obtained in the singular limit of this DDE are very different. This difference has been previously noted from the time series point of view by Chow and Green[134].

There is a striking connection between the Hopf bifurcation in a DDE and the first period-doubling (pitchfork) bifurcation in the map obtained in the singular limit of this DDE. Consider the DDE given by (4.3.13) and the corresponding map (4.6.2) obtained in the singular limit. Both these equations have the same fixed point x^* which satisfies $x^* = \alpha^{-1} f(x^*)$. As shown in Sections 2.2.4 and 5.2.1, the complex conjugate pair of roots of the characteristic equation for the DDE (linearized around x^*) lies in the right hand plane if

$$\omega\tau > cos^{-1}\left(-\frac{\alpha}{B}\right) \tag{4.6.3}$$

where $\omega = \sqrt{B^2 - \alpha^2}$ and $B \equiv -f'(x^*) > 0$ (this last restriction is not necessary, but it corresponds to the negative and mixed feedback cases we have been most interested in). Defining $X \equiv -\frac{\alpha}{B} < 0$ (since $\alpha > 0$), (4.6.3) can be written as

$$\alpha\tau > \frac{cos^{-1}(X)}{\sqrt{(1/X)^2 - 1}}. \tag{4.6.4}$$

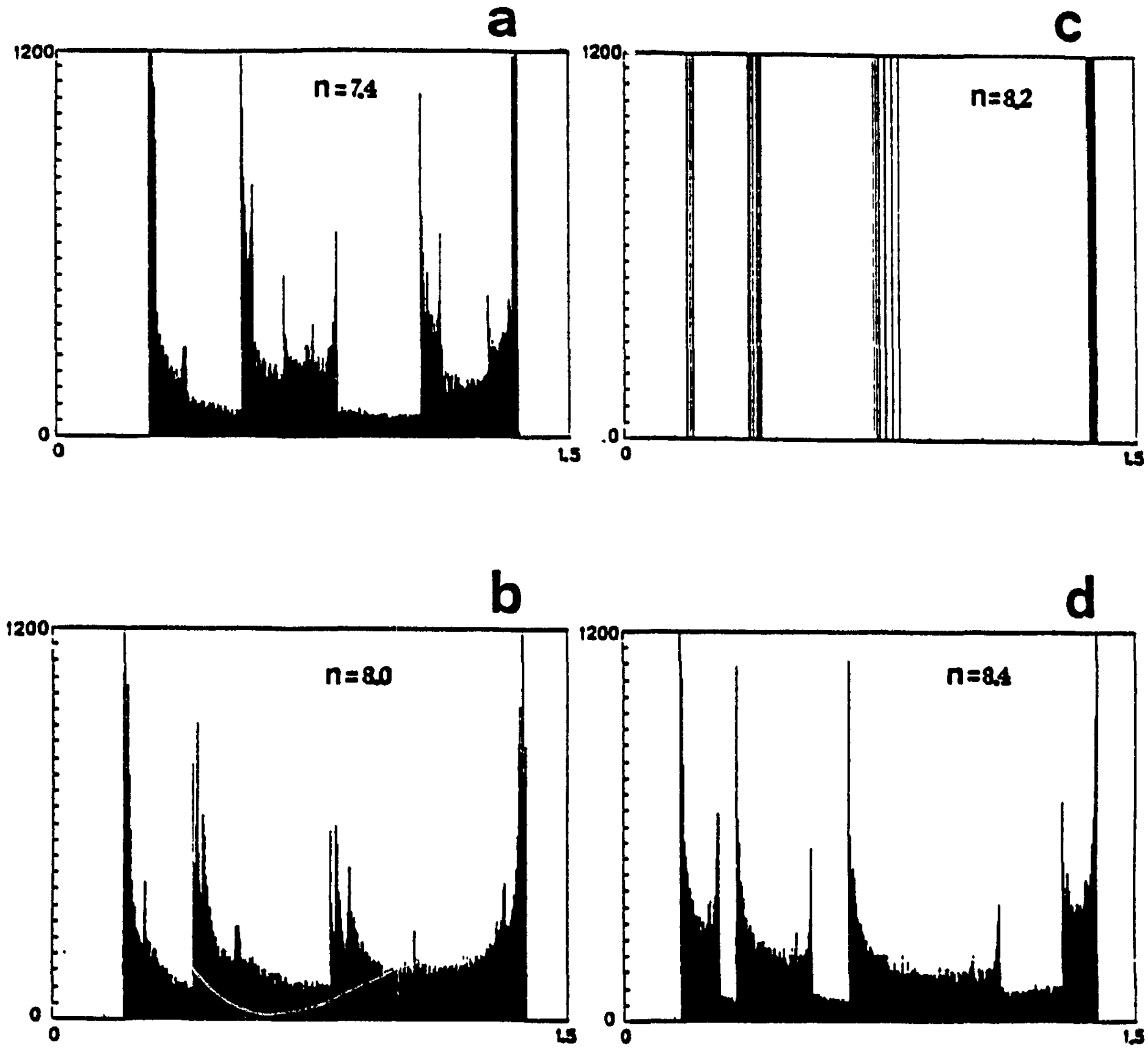

Figure 4.6.1 Densities obtained from numerically generated iterates of the map (4.6.2) obtained in the limit $\alpha\tau \gg 1$ in the Mackey-Glass equation (4.4.14). The densities are computed for values of n similar to the ones used in Figure 4.3.1. The other parameters are the same as in Figure 4.3.1. In c), a periodic solution is seen as n is increased from a value at which the solution is chaotic (b). Chaos again appears as n is increased on going from c) to d). The rounded form of the densities when the map undergoes chaotic motion is similar to that of the densities corresponding to periodic solutions of the Mackey-Glass equation (compare e.g. 4.3.1c and 4.6.1b).

A plot of the stability of the fixed point as a function of $\alpha\tau$ and X is shown in Figure 4.6.2. If $X < -1$ or $X > 1$, the fixed point is stable; these regions are labelled "S". Also, from Section 2.2.4 we know that (4.3.13) has stable limit cycle solutions when inequality (4.6.4) is satisfied. These unstable solutions are found in the regions labelled "U".

The onset of oscillatory motion in the map (4.6.2) occurs at the first pitchfork (or "period-doubling") bifurcation, at which $\alpha^{-1}f'(x^*) = -1$ (corresponding to $\frac{B}{\alpha} = 1$). The fixed point also loses stability when $\alpha^{-1}f'(x^*) = 1$ (or $\frac{B}{\alpha} = -1$), at which a tangent bifurcation occurs. In fact, for $-1 < \frac{B}{\alpha} < 1$, the fixed point of the map is stable. Since $\frac{1}{X} = \frac{B}{\alpha}$, both the map and the DDE have a stable fixed point over the same values of X, i.e for X outside the interval $[-1, 1]$. Thus, the stability diagram for the map simply consists of the x-axis in Figure (4.6.2). The condition $X = -1$ corresponds to the period-doubling bifurcation in the map, while $X = 1$ corresponds to the tangent bifurcation.

When the fixed point is unstable for the map, i.e. for $-1 < X < 1$, the fixed point of the DDE can be either stable or unstable, depending on the value of $\alpha\tau$. The fact that the map is obtained formally by taking the limit $\alpha\tau \longrightarrow \infty$ in the DDE implies that only region "U" is relevant for the map. Hence, when $-1 < X < 1$ for the map, there is always a stable period 2 solution. The stability diagram for the DDE is then seen as a simple prolongation in 2 dimensions (along the $\alpha\tau$ axis) of the one-dimensional diagram for the map.

4.7 THE CONTINUOUS TIME DIFFERENCE EQUATION LIMIT OF THE DDE.

In this section we consider the same singular limit as in the preceding section, but time is taken to be continuous as in the original DDE, rather than discrete (in units of the delay). This limit has also been studied by Zhang et al.[135].

The behavior of the continuous time difference equation (4.6.1) can be understood from Figure 4.7.1, in which numerically computed solutions of this equation are plotted for two different initial conditions. The integration time step equals one two-hundreth of the delay. The value of n is such that the discrete time map (4.6.2) has a period 2 orbit. The behavior of (4.6.1) depends on the initial condition. In Figure 4.7.1a, the initial condition is a constant, and a symmetric square wave of period 2τ ensues. The two values taken by the square wave are the same as those of the period 2 orbit of (4.6.2). In fact, every point on the interval $(-\tau, 0)$ follows the

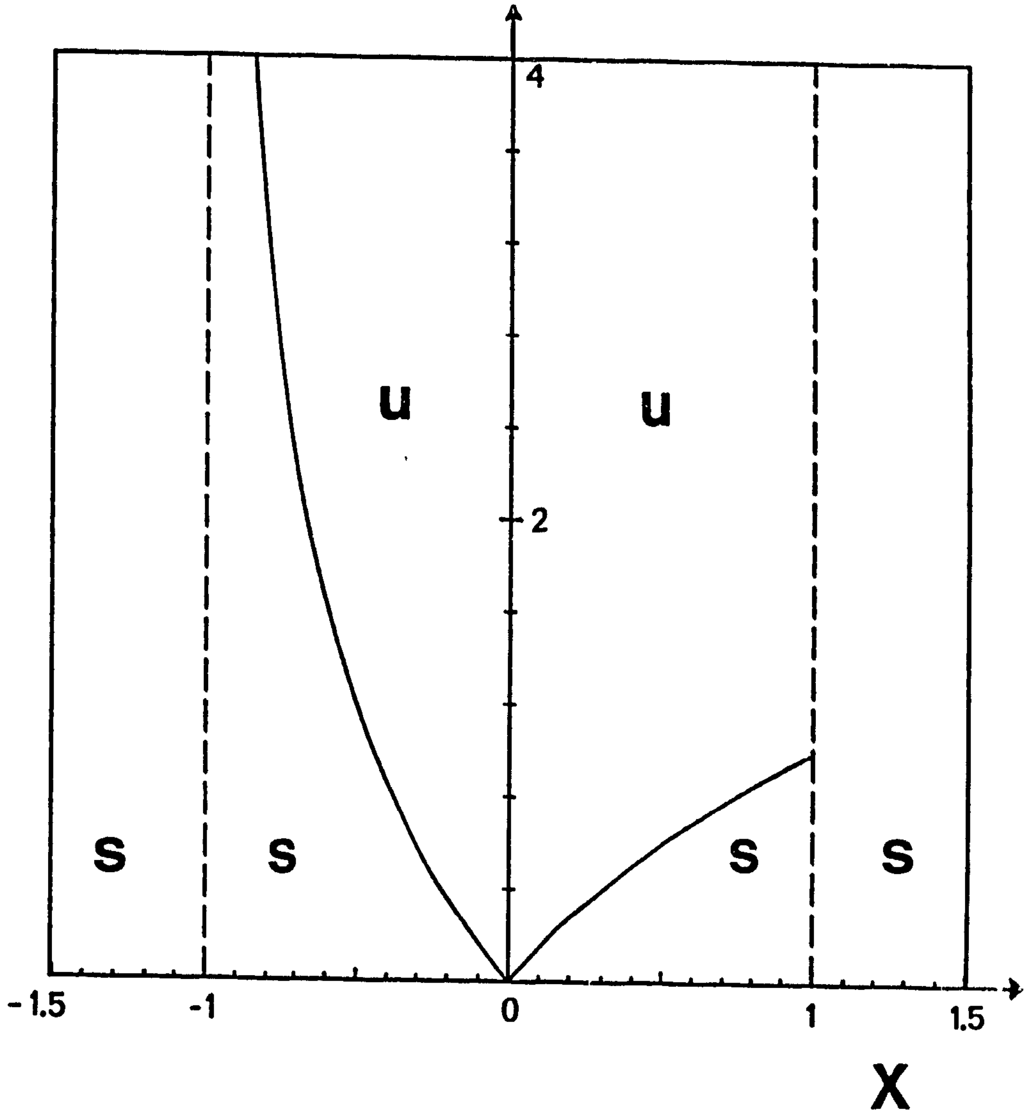

Figure 4.6.2 Stability diagram for Hopf bifurcation in the first order DDE (4.3.11). The largest complex conjugate pair of roots of the characteristic equation of (4.3.11) has negative real part in the regions labeled **S**, and positive real part in those labeled **U**. The abscissa is $x \equiv \frac{-\alpha}{B}$ and is negative for smooth negative or mixed feedback. For $-1 < X < 1$, the stability curve which separates the **U** and **S** regions and corresponding to the right hand side of (4.6.4) is plotted as a function of X For X values in this interval, the singular limit $\alpha\tau \gg 1$ of (4.3.11) implies that inequality (4.6.4) is always satisfied, and hence the system lies in region **U**. In this limit, the stability diagram of the DDE collapses down to the X axis, which is the stability diagram for the map (4.6.2). This map undergoes a period-doubling bifurcation at $X = -1$ and a tangent bifurcation at $X = 1$.

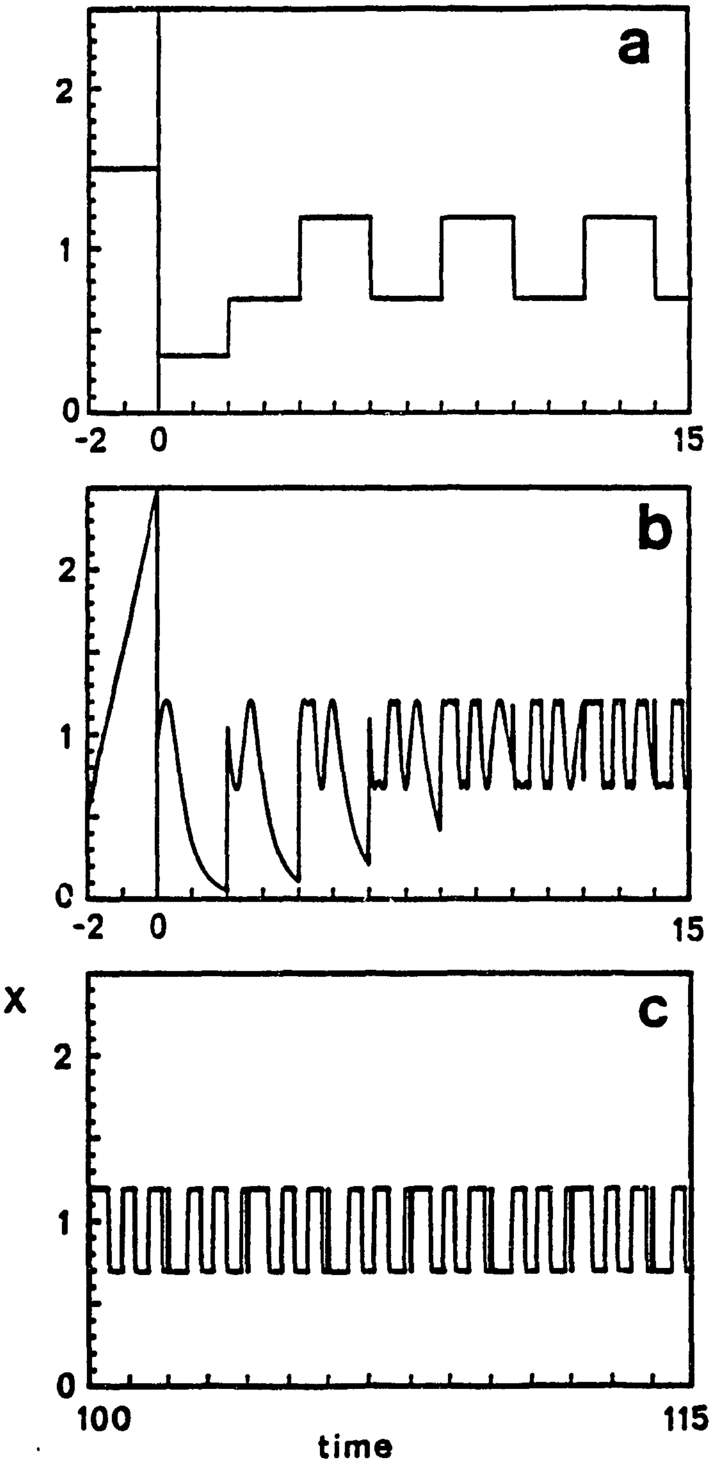

Figure 4.7.1 Time solutions of the continuous time difference equation (4.6.1) for two different initial conditions. The parameter values are $\lambda = 2$, $\theta = 1$, $\alpha = 1$, $\tau = 2$ and $n = 5$, for which the discrete time map has a period 2 orbit. a) Constant initial condition $x = 1.5$; b) linear initial condition. c) stationary solution of b. The integration time step is $\tau/200$.

same trajectory, and the evolution of each point is independent of that of its neighbors.

In Figure 4.7.1b-c, a non-constant monotonic initial condition gives a different asymptotic solution. Comparison with 4 7.1a reveals that, although the period of the oscillation has not changed, the shape has. Different parts of the initial condition are attracted to opposite values of the period 2 orbit, because they behave independently. Notice the spikes which are spaced a time delay apart. In fact they occur at times equal to integer multiples of the delay, and are a consequence of the initial discontinuity at time zero. This discontinuity is due to the fact that the first and last portions of the initial function take on different values. Any discontinuity in the initial function will be preserved with time, because this dynamical system does not smooth them out. Our simulation of (4.6.1) behaves more like an N-dimensional map, where N is the number of points at which the initial function is evaluated to perform the numerical integration. In theory, (4.6.1) is simply an infinite dimensional map in which each variable is independent of the other variables.

The effect of the differential term in the DDE is to make the behavior of a point dependent on its neighborhood (see Section 4.8). The DDE can be seen as an infinite dimensional map in which the variables are coupled. Numerical integration of the DDE using, e g., an Euler algorithm corresponds to the iteration of an N-dimensional map in which the variables are coupled, as pointed out by Farmer[11]. From this point of view, the continuous time difference equation and the DDE simply transform a function on the interval $(n\tau, (n+1)\tau]$ to another function on the interval $((n+1)\tau, (n+2)\tau]$. This behavior is clearly seen in Figure 4 7 1. The fact that neighboring points are coupled by the differential term in the DDE changes the picture drastically. In fact, numerical integration of the original DDE with the same two initial conditions as in Figure 4.7.1 leads to the same asymptotic solution (not shown).

Comparison of Figures 4.3.1 and 4.6.1 shows that the value of n at which the $T \rightarrow 2T$ bifurcation occurs for the discrete or continuous time difference equations is smaller (n_o=4) than the value at which the Hopf bifurcation occurs in the original DDE (n_o=5.04). But how does the period of the oscillatory solution of the DDE compare with that of the continuous time difference equation? For the difference equation, the period is simply $2\tau = 4$, while for the DDE it is $\frac{2\pi}{\sqrt{\beta^2 - \alpha^2}} = 5.49$ (see section 2.2.4). There is a significant difference in the periods.

Better agreement is obtained if the singular limit is taken differently. Rewrite

(4.3.13) as

$$K\frac{dx}{dt} + x(t) = \alpha^{-1} f\big(x(t-1)\big) \tag{4.7.1}$$

where $K \equiv (\alpha\tau)^{-1}$. The left hand side of (4.7.1) can be approximated, if $K \ll 1$ (which is the singular limit we are interested in), by

$$K\frac{dx}{dt} + x(t) \approx e^{[K\frac{d}{dt}]}\, x(t) \tag{4.7.2}$$

Equation (4.7.2) can now be written

$$x(t) \approx \alpha^{-1} e^{-K\frac{d}{dt}} f\big(x(t-1)\big) = \alpha^{-1} f\big(x(t-1-K)\big) \tag{4.7.3}$$

since the exponential operator is a finite time-translation operator. In this case, the period in units of delay is $2(1+K)$, i.e. 6 since $K = 0.5$. This gives closer agreement with the real value of 5.49 . Although it is not clear how to generalize this procedure, nor how to prove that it converges to the right period value, this limit seems to better preserve the time scale of the original DDE.

4.8 NEW NUMERICAL INTEGRATION METHOD FOR DDE's.

The results of the last two sections suggest that the behavior of the first order DDE may be understood as follows Assume that the system evolves in time steps equal to some fraction of the delay (as for the numerical simulation of the continuous time difference equation in Section 4.7). Suppose further that, at every time step t, the system behaves like a map, and therefore generates a value of x at time $(t + \Delta t)$ according to (4.6.2). However, because the system has a nonzero response time, it can not reach this value during the time step Δt. Rather it tends exponentially towards this value from its value at time t. Also, during this time step, the initial condition at time t decays exponentially. Thus we have :

$$x(t+\Delta t) = x(t)\, e^{-\alpha\Delta t} + \frac{f\big(x(t-\tau)\big)}{\alpha}\big(1 - e^{-\alpha\Delta t}\big). \tag{4.8.1}$$

We now have at our disposal a new integration method for DDE's which is, in fact, an integral version of the Euler algorithm. To see this, write (4.3.11) in integral form:

$$x(t) = x(0)\, e^{-\alpha t} + \int_{-\tau}^{t} e^{-\alpha(t-s)} f\big(x(s-\tau)\big)\, ds\,, \tag{4.8.2}$$

so

$$x(t+\Delta t) = x(0)\, e^{-\alpha(t+\Delta t)} + \int_{-\tau}^{t+\Delta t} f\big(x(s-\tau)\big)\, e^{-\alpha(t+\Delta t-s)}\, ds \tag{4.8.3}$$

$$= x(t)\, e^{-\alpha\Delta t} + \int_t^{t+\Delta t} f\big(x(s-\tau)\big)\, e^{-\alpha(t+\Delta t-s)}\, ds\,. \tag{4.8.4}$$

The integral in (4.8.4) can be approximated by

$$x(t+\Delta t) \approx f\big(x(t-\tau)\big)\, e^{-\alpha(t+\Delta t)} \int_t^{t+\Delta t} e^{\alpha s}\, ds \tag{4.8.5}$$

$$= \frac{f\big(x(t-\tau)\big)}{\alpha}\big(1 - e^{-\alpha\Delta t}\big) \tag{4.8.6}$$

so that the integral method becomes:

$$x(t+\Delta t) = x(t)e^{-\alpha\Delta t} + \frac{f\big(x(t-\tau)\big)}{\alpha}\big(1 - e^{-\alpha\Delta t}\big)\,. \tag{4.8.7}$$

Expanding the exponential yields

$$x(t+\Delta t) \cong \frac{f\big(x(t-\tau)\big)}{\alpha}\big(\alpha\Delta t - \frac{\alpha^2\Delta t^2}{2}\big) \tag{4.8.8}$$

This shows that the method is of higher order than the Euler method, to which it reduces if only the first order term in Δt is kept.

We tested this algorithm (4.8.7) around the Hopf bifurcation of the Mackey-Glass equation (4.4.14) which occurs at $n = 4.0818$ for the parameter values $\tau = 10$, $\lambda = 2$, $\alpha = 1$ and $\theta = 1$. This equation was integrated using for 5000 time delays starting from a constant initial function. The density was then constructed from the solution for the next 500 delays by dividing the interval $(0.5, 1.5)$ into 500 bins. An integration time step of $\tau/200$ was used. The distance between the two peaks of the density corresponds to the limit cycle amplitude. The position of these peaks is plotted versus the bifurcation parameter n in Figure 4.8.1. We have also plotted the peak positions obtained with an Euler method and a fourth order Runge-Kutta method. Notice that the interval of n values used corresponds to the immediate vicinity of the Hopf bifurcation. In fact, for $n > 4.15$ (not shown), the three methods yield similar results for this integration time step. Below this value of n, the three curves become distinct.

Figure 4.8.1 shows that the Euler method predicts a nonzero limit cycle amplitude even though the theoretical value of this amplitude is zero. In fact all three methods exhibit this problem to some extent, because of the extremely long transients in the vicinity of the bifurcation point (see Section 5.1). However, Figure 4.8.1 shows that the Runge-Kutta method converges more rapidly than the other methods

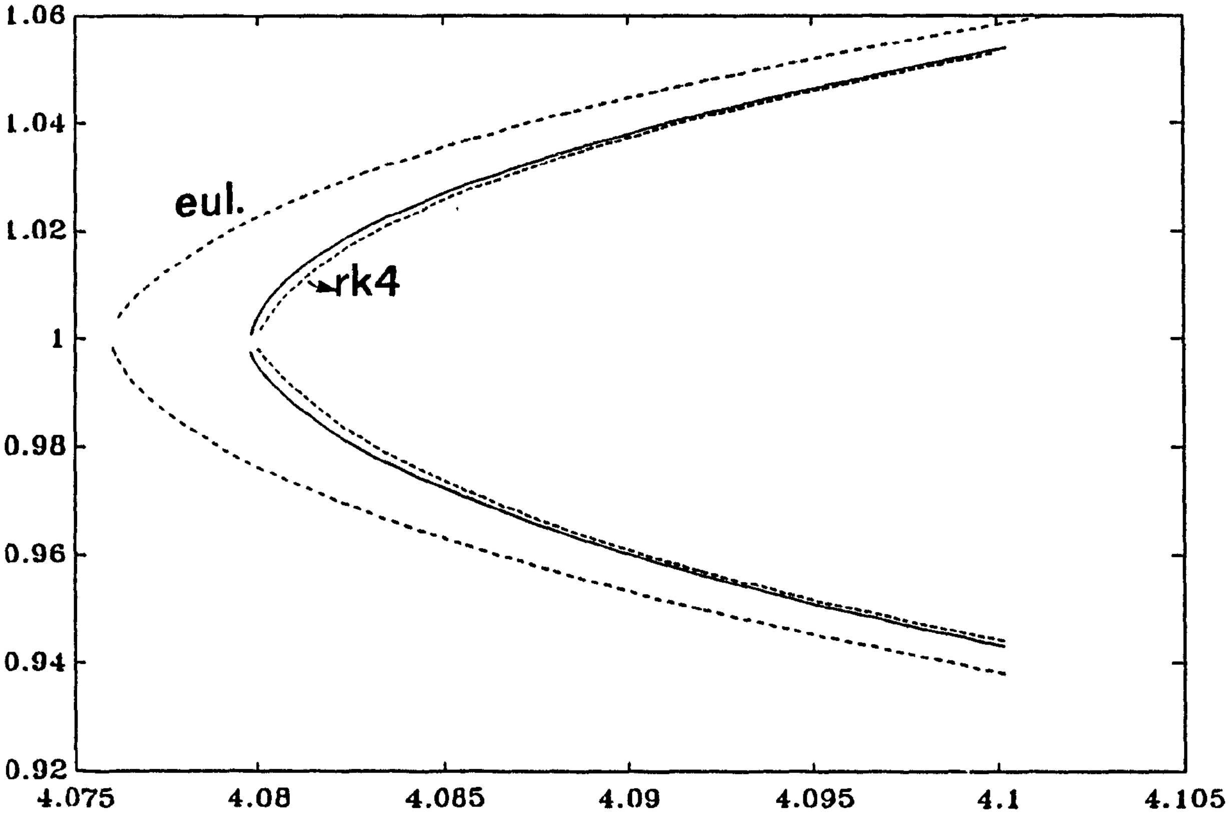

Figure 4.8.1 Comparison of the performance of the numerical integration algorithm described in Section 4.8 (solid line) with standard Euler and fourth order Runge-Kutta algorithms. Limit cycle amplitude is plotted as a function of n at the Hopf bifurcation occurring at $n = 4.0818$ in the Mackey-Glass equation (4.4.14). The parameter values are $\tau = 10$, $\lambda = 2$, $\alpha = 1$ and $\theta = 1$ and the integration time step is $\tau/200$. The new method and the fourth order Runge-Kutta algorithm are in close agreement, and the new method is four times faster than the Runge-Kutta method. Each method yields a nonzero amplitude even when the theoretical value is zero, due to the lengthening of the transients as the bifurcation point is approached.

to the theoretical value for the limit cycle amplitude. Notice also that the accuracy of this new method (4.8.7) is quite close to that of the Runge-Kutta method. Further, its accuracy is superior to that of the Euler method. All three methods give similar values for the period of the limit cycle, which is known (see Section 2.3.7) to vary only slightly around the Hopf bifurcation.

However, the real difference is speed: the new algorithm is as fast as the Euler algorithm, which is four times faster than the Runge-Kutta algorithm. To our knowledge, the integral method (4.8.7) presented here has never been proposed for the numerical integration of DDE's. Further investigation is warranted, since the new method is almost as accurate as the fourth order Runge-Kutta algorithm and much faster. A precise assessment of its overall accuracy and speed is still needed, as we have only tested it against other methods for the specific problem of the Hopf bifurcation. The method may also prove advantageous for the numerical integration of stochastic DDE's, since the simplicity of the algorithm should make the evaluation of, e.g., correlation functions easier than for other higher order methods (such as Runge-Kutta) when white or colored noise is present (see Section 5.2). In fact a similar Euler integral method has been recently proposed by Fox et al.[136], which allows the use of a larger time step for the integration of colored noise processes (see Section 5.2).

CHAPTER 5
CRITICAL BEHAVIOR OF DELAYED FEEDBACK SYSTEMS AT OSCILLATION ONSET

...How noiseless falls the foot of time...
W.R. Spencer

This chapter investigates the solution properties of deterministic and stochastic delay-differential equations (DDE's) at the onset of oscillatory behavior. These properties are used to explain results of experiments in which oscillations are induced in the pupil light reflex using smooth (SNF) and piecewise constant (PCNF) negative feedback.

This last chapter is motivated by the question of the origin of noise in the pupil light reflex, as well as by the more general question of whether or not it is possible to quantitatively analyze a bifurcation in a neural system in quantitative terms. Special attention is given to the relationship between these two kinds of feedback, because although SNF is closer to the normal feedback occurring in the pupil light reflex, PCNF is much easier to implement experimentally and has been shown (Section 3.2) to provide insight into the properties of this reflex. The transition from SNF to PCNF is also a mathematically well-defined problem (Section 2.2.6). The results of this chapter show that the mean and variance of the oscillation amplitude and period behave differently as the bifurcation point is approached in SNF and PCNF.

The onset of oscillation in the SNF case occurs through a Hopf bifurcation (Sections 2.2.4 and 2.3.6). Although extensive reference has been made to the Hopf bifurcation, the full Hopf bifurcation theorem has not been given. A detailed description of this bifurcation in ordinary differential equations (ODE's) is given in Section 5.1.1 and for DDE's in Section 5.1.2. Further, Appendix A consists of a paper, published in the *Journal of Statistical Physics* (in press, 1989), which looks at the effect of additive and multiplicative noise on the Hopf bifurcation in a simple ODE. It is an application of Fokker-Planck analysis (Section 4.2) to the study of the influence of noise on a bifurcation.

In Section 5.2.1, an introduction to "noise-induced transitions", which belong to the more general class of nonequilibrium phase-transitions, is given. The theoretical treatment of these transitions in terms of stochastic differential equations (SDE's) is discussed. Following this, the concepts of white noise (Section 5.2.2) and colored noise

(Section 5.2.3) are presented. Finally, a numerical algorithm to integrate a DDE with additive and multiplicative noise is described in Section 5.2.4.

Section 5.3 comprises the manuscript of a paper to be submitted to *Physical Review A*. The critical behavior of the pupil light reflex at oscillation onset is measured experimentally and the results are explained theoretically and by numerical simulation of a stochastic DDE.

Section 5.4 examines ways to understand the postponement of the Hopf bifurcation in a DDE by both additive and multiplicative noise, a phenomena discovered in the analysis of Section 5.3.

5.1 DETERMINISTIC HOPF BIFURCATION IN ODE's AND DDE's.

In this chapter we consider the effect of additive and multiplicative noise on the Hopf bifurcation exhibited by a simple first order delay- differential equation with smooth negative feedback,

$$\frac{dA}{dt} = -\alpha A(t) + \frac{c\theta^n}{\theta^n + A^n(t-\tau)} + k\,, \tag{5.1.1}$$

as the parameter n is varied. We chose to study this DDE rather than the Mackey-Glass equation[24] with mixed feedback because it is of direct interest to the experimental study of oscillation onset in the pupil light reflex studied in Section 5.3. Further, we have found no qualitative difference between the critical behavior at oscillation onset of a first order DDE with mixed feedback and one with negative feedback. Locally, the Hopf bifurcation is the same in both cases. However, after the first bifurcation obtained by increasing either the slope of the feedback function at the fixed point or the delay, a sequence of period doubling bifurcations will occur in the mixed feedback case[24], while no further bifurcations are seen in the negative feedback case (Section 2.3.8).

We chose the parameters to be $\tau = 0.3$, $c = 200$, $\alpha = 3.21$, $k = 20$ and $\theta = 50$ because they produce realistic simulated pupil area values. With these parameters, a supercritical Hopf bifurcation occurs at $n = 8.18$. We have already studied (5.1.1) with these parameters in Section 2.3. In this section, the deterministic Hopf bifurcation is examined in more detail than in Sections 2.2 and 2.3.

5.1.1. Hopf Bifurcation in a deterministic ODE.

We start with the Hopf bifurcation for ordinary differential equations (ODE's)[137] following Guckenheimer and Holmes[10], and for delay-differential equations (DDE's) following Stech[78]. We state the following results for completeness, and to show why the amplitude and frequency calculations are rarely carried out unless there is a good reason to do it analytically rather than numerically.

We have already given a flavor of the Hopf bifurcation analysis in sections 2.2.4 and 2.3.6. The Poincaré - Bendixon theorem[10] requires that a system of ODE's be of dimension 2 or greater for autonomous oscillations to occur. For simplicity, we consider the Hopf bifurcation in the following two-dimensional system of ODE's

$$\frac{d\vec{x}}{dt} = f(\vec{x}, \mu) \tag{5.1.2}$$

having an equilibrium point $x^*(\mu_0)$ at the parameter value μ_0, at which the Jacobian of the flow, Df, has a simple pair of pure imaginary eigenvalues, $(\lambda(\mu_0), \bar{\lambda}(\mu_0)) = (+i\omega, -i\omega)$, $\omega > 0$ and no other eigenvalues with zero real part.

The implicit function theorem guarantees that for each μ near μ_0 there is an equilibrium $x^*(\mu)$ near $x^*(\mu_0)$ which varies smoothly with μ. However, there is a change in the dimension of the stable and unstable manifolds[*] of $x^*(\mu)$ at μ_0, leading to a qualitative change in the flow near $x^*(\mu_0)$.

Consider the following system of linear ODE's

$$\begin{aligned} \dot{x} &= \mu x - \omega y \\ \dot{y} &= \omega x + \mu y \end{aligned} \tag{5.1.3}$$

whose solution, corresponding to the initial condition (x_0, y_0), is

$$\begin{pmatrix} x(t) \\ y(t) \end{pmatrix} = e^{\mu t} \begin{pmatrix} \cos \omega t & -\sin \omega t \\ \sin \omega t & \cos \omega t \end{pmatrix} \begin{pmatrix} x_0 \\ y_0 \end{pmatrix} . \tag{5.1.4}$$

When $\mu < 0$, solutions spiral into the origin, and when $\mu > 0$ they spiral away from the origin. All solutions are periodic when $\mu = 0$. The normal form theorem (Guckenheimer and Holmes[10], Section 3.3) shows how the generic nonlinear problem (5.1.2) differs from system (5.1.3). Smooth coordinate changes on (5.1.2) result in the following form for the third order Taylor expansion of f:

$$\begin{aligned} \dot{x} &= (d\mu + a(x^2 + y^2))x - (\omega + c\mu + b(x^2 + y^2))y \\ \dot{y} &= (\omega + c\mu + b(x^2 + y^2))x + (d\mu + a(x^2 + y^2))y \, , \end{aligned} \tag{5.1.5}$$

---

[*] The stable (unstable) manifold is the set of phase space points which converge to the attractor (here, the fixed point) in the limit $t \to \infty$ ($t \to -\infty$). The stable (unstable) manifold is spanned by the eigenvectors of Df at $x^*(\mu_0)$ whose real part is negative (positive). The manifold spanned by the eigenvectors corresponding to the purely imaginary eigenvalues is called the center manifold.

which becomes

$$\begin{aligned} \dot{r} &= (d\mu + ar^2)r + O(r^5) \\ \dot{\theta} &= (\omega + c\mu + br^2) + O(r^4)\,. \end{aligned} \tag{5.1.6}$$

in polar coordinates. Notice the radial equation is uncoupled from the phase equation. The stationary solutions of the radial equation are the origin as well as solutions that lie along the parabola

$$\mu = -\frac{a}{d}r^2 = -\frac{a}{d}(x^2 + y^2)\,, \tag{5.1.7}$$

provided a and d are nonzero. This parabola is embedded in the product space $R^2 \times R$, where R^2 refers to the {x,y} plane and R corresponds to the bifurcation parameter μ. In the words of Guckenheimer and Holmes[10] (p.151), "...this implies that the surface of periodic orbits has a quadratic tangency with its tangent plane $\mu = 0$ in $R^2 \times R$. The content of the Hopf bifurcation theorem[137] is that the qualitative properties of (5.1.5) near the origin remain unchanged if higher-order terms are added to the system." This means (ibid, p.152) that "...there is a surface of periodic solutions in the center manifold which has quadratic tangency with the eigenspace of $\lambda(\mu_0)$, $\lambda(\mu_0)$ agreeing to second order with the paraboloid $\mu = -(a/d)(x^2 + y^2)$. If $a < 0$, then these periodic solutions are stable limit cycles, while if $a > 0$, the periodic solutions are repelling."

The parameters in (5.1.5) have been chosen so that the bifurcation occurs at $\mu_0 = 0$. From the radial equation we see that the fate of the periodic solution at the bifurcation is determined by the sign of a, which is the coefficient of the first nonlinear term. If the two-dimensional nonlinear flow is obtained by adding the transpose of the vector $(f(x,y), g(x,y))$ to (5.1.3) with $f(0) = g(0) = 0$ and $Df(0) = Dg(0) = 0$, then it can be shown that :

$$a = \frac{1}{16}[f_{xxx} + f_{xyy} + g_{xxy} + g_{yyy}] + \frac{1}{16\omega}[f_{xy}(f_{xx} + f_{yy}) - g_{xy}(g_{xx} + g_{yy}) - f_{xx}g_{xx} + f_{yy}g_{yy}] \tag{5.1.8}$$

The condition $d \equiv \frac{d}{d\mu}(Re\,\lambda(\mu))\Big|_{\mu=\mu_0} \neq 0$ is the transversality condition encountered in Section 2.2.4, which prevents the tangential intersection of the imaginary axis by the complex conjugate pair of eigenvalues.

5.1.2 Hopf bifurcation in a deterministic DDE.

The Hopf bifurcation theorem for DDE's is basically the same as for ODE's, except that its proof requires more sophisticated techniques from the theory of functional differential equations (see Hale[122], Section 11). Further it has been shown that the delay itself can serve as the bifurcation parameter[79]. We will concentrate on the first order DDE encountered in the previous chapters:

$$\dot{x} = f(x(t), x(t-\tau)). \tag{5.1.9}$$

Linearization of (5.1.9) about its fixed point x^*, defined by $\dot{x} = 0$, or $f(x^*, x^*) = 0$, yields the characteristic equation

$$\lambda + A + Be^{-\lambda\tau} = 0. \tag{5.1.10}$$

Defining $s \equiv \frac{\lambda}{B}$, $Q \equiv \frac{A}{B}$ and $T = B\tau$, we have the equivalent equation

$$s + Q + e^{-sT} = 0. \tag{5.1.11}$$

Then $Re(s) < 0$ if[76]

$$\begin{aligned} &1) \quad |Q| > 1 \text{ or} \\ &2) \quad |Q| \leq 1 \text{ and } T < T_{crit} \end{aligned} \tag{5.1.12}$$

where

$$T_{crit} = B\tau_{crit} = \frac{cos^{-1}(-Q)}{(1-Q^2)^{1/2}} \tag{5.1.13}$$

and the inverse cosine takes its value in $[\frac{\pi}{2}, \pi]$. When $|Q| \leq 1$ and $T = T_{crit}$, there exists a periodic solution of period

$$P = \frac{2\pi}{B(1-Q^2)^{1/2}}. \tag{5.1.14}$$

A supercritical Hopf bifurcation occurs when $T = T_{crit}$, leading to a stable periodic orbit (i.e. a limit cycle), when certain nondegeneracy conditions are satisfied by the nonlinear terms in (5.1.9). A quite involved computation (see Stech[78] ; Bélair and Mackey[138]) leads to the following conditions for the supercritical Hopf bifurcation. If $Q < 1$ and the parameters $\{A, B, \tau\}$ are such that $T > T_{crit}$, there exists an orbitally asymptotically stable periodic solution $x(t)$ to (5.1.9) satisfying $\|x(t) - x^*\| < \varepsilon$, for all $\varepsilon > 0$ and sufficiently large t, provided that :

$$Re\left\{ \frac{[3h_3(\phi,\phi,\bar{\phi}) + 2h_2(\bar{\phi}, a_2 e^{2\imath\omega}) + 2h_2(\phi, a_0)]}{[1 - Te^{-i\omega T}]} \right\} < 0, \tag{5.1.15}$$

where

$$\phi(s) = e^{2i\omega}\,,\ a_2 = h_2(\phi,\phi)/\left(2i\omega + Q + e^{-2i\omega T}\right),$$

$$a_0 = 2h_2(\phi,\bar{\phi})/\left(Q+1\right),$$

$$h_2(\phi,\zeta) = C\phi(0)\zeta(0) + D\phi(-T)\zeta(-T) + \frac{E}{2}\left[\phi(0)\zeta(-T) + \phi(-T)\zeta(0)\right], \quad (5.1.16)$$

$$\begin{aligned} h_3(\phi,\zeta,\eta) = {} & F\phi(0)\zeta(0)\eta(0) + G\phi(-T)\zeta(-T)\eta(-T) \\ & + \frac{H}{3}\left[\phi(0)\zeta(-T)\eta(-T) + \phi(-T)\zeta(0)\eta(-T) + \phi(-T)\zeta(-T)\eta(0)\right] \end{aligned}$$

and the Taylor expansion about x^* is given, to third order, by

$$\begin{aligned} f[x(t), x(t-\tau)] = {} & A(x-x^*) + B(x_\tau - x^*) \\ & + C(x-x^*)^2 + D(x_\tau - x^*) + E(x-x^*)(x_\tau - x^*) \\ & + F(x-x^*)^3 + G(x_\tau - x^*)^3 + H(x-x^*)(x_\tau - x^*)^2 . \end{aligned} \quad (5.1.17)$$

In practice this calculation is difficult, and one often verifies numerically whether the bifurcation is supercritical or subcritical.

Finally, the exponential relaxation time γ of transients onto the limit cycle near the Hopf bifurcation in DDE's is given by

$$t_r \propto (\mu - \mu_0)^{-1}\,, \quad (5.1.18)$$

as shown by Sirkus[79] using Floquet theory. This predicted divergence of the relaxation time $t_r \to \infty$ as $\mu \to \mu_0$, known as "critical slowing down" at a Hopf bifurcation in a DDE, has been verified in laser experiments by Gao et al.[139]. The critical exponent t_r is the same as for the supercritical Hopf bifurcation in ODE's and for second order phase transitions in general[21]. The critical slowing down for second order phase transitions does not depend on the direction from which the bifurcation point is approached. This means that the relaxation time onto the fixed point which looses stability at the Hopf bifurcation is given by $t_r \propto (\mu_0 - \mu)^{-1}$. This symmetry does not hold for a subcritical Hopf bifurcation, which is analogous to a first order phase transition.

5.2 STOCHASTIC DIFFERENTIAL EQUATIONS AND NOISE-INDUCED TRANSITIONS.

5.2.1 Generalities.

There is a natural inclination to view noise as a disorganizing influence in nature. In the past few decades, however, the discovery of three new classes of phenomena has forced us to reappraise the importance of randomness in macroscopic physical systems[21].

The first class comprises the mechanisms of "self-organization" which occur in strongly dissipative systems. Dissipative systems are characterized by the property that their evolution contracts phase space volume. A set of points may thus evolve towards an attractor whose dimension is less than that of the total phase space. Strongly dissipative systems are those in which the contribution of the nonlinear terms to the evolution are large (for example, the coefficients of these terms are large). The evolution of weakly dissipative systems is easily predictable as they possess a unique stable attractor, known as the thermodynamic branch, which is in the vicinity of the stable state of thermodynamic equilibrium Far from equilibrium, these systems can undergo complex sequences of bifurcations to more complicated attractors, which may no longer be globally stable. The influence of noise now becomes crucial since it may determine which basins of attraction, or "dissipative structures" (Nicolis and Prigogine[140]), the system will visit in the course of its evolution.

The second class refers to chaotic systems, i.e. systems that are intrinsically noisy despite the fact that they are deterministic. Because of their sensitivity to initial conditions, which is a deterministic property, the evolution of chaotic systems will be further complicated by noise.

The third class refers to nonequilibrium systems which are coupled to a fluctuating environment. There is again a natural tendency to believe, in the words of Horsthemke and Lefever[21] (p.5) that "... i) rapid noise is averaged out and thus a macroscopic system essentially adjusts its state to the average environmental conditions; ii) there will be a spreading or smearing out of the system's state around that average state due to the stochastic variability of the surroundings." However, "... an increase in environmental variability can lead to a structuring of nonlinear systems which has no deterministic analog." This structuring displays features similar to those of equilibrium phase transitions, and also to those seen in nonequilibrium systems of the first class mentioned above. In the same way that the latter have come to be known as "nonequilibrium phase transitions", the phenomena described in this third class have been labelled "noise-induced transitions".

Biological systems are examples of dissipative systems that self-organize in noisy environments. Noise-induced transitions have been shown[21] to occur in models of the immune response, photosynthesis, population biology, population genetics and neuron membrane voltage (Hogdkin-Huxley equations) It is important, as these studies have shown, to properly characterize the origin and properties of the noise, as different kinds of noise can lead to different types of transitions as parameters are varied.

It is also important to distinguish between internal and external noise in physical systems. The noise known as "internal fluctuations" derives from the many degrees of freedom involved in the microscopic interactions in the system. Because of these fluctuations , stationary states of the system are not constant and must be described in probabilistic terms. Further, near stable macroscopic states, fluctuations of intensive variables scale as V^{-1}, where V is the volume of the system, and near a critical point they scale as $V^{-1/2}$ Hence in the thermodynamic limit $V \to \infty$ these fluctuations become negligible. This is the main reason why internal fluctuations can be safely neglected in the theoretical description of macroscopic systems.

The main focus of our attention in this chapter is external noise. In general, the intensity of external noise does not depend on the size of the system as is the case for internal fluctuations. Rather the effect of an external noise of a given intensity depends on the state of the system; it is also called, for this reason, multiplicative noise. External noise can profoundly affect the local stability properties of a macroscopic system For example, the position of bifurcation points can be shifted. This is the weakest type of noise-induced transition, because it shifts the parameter values at which occur behaviors that exist in the deterministic case. Noise can also cause behaviors unforeseen in the deterministic case to suddenly appear as a parameter is varied. These phenomena are known as pure noise-induced transitions.

In contrast to external multiplicative noise, the effect of additive noise on a system does not depend on the state of this system. Additive noise can arise, for example, as a result of phenomena evolving on a scale smaller than the one where the phenomena being modeled by the dynamical equations occur It does not affect the value of parameters; it is simply superimposed on the dynamics. In this sense additive noise is different from the internal fluctuations discussed earlier. It is also different from observational noise, which occurs e.g. in the measuring process, and which is added to the solution rather than the dynamical equations of motion. For example, the stochastic activity of a neuron in the absence of any input can be viewed as the result of additive noise. A characteristic of additive noise is that it is more readily observable when the system is quiescent, i.e. when the time derivative of the state variable is small. Mathematically, this is a consequence of the balance between the deterministic flow term and the stochastic term in a generalized Langevin equation with additive noise (see Equation (4.2.25) with $\sigma(\vec{x}) = \sigma = constant$).

The bifurcation diagrams of one-dimensional systems are not modified by additive noise (see Appendix A). However, additive noise can drastically modify the deterministic behavior of higher dimensional systems, as discussed in Section 5.3. In the next sections, the problem of modelling additive and multiplicative noise is addressed.

The macroscopic systems we are interested in can be modelled by ordinary or delay-differential equations; there are no spatial derivatives. It is known[21] that the local stability properties of such spatially homogeneous systems are not modified by the presence of internal fluctuations[*]. This means that the extrema of the probability densities, which correspond to the macroscopic states of the system (or "order parameters"), are in the vicinity of the stationary solutions of the deterministic system (they coincide with these solutions in the thermodynamic limit).

5.2.2 White noise and colored noise.

The three main properties that characterize a given noise are 1) its intensity; 2) the probability density of its distribution; and 3) its correlation time.

Internal or external noise is typically made up of contributions from many independent sources. Hence, it is generally assumed that the central limit theorem holds and that the noise values are distributed according to a Gaussian probability density. Throughout this chapter we will only consider Gaussian noise.

The correlation time t_{cor} of a stationary stochastic process X_t is defined by

$$t_{cor} = \frac{1}{C(0)} \int_0^{\infty} C(\tau)\, d\tau \,, \tag{5.2.1}$$

where $C(\tau)$ is the autocorrelation function of the noise process. The rate at which $C(\tau)$ goes to zero as $\tau \to \infty$ is a measure of the memory time of the stochastic

---

[*] The question of whether DDE's are spatially homogeneous is certainly debatable, in view of the fact that under certain conditions they are equivalent to partial differential equations. The results of this chapter are, to our knowledge, first steps towards the study of nonequilibrium phase transitions in DDE's.

process. A process for which $C(\tau)$ decays rapidly is said to have short memory, because values of the noise separated by more than one correlation time are almost uncorrelated. This is reflected in (5.2.1) by the fact that the area beneath $C(\tau)$ is small for short-correlated noise. Noise with a small t_{cor} is also said to fluctuate rapidly. In general, whether a noise qualifies as rapid or slow depends on the ratio $\frac{t_{cor}}{t_{sys}}$, where t_{sy}, is the characteristic relaxation time of the system. For example, noise with a correlation time of 1 millisecond will be considered fast for a system whose characteristic relaxation time to a limit cycle is on the order of 1 second.

Noise with a finite t_{cor} is called colored noise. When $t_{cor} \ll t_{sys}$, it is natural to consider the limit $t_{cor} \rightarrow 0$. In this case the autocorrelation function $C(\tau)$ is a Dirac delta function, and the noise is said to be δ-correlated. The stochastic process ξ_t obtained in this limit is called a "white-noise" process because, as will be shown below, the power spectrum for this process (given by the Fourier transform of $C(\tau)$) is constant, as for white light. White noise is a generalized stochastic process, in the same sense that the delta function is a generalized function. Since a constant power spectrum implies infinite total power, white noise is not physically realistic. Further, it is difficult to see how a memoryless noise such as Gaussian white noise, taking on a different value at every instant of time, can have any effect on a system. However, this becomes more plausible upon realizing that the variance of this stochastic process is infinite (see below). In fact, white noise describes real noise rather well when $t_{cor} \ll t_{sys}$, and further facilitates the mathematical description of the noisy system (see Section 5.2.3).

It is easier to understand white noise by considering its relation to colored noise and a Wiener process[21] W_t. Wiener processes have been proposed as models of the perpetual irregular motion of small particles suspended in a fluid known as Brownian motion. They are Gaussian processes with stationary independent increments. This latter property means that the probability density of the increment $(W_t - W_s)$ depends only on the time difference $(t - s)$, and is thus invariant with respect to time shifts. This implies that the successive values of W_t are independent[21]; however, it does not imply that a Wiener process is stationary. In fact, although it has zero mean, its variance increases linearly with time.

The sample paths of a Wiener process are continuous, but irregular. In fact, the velocity is undefined and the sample paths are nowhere differentiable. Wiener processes approximate the behavior of a Brownian particle very well, and their simple features compensate for the curious properties which arise because they are mathematical idealizations. Further, it can be shown that there is a one to one relation between white noise processes and processes with stationary independent increments such as Wiener processes. This relation is simply the time derivative, and we will write

$$\xi_t = \frac{dW_t}{dt}\,. \tag{5.2.2}$$

It is possible to obtain differentiable sample paths by considering that the state variable of the Wiener process is velocity rather than position. The resulting process is called the Ornstein-Uhlenbeck process[21], and is denoted by ζ_t. It satisfies the stochastic differential equation

$$\frac{d\zeta_t}{dt} = -\gamma\zeta_t + \xi_t\,, \tag{5.2.3}$$

where ξ_t is a white noise process as in (5.2.2). It can be shown[21] that the Ornstein-Uhlenbeck process is stationary. Its autocorrelation function decreases exponentially:

$$C(t,s) = E\{X_t X_s\} = \frac{\sigma^2}{2\gamma} e^{-\gamma|t-s|}\,, \tag{5.2.4}$$

where σ^2 is the intensity of the white noise process defined by the mathematical expectation $E\{\xi_t\xi_s\} = \sigma^2\delta(t-s)$. However, successive increments are now correlated, and the sample paths are differentiable. From (5.2.1) and (5.2.4), it follows that the correlation time of the O-U process is simply $t_{cor} = \gamma^{-1}$.

The limit $\gamma \to \infty$ of the O-U process does not correspond to the white noise process, as can be seen by looking at the power spectrum of the Ornstein-Uhlenbeck process :

$$\begin{aligned} S(\nu) &= \frac{1}{2\pi}\int_{-\infty}^{\infty} C(\tau)\,d\tau \\ &= \frac{\sigma^2}{2\pi}(\nu^2+\gamma^2)^{-1}\,. \end{aligned} \tag{5.2.5}$$

The white noise limit yields

$$\lim_{\gamma\to\infty} S(\nu) = 0\,, \tag{5.2.6}$$

for all frequencies ν. This is called the noiseless limit. The proper white noise limit involves increasing the strength of the fluctuations as γ is increased, keeping the ratio

$\frac{\sigma^2}{\gamma^2} = \bar{\sigma}^2$ constant rather than variance. In fact this is the limit in which the integrated Ornstein-Uhlenbeck process converges to the Wiener process[21] and the flat spectrum

$$S(\nu) = \frac{\bar{\sigma}^2}{2\pi} \tag{5.2.7}$$

characteristic of white noise is recovered. Finally, the Ornstein-Uhlenbeck process ζ_t is distributed with a Gaussian density which is independent of the value of the correlation time :

$$g(\zeta) = \frac{1}{(2\pi\bar{\sigma}^2)^{1/2}}\, e^{-\frac{\zeta^2}{2\bar{\sigma}^2}} \,. \tag{5.2.8}$$

This means that (5.2.8) is also the density of the white noise process obtained in the limit of the Ornstein-Uhlenbeck process.

5.2.3 Modelling the effect of noise.

Once the noise characteristics have been specified, one is faced with the problem of coupling this noise to the deterministic dynamics of the system. Let $\tilde{X}_t$ and $\hat{X}_t$ denote the (one-dimensional) stochastic state variables under the influence of, respectively, colored noise (given by the Ornstein-Uhlenbeck process (O-U)) and white noise. Assume these variables satisfy the stochastic differential equations

$$d\tilde{X}_t = B(\tilde{X}_t)\,dt + Z(\tilde{X}_t)\zeta_t\,dt \qquad (O - U) \tag{5.2.9}$$

$$d\hat{X}_t = B(\hat{X}_t)\,dt + Z(\hat{X}_t)\xi_t\,dt \qquad (white) \tag{5.2.10}$$

known as generalized Langevin equations (see Equation (4.2.25)). Their integral form is

$$\tilde{X}_t = \tilde{X}_0 + \int_{t_0}^{t} B(\tilde{X}_s)\,ds + \int_{t_0}^{t} C(\tilde{X}_s)\zeta_s\,ds \qquad (O - U) \tag{5.2.11}$$

and

$$\hat{X}_t = \hat{X}_0 + \int_{t_0}^{t} B(\hat{X}_s)\,ds + \int_{t_0}^{t} C(\hat{X}_s)\xi_s\,ds\,. \qquad (white) \tag{5.2.12}$$

respectively. Because the Ornstein-Uhlenbeck process has continuous realizations (i.e. continuous sample paths), both integrals on the right hand side of (5.2.11) can be interpreted as ordinary Riemann integrals. The first integral on the right hand side of (5.2.12) can also be interpreted as a Riemann integral. However, the sample paths of the white noise process are nowhere differentiable, and the second integral in (5.2.12) must be interpreted according to the stochastic calculus of either Ito or Stratonovich[21] (see also Appendix A). Although $\hat{X}_t$ has continuous realizations, these are, as for the Wiener process, nowhere differentiable. On the other hand, since integration has a smoothing effect, the realizations of $\tilde{X}_t$ are differentiable.

We have seen that for Gaussian white noise, a description in terms of a stochastic state variable can be replaced by another in terms of a probability density whose deterministic evolution is governed by the Fokker-Planck equation (4.2.26). However, for nonlinear equations, it is generally impossible to analytically solve this equation, even for its stationary solution, and one is obliged to resort to approximation techniques (see e.g. Risken[141]).

A system subjected to colored noise case can be modelled as a pair process $(\tilde{X}_t, \zeta_t)$ given by (5.2.9) and (5.2.3). Since (5.2.3) involves Gaussian white noise, it is straightforward to write the corresponding two-dimensional Fokker-Planck equation for this system of SDE's (even though in this interpretation (5.2.9) is, strictly speaking, an ODE coupled to a SDE). Again, it is in general impossible to obtain an analytical expression for the stationary solution of this Fokker-Planck equation[21]. Approximations are available for the cases of very short-correlated noise and very long-correlated noise. For short-correlated noise, it is possible, after appropriate scaling, to expand the stationary density in powers of t_{cor}. This is also known as an expansion in the inverse bandwidth of the noise, since this noise bandwidth is inversely proportional to t_{cor}.

A system subjected to long-correlated noise is able to "equilibrate" to the fluctuations of the noise. It is as if the spectrum of the noise were simply a Dirac delta function at the origin, i.e. the noise behaves like a constant. Thus the state variable $\tilde{X}_t$ can be adiabatically eliminated, i.e. $\dfrac{d\tilde{X}_t}{dt}$ can be considered to be zero. An approximation similar to this so-called "switching curve approximation"[21] will be used in Section 5.3.

5.2.4 Numerical integration algorithm for a stochastic DDE.

Although various approximation techniques are available to solve Fokker-Planck equations, it is often desirable to obtain a numerical solution to the full problem. The numerical solution of the Fokker-Planck partial differential equation in more than one dimension is in general a formidable problem. Another alternative is to numerically integrate the stochastic differential equation itself, which is the method we use.

As mentioned in Section 5.1, we are interested in the behavior of the delay-differential equation (5.1.1) with additive and multiplicative colored noise at a Hopf bifurcation. We are not aware of any theoretical results concerning the numerical integration of a stochastic DDE. Hence we must procede with caution in developing a numerical algorithm for its integration.

Since noise-induced shifts in the bifurcation point are anticipated (Appendix A), it is important to use a method that converges rapidly and accurately to the limit cycle in the absence of noise, especially in the vicinity of the bifurcation point where transients are extremely long. We have shown in Section 4.8 that the fourth order Runge-Kutta algorithm is accurate near the Hopf bifurcation for an integration time step equal to $\tau/200$. In fact, the accuracy is satisfactory even for a time step of $\tau/100$. Although the new method presented in Section 4.8 is, for a given time step, almost as accurate as the Runge-Kutta algorithm and four times faster, we have opted for the Runge-Kutta method, since the new method has not been sufficiently analyzed. Furthermore, for the fourth order Runge-Kutta method, there are analytical results concerning convergence for stochastic simulations. In fact, for additive white noise problems, there are algorithms that are well tested for accuracy[142,143]. There are also straightforward extensions for the additive colored noise case[144,141].

More recently, numerical integration algorithms for problems involving multiplicative colored noise have been tested (see e.g. Fox and Roy[145]). These authors suggest using a coupled equation algorithm in which the ODE (e.g. Equation 5.1.1) for the state variable is integrated using a standard algorithm (such as a Runge-Kutta method), while the O-U process (5.2.3) is integrated using the Box-Muller algorithm for white noise (see below). They also suggest that the white noise limit be studied using this algorithm with short-correlated noise.

In Section 5.3, the case where the parameters c and k in

$$\frac{dA}{dt} = -\alpha A(t) + \frac{c\theta^n}{\theta^n + A^n(t-\tau)} + k\,, \tag{5.1.1}$$

fluctuate under the action of separate Ornstein-Uhlenbeck processes will be of interest. Fluctuations in c around a mean value $\bar{c}$,

$$c = \bar{c} + \zeta_t\,, \tag{5.2.13}$$

correspond to multiplicative noise. However, fluctuations in k,

$$k = \bar{k} + \zeta_t\,, \tag{5.2.14}$$

correspond to additive noise because the intensity of this noise does not depend on the state variable A (pupil area). Equation (5.1.1) together with (5.2.3), (5.2.13) and (5.2.14) defines the pair process $(A(t), \zeta_t)$ to be integrated using the coupled equation algorithm. We describe first the Box-Muller algorithm (see Knuth[146]).

The statistical features of Gaussian white noise ξ_t are completely determined by the requirements

$$\begin{aligned} \langle \xi_t \rangle &= 0 \\ \langle \xi_t \xi_s \rangle &= \sigma^2 \delta(t-s) . \end{aligned} \tag{5.2.15}$$

At each integration time step, the Box-Muller algorithm generates a number N distributed with a Gaussian density of zero mean and unit variance using two numbers v1 and v2 from a uniform distribution on [0,1]. For our simulations, the uniformly distributed random numbers were generated using the routine RAN1 (also due to Knuth[146]) from Numerical Recipes[147]. A Gaussian number ξ of zero mean and standard deviation σ is then given by

$$\xi = \sigma \sqrt{-2ln(v1)}\, cos(2\pi v2) . \tag{5.2.16}$$

In this section we use a slightly different scaling for the O-U process to conform with Fox et al.[136] and Sancho et al.[144]. It consists in dividing the standard deviation σ of the noise by the correlation time t_{cor} so that (5.2.3) becomes

$$\frac{d\zeta_t}{dt} = -\gamma\zeta_t + \gamma\xi_t . \tag{5.2.17}$$

The autocorrelation function (5.2.4) is then given by

$$C(t,s) = \frac{\sigma^2}{2t_{cor}} e^{-\gamma|t-s|} . \tag{5.2.18}$$

The white noise limit now corresponds to the limit $t_{cor} \to 0$ and the intensity of the resulting white noise is σ^2; however, the strength of the random term is $\dfrac{\sigma^2}{2t_{cor}}$ by (5.2.18).

The standard way (see e.g. Sancho et al.[144]) to integrate the O-U process (5.2.17) is to use an Euler differential algorithm:

$$\zeta(t+\Delta t) = \zeta(t) - \gamma\zeta(t)(\Delta t) + \gamma\xi\sqrt{\Delta t} . \tag{5.2.19}$$

Notice that the stochastic term is multiplied by the square root of the integration time step. This is a feature of the stochastic calculus used to give a meaning to the second integral on the right hand side of (5.2.12)[21].

In the coupled algorithm, the size of the time step is limited by the Euler integration of the O-U process. In order to take advantage of the larger step sizes that higher order techniques (such as Runge-Kutta) allow, a more efficient algorithm for the O-U process should be used. Such an algorithm has been recently proposed by Fox et al.[136]. It uses an integral Euler algorithm, which is very similar to the new algorithm for DDE's presented in Section 4.8 :

$$\begin{aligned}\zeta(t+\Delta t) &= e^{-\gamma(\Delta t)}\zeta(t) + \gamma\int_t^{t+\Delta t} e^{-\gamma(t+\Delta t-s)}\sigma\xi(s)\,ds \\ &= e^{-\gamma(\Delta t)}\zeta(t) + h(t,\Delta t)\,. \end{aligned} \tag{5.2.20}$$

Since a linear operator transforms a Gaussian process into a Gaussian process, $h(t,\Delta t)$ is also Gaussian distributed with zero mean. Therefore, all its properties are determined by its second moment

$$\langle h^2(t,\Delta t)\rangle = \frac{\sigma^2\gamma}{2}(1-e^{-2\gamma(\Delta t)})\,. \tag{5.2.21}$$

The algorithm is thus given by (5.2.20) with the same Box-Muller algorithm, except that σ in (5.2.16) is replaced by the square root of (5.2.21). This algorithm, combined with a fourth order Runge-kutta method, was used to integrate the stochastic DDE. A time step of $\tau/100$ was found to be satisfactory.

5.3 NOISE AND CRITICAL BEHAVIOR OF THE PUPIL LIGHT REFLEX AT OSCILLATION ONSET.

Abstract. We have induced oscillations in the human pupil light reflex using two different kinds of external electronic feedback: smooth negative feedback (SNF) and piecewise constant negative feedback (PCNF). The behaviour of the mean amplitude and period at oscillation onset are shown to be in good agreement with a model of this neural system incorporating the external feedback. The critical behaviour displayed through amplitude and period fluctuations is different in each case. The observation that amplitude fluctuations are larger (smaller) than period fluctuations for SNF (PCNF) is explained theoretically and by numerical integration of a stochastic delay-differential equation with additive and multiplicative colored noise. We find that both types of noise postpone the Hopf bifurcation in SNF by an amount proportional to the noise intensity and inversely proportional to the correlation time. The implications for analyzing bifurcations in neural systems are discussed.

5.3.1 Introduction.

Oscillations occur in a wide variety of neuro-physiological control systems under normal and pathological conditions[20,24,25,54]. Experimental and theoretical investigation of the properties of these oscillations from the point of view of nonlinear dynamics has been hindered by: 1) the scarcity of suitable systems in which parameters can be manipulated; and 2) the presence of high amplitude noise. Thus it has been difficult to untangle the deterministic and stochastic processes which shape the observed dynamics.

As a paradigm for neurological control systems, the human pupil light reflex exhibits oscillatory phenomena of varying complexity[32,99]. For example, regular oscillations in pupil area occur when the gain of the feedback loop is sufficiently high[67] and aperiodic oscillations in pupil area occur spontaneously (a phenomenon known as "hippus"[46,88]). There have been studies[47,74] of the behaviour of hippus as a function of light level and of its interaction with pupil oscillations produced by sinusoidally varying light stimuli. These have concluded that many properties of hippus can be explained by assuming that it represents multiplicative gaussian white noise injected into the reflex at the level of the brainstem nuclei. However, the precise origin and nature of hippus is still not known, and new experimental paradigms, such as the one presented in this paper, are needed to deepen our understanding of its properties.

One advantage of studying the pupil light reflex is that it can be easily and non-invasively monitored. A second advantage is the ease with which the feedback loop can be opened[31] (i.e. the effect of the output on the input can be removed). This has led to extensive studies (see Stark[32] for a review) of the linear and nonlinear properties of the reflex components and of the noise under open loop conditions. Finally, closed loop oscillations can be studied using an experimental setup in which the normal feedback is replaced by controllable external electronic feedback[1]. This "clamping" method produces a hybrid system in which autonomous oscillations and bifurcations can be produced and studied as a function of the control parameters[1,62,64,65,89].

Recently, it has been shown[84,99] that autonomous oscillations in the normal pupil light reflex can be modelled using the nonlinear delay-differential equation (DDE)

$$\frac{dg}{dA}\frac{dA(t)}{dt} + \alpha g\big[A(t)\big] = F\big[\bar{\phi}, \phi(t-\tau)\big] . \tag{5.3.1}$$

Here $A(t)$ is the pupil area, $g(A)$ is a monotonically decreasing nonlinear function relating iris muscle activity to pupil area, τ is the total time delay in the system, α is related to the rate constant for pupillary movements, ϕ is the retinal light flux (equal to the product of light intensity and pupil area) and $\bar{\phi}$ is the light flux below which no response occurs. The model also takes into account the logarithmic compression of light intensities in the transduction process at the retina. For the intact pupil light reflex with negative feedback,

$$F\big[\bar{\phi}, \phi(t-\tau)\big] = \gamma \ \ln\left[\frac{\phi(t-\tau)}{\bar{\phi}}\right] , \tag{5.3.2}$$

where γ is a physiological parameter related to the transduction of light intensity into neural firing frequency in the optic nerve and the midbrain.

In this paper we study the noisy behaviour of the period and the amplitude of oscillations induced in the human pupil light reflex by replacing the function F with two kinds of external feedback: 1) piecewise constant negative feedback (PCNF: Figure 5.3.1a); and 2) smooth (i.e. differentiable) negative feedback (SNF: Figure 5.3.1b). Equations (5.3.1) and (5.3.2) contain many parameters which are difficult to estimate exprimentally. A simpler model for SNF oscillations which displays the same qualitative behavior as (5.3.1) with F given by (5.3.2) is obtained[99] by replacing F with a Hill type function (Figure 5.3.1b) and by making $g(A)$ a linear function of A:

$$\frac{dA(t)}{dt} + \alpha A(t) = \frac{c\theta^n}{\theta^n + A^n(t-\tau)} + k . \tag{5.3.3}$$

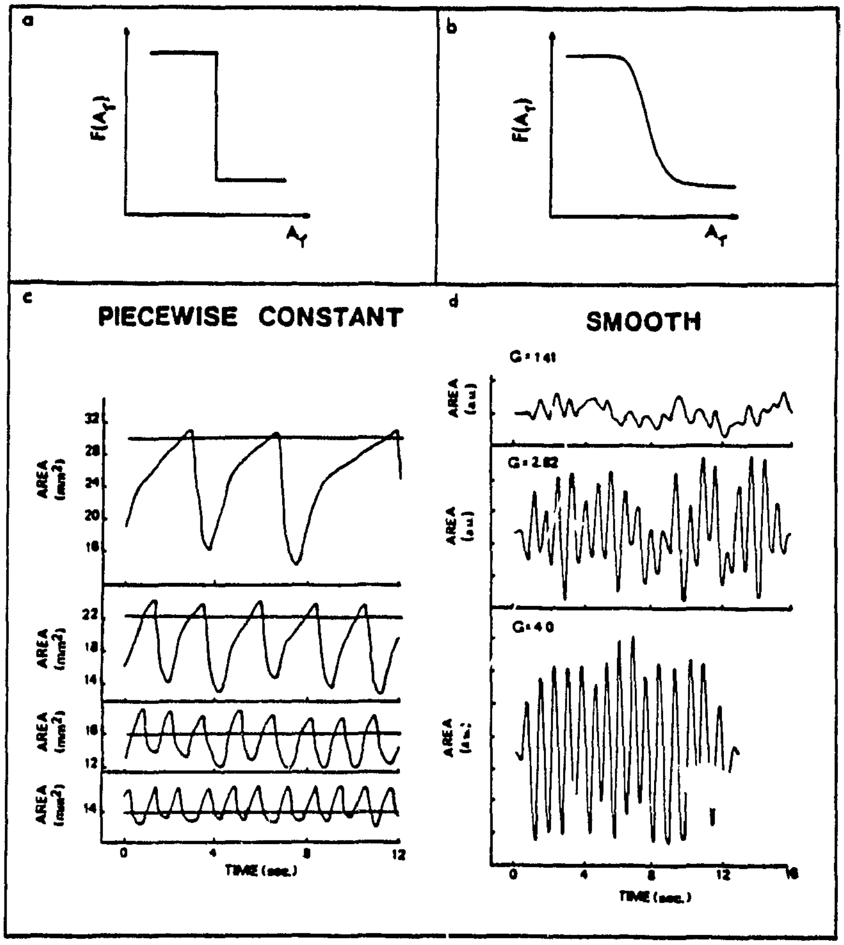

Figure 5.3.1 Pupil area oscillations induced using external piecewise constant negative feedback (PCNF, a) and smooth negative feedback (SNF, b). The PCNF oscillations in (c), measured using an infrared videopupillometer, were obtained for the following area threshold values (dotted line): $30.1 mm^2$ (upper panel), $22.5 mm^2$, $16.2 mm^2$ and $14.0 mm^2$. Note that the time scale differs between the records. The SNF oscillations in (d) are obtained for increasing values of the feedback gain (proportional to the slope in (a)). Oscillation onset occurs at $G \simeq 1$. The SNF oscillations were measured using a reflectance technique which does not allow calibration in absolute units of area. Correcting for baseline drift in SNF by linear trend subtraction produced 12-15 second long data sets. The PCNF oscillations did not exhibit baseline drift.

This equation has been used as a paradigm for delayed smooth negative feedback systems[24,25] (more complicated oscillations and chaos arise when the Hill's function is non-monotonic, i.e. in the presence of "mixed feedback": see Ref. 24). Equation (5.3.3) exhibits a supercritical Hopf bifurcation as the parameter n or τ is increased past a certain value. In the PCNF case, we linearize $g(A)$ and take F to be piecewise constant so that (5.3.1) is replaced by the piecewise linear DDE[61,99]

$$\alpha^{-1}\frac{dA}{dt} + A(t) = \begin{cases} A_{off} & A(t-\tau) < \theta \\ A_{on} & A(t-\tau) > \theta \end{cases} \tag{5.3.4}$$

where A_{off} and A_{on} are constants. The oscillatory solutions to (5.3.4) have been shown to be in good agreement with experimental data[20,62,64,89]. Besides being important clinically, PCNF allows certain nonlinearities of the reflex to be isolated for study[62,89,99].

Specifically we examine the onset of oscillation with SNF and PCNF and look at how the period and amplitude vary as a function of gain (SNF) and threshold (PCNF). As the Hopf bifurcation is approached, critical slowing down occurs, i.e. the decay time of perturbations increases which leads to noise amplification. We find that the critical behaviour at oscillation onset, manifested in period and amplitude fluctuations, is interesting and different in each case. We show that theoretical and numerical analysis of simple stochastic DDE's can explain this behaviour. We are not aware of any previous studies of the interaction of noise with autonomous oscillations in either the pupil light reflex or any other neural reflex. Thus, our study provides insight into the origins of noise in neural systems, as well as the effect of noise on solutions of DDE's. These results are of interest since physiological systems are inherently noisy and the transition from equilibrium to dynamic behavior is frequently encountered[20,24,25,54].

The experimental method is described in Section 5.3.2. In Section 5.3.3 we present the experimental results for both the SNF and PCNF case. Section 5.3.4 is devoted to a theoretical and numerical analysis of the deterministic and stochastic behaviors of amplitude and period for both cases. The transition from SNF to PCNF is the subject of Section 5.3.5. The paper concludes with a discussion in Section 5.3.6.

5.3.2 Experimental methods.

5.3.2.1 Background.

The pupil light reflex is a negative feedback neurological control system which keeps the light flux falling on the retina (ϕ in (5.3.1)) within a certain range. An increase in retinal light flux due to an increase in light intensity is compensated by a decrease in flux due to pupil constriction, and *vice versa.* This constriction results from the increase in neural activity to the iris sphincter muscle, which is proportional to the logarithm of the light flux. During pupil cycling, dilation is thought to be primarily due to passive relaxation of the sphincter muscle and to inhibition of the neural activity to this muscle[99]. This describes "closed-loop" operation under normal smooth negative feedback conditions.

The feedback loop can be opened using illumination in Maxwellian view[31], i.e. by focussing a narrow beam of light down the center of the pupil. The diameter of this beam is so small that the iris can never shade the retina from the beam. Under these conditions, the pupil response has no influence on retinal light flux.

The idea behind "clamping" the pupil light reflex is to electronically control the intensity of a light source (in Maxwellian view) using an analog signal proportional to pupil area (provided by a pupillometer). For example, one can choose to synthesize the naturally occurring negative feedback characteristic. This involves clamping the pupil light reflex using a linear amplifier with controllable positive gain to convert area variations into light intensity variations[1,65]. The retinal flux variations are then given by the product of this varying light intensity and the fixed beam area

When the electronic feedback mimics a negative gain linear amplifier, the pupil exhibits limit cycle oscillations, which is possible only if nonlinearities in the reflex constrain the amplitude of the oscillation. In the SNF case[99], the effective feedback in the whole circuit can be modelled by a sigmoidal curve (Figure 5.3.1b). In other words, the linear amplifier contributes to the steep slope in Figure 5.3.1b, while pupil nonlinearities are responsible for the saturation at high and low area values. In the PCNF case the effective feedback is as shown in Figure 5.3.1a. While the oscillations obtained in the SNF case are often difficult to control due to drifts in mean pupil area[1,65], by comparison those obtained in the PCNF case are more stable[62,64,80]

An infrared videopupillography technique[64] was used for the PCNF study while a reflectance technique[65] was used for the SNF study, as a result of the collaboration between the authors. While each method has its advantages, they are both efficient recording techniques with high enough sampling rate and accuracy for the proper assessment of the phenomena presented here. Hence our results are not a consequence of the different pupil area measuring techniques for SNF and PCNF.

5.3.2.2 Piecewise constant negative feedback.

The experimental method has been described previously[64]. The 1.2mm diameter light beam used for open-loop illumination was provided by a 605nm peak wavelength LED. The retinal illumination provided by the light beam was fixed at a value of 750 trolands. Subjects were dark adapted for at least 15 minutes in a room lit by a dim red light; this was the background illumination for the experiment. The analog output of an infrared binocular videopupillometer (Hamamatsu Iriscorder Model C-2515, sampling rate 60 Hz), which is proportional to pupil area, was electronically compared to an adjustable area threshold, θ. Through this area comparator (Figure 5.3.1a), the state of the system, i.e. pupil area $A(t)$, controls the timing and duration of the light pulses. The light is turned on whenever $A > \theta$. The linearity of area measurement is better than 1% from 0 to 150 mm^2 with an accuracy of 0.01 mm^2. Pupil responses to light changes are not instantaneous. They follow a neural delay of $\approx 300msec$ (approximately the same for light onset and offset[89]) plus a 100 $msec$ delay due to electronic processing. In all experiments the pupil being measured was also the one being stimulated.

5.3.2.3 Smooth negative feedback.

The IRIS pupillometer used for the SNF experiments is based on an infrared reflectance technique which has been described previously[65]. It yields a relative measure of pupil size which is linearly related to pupil area. Infrared emitters and detectors are mounted in units attached to a head band and are positioned approximately 3cm in front of both eyes. The light stimulus for SNF was provided by a small yellow (583 nm peak wavelength) LED which illuminates the retina in Maxwellian view by means of two lenses. The retina is centrally illuminated with a circular field approximately 30 degrees wide. In between the two lenses, a fixation target is mounted. In order to prevent the visible light of the stimulus LED from adding to the signal from the infrared detectors, the stimulus LED current and the infrared detection are pulsed out of phase at 4000 Hz. The retinal illuminance was typically adjusted to between 500 and 1000 trolands.

The SNF was synthesized using a linear amplifier relating the analog pupil area signal to the stimulus LED current. No significant delay was introduced by the external feedback. The offset and the gain of the amplifier were adjusted by the experimenter. Signals representing pupil area together with a calibrated signal related to stimulus intensity were recorded digitally at a sampling rate of 50 Hz. Because of very slow noisy fluctuations in the pupillary system, the mean light intensity can not control the mean pupil area, which leads to baseline drift. Correcting for baseline drift by linear trend subtraction produced 12-15 second long data sets. The pupil being measured was also the one being stimulated.

5.3.3 Experimental results.

5.3.3.1 Piecewise constant negative feedback (PCNF).

Figures 5.3.1c show typical time series of PCNF-induced pupillary oscillations for different area threshold values. We restricted our attention to values of θ that produce an oscillation. The oscillations have one maximum per period. The power spectra for these oscillations are shown in Figure 5.3.2a-c. The high threshold oscillations have a richer harmonic content than the lower threshold ones which are nearly sinusoidal. Also, the spectra show little power below the fundamental frequency. The oscillation waveforms in PCNF have no particular symmetry that would be reflected in the power spectra (like for a square wave). In fact, the waveform is clearly asymmetric, especially at high threshold. This is due to the fact that constriction is faster than dilation. This asymmetry is highlighted by transient responses to light steps as occurs in PCNF, and not by responses to the continuously varying light intensity as occurs in SNF[84,99].

In Figure 5.3.3a,b we have plotted $\overline{A}$ and $\overline{P}$ as a function of θ. Note that the bifurcation point BP corresponding to oscillation onset is to the right of the figure. When $A_{off} < \theta$ the pupil is in an equilibrium state characterized by less than 5% fluctuations around the mean pupil area (low amplitude hippus occurring at large pupil areas). When $A_{off} > \theta$, a transition occurs between this state and an oscillatory state. $\overline{P}$ and $\overline{A}$ are monotonically increasing functions of θ.

In Figure 5.3.3c,d we plot the relative amplitude and period fluctuations $\frac{\Delta A}{A}$ and $\frac{\Delta P}{P}$ for the same range of thresholds. ΔA does not vary much over the range of θ values. Since $\overline{A}$ increases as the bifurcation point is approached (i.e. as θ increase), $\frac{\Delta A}{A}$ will decrease. However, ΔP increases as θ increases. Further, ΔP increases faster than $\overline{P}$, yielding a value of $\frac{\Delta P}{P}$ that increases with θ. We would obtain the same result if, instead of $\frac{\Delta P}{P}$, we plotted $\frac{\Delta f}{f}$ where $f = \frac{1}{P}$ is the oscillation frequency. In fact at higher thresholds the power spectra have a high background, especially in the 0.1 - 0.5 Hz range, and the peak of the fundamental mode has less power as the bifurcation point is approached.

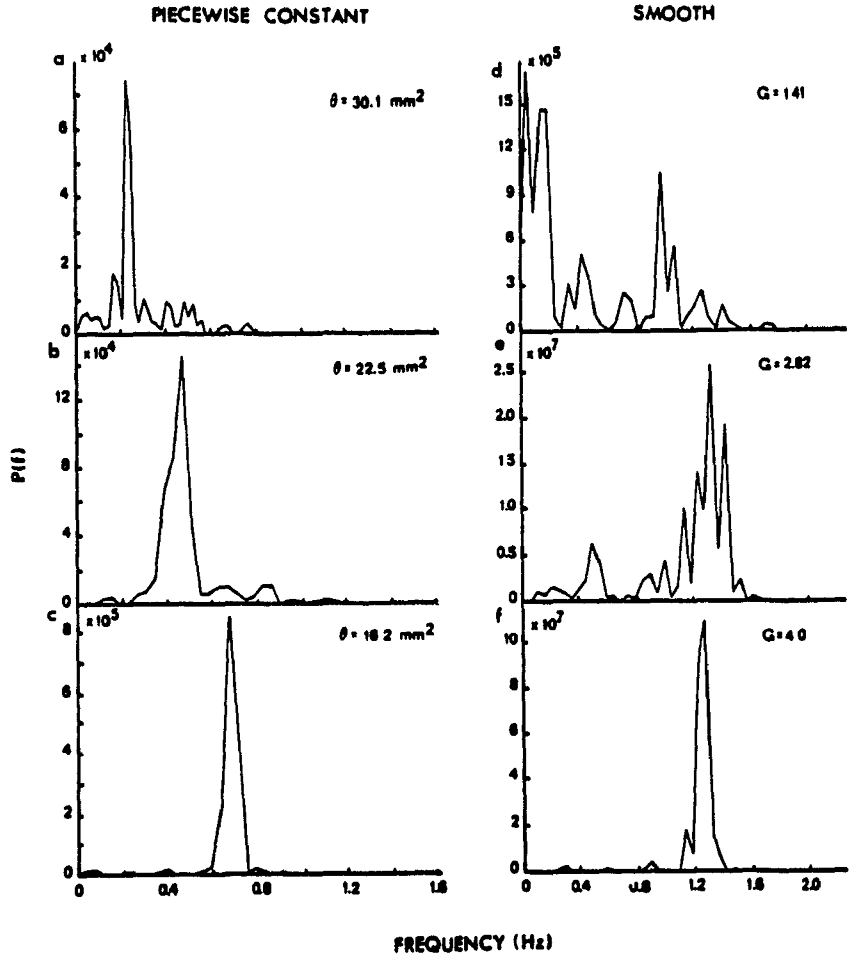

Figure 5.3.2 a) Power spectra of pupil oscillations shown in Figure 5.3.1. For PCNF (a-c) the spectra were obtained by running a FFT on Parzen-windowed data resampled at 20 Hz. Note the shift in the dominant peak as the threshold changes. For SNF (d-f), the spectra were obtained by performing a FFT on the data. As the gain increases, low frequency power disappear as the power becomes concentrated in the dominant peak.

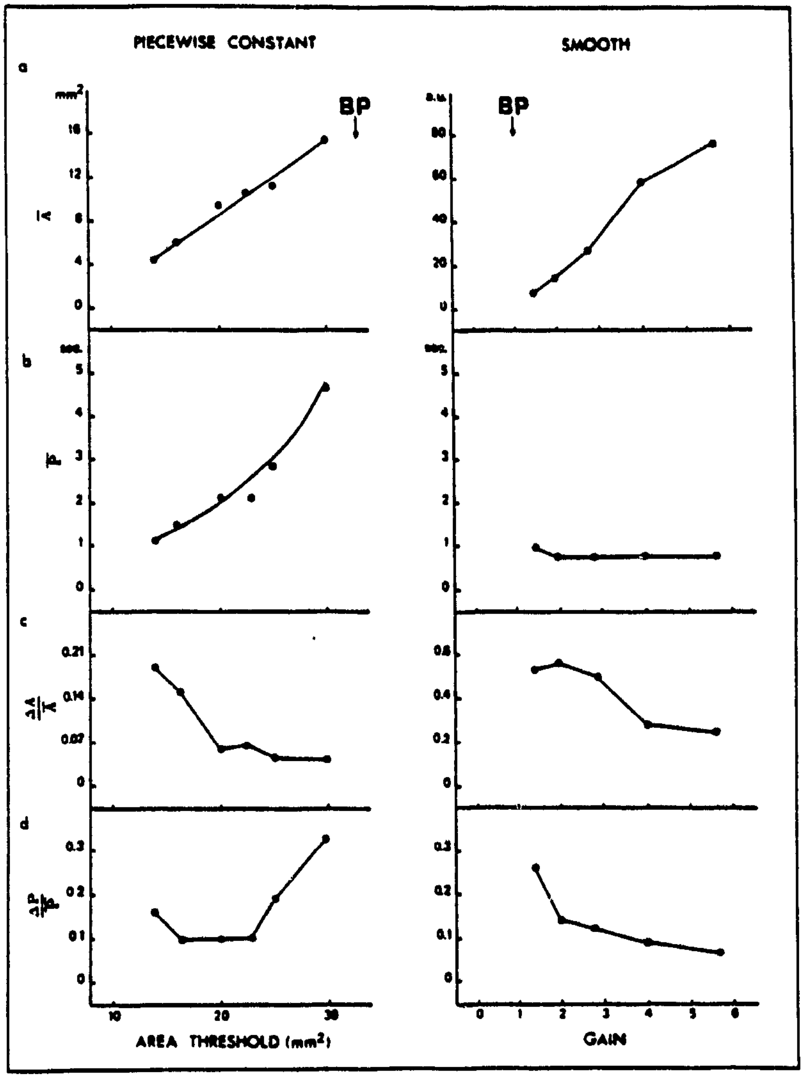

Figure 5.3.3 Means and fluctuations of oscillation amplitude and period as a function of threshold (PCNF) and gain (SNF). Oscillation onset occurs at the threshold or gain value marked **BP** (bifurcation point). Oscillations occur to the left of **BP** for PCNF and to its right for SNF. a) Mean amplitude $\overline{A}$; b) mean period $\overline{P}$; c) relative amplitude $\frac{\Delta A}{A}$ fluctuations; d) relative period $\frac{\Delta P}{P}$ fluctuations. The fluctuations ΔA and ΔP are the standard deviations of the means $\overline{A}$ and $\overline{P}$ at corresponding gain or threshold settings. The PCNF data was obtained from one subject (to minimize variability) by measuring pupil area at for $\approx 20-25 sec$ at each threshold setting. The SNF data was also obtained from a single (but different) subject. At each gain setting, area was measured during 2-3 runs totalling $\approx 40 sec$. Amplitudes were measured from peak to trough, while periods were measured as the time between successive peaks. Note that $\frac{\Delta A}{A}$ is larger for SNF than for PCNF and larger than $\frac{\Delta P}{P}$ in SNF. Also, $\frac{\Delta P}{P}$ is larger in PCNF than in SNF and larger than $\frac{\Delta A}{A}$ in PCNF.

5.3.3.2 Smooth negative feedback (SNF).

Figures 5.3.1d and 5.3.2d-f respectively show time series of the oscillations in pupil area that occur with SNF and the corresponding power spectra. The oscillations have a nearly sinusoidal shape with a randomly fluctuating amplitude and period. In fact, the spectra for the higher gains are dominated by the fundamental mode (1.1 − 1.3 Hz), and there is little harmonic content. At the lower gain setting (Figure 5.3.2d) there is a more pronounced 0.1 − 0.2 Hz rhythm in addition to the fundamental mode. The data set length is limited by saturation of the area signal which results in a clipped oscillation (not shown). These saturations appear to be due to uncontrollable baseline (mean area) drift which in turn is caused by pupillary noise. These oscillations, as well as those for PCNF, were found to not be significantly affected by blinking. Further, the waveforms are symmetric in contrast with those for the PCNF case.

The mean amplitude and mean period of the SNF oscillations are plotted as a function of the feedback gain G in Figure 5.3.3a,b. The gain has been normalized such that $G \simeq 1$ when the pupil starts to oscillate. In this case the bifurcation point (BP) is at the left of the figure, and the oscillations become more prominent as the gain is increased. $\overline{A}$ increases with G in a roughly sigmoidal fashion. Over the same range of gain values, $\overline{P}$ is quite constant but there are relatively larger fluctuations at small G values.

The relative fluctuations in amplitude and period are plotted in Figure 5.3.3c,d for the range of gain values studied. Amplitudes are measured as peak to trough differences while periods are measured as the time between successive peaks. $\frac{\Delta A}{A}$ is larger than $\frac{\Delta P}{P}$ over this whole range. However, both increase rapidly at lower gains, reaching values of $\frac{\Delta A}{A} \sim 0.5$ and $\frac{\Delta P}{P} \sim 0.2$. At higher gains, these values level off at $\frac{\Delta A}{A} \sim 0.2$ for amplitude and $\frac{\Delta P}{P} \sim 0.05$ for the period.

The spectra in Figure 5.3.2d-f show that there is considerable power below the fundamental frequency. This reflects the baseline and amplitude fluctuations within each data set. These fluctuations also make ambiguous the determination of the point of oscillation onset by extrapolation to zero amplitude. The spectra show that the noise is more prominent around 0.5 Hz, and that its bandwidth does not seem to excede 1 Hz. This implies that the correlation time of these fluctuations is on the order of 1-2 seconds (reciprocal of the low frequency noise bandwidth). This is in agreement with previous studies which indicate that the spectrum of noise in open-loop is quasi-white up to a cutoff frequency of $\simeq 0.5$ Hz[46,47,88]. In fact, high frequency noise (observable up to $\sim$ 25 Hz by Nyquist's criterion) is very small, and inspection of the oscillations reveals that they are smooth. Previous investigations[1] have shown that autonomous oscillations exhibit less high frequency noise than those obtained using e.g. external periodic forcing. This can be explained by the fact that the autonomous system behaves like a resonant lowpass filter when it oscillates[1]. However, the slower extraneous oscillations are not suppressed and are clearly apparent in our data.

5.3.4 Theoretical analysis.

5.3.4.1 Deterministic analysis.

In this section we explain the deterministic results for the SNF and PCNF cases.

A. SNF. For the SNF case, Equation (5.3.1) has periodic solutions[24,25,90] when

$$\omega\tau = cos^{-1}(-\frac{\alpha}{\beta}), \tag{5.3.5}$$

where $\omega = \sqrt{\beta^2 - \alpha^2}$ is the angular frequency of the oscillation at the bifurcation and the inverse cosine takes its value in the interval $[\frac{\pi}{2}, \pi]$. β is the slope of the feedback function evaluated at the fixed point $F'(A^*)$. A supercritical Hopf bifurcation occurs when $F'(A^*)$ or τ are made sufficiently large, in which case the left hand side of (5.3.5) is greater than the right hand side. Thus the amplitude of the limit cycle increases near the bifurcation as the square root of the distance from the bifurcation point (like the order parameter in a second order phase transition[21]). This amplitude behaviour is roughly seen in our data (Figure 5.3.3a) at higher gain. The origin of the behavior of the mean amplitude near oscillation onset will be explained in the stochastic analysis section below.

Assuming that F is given by the Hill's function in (5.3.3), it is straightforward to show that $\frac{\partial T}{\partial n} < 0$ at the bifurcation point, where $T = \frac{2\pi}{\omega}$ is the oscillation period. However, numerical integration of (5.3.3) reveals that the period remains constant near the bifurcation point and increases monotonically thereafter until it reaches the value of the period analytically predicted for PCNF (see below). This is true for different values of α; further the period increases very slowly as α is decreased ($\alpha = 3.21 : T = 0.936; \alpha = 0.1 : T = 1.185$). This slow variation in period is observed in Figure 5.3.3b except near oscillation onset where fluctuations are large. The relative constancy of the period, when compared to the amplitude, can be understood from the normal form for the Hopf bifurcation. In fact the frequency is given by an expansion in even powers of the amplitude and hence the zeroth order term (a constant) dominates near the bifurcation[10].

B. PCNF. The dynamics of PCNF-induced oscillations are governed by (5.3.4). The solutions of (5.3.4) are simple increasing or decreasing exponentials because at any given time the forcing (i.e. the right hand side) is constant. The oscillation is bounded from above by an upper asymptote A_{off} towards which the pupil dilates whenthe light is off. Likewise, when the light is on, the area tends to a lower asymptote A_{on}. Note that on crossing θ the slope of the solution does not change instantly. This is due to the finite (neural plus electronic) delay in the system. The exact shape of the observed oscillations is not reproduced by this piecewise linear model, e.g. the derivative is not continuous (at least a second order piecewise linear model would be required). However, the model has the advantage that analytical expressions exist for the period P and amplitude $\tilde{A}$[89,99]:

$$P = 2\tau + \alpha_c^{-1} \ln\left[\frac{A_{max} - A_{on}}{\theta - A_{on}}\right] + \alpha_d^{-1} \ln\left[\frac{A_{min} - A_{off}}{\theta - A_{off}}\right] \tag{5.3.6}$$

$$\tilde{A} = A_{max} - A_{min} \, , \tag{5.3.7}$$

where A_{max} and A_{min} are the maximum and minimum areas reached by the oscillation as it approaches, respectively, the asymptotes A_{off} and A_{on} :

$$A_{max} = \theta e^{-\alpha_d \tau} + A_{off}\left[1 - e^{-\alpha_d \tau}\right] \tag{5.3.8}$$

$$A_{min} = \theta e^{-\alpha_c \tau} + A_{on}\left[1 - e^{-\alpha_c \tau}\right] \tag{5.3.9}$$

Note that $A_{on} < A_{min} < A_{max} < A_{off}$.

Further, all parameters can be estimated experimentally[20,89]: α_d is determined from the slope and A_{off} from the intercept of the plot of A_{max} vs θ. In the same manner, A_{min} vs θ yields A_{on} and α_c. The threshold θ is set electronically, and the delay τ is measured independently from the pupil response to a single pulse of light. We have taken the response asymmetry into account by making α dependent on the area derivative, i.e. $\alpha = \alpha_c$ when $\dot{A} < 0$ (constriction), and $\alpha = \alpha_d$ otherwise. Asymmetry can be neglected in the SNF case where continuous variations in light intensity (as opposed to the abrupt changes in PCNF) emphasize steady-state rather than transient behaviour, leading to an averaging of the rate constants[84].

Equation (5.3.4) has been shown[64,89] to predict the period, amplitude and light pulse widths in the PCNF case to an accuracy of 5-10% (not shown here). Equation (5.3.7) predicts that the amplitude should be independent of θ in the symmetric case

$\alpha_c = \alpha_d$, and increase linearly with θ when $\alpha_c > \alpha_d$. Our data clearly supports the asymmetric treatment. Further, as θ is increased from low values, the period should first decrease slightly, then increase over the major portion of its range. Apart from the slight decrease in period, this is observed.

5.3.4.2 Stochastic analysis.

A. PCNF. The power spectra in the PCNF case have less power at low frequencies than in the SNF case (compare Figures 5.3.2 a and d). These spectra are different because the two types of feedback affect the expression of the same noise sources differently. The noise in our system has a correlation time on the order of 1-2 seconds (Section 5.3.3.1). This compares well with the reports of the inverse bandwidth of the power spectra of pupil fluctuations ("hippus") under constant illumination[16,47]. The response time of the pupil light reflex, which varies from 0.25 sec (constriction) to 1.5-2 secs (dilation), is of the same order. Further the transients in (5.3.1) are very short (less than one oscillation period) due to the stability of these limit cycles. To obtain a qualitative understanding of how period and amplitude fluctuations depend on θ, we assume that the expressions for amplitude and period, based on the steady state solution of (5.3.4), always hold. In other words, the system equilibrates to the fluctuations. We can then compute period and amplitude fluctuations by taking partial derivatives with respect to fluctuating parameters.

Previous studies have shown that the asymptotes undergo cycle to cycle variations during PCNF oscillations[64]. The asymptotes are defined in terms of physiological parameters by[99]:

$$A_{off} = A_0 + \frac{\gamma}{\alpha_d \beta} ln\left[\frac{\phi_{off}}{\bar{\phi}}\right] \tag{5.3.10}$$

$$A_{on} = A_0 + \frac{\gamma}{\alpha_c \beta} ln\left[\frac{(\phi_{off} + \phi_b)}{\bar{\phi}}\right] \tag{5.3.11}$$

where β is the slope of the feedback function $g(A)$ (defined in (5.3.1)) at the fixed point of (5.3.1) when F is given by (5.3.2), and A_0 is the maximum pupil area (note that $A_{off} > A_{on}$ since $\beta < 0$). These expressions imply that if any physiological parameter fluctuates, this will affect the value of the asymptotes since they are functions of all the parameters. Furthermore, the parameter estimation scheme of the preceding section endows the asymptotes with the largest relative error since they are obtained as intercepts of linear fits. Hence we assume that only the asymptotes fluctuate significantly, and that the asymptote, period and amplitude fluctuations are normally distributed[47,74].

Using a standard error propagation formula, the variances of the amplitude $\sigma^2_{\tilde{A}}$ and period σ^2_P are (remembering that $\tilde{A}$ is the amplitude from (5.3.7)):

$$\sigma^2_{\tilde{A}} = \Big(\frac{\partial \tilde{A}}{\partial A_{off}}\Big)^2 \sigma^2_{A_{off}} + \Big(\frac{\partial \tilde{A}}{\partial A_{on}}\Big)^2 \sigma^2_{A_{on}} \tag{5.3.12}$$

$$= \left[1 - e^{-\alpha_d \tau}\right]^2 \sigma^2_{A_{off}} + \left[1 - e^{-\alpha_c \tau}\right]^2 \sigma^2_{A_{on}} \tag{5.3.13}$$

$$\sigma^2_P = \Big(\frac{\partial P}{\partial A_{off}}\Big)^2 \sigma^2_{A_{off}} + \Big(\frac{\partial P}{\partial A_{on}}\Big)^2 \sigma^2_{A_{on}} \tag{5.3.14}$$

where

$$\frac{\partial P}{\partial A_{on}} = \frac{A_{max} - \theta}{\alpha_c(A_{max} - A_{on})(\theta - A_{on})} + \frac{1 - e^{-\alpha_c \tau}}{\alpha_d(A_{min} - A_{off})} \tag{5.3.15}$$

$$\frac{\partial P}{\partial A_{off}} = \frac{1 - e^{-\alpha_d \tau}}{\alpha_c(A_{max} - A_{on})} - \frac{\theta - A_{min}}{(A_{off} - \theta)(A_{off} - A_{min})} \tag{5.3.16}$$

From this analysis we see that the amplitude variance does not depend on θ, while the period variance does. Since the amplitude increases as the bifurcation point is approached, the relative amplitude fluctuations will decrease, as shown in Figure 5.3.3c. Furthermore the critical behaviour of the period is seen in the divergence of σ_P at the bifurcation point $\theta = A_{off}$ in (5.3.16). A simple calculation shows that as $\theta \rightarrow A_{off}$, $P \approx ln(A_{off} - \theta)$ and thus

$$\frac{\Delta P}{P} \approx \left\{(A_{off} - \theta)\ln\left[\frac{A_{off} - A_{min}}{A_{off} - \theta}\right]\right\}^{-1} . \tag{5.3.17}$$

Note that the argument of the logarithm is greater than one except when $\theta = A_{min} = A_{on}$. Our analysis thus predicts that as the point of oscillation onset is approached, the relative period fluctuations should increase rapidly, which is also in agreement with the data of Figure 5.3.3d.

B. SNF. In this section we first discuss problems involved with the analysis of fluctuations in the SNF case using standard theoretical approaches. We then justify our choice of which parameters fluctuate, and show how numerical integration of a simple stochastic DDE explains the observed stochastic behavior of the amplitude and period.

Additive and multiplicative noise

The behavior of ODE's near bifurcation points can be studied by looking at the extrema of the stationary probability density of the Fokker-Planck equation. These extrema are the quantities that undergo bifurcations. This is true for the Hopf bifurcation in ODE's, where other quantities such as the power spectrum and the autocorrelation function do not display this critical behavior[148]. For DDE's, the Fokker-Planck equation takes the form of a PDE with retarded argument. There are no analytical techniques available to solve such an equation for its stationary density. Further, to compute the density from an experimentally measured time series requires extensive data sets so the fluctuations can be averaged over many oscillation cycles[148]. Since our time series are short, such an approach would yield inaccurate results, especially in regard to the position of the extrema of densities.

It is known that the relaxation time t_r of perturbations from the limit cycle (a measure of stability) is, according to Floquet theory[149], given by $t_r \propto (n - n_0)^{-1}$ where n_0 is the parameter value at which the bifurcation occurs. This critical slowing down has been measured in the vicinity of the self-pulsing threshold of a bistable optical system governed by a DDE (the Ikeda equation)[139]. The divergence of t_r is, along with $\tilde{A} \propto \sqrt{n - n_0}$, characteristic of second order phase transitions[21]. We cannot measure the relaxation time to the limit cycle because of the limit on the length of our data sets and the high noise levels. Even if we could measure this rate, it is not clear how to relate it to the amplitude and period fluctuations we are interested in. In view of this and of the problems involved with the density approach, we resort instead to numerical simulation. We apply noise to (5.3.3) since this equation is simpler than (5.3.1) together with (5.3.2) and explains qualitatively the deterministic behavior seen for SNF[99].

To identify which parameters in (5.3.3) are subject to noise, we equate the asymptotes in the PCNF case (which we assumed are fluctuating) with the upper and lower bounds of the SNF function as in Figure 5.3.3a. This identification yields (setting $\alpha_c = \alpha_d$ for SNF):

$$c = -\frac{\gamma}{\beta} ln\left[\frac{\phi_{off} + \phi_b}{\phi_{off}}\right] \qquad (5.3.18)$$

$$k = \alpha A_0 + \frac{\gamma}{\beta} ln\left[\frac{\phi_{off} + \phi_b}{\bar{\phi}}\right] \qquad (5.3.19)$$

and similar expressions if asymmetry (i.e. $\alpha_c \geq \alpha_d$) is kept. The physiological parameter that is probably fluctuating the most is γ since it is related to hippus. This is in agreement with earlier work showing that the amplitude of the noise depends on the state of the system, i.e. that the noise is multiplicative. In fact it has been shown[47,74] that neural output of the midbrain (which drives the iris constrictor muscle) is primarily the sum of two components: one proportional to light intensity and one proportional to both intensity and noise level. $\bar{\phi}$, related to the adaptation state of the retina, is also likely to fluctuate because of variations in light intensity.

It is obvious from (5.3.18) and (5.3.19) that if either γ and/or $\bar{\phi}$ vary, c and k will also vary Hence, the amplitude and period fluctuations in SNF should be qualitatively explained using (5.3.3) with additive noise (on k) and multiplicative noise (on c). When noise is assumed to affect γ and $\bar{\phi}$ in (5.3.2), it is considered multiplicative. If instead we use (5 3.3) with noise on c and k, we are assuming that the noise is both additive and multiplicative. *A priori*, this additive noise does not seem justified. However, additive noise is also expected in the general case (i.e. it could have been added to F in (5.3.2)), and could be due, for example, to random neuron firings in the absence of perturbations originating outside the reflex arc.

We assume colored Gaussian noise with a correlation time $t_{cor} \approx 1$ second (see Section 5.3.3). Explicitely, we have $c = \bar{c} + \varepsilon(t)$ (multiplicative noise) and $k = k + \varepsilon(t)$ (additive noise) where $\varepsilon(t)$ obeys an Ornstein-Uhlenbeck process[150]

$$\frac{d\varepsilon}{dt} = -\Gamma\varepsilon(t) + \Gamma\xi(t) \tag{5.3.20}$$

where $\Gamma \equiv t_{cor}^{-1}$ and $\xi(t)$ is a Gaussian white noise of zero mean and variance σ^2, i.e. $\langle\xi(s)\xi(t)\rangle = \sigma^2\delta(t-s)$. The correlation function of the Ornstein-Uhlenbeck process (5.3.20) is

$$C(t,s) = \frac{\sigma^2}{2t_{cor}} e^{-\Gamma|t-s|}. \tag{5.3.21}$$

The white noise limit is obtained by letting $t_{cor} \to 0$ in (5.3.21), and the strength of the Ornstein-Uhlenbeck noise is $\frac{\sigma^2}{2t_{cor}}$.

Numerical Algorithm

Our stochastic simulations were done separately for additive and multiplicative noise[136,144,145]. The Ornstein-Uhlenbeck process (5.3.20) was integrated using an integral Euler method recently proposed by Fox et al.[136], which has been shown to be more accurate than the usual differential method, while (5.3.3) was integrated using a fourth order Runge-Kutta with linear interpolation for the delay. The time step of $\tau/100$ was the same for both methods and was limited by the accuracy requirements for the integration of the Ornstein-Uhlenbeck process. The parameters were chosen to be $\alpha = 3.21$, $\tau = 0.3$, $\bar{c} = 200$, $\bar{k} = 0$ and $\theta =$ [illegible] to yield reasonable pupil area values[64,84] in mm^2. The gain G in the SNF experiments is proportional to the parameter n, which controls the steepness of the Hill function at the fixed point. We varied n from its value at the Hopf bifurcation, $n_H = 8.18$, to a value above which the amplitude grows very slowly ($n = 12$). n was varied in steps of 0.02 from 8.18 to 8.30, and then by steps of 0.2 from 8.40 to 12.0.

Equation (5.3.3) was integrated using an initial function $A(t') = 40$, $t' \in [-\tau, 0]$, which is close to the fixed point of (5.3.2) ($A^* = 44.6$). For a given value of n, the solution is first allowed to settle onto the limit cycle in the absence of noise for an integration time equal to 2500 delays; then noise is applied, and another 2500 delays are discarded as transients. (5.3.3) is further integrated for another 20000 delays during which the amplitude and period histograms are constructed. Periods and amplitudes were determined from the zero slope points of the solution as in the data analysis (Section 5.3.3). We required two such points to be separated by at least 20 time steps (60 $msec$) in order to neglect very rapid changes in the derivative which could not be measured from the data.

It is difficult to numerically obtain an accurate description of steady state behavior in the vicinity of a bifurcation point because of critical slowing down. Since the amplitude of the limit cycle at a Hopf bifurcation grows as $\tilde{A} \propto (n - n_H)^{1/2}$ and the relaxation time of transients onto the limit cycle goes as $t_r \propto (n - n_H)^{-1}$, it follows that $t_r \propto \tilde{A}^{-2}$. This implies that if we allow sufficient time for the transients to decay in the vicinity of the Hopf bifurcation point (i.e. for $n \approx n_H$), then this time should also be sufficient to obtain an accurate picture of the steady state behavior for $n > n_H$. Hence, for all values of n, the same time (5000 delays) was allowed for the transients to decay. We have numerically verified that this transient period was sufficient by comparing our results in the vicinity of the Hopf bifurcation with those of simulations for 60000 delays where the first 30000 delays are discarded as transients.

A histogram of the amplitude values from the numerical solution of the system (5.3.3) with multiplicative noise (5.3.21) on c was obtained by dividing the interval (0,40) mm^2 into 200 bins. In Figure 5.3.4a, the mean amplitude calculated from this histogram is plotted as a function of the bifurcation parameter n for different intensities of the multiplicative noise ($t_{cor} = 1$) as well as for the deterministic case. The curves were obtained by smoothing the simulation results at the discrete values

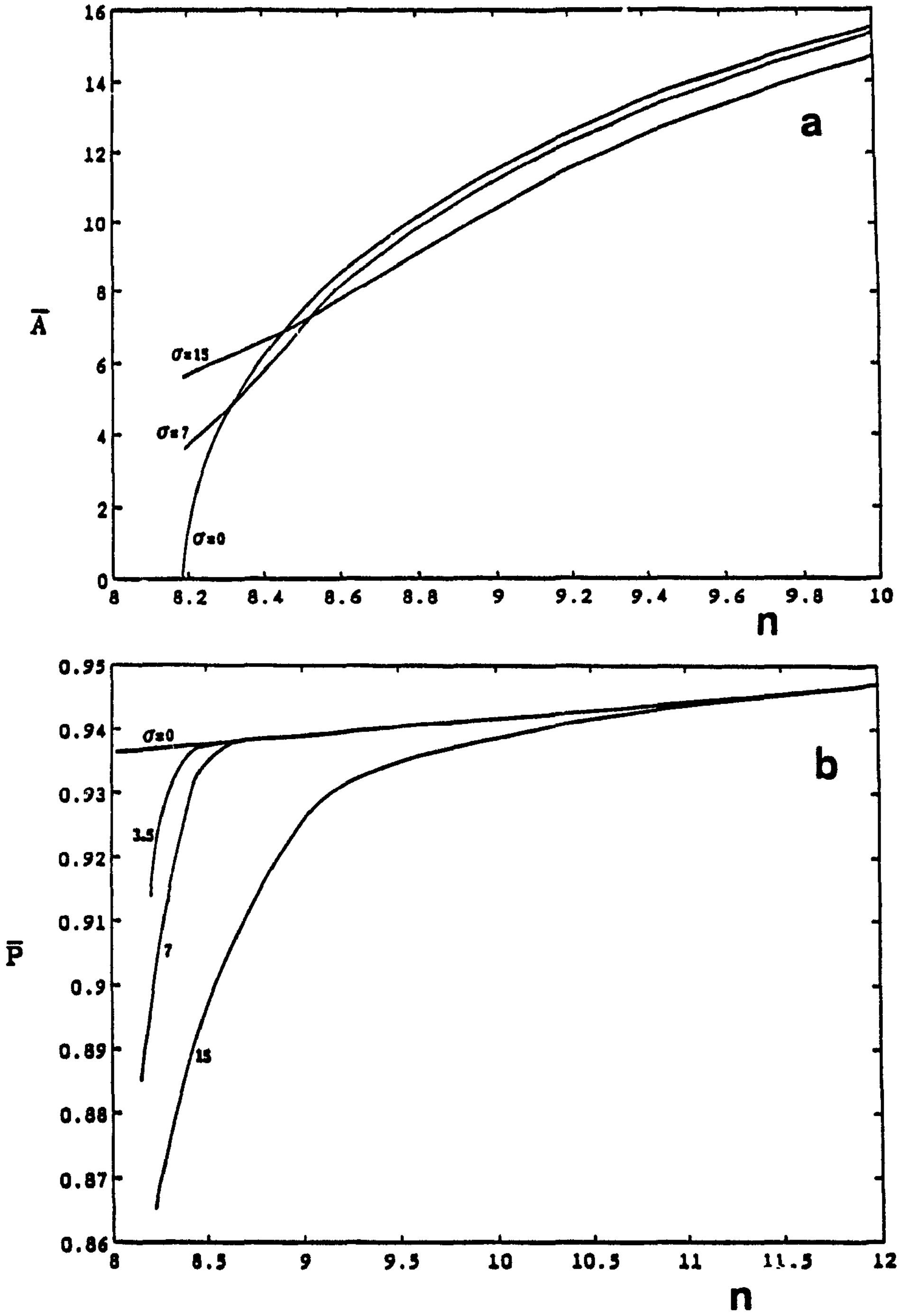

Figure 5.3.4 Predicted means and fluctuations in amplitude and period for the SNF case, computed from the numerical integration of Equation (5.3.3) with multiplicative Gaussian colored noise (5.3.20) on the parameter c. Parameter values are $\tau = 0.3 sec$, $\bar{c} = 200 mm^2 sec^{-1}$, $\theta = 50$, $\alpha = 3.21 sec^{-1}$, $k = 0 mm^2 sec^{-1}$ and the initial area was constant ($40 mm^2$) on the interval $(-\tau, 0)$. The bifurcation parameter is n (which is proportional to the feedback gain), and a Hopf bifurcation occurs at $n = 8.18$. The noise correlation time is one second. a) Mean limit cycle amplitude as a function of n for the deterministic case ($\sigma = 0$) and for $\sigma = 7.0$ and 15.0. b) Mean limit cycle period as a function of n for the deterministic case and for $\sigma = 3.5, 7.0, 15.0$. c) Relative amplitude fluctuations as a function of n for $\sigma = 3.5, 7.0, 15.0$. d) Relative period fluctuations for the same values of σ as in (c). Note that the mean period in (b) varies slowly with n, even though the expanded vertical scale suggests the opposite.

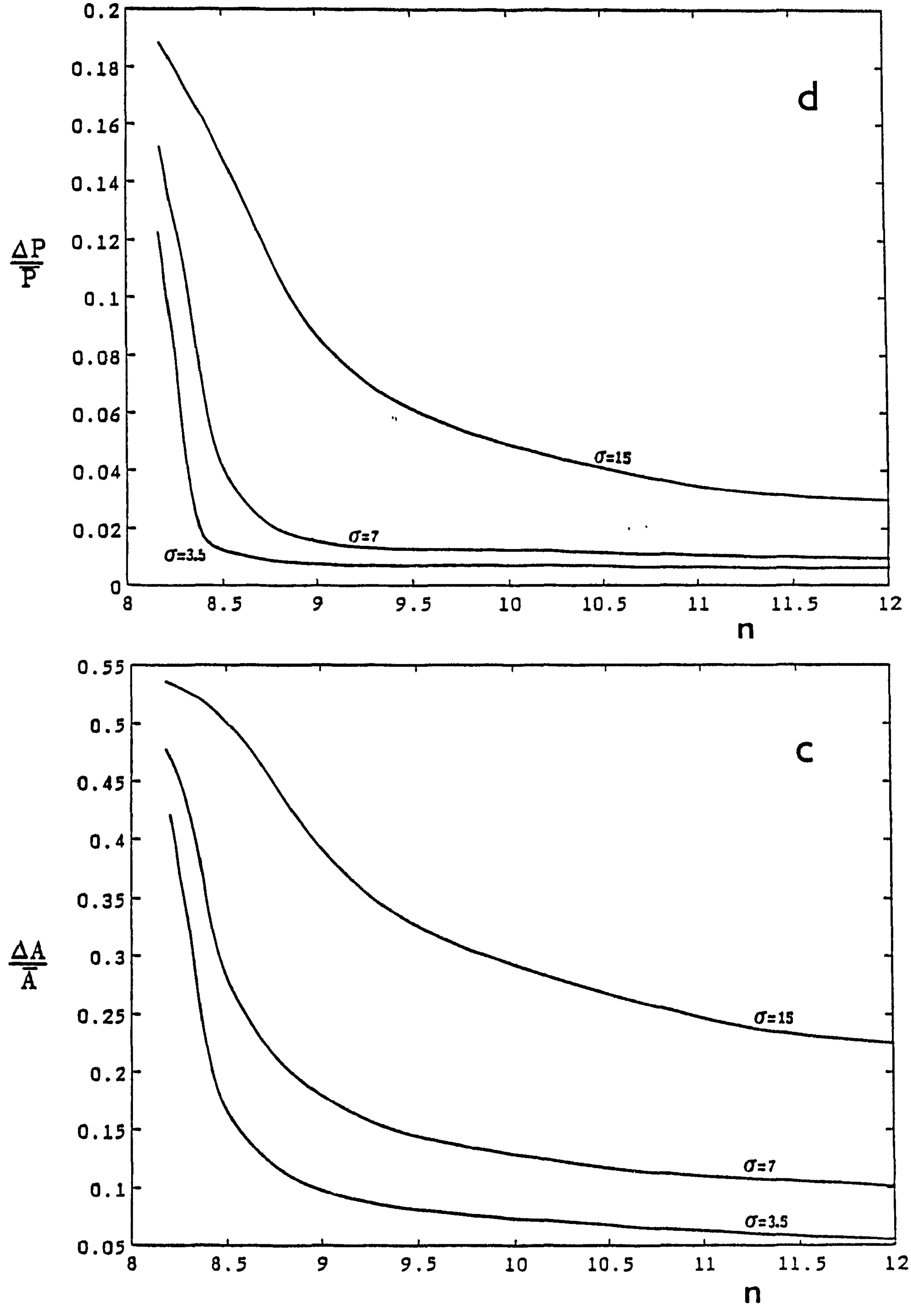

Figure 5.3.4 (c) and (d)

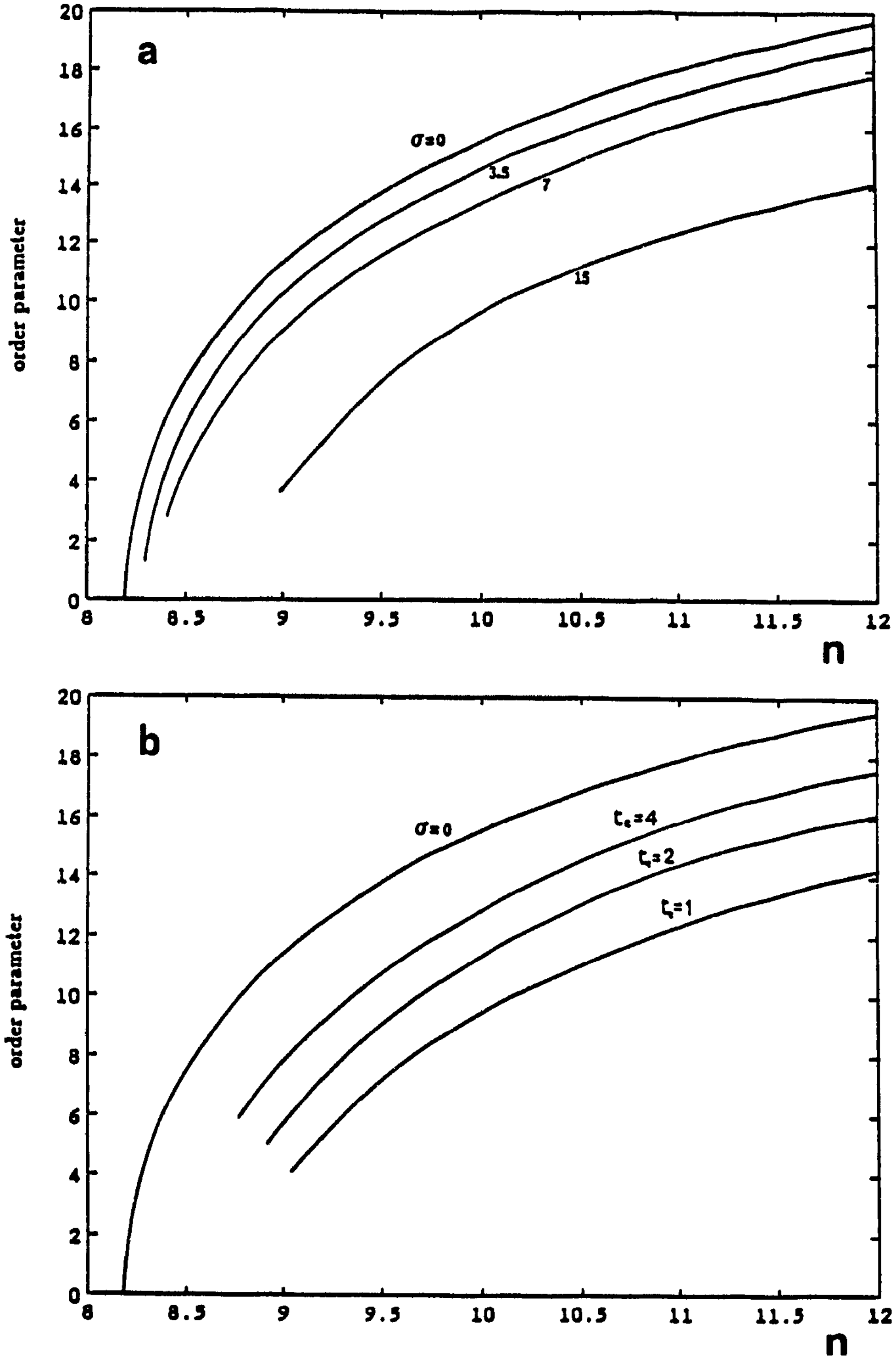

Figure 5.3.5 Magnitude of the separation between the peaks (order parameter) in the density of the solution of (5.3.3) as a function of n for multiplicative (a,b) and additive (c,d) colored Gaussian noise (5.3.20). The parameters are the same as in Figure 5.3.4. In all plots, the amplitude of the limit cycle in the deterministic case is included for reference. a) Peak separation for multiplicative noise of correlation time $t_{cor} = 1sec$ and for $\sigma = 3.5, 7.0$ and 15.0. b) Peak separation for multiplicative noise with $\sigma = 15.0$ and for 3 different noise correlation times: $t_{cor} = 1.0, 2.0, 4.0$. c) and d) are the same as, respectively, a) and b), except that the noise is additive (on the parameter k in (5.3.3)).

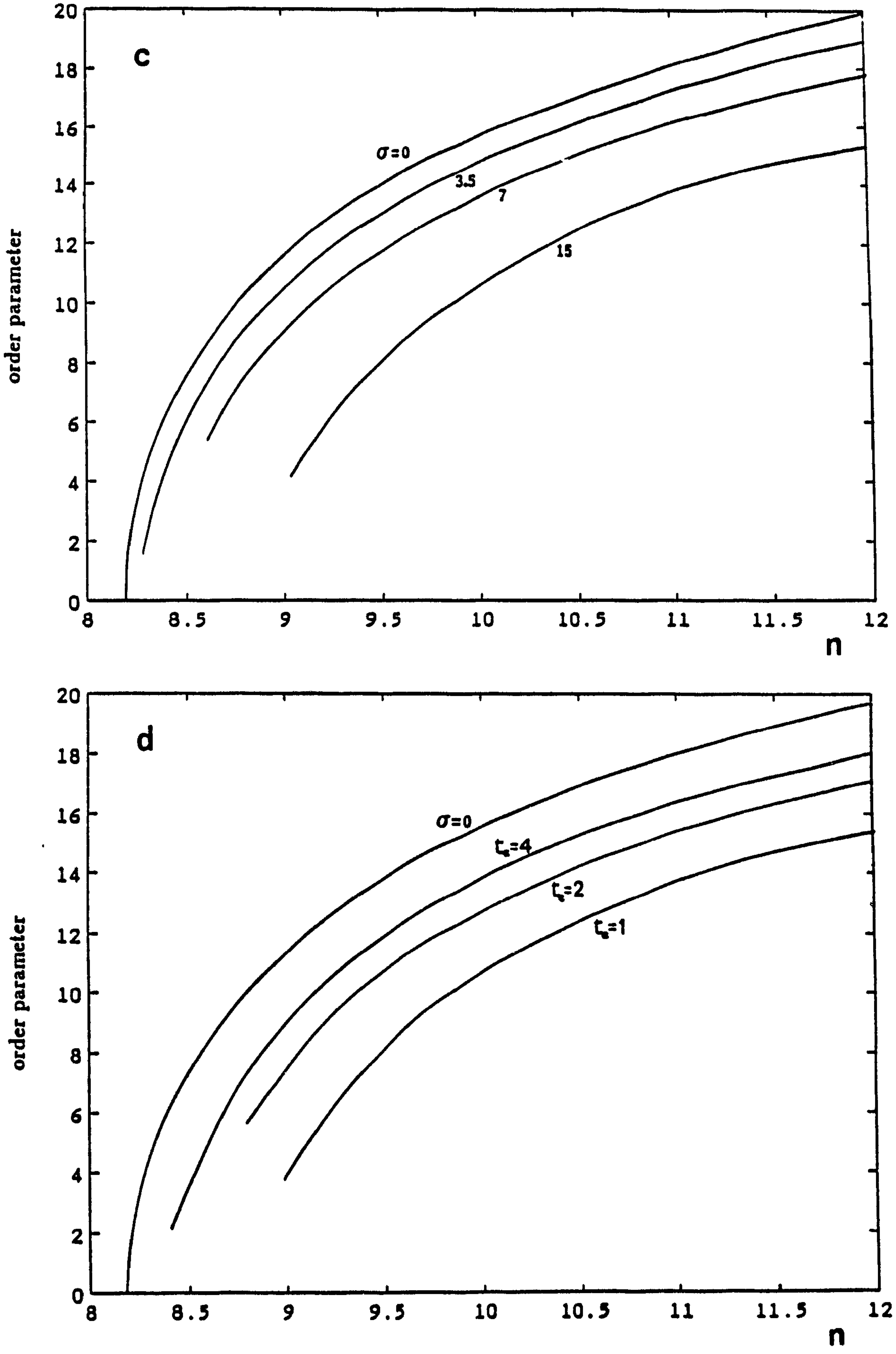

Figure 5.3.5 (c) and (d)

of n. The mean amplitude in the presence of noise does not go to zero at the bifurcation as does the deterministic amplitude. This is in agreement with the observed behavior of the mean amplitude in Figure 5.3.3a. Rather, it levels off at a finite value proportional to the noise intensity. The sigmoidal shape of the curve for $\sigma = 15$ is in good agrement with that of the experimental curve (Figure 5.3.3a). In this calculation, the very small amplitude fluctuations (corresponding to the first three bins of the amplitude histogram, equivalent to (0,0.6) mm^2 were neglected from the computation of the amplitude mean and standard deviation, to account for the fact that these small fluctuations are not measurable experimentally. The value at which the mean amplitude curve levels off at the bifurcation point is proportional to the number of low amplitude bins neglected. Note that below the bifurcation point (i.e. for $G < G_0$), the mean amplitude is still finite, and goes to zero as the equilibrium point becomes more attracting (not shown).

The mean period is computed (as is the mean amplitude) from a histogram of the period values in the numerical solution of the stochastic DDE. The period value interval (0.5,1.5) *sec* was divided into 200 bins. The mean period value for the same range of noise intensities as in Figure 5.3.4a is plotted as a function of n, as well as the period for the deterministic case. Figure 5 3.4b shows that the mean period is fairly constant over the values of n investigated, as observed in the data (Figure 5.3.3b). In all cases, the period increases slightly with n; however, for a given value of n, the mean period decreases as the noise intensity increases.

For the PCNF case, it is possible to estimate the parameters of (5.3.4) from the PCNF data[89]. However, it is difficult to estimate the parameters of (5.3.3) from the SNF data, which is the reason why we are looking for qualitative agreement with the data in Figure 5.3.3. The noise intensity was chosen to reproduce the values of relative amplitude and period fluctuations measured from the data (Figure 5.3.3c,d). Good agreement between these values and between the shape of the time series (not shown) was obtained when $\sigma^2 = 15$ (Figure 5.3.4c,d). This implies that the dependence of mean amplitude on n is given by the $\sigma = 15$ curve in Figure 5.3.4a. This curve is in fact the one whose shape agrees the best with that of Figure 5.3.3a.

By repeating the simulations at a given value of n for the highest intensity used ($\sigma = 15$), it was found that the mean and standard deviation values fluctuate by approximately 2%. This accuracy could be reduced by averaging these values over many realizations of the Ornstein-Uhlenbeck process. However, given the large variability exhibited by physiological systems, and given that we are looking for qualitative agreement, this averaging procedure was not warranted.

The simulations were repeated for the case of additive noise on k in (5.3.3). Note that c and k in (5.3.3) both determine the height of the SNF function. The results (not shown) are qualitatively the same as for the multiplicative case, except that for equal noise intensities, the additive noise has a lesser effect on the dynamics.

Pinpointing the Hopf bifurcation

Theoretically it is important to pinpoint the occurrence of the Hopf bifurcation. The fact that the mean limit cycle amplitude is still finite for $G < G_0$ might suggest that the bifurcation has occurred at a smaller parameter value than in the absence of noise. However, the onset of oscillation must be understood from the statistical behavior of the system. It has been shown that the stationary density of the Fokker-Planck equation corresponding to a generalized Langevin equation exhibits critical behavior, while other quantities such as the correlation function or the power spectrum do not exhibit such behavior[21,148]. A criterion for determining the Hopf bifurcation point in the presence of noise consists in finding the parameter value at which the stationary density goes from unimodal to bimodal. The separation of the peaks is proportional to the mean limit cycle amplitude which is different from the mean amplitude shown in Figure 5.3.4a. To distinguish between these two statistically determined amplitudes, the peak separation will be referred to as the *order parameter*.

The theory of invariant densities for delay-differential equations (DDE's) in general, and for stochastic DDE's in particular, is non-existent. Although the first order DDE (5.3.3) is infinite-dimensional (it evolves in a functional space), it might be appropriate to look at the one-dimensional density constructed from the values of the state variable. Histograms of the numerically computed solution of (5.3.3) with (5.3.20) for both the additive and multiplicative noise cases were constructed by dividing the interval (10,75) mm^2 of solution values into 500 bins. These histograms were found to have an invariant form when enough time was allowed for the transients to decay. This is an indication that these histograms may qualify as "invariant densities" for the DDE of interest. The peak separation was measured graphically from the densities. Again, repeated simulations for a fixed value of n revealed that peak separation values fluctuated by $\approx 5\%$ at the highest noise intensity used, and that the accuracy increased (the peaks were better defined) as n increased.

Figure 5.3.5 plots the magnitude of the order parameter as a function of the bifurcation parameter n for both multiplicative (5.3.5a,b) and additive (5.3.5c,d) noise. The computations were done on the same time series used for Figure 5.3.1. In Figure 5.3.5a and c, the correlation time is fixed and the intensity varies over the same values as in Figure 5.3.4. The curves are obtained by smoothing the simulation results at the discrete n values. Note that the deterministic curve is the same as that in Figure (5.3.4a): the amplitude is proportional to $\sqrt{n - n_0}$ (Section 5.3.4.1 A). The curves corresponding to finite noise intensities have the same shape as the deterministic curve but are shifted to its left (i.e. to higher values of n) by an amount proportional to the noise intensity. This implies that the noise actually postpones the Hopf bifurcation (from the statistical point of view) in both the additive and multiplicative noise case.

In Figure 5.3.5b and d, the magnitude of the order parameter is again plotted as a function of n, but the noise intensity is fixed and the correlation time is varied from 1 to 4 seconds. In both the additive and multiplicative case, the shift of the bifurcation point increases as the correlation time decreases.

5.3.5 Transition from SNF to PCNF.

In this section the relation between the different deterministic properties of SNF and PCNF are investigated. Equation (5.3.3) can be obtained from (5.3.1-2) by letting n go to infinity and by equating $A_{off} = \dfrac{c+k}{\alpha}$ and $A_{on} = \dfrac{k}{\alpha}$, as shown in Figure 5.3.6. In this case, the forcing function F in (5.3.1) becomes a Heaviside function of the delayed pupil area. This limit produces a transition from the nearly sinusoidal oscillations in SNF to a switching type behaviour, characteristic of relaxation oscillations, in PCNF.

The oscillation condition changes from (5.3.5) to the condition $\theta \geq \dfrac{\lambda}{\alpha}$, where θ is the inflection point of the Hill's function when $n \to \infty$. This is illustrated in Figure 5.3.6 where numerical solutions of (5.3.3) are plotted for different values of α. The PCNF waveform depends on the value of α at which the limit is taken. This depends on the intersection of the curve αA with the piecewise constant function. In the PCNF limit the inflection point of the Hill function becomes equal to θ. The oscillation condition is now that the intersection point be on the infinite slope portion of the PCNF function. Hence, in Figure 5.3.6, when $\alpha = \alpha_1$ or α_5, the condition $\theta \geq \dfrac{\lambda}{\alpha}$ is not satisfied and there is no oscillation. When $\alpha = \alpha_2$ the limit produces a high threshold oscillation, as in the case $\alpha = 4$, and $\alpha = \alpha_4$ produces a low threshold oscillation, as in the case $\alpha = 0.7$.

For SNF the Hopf bifurcation criterion corresponds to a condition on the period involving the slope of the feedback function at the fixed point. For PCNF, the oscillation condition is a condition on the amplitude. In the SNF case at oscillation onset, the frequency is fixed while the amplitude is zero (in the supercritical case[99]), while in the PCNF case the amplitude is fixed while the frequency is zero. For SNF, once n increases past its value at the Hopf bifurcation, the amplitude first grows as $\sqrt{n - n_0}$ but rapidly reaches its maximum value, i.e. that for the PCNF case.

5.3.6 Discussion.

Oscillations in the human pupil light reflex were produced by two kinds of external electronic feedback which modify the normal functional dependence of retinal light flux on light intensity and pupil area. The parameters of the external feedback circuit were varied to induce a bifurcation from an equilibrium state to an oscillatory state: the gain of the amplifier relating light intensity to pupil area was varied in the SNF case, while the position of the threshold area θ was varied in the PCNF case.

Experimentally, it is observed that the period fluctuates more than the amplitude at oscillation onset in PCNF, while the opposite holds for the SNF case. We have related this to the different kind of critical behaviour displayed by a first order DDE at oscillation onset in the SNF and PCNF case, under the assumption that the correlation time of the noise is of the same order or larger than the response time of the system. In fact, our simulations of (5.3.3) with multiplicative or additive noise (Figure 5.3.4) indicate that this model of autonomous oscillations in pupil area qualitatively reproduces the observed behavior (Figure 5.3.3) in the vicinity of oscillation onset.

Generally, relative amplitude fluctuations are greater than relative period fluctuations in SNF for a broad range of noise correlation times. Although our simulations account for the cycle to cycle fluctuations in period and amplitude in SNF, they do not reproduce the experimentally observed baseline drift over 10-15 second periods (the data shown in Figure 5.3.1d has been corrected for this drift). This drift is probably due to an unmodelled deterministic phenomenon or to a noise source with a correlation time longer than that for the noise used in our simulations in Section 5.3.4.2. This long-correlated noise could affect either c or k because a variation in either of these would result in a proportional variation in the mean value of the oscillation.

We have observed both experimentally and in our simulations that the period of SNF-induced pupillary oscillations remains constant despite variations in k, λ and n in the SNF case. The constancy of frequency in negative feedback systems in biology

Figure 5.3.6

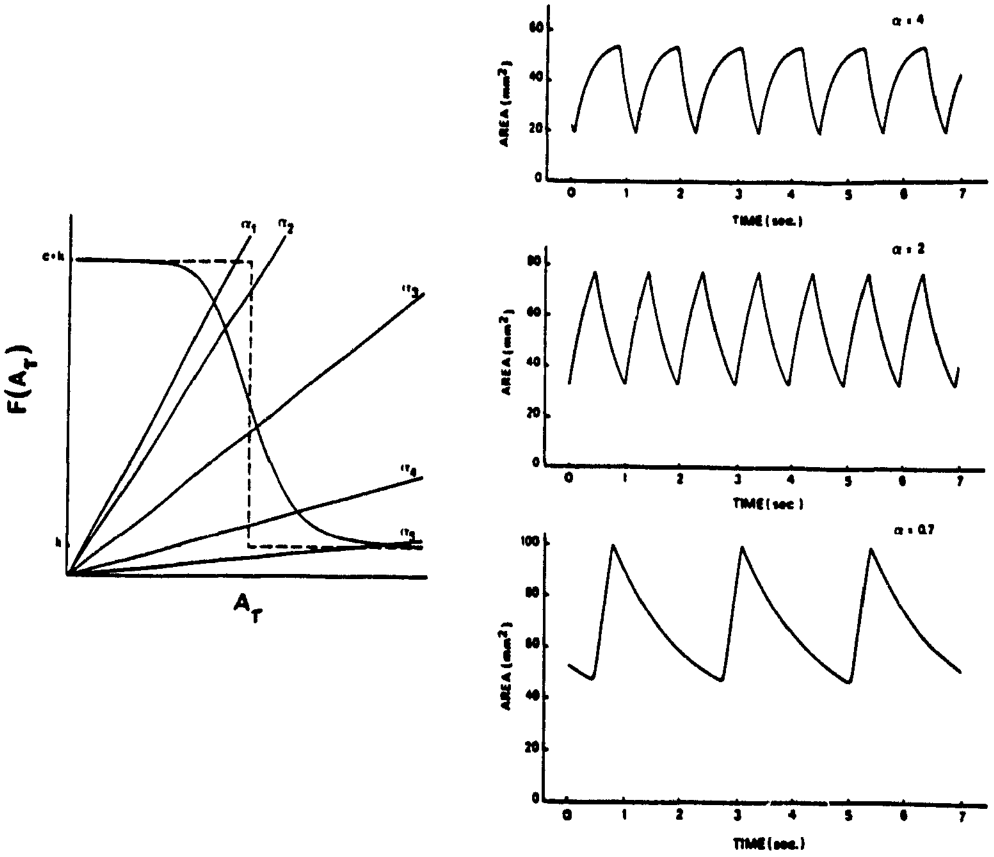

Figure 5.3.6 Transition from SNF (solid line) to PCNF (dashed line) is achieved by increasing the slope of the feedback function until it approaches ∞ at θ and zero elsewhere ($\lim n \to \infty$ in the Hill's function on the left hand side of (5.3.3)). In this limit, the inflection point of the Hill's function coincides with θ, the upper bound $\frac{c+k}{\alpha}$ with the upper asymptote A_{off} and the lower bound $\frac{k}{\alpha}$ with A_{on}. Limit cycles bifurcate from the fixed point A^* of (5.3.3) when $\omega\tau \geq cos^{-1}(-\frac{\alpha}{\beta})$ (5.3.5). In the PCNF limit, oscillation onset occurs when $\theta < A_{off}$. Depending on the value of α, the PCNF limit will yield solutions of (5.3.3) that either do not oscillate (α_1, α_5), or which oscillate around a high ($\alpha_2 = 4$) or a low ($\alpha_4 = 0.7$) threshold. Response asymmetry (i.e. $\alpha_c > \alpha_d$) observed in PCNF has been neglected for clarity. Parameters are: $\tau = 0.3$, $n = 200$, $k = 20$, $c = 200$, $\theta = 50$, $\alpha = 3.21$ and the initial area was equal to 40.

has been pointed out previously[84,99,151] However, in the PCNF case, the period fluctuations are a consequence of the asymptotes fluctuations (principally A_{off}). The theoretical result of Section 5.3.4.2 for the amplitude and period fluctuations in PCNF corresponds to an adiabatic elimination[21] in the sense that the system is considered to always be in a quasi-stationary state with respect to the instantaneous value of the fluctuating parameters.

The influence of the correlated noise in the PCNF case can also be qualitatively understood as follows. When pupil area approaches θ on the way to A_{off}, a slight fluctuation in A_{off} will affect the crossing time. Fluctuations in this crossing time are inversely proportional to the area derivative in the vicinity of the threshold. Hence near oscillation onset this derivative is nearly zero, making the period very sensitive to fluctuations in A_{off}. These conclusions hold under the hypothesis of colored multiplicative noise on the asymptotes. In the white noise limit both period and amplitude are sensitive to the noise (data not shown). However, in PCNF, as t_{cor} decreases, relative period and amplitude fluctuations are of the same order. In fact, whenever θ is approached, noise will cause transitions in pupil area from one side of the threshold to the other and back. Hence, the noise can shorten the time spent above θ, which will decrease the period and the amplitude. The fact that the amplitude fluctuations are not very large in PCNF is an indication that experimentally the noise is colored.

Oscillation onset in PCNF does not correspond to a supercritical Hopf bifurcation as in the SNF case because the oscillation appears with a finite amplitude. Nor is it a subcritical Hopf bifurcation because the fixed point is globally asymptotically stable when $\lambda < \alpha\theta$ [66]. The difference lies in the exchange of stability that occurs at the bifurcation. As a supercritical Hopf bifurcation is approached, the stability of the fixed point decreases. Going through the bifurcation point, it becomes unstable and the solution is attracted to the limit cycle that came into existence at the bifurcation. In PCNF, the bifurcation is characterized by an abrupt exchange of stability leading to the appearance of an oscillation of infinite period but fixed amplitude. Closer inspection of the SNF-PCNF transition shows that oscillation onset is determined by a condition on the period in the SNF case (Hopf bifurcation criterion) and by one on the amplitude in the PCNF case ($A_i > \theta$, where A_i is the initial pupil area; or equivalently, $\lambda > \alpha\theta$). It is interesting that in each case the assumed noise has less of an affect on the quantity which determines the oscillation condition (i.e. the noise does not effect the period as much as the amplitude in SNF, and *vice versa* in PCNF).

To identify whether a bifurcation has occurred or not in a physical system depends on which theory one uses. One such theory holds that a supercritical Hopf bifurcation occurs when the unique maximum of the stationary solution of the Fokker-Planck equation is replaced by two maxima which separate as the bifurcation parameter is increased This does not mean that oscillations are not visible in the time series prior to the Hopf bifurcation. In fact, well defined peaks in the power spectrum as well as oscillations in the autocorrelation function appear, in the presence of noise, even when the bifurcation parameter is well below the deterministic bifurcation value[148]. But these quantities do not exhibit a qualitative change at some parameter value. However, the probability density does display critical behaviour. For physiological data, it is practically difficult to construct such a density due to the length of the available time series. Instead, we have made certain hypotheses on the noise sources and numerically simulated the stochastic dynamics of the system to see whether some aspects of the data can be reproduced. We were thus able to account for the observed behavior of period and amplitude fluctuations at oscillation onset.

In Figure 5 3.5, it is shown that the bifurcation is shifted to higher values of the bifurcation parameter when noise is present. This postponement of the deterministic Hopf bifurcation in a DDE has not, to our knowledge, been reported previously, but is known to occur in ODE's when multiplicative noise is present[21,148,152,253]. We found the shift was proportional to the noise intensity σ, and inversely proportional to t_{cor}, as observed previously[148].

A more surprising fact is that this shift also occurs for additive noise, with the same qualitative dependence on σ and t_{cor}. Noise-induced transitions due to additive noise are not possible in one dimension[21]. They have been reported in a 2-dimensional Fokker-Planck equation[154]. However, DDE's are infinite dimensional, and thus the possibility exists for such transitions. Further, shifts of the first transcritical bifurcation and of the first period-doubling bifurcation in the logistic map have been predicted and observed in numerical experiments involving additive and multiplicative noise[155]. In fact, for discrete time systems, there is an equivalence between additive and multiplicative noise[22,155]. Since the DDE reduces to such a map in the singular perturbation limit, where the response time of the system is much smaller than the delay[125,156,157], it is not surprising that shifts occur for both additive and multiplicative noise.

The shift of the bifurcation point makes the application of the deterministic analysis to experimental data more difficult since a knowledge of the noise characteristics is needed to determine the deterministic bifurcation diagram. In view of the high noise levels in neural systems, it appears difficult to avoid this issue. More work is needed to determine the precise conditions under which postponements occur and whether advancements are possible[148,152,153,158]. In particular, other order parameters such as the root-mean-square amplitude may more appropriately describe the Hopf-type of time translational symmetry-breaking bifurcation in the presence of noise studied here[155,161]. Also of interest is whether a two-dimensional stationary probability density is required to pinpoint the Hopf bifurcation, in the event where the radial and angular variables describing the oscillation are significantly coupled[148,162]. Natural coordinates in which to investigate this possibility are $A(t)$ and $A(t - \tau)$ in (5.3.3). Note that the shifts observed here are different from those obtained when the bifurcation parameter is swept at a finite rate across the bifurcation[159,160].

The postponement of the Hopf bifurcation is expected to be qualitatively similar in the event that the fluctuations are not Gaussian distributed. Although we have not performed a precise assessment of noise statistics, the inclusion of Gaussian noise in our deterministic model does reproduce the data when given an adequate intensity. There have also been previous reports[17,74] which support the Gaussian nature of the pupil noise for midrange pupil sizes under constant illumination. At large and small pupil sizes, the probability density of the noise is slightly skewed toward midrange values, presumably because the injected Gaussian noise is filtered by the nonlinearities in the motor pathway of this reflex. Our model would reproduce this behavior if the distribution of area values were computed prior to the Hopf bifurcation at small and large pupil sizes.

There have been previous studies of fluctuations in neuron membrane potential at rest[165] and at oscillation onset[166,167], and in a simple motor task[168]. Here we have considered the onset of oscillation in a neural control system for which a simple, physiologically sound, model exists, and shown how this model can explain observed deterministic and stochastic behavior. We have further strived to identify the noise sources and to understand their dynamical behavior. Although a partly deterministic origin for the aperiodic behavior of the pupil (such as chaos) can not be excluded, our results concerning the critical behavior of the pupil suggest that hippus is a reflection of an underlying stochastic process. Further, there does not seem to be any interaction between the dynamics of the noise source and the dynamics of the reflex, even though the pupil modifies the characteristics of the noise. This supports the hypothesis that the noise is injected into the reflex pathways, as suggested previously[47,74].

On the basis of our analysis, it is difficult to decide whether additive or multiplicative noise is responsible for the observed behaviour of period and amplitude in SNF. Both mechanisms yield qualitatively similar results, and it is quite probable that both contribute to the observed behaviour.

Noise is amplified in the SNF case near the Hopf bifurcation due to critical slowing down (loss of linear stability), which is responsible for the large amplitude fluctuations. In comparison, the PCNF case appears to be immune to this effect. The critical behavior is displayed by the mean period rather than the mean amplitude. This is interesting because it means that no noise amplification occurs at the bifurcations. Instead the multiplicative noise causes period fluctuations and kicks the system between the limit cycle and fixed point behaviors.

The SNF-PCNF limit has not, to our knowledge, been studied in DDE's. For the Ikeda equation in optical bistability[130], another well-studied first order DDE with nonlinear feedback, attention has been focussed on the singular perturbation limit in which the ratio of the delay to the system response time goes to infinity (i.e. $\alpha\tau \gg 1$ in (5.3.3)). Studies[101,125,156,157] have shown that certain properties of the map obtained in this limit carry over to the continuous solutions of the DDE, while others do not. This applies to the noisy DDE as well, since the noise is responsible for the bifurcation gap in the subharmonic cascade[163]. Also, a noisy one-dimensional map has been used in the study of noise-induced transitions between coexisting states of the Ikeda equation[164]. The PCNF limit of SNF yields a degenerate map with no interesting behavior. However, we have found (data not shown) that the mode frequencies obtained from a linear stability analysis converge to the odd harmonics of the fundamental mode as seen in the singular limit of the Ikeda equation[101]. Of course the mode amplitudes differ, since the singular limit produces a square wave while the PCNF limit produces the waveforms in Figure 5.3.1c.

Different methods are available for the analytical treatment of colored noise, depending on the ratio of system response time to noise correlation time[21]. If this ratio is large (the weakly colored noise case), the Fokker-Planck equation can be approximated using expansions in the inverse bandwidth of the noise. In the other case where the system is always at equilibrium with respect to the slowly varying noise, adiabatic elimination techniques (or switching-curve approximations[21]) can be used, as in Section 5.3.4.2 for the PCNF case. In developing a quantitative analysis for autonomous oscillations in the pupil light reflex, one is faced with the problem that the noise correlation time (for the dominant noise components), the system response time and the delay are all of the same order of magnitude. This implies that the effect of noise on the dynamics may not be effectively studied using the aforementioned techniques. Further, it is not clear how to define the evolution of probability densities for DDE's. We expect that studies of other "untampered" or clamped neural control systems will face the same problems of equal time scales for noise, delay and system response. Noise is an important component of neural activity, and it is our hope that this work will stimulate further studies to untangle the deterministic and stochastic contributions to neural oscillations. Further, the results reported here may be useful for the analysis of other experimental systems (e.g. in nonlinear optics, biochemical regulatory networks, Boolean kinetic networks, gene regulation and transcription) where noise is thought to play an important role and feedback dynamics can be modelled using smooth or piecewise constant nonlinearities.

5.4 REMARKS ON NOISE-INDUCED SHIFT OF HOPF BIFURCATION IN A DDE.

In this section, we develop a qualitative understanding of the origin and properties of the noise-induced transition encountered in the previous section. This is required because there are no analytical tools available to study these transitions in DDE's.

Noise postpones the onset of oscillation at a Hopf bifurcation in a DDE (Section 5.3). However, oscillations are apparent in the solution even though the maxima of the invariant density constructed from this solution have not become distinct; in other words, the oscillation is apparent even though the bifurcation has not occurred. The oscillations are precursors of the bifurcation (Wiesenfeld, 1985) and do not display any critical behavior. Consequently, the shift in the bifurcation point has to be understood from the statistical point of view of densities.

5.4.1 Dependence of shift on noise correlation time.

In the deterministic (noise free) case, the solution spends more time near the extrema of the oscillation (i.e. where the time-derivative is zero) than anywhere else (see Section 4.5). As a consequence, peaks corresponding to these extrema appear in the numerically computed densities. In the stochastic case, the invariant density will have two maxima if: 1) the solution spends enough time near the oscillation peaks; and 2) if the deterministic amplitude is large enough. From the point of view of a generalized Langevin equation, noise affects the value of the derivative of the state variable. Near the bifurcation, noise traps the system around the mean value of the oscillatory solution (i.e. around the fixed point) more often than near the peaks, since the time derivative is constantly changing and the limit cycle is not strongly attracting. Hence, more numerically generated iterates contribute to the mean than to the extrema, and the density will appear single-peaked around the fixed point.

The shift of the Hopf bifurcation is more pronounced for short-correlated noise (i.e. for wideband noise) than for long-correlated noise. This is a consequence of the fact that the shift is proportional to the strength of the noise, and that the effective strength of colored noise is proportional to $\frac{\sigma^2}{t_{cor}}$ (Section 5.2.4). The influence of noise correlation time on the shift can also be understood qualitatively as follows. Short-correlated noise can trap the oscillation around its mean value because it significantly changes the time-derivative of the state variable over short periods of time. For long-correlated noise, the time derivative does not change as abruptly as with short-correlated noise. Conversely, long-correlated noise changes the parameters and the derivatives slowly, so the solution can still freely swing between maximum and minimum values which are slowly modulated by the noise. Hence, the solution spends more time near the peaks than if the noise were rapidly changing. This implies that, for a given noise intensity, the shift will be smaller for long-correlated noise than for short-correlated noise.

5.4.2 Understanding the shift from the "ODE" point of view.

Though no theory seems to exist for generalized Langevin-type equations with delays, there are two limits in which a stochastic DDE can be studied (Sections 4.4 and 4.6), depending on the value of $\alpha\tau$. If $\alpha\tau \ll 1$, the behavior of the DDE may be approximated by that of an ODE We have seen that this approximation is good only when the delay is quite small, which is not the case for the pupil light reflex (Section 4.4.1).

A potentially more interesting avenue would be to look at the effect of noise on the distributed delay system (section 4.8) which does provide a suitable approximation to the behavior of the DDE at the Hopf bifurcation. Since at least three equations are needed to study deterministic oscillations in this approximation (only one of which is nonlinear), the inclusion of Gaussian white noise would require numerically integrating at least a three-dimensional Fokker-Planck equation. This is a hideous task, and probably one which gives little insight into the properties of the shift.

It is possible to linearize the one nonlinear equation in the coupled system of ODE's. The corresponding Fokker-Planck equation would then have linear drift coefficients and constant diffusion coefficients. The exact solution for the time-dependent density of this equation has been given (see e.g. Haken, Advanced Synergetics, Section 10.4.9). The density of the variable of interest, i.e. x in the original DDE, can be obtained by integrating the multivariate probability distribution over all the other degrees of freedom. However, this approach would be useful only for studying equilibria, since the Langevin equation in this case is linear, implying that the deterministic flow can not have limit cycle solutions. Linearization about the oscillatory solution at the Hopf bifurcation may be more fruitful, although the analysis would then involve ODE's with time-dependent coefficients, which considerably complicates the problem.

5.4.3 Understanding the shift from the "map" point of view.

The study of the limit $\alpha\tau \gg 1$, in which the DDE has maplike behavior (Section 4.6), may also yield insight into the origin of the shift, because much is known on the effect of additive and multiplicative noise in maps[22,155]. The study of maps may show how the shift depends on the parameters of the DDE, as well as on the choice of the fluctuating parameter.

In principle, the invariant density for a stochastically perturbed map can be calculated by iterating an initial density using a Markov operator as in (4.2.23) (assuming, as is usually the case, that the fixed point of this operator can not be readily found analytically). Consider first the logistic map with additive noise of density $g(\xi)$

$$x_{i+1} = S(x_i) + \xi_i = \alpha x_i(1 - x_i) + \xi_i \tag{5.4.1}$$

Since the period 2 solution is of interest, α should be slightly greater than 3, the value at which the first period doubling occurs in the deterministic case. The invariant density for the dynamical system (5.4.1) can be obtained by iterating the invariant density corresponding to the deterministic case,

$$f_0(x) = \tfrac{1}{2}\left[\delta(x - x_+) + \delta(x - x_-)\right] \tag{5.4.2}$$

where x_+ and x_- are the two points on the period 2 orbit. The first iteration produces

$$\begin{aligned} f_1(x) = Pf_0(x) &= \int_{-\infty}^{\infty} g\big(S(y) - x\big) f_0(y)\, dy \\ &= \tfrac{1}{2} g\big(S(x_+) - x\big) + \tfrac{1}{2} g\big(S(x_-) - x\big) \\ &= \tfrac{1}{2}\big[g(x_- - x) + g(x_+ - x)\big] \end{aligned} \tag{5.4.3}$$

where we have used the fact that $S(x_+) = x_-$ and $S(x_-) = x_+$ for the period 2 orbit. Note that $f_1(x)$ is simply the convolution of the noise probability density with the initial function (5.4.2).

The logistic map with multiplicative noise on α, i.e. $\alpha = \overline{\alpha} + \xi_i$, is written

$$x_{i+1} = S(x_i, \xi_i) = \overline{\alpha} x_i (1 - x_i) + \xi_i x_i (1 - x_i) \tag{5.4.4}$$

Defining $x_i \equiv y$ and $x_{i+1} \equiv x$, the stochastic variable becomes

$$\xi = \frac{x}{y(1-y)} - \overline{\alpha} \tag{5.4.5}$$

This expression is then substituted for the argument of $g(\xi)$ in (4.2.23). In the multiplicative case, one iteration of (5.4.2) using the resulting Markov operator (4.2.23) yields

$$f_1(x) = \tfrac{1}{2}\Big[g\Big(\frac{\alpha x}{x_+} - \overline{\alpha}\Big) + g\Big(\frac{\alpha x}{x_-} - \overline{\alpha}\Big)\Big] \tag{5.4.6}$$

For Gaussian noise, we have not found it possible to analytically compute the invariant density beyond $f_1(x)$ in either the additive or the multiplicative case. The use of uniformly distributed noise rather than Gaussian noise circumvents the integration problem, but at the expense of tedious bookkeeping for the successive convolutions.

However, this approach based on the Markov operator (4.2.23) sheds some light on the origin of the shift. In fact, from (5.4.3), $f_1(x)$ is the sum of two Gaussians centered about x_+ and x_-. The overlap of the two Gaussians causes the two extrema to move from x_+ and x_- towards the origin. For a given noise variance, this deviation is more pronounced as the amplitude of the deterministic limit cycle $(x_+ - x_-)$ is decreased, i.e. as the bifurcation point is approached. At a critical value of the bifurcation parameter, the two extrema will merge. The shift is simply the difference between this critical parameter value and the deterministic bifurcation parameter.

It has been shown numerically, and analytically using small-Δ perturbation expansions (Δ is the noise variance) around the first period-doubling bifurcation, that both additive and multiplicative noise induce shifts in the logistic map (see Linz and Lücke[155]). In fact, for maps, there is an equivalence between the two types of noise. In general, an additive noise of intensity Δ_{add} has a greater effect than a multiplicative noise of equal intensity Δ_{mult}. For the logistic map, the noise amplitudes have been shown to be equivalent when $\Delta_{add} = (\frac{\alpha-1}{\alpha})\Delta_{mult}$ (Linz and Lücke[155]). This equivalence has been verified numerically for values of α below and above 3. The fact that bifurcation shifts occur in DDE's with either additive or multiplicative noise may in fact be a consequence of the equivalence between these noises in maps.

The study of shifts at the first period-doubling threshold in maps, using either small-Δ expansions or by looking at the action of a Markov operator on the deterministic invariant density, is based on the deterministic bifurcation diagram of the map. It is interesting that the same type of insight into the shift at the Hopf bifurcation in the DDE (5.2.1) can be obtained by looking at the corresponding bifurcation diagram.

It is easier to see this by considering the supercritical case with multiplicative noise in the DDE and in the Landau equation (Appendix A). For both these systems, the bifurcation diagram is the same and involves only one state variable (see inset of Figure 2, Appendix A). One can imagine that fluctuations in the control parameter c (abscissa) are mapped by the bifurcation curve into fluctuations in the limit cycle amplitude X' (ordinate). This mapping occurs for both the upper and the lower branch of the parabola. It is not possible to calculate the density of x' given the density of c, because the mapping (i.e. coordinate transformation) is singular to the left of the bifurcation point (application of the Frobenius-Perron operator requires that the mapping be nonsingular). Nevertheless, the two resulting densities on the y-axis (each one corresponding to one branch of the parabola) will overlap significantly as the bifurcation point is approached or the noise intensity increased. This situation is analogous to that discussed above for the iteration of densities in maps. Hence, it is possible to qualitatively understand the origin of the shift in the DDE by looking at the bifurcation diagram.

6. CONCLUSION

> "J'ai cessé d'ignorer à l'âge de trois ou quatre ans et parfois
> ça me manque."
>
> Romain Gary

This thesis has shown that the macroscopic behavior of neural systems possessing delayed feedback characteristics is amenable to quantitative analysis using tools from nonlinear dynamics and stochastic processes. The motivation for most of the modelling and theoretical work was derived from the analysis of experimentally induced oscillations in a specific neural system, the human pupil light reflex. The study of simple mathematical models in which all parameters can be experimentally measured has provided much insight into neural delayed feedback which is ubiquitous throughout the nervous system. The quantitative analysis of bifurcations in the pupil light reflex has led to a treatment of deterministic and stochastic properties of nonlinear delay-differential equations.

The major conclusions are summarized in the section "Contributions to original knowledge" at the beginning of this thesis. This concluding section is an outlook to investigations of interest for the future.

ORIGIN OF HIPPUS

A major concern in this thesis has been the origin and behavior of the irregular fluctuations in pupil area known as hippus. The analysis in Chapter 3 and in Section 5.3 strongly suggests that hippus is due to noise injected into the pupil light reflex pathways. Pupillary dynamics modify the characteristics of the noise, but do not seem to affect the noise source itself.

However, the possibility that hippus is in part of deterministic origin can not be excluded at this time. If a component of hippus were generated by a chaotic process, it should be possible to induce bifurcations in its dynamics. It is not clear which parameters to vary in order to induce these bifurcations, since hippus occurs in open-loop. In our approach, the functional dependence of retinal light flux on light intensity and pupil area was modified using imposed external feedback. Though producing bifurcations in pupillary dynamics, it did not produce bifurcations in hippus dynamics. Another approach would be to study the effect of drugs (e.g. anaesthetics) on hippus, or to look at hippus in patients with well characterized midbrain lesions.

Two aspects of hippus are of particular interest: 1) the regular $\approx 5sec$-period pupillary oscillations in narcoleptics (and sometimes in normals) which replace the irregular hippus at sleep onset (Section 2.1.3); and 2) the fact that a component of hippus is correlated with respiration. In fact, small constrictions and dilations have been shown to correlate with, respectively, inspiration and exhalation in cats[171] and humans[172]. The respiratory rhythm, whose period is $\approx 4 - 5sec$, may be the origin of the regular oscillations. The proximity of the respiratory centers and pupillary pathways further supports this hypothesis.

The appearance of the regular oscillations occurs when pupil area reaches midrange values, at which pupil gain (and thus hippus amplitude) is highest. It is possible that the activity from the respiratory centers in the midbrain modulates that of neurons in the pupillary pathways, and that the pupil is particularly sensitive to this influence for midrange area values. The five-second rhythm may also be a noisy precursor of a Hopf bifurcation[169] in a neural system whose activity modulates that of the pupil. It may also reflect oscillations in the accommodation reflex at sleep onset. The data on this qualitative change from hippus to periodicity is scarce, and the link between theory and experiment will remain tenuous until more elaborate experiments are carried out.

The study of pupillary oscillations would largely benefit from further experimental investigations into the following problems: 1) the correlation of hippus and accommodation fluctuations; 2) the behavior of the noisy cells and the dilator cells[38] present in the parasympathetic pathways of the pupil light reflex of the cat; 3) the role of the sympathetic pathway and the dynamics of dilation; and 4) the phasic behavior of the retinal cells.

NEURAL DYNAMICS, NOISE AND CHAOS

Noisy oscillations are commonly seen in physiological dynamics[20]. In Section 5.3, the observed aperiodicity of autonomous pupillary oscillations was explained by studying the effect of noise on limit cycle oscillations. An alternate approach would have been to construct a model that generates chaotic behavior in parameter ranges corresponding to our experimental conditions, since this would also yield aperiodic dynamics. However this approach did not seem justified, as previous investigations suggest that noise plays an important role in this reflex. It is possible that noisy oscillations in many physiological systems correspond, in fact, to simple deterministic motion complicated by noise-induced transitions and noise amplification, leading to large fluctuations in amplitude, period and phase.

How long the current flurry of interest in chaotic dynamics will last will depend, to a large extent, on what phenomena chaos can explain. Chaos tells us that the centuries old assumption that a Newtonian world is predictable, stable and orderly may be a mistake, and that a complete description of nature must include complicated behavior as well[173]. As a means of probing irregular behavior, chaos is similar to statistical mechanics which provided new mathematical tools to study systems exhibiting statistical behavior. In my opinion, the study of chaos and of its interaction with noise will continue to deepen our understanding of randomness and of irreversible processes in nature (see e.g. Eckmann and Ruelle[174]; Wolfram[175]; Mackey[176]).

POSTPONEMENT OF HOPF BIFURCATION IN DDE's

For a system of stochastically perturbed ODE's, a multivariate stationary probability density can be calculated from the Fokker-Planck equation (Section 4.2.2). Considered in the center manifold, the Hopf bifurcation in an n-dimensional system essentially reduces to a two-dimensional problem (Section 5.1). The symmetry of the corresponding two-dimensional probability density will depend on the coupling of the noise to the angular variable as well as to the radial variable[148,177]. Hence, (one-dimensional) density profiles in planes cutting this density at different angles may be different. This implies that determining the bifurcation point by looking at one-dimensional densities (obtained either by approximating the solution of the Fokker-Planck equation or for special cases as in Appendix A) may lead to erroneous results.

Criteria have been defined to pinpoint the occurrence of a Hopf bifurcation by looking at the two-dimensional probability density constructed from two time series. In the presence of noise, this density will appear as a ring of mountains of varying heights with a crater at its center. Fronzoni et al. have suggested that the Hopf bifurcation occurs at the parameter value at which the floor of the crater reaches the lowest mountain in the ring.

It is possible that the one-dimensional densities used to pinpoint the Hopf bifurcation in stochastic first order DDE's (Section 5.3) correspond to projections of a multivariate density which does not have rotational symmetry. It would be interesting to study the Hopf bifurcation in these DDE's by applying the criterion of Fronzoni et al.[148] to two-dimensional densities in which, $x(t)$ and $x(t-\tau)$ are the independent coordinates.

The magnitude of the shift of the bifurcation point should depend on the ratio

$\alpha\tau$ of the delay to the response time of the system. When this ratio is small, the DDE behaves more like an ODE, while it behaves more like a map when the ratio is large (Sections 4.4 and 4.6). Since additive noise can not induce shifts in the point of oscillation onset in one-dimensional ODE's (see Ref. 21 and Appendix A) but can in one-dimensional maps, shifts due to additive noise should be more obvious at large delays. This would imply that the maplike properties of the DDE are responsible for the noise-induced transitions in the presence of additive noise. This conjecture remains to be investigated.

BIFURCATIONS IN NEURAL SYSTEMS AND DYNAMICAL DISEASES

In numerical simulations, extremely long time series are needed to resolve the extrema of the stationary density near a Hopf bifurcation. Hence, the analysis of even a simple bifurcation in a noisy neural system from the density point of view may not be possible due to the limited length of the data sets. Rather, the analysis can focus on the influence of the fluctuations on certain measurable quantities, such as the mean and variance of the amplitude and period, as in Section 5.3. The theoretical knowledge of the behavior of the densities can guide the analysis and indicate what special features to look for.

The postponement of the Hopf bifurcation in first order DDE's is proportional to the noise intensity and inversely proportional to the noise correlation time (Section 5.3). If the noise level decreases or the noise correlation time increases, all other parameters remaining constant, then the oscillation will become more prominent, because the noise would no longer be strong enough to stabilize the equilibrium solution. This suggests a mechanism whereby external and internal noise sources can control an oscillation. Applied to physiology, this mechanism also extends the concept of dynamical disease (see Refs. 20, 54 and the Introduction) by allowing noise characteristics to be bifurcation parameters, a possibility already recognized in the field of noise-induced transitions.

NEURAL OSCILLATORS AND MEMORY

The frequency of the limit cycle that appears at the Hopf bifurcation is a slowly varying function of the bifurcation parameter (except when this parameter is the delay) (see Sections 2.2.8 and 2.3.7). Further, the period of the limit cycle is less vulnerable than the amplitude to additive and multiplicative noise (Section 5.3). These two facts suggest that a neural circuit modelled by a delayed feedback equation of the type considered in this thesis could be used as a time reference (like the clock in a computer) if maintained in the vicinity of its Hopf bifurcation point. One possible circuit to perform this function could be the reverberatory circuits proposed in certain theories of memory (see e.g. MacGregor and Lewis[178]).

Feedback systems with a distribution of delays (modelled by an integro-differential equation like (4.4.5)) are less prone to oscillate than systems with fixed delays (Section 4.4). This fact may have interesting implications for the theory of memory. For example, it may imply that "memories" that are localized in time destabilize delayed feedback systems. It remains to be seen if the oscillation period of distributed delay systems is as robust with respect to additive and multiplicative noise as that for fixed delay systems.

Finally, a correspondence may be drawn between the stabilization of the equilibrium by distributed delays and the postponement of the onset of oscillatory behavior by noise. In a certain sense, it appears plausible to view the disorganizing influence of noise as similar to the operation of a system with distributed delays. In other words, it may be possible to establish an equivalence between additive or parametric fluctuations and fluctuations in the delay. From this point of view, the postponement of the Hopf bifurcation by noise is compatible with the stabilization of the equilibrium by distributed delays.

EPILOGUE

Our detailed theoretical and experimental study of oscillatory behavior in a specific neural system puts us in a position to extend our conclusions to broader classes of physiological systems in particular, and more generally to nonlinear physical systems in which delayed action is an essential part of the dynamics. Although it may be very difficult to experimentally verify modelling predictions, especially in physiological systems where noise levels are high, further studies based on the approach of this thesis may provide clues of the phenomena to look for, and of how to perturb and analyze these phenomena.

If a professor were to tell me that he is trying to get his physics graduate student interested in pursuing some of the directions outlined in this concluding chapter, I would probably wish this professor "Good luck". However, if this innocent graduate student actually sees a six inch-wide pupil gently swaying to the vagaries of hippus on a TV monitor, he just may, like I was, or like Alice peering through the looking glass, be enthralled and plunge into the mirror of the soul.

APPENDICES

Appendix A consists of the manuscript of a paper in press in the *Journal of Statistical Physics*. It is shown that additive or multiplicative Gaussian noise induce global asymptotic stability in two dynamical systems. The dynamical systems are two-dimensional ODE's in which the noise affects only the dynamics of the radial variable (in polar coordinates). The resulting one-dimensional stochastic differential equation is often referred to as "a reduced amplitude equation". The first equation, known as the Landau equation, exhibits a supercritical Hopf bifurcation, while the second system exhibits a subcritical Hopf bifurcation. Global asymptotic stability implies that the stationary solution of the corresponding Fokker-Planck equation is globally attracting in the space of initial functions. In other words, the limiting density is independent of the initial density. This study also discusses noise-induced transitions (Sections 5.2 and 5.3) at the Hopf bifurcation due to multiplicative noise.

Appendix B presents a study (published in the *American Journal of Ophthalmology*) of pupillary oscillations induced by piecewise constant negative feedback (as in Section 3.2) in patients affected by the demyelinative disease known as multiple sclerosis. (A demyelinative disease causes the nerve axons to lose the insulating myelin sheath which is responsible for the special type of wave propagation known as saltatory conduction[35].) One of the first signs of multiple sclerosis is optic neuritis, in which the optic nerve undergoes partial demyelination. This causes intermittent conduction block and an increase in propagation delay. One way to diagnose multiple sclerosis is to shine a narrow light beam on the pupillary margin and observe whether the period of the resulting "high gain" oscillations (pupil cycling) differs from an established norm. This test is difficult to carry out for reasons discussed in the paper. Our new method for pupil cycling eliminates many of the artifacts of the usual method, and provides a sensitive measure of demyelination. The method indicates that more information is readily available from pupil cycling amplitude rather than period measurements. It also allows one to discriminate between demyelination and ischemia in the optic nerve. The theoretical basis for this method is found in Section 3.2.

Appendix C describes the fitting techniques used in Sections 3.2, 3.3 and 3.4.

Appendix D contains the source code for the most important programs used in this thesis. We give the algorithm for the "exact" numerical integration of the first order DDE with piecewise constant mixed feedback encountered in Sections 3.3 and 3.4. The program for the numerical integration of the stochastic delay-differential equation 5.1.1 with additive and/or multiplicative colored noise is also given, along with that for the numerical integration of the C1D2 model in Section 3.4.5.

The programs were run on either a Hewlett-Packard 9816, a NEC Powermate Plus (AT) or a VAX 3200. The 3D graphics and density normalization in Appendix A as well as the FFT's in Section 5.3 were done on MATLAB. The thesis was typeset using *AmS-TeX*.

APPENDIX A

NOISE INDUCED GLOBAL ASYMPTOTIC STABILITY

Abstract. In this paper we prove analytically that additive and parametric (multiplicative) Gaussian distributed white noise, interpreted in either the Ito or Stratonovich formalism, induce global asymptotic stability in two prototypical dynamical systems designated as supercritical (the Landau equation) and subcritical respectively. In both systems without noise, variation of a parameter leads to a switching between a single globally stable steady state and multiple locally stable steady states. With additive noise this switching is mirrored in the behaviour of the extrema of probability densities at the same value of the parameter. However, parametric noise causes a noise amplitude dependent shift (postponement) in the parameter value at which the switching occurs. It is found both analytically and numerically that the density converges to a Dirac delta function when the solution of the Fokker-Planck equation is no longer normalizable.

A.1. Introduction.

The effects of additive and parametric (multiplicative) noise in nonlinear dynamical systems has been the object of intense study[21]. Systems that display bifurcations in dynamics in the absence of noise have received the most attention, in part because noise effects in these systems qualitatively mimic 1st and 2nd order phase transitions[21].

The presence of noise in combination with dynamics leads to a situation in which one may describe the global behaviour of the system by the evolution of densities. That evolution is described by the Fokker-Planck (parabolic) partial differential equation. The steady state solutions to the Fokker-Planck equation are known as stationary densities.

Most studies[179-181] indicate that additive noise, a term usually taken to imply that noise amplitude is independent of the state variable(s), leads to a bifurcation in the qualitative form of the stationary density at precisely the same parameter value at which the bifurcation occurred in the noise free system. However parametric noise, in which the noise amplitude depends on the state variable(s), induces different behaviours in the stationary density Usually [177 182 183] parametric noise induces a noise amplitude dependent postponement in the parameter value at which these qualitative changes in the stationary density take place relative to the noise free system, though one study [152] indicates the possibility of an advancement in the bifurcation parameter depending on the relative values of the noise correlation time and the system response time.

In spite of the intense interest in the changes that additive and parametric noise give rise to in stationary densities, there has not–to our knowledge–been any proof of the global convergence of the time dependent solutions of the Fokker-Planck equation to the (generally unique) stationary density. In this paper we consider two prototypical systems in the presence of additive and parametric noise, and use a recent result to prove the global asymptotic stability of the solutions of the Fokker-Planck equation.

A.2. Preliminaries.

A.2.1. The Model Systems.

In our investigation of the effects of additive and parametric noise, we will consider two specific systems.

Supercritical System. The two dimensional oscillator system

$$\begin{aligned} \frac{dr}{dt} &= r(c - r^2) \\ \frac{d\theta}{dt} &= 2\pi \end{aligned} \tag{A1}$$

in (r, θ) space is an example of a system with a supercritical Hopf bifurcation. For $c < 0$ the origin $r_* = 0$ is the globally stable steady state, while for $c > 0$ all solutions are attracted to the limit cycle defined by $r = \sqrt{c}$.

Here we consider the effects of noise in the analogous one dimensional system

$$\frac{dx}{dt} = x(c - x^2), \tag{A2}$$

obtained by ignoring the angular coordinate θ in equations (A1), and designate this the *supercritical system.* This equation appears, for example, as the reduced amplitude equation for systems undergoing a supercritical Hopf bifurcation[153,179–184]. For equation (A2), it is simple to show that when $c < 0$ all solutions are attracted to the single steady state $x_* = 0$. Further, when $c > 0$ the steady state $x_* = 0$ is unstable and $x(t) \rightarrow \sqrt{c}$ if $x(0) = x_0 > 0$, while $x(t) \rightarrow -\sqrt{c}$ for $x_0 < 0$.

Subcritical System.

A second simple oscillator system

$$\begin{aligned} \frac{dr}{dt} &= r(c + 2r^2 - r^4) \\ \frac{d\theta}{dt} &= 2\pi \end{aligned} \tag{A3}$$

has a subcritical Hopf bifurcation at $c = -1$, as have other systems studied in the presence of noise[179,182].

In analogy with the previous case, we treat the effects of noise in the one dimensional system

$$\frac{dx}{dt} = x(c + 2x^2 - x^4), \tag{A4}$$

which we call the *subcritical system.* The solutions of equation (A4) have the following behaviour. For $c < -1$ all solutions $x(t) \rightarrow 0$ regardless of the initial condition x_0. However, for $-1 < c < 0$ there is a tristability in that

$$x(t) \rightarrow \begin{cases} -\sqrt{1+\sqrt{1+c}}, & \text{for } x_0 < -x_*^+ \qquad \text{and } -x_*^+ < x_0 < -x_*^- \\ 0, & \text{for } -x_*^- < x_0 < x_*^- \\ \sqrt{1+\sqrt{1+c}}, & \text{for } x_*^+ < x_0 \qquad \text{and}\, x_*^- < x_0 < x_*^+. \end{cases} \tag{A5}$$

where $x_*^+ = \sqrt{1+\sqrt{1+c}}$ and $x_*^- = \sqrt{1-\sqrt{1+c}}$. For $c > 0$, the steady state $x_* = 0$ becomes unstable and this tristable behaviour gives way to a bistability such that

$$x(t) \rightarrow \begin{cases} -\sqrt{1+\sqrt{1+c}}, & \text{for } x_0 < 0 \\ \sqrt{1+\sqrt{1+c}}, & \text{for } x_0 > 0. \end{cases} \tag{A6}$$

A.2.2 Densities and the Fokker-Planck Equation.

In considering the effects of noise in systems like (A2) or (A4), we may think of the general one dimensional differential equation

$$\frac{dx}{dt} = g(x),$$

and the corresponding stochastic differential equation

$$\frac{dx}{dt} = g(x) + \sigma(x)\xi, \tag{A7}$$

where ξ is a (Gaussian distributed) white noise perturbation with zero mean and unit variance, and $\sigma(x)$ is the amplitude of the perturbation.

Under some standard regularity conditions, the process $x(t)$, which is the solution of the stochastic differential equation (A7), has a density function $u(t,x)$ defined by

$$prob\{a < x(t) < b\} = \int_a^b u(t,z)\,dz, \qquad a,b \in R.$$

It is well known that the density $u(t,x)$ satisfies the parabolic differential equation (*Fokker-Planck equation*)

$$\frac{\partial u}{\partial t} = \frac{1}{2}\frac{\partial^2[\sigma^2(x)u]}{\partial x^2} - \frac{\partial[G(x)u]}{\partial x} \tag{A8}$$

where the function G is given by

$$G = g \tag{A9a}$$

when the Ito calculus is used to interpret (A7), or

$$G = g + \frac{1}{4}\frac{\partial[\sigma^2(x)]}{\partial x} \tag{A9b}$$

when the Stratonovich calculus is used[21]. The Fokker-Planck equation can also be written in the equivalent form

$$\frac{\partial u}{\partial t} = -\frac{\partial S}{\partial x} \tag{A10}$$

where

$$S = -\frac{1}{2}\frac{\partial[\sigma^2(x)u]}{\partial x} + Gu \tag{A11}$$

is called the *probability current.*

As usual, we say that an L^1 function f is a density if f is nonnegative and its integral over its domain is identically equal to 1, i.e., it is *normalized.* Given an initial density $f(x) = u(0,x)$ and the solution $u(t,x)$ of (A8) we may write this solution formally as

$$u(t,x) = P_t f(x),$$

where P_t is a *Markov operator*, i.e. P_t is a linear operator and for every density f, $P_t f$ is also a density. Thus the Fokker-Planck equation governs the evolution of the flow of densities $\{P_t f\}$.

When stationary solutions of (8), denoted by $f_*(x)$ and defined by $P_t f_* = f_*$ for all t, exist they are given as the generally unique (up to a multiplicative constant) solution of

$$\frac{1}{2}\frac{\partial^2[\sigma^2 f_*]}{\partial x^2} - \frac{\partial[G f_*]}{\partial x} = 0. \tag{A12}$$

Integration of equation (A12) by parts with the assumption that the probability current S vanishes at the integration limits, followed by a second integration yields the solution

$$f_*(x) = \frac{K}{\sigma^2(x)} exp\left[\int^x \frac{2G(z)}{\sigma^2(z)}\,dz\right]. \tag{A13}$$

This stationary solution f_* will be a density if and only if there exists a positive constant $K > 0$ such that f_* can be normalized.

A.3. Additive Noise.

For the supercritical system (A2) and the subcritical system (A4) in the presence of additive noise, the corresponding stochastic differential equations are of the form

$$\frac{dx}{dt} = g(x) + \sigma\xi \tag{A14}$$

where σ is a positive constant and

$$g(x) = \begin{cases} x(c - x^2), & \text{supercritical} \\ x(c + 2x^2 - x^4), & \text{subcritical.} \end{cases} \tag{A15}$$

Thus in the additive noise case, reference to equations (A14) and (A15) makes it clear that there is always a positive probability that $x(t)$ may take on negative values starting from a positive position and *vice versa*. Therefore it is natural to consider this problem for $-\infty < x < \infty$.

Furthermore, since the noise amplitude σ is constant with additive noise, equations (A9a) and (A9b) make it clear that the corresponding Fokker-Planck equations are identical in the Ito and Stratonovich interpretations. Specifically, they take the forms

$$\frac{\partial u}{\partial t} = \frac{1}{2}\sigma^2\frac{\partial^2 u}{\partial x^2} - \frac{\partial}{\partial x}[x(c - x^2)u] \tag{A16}$$

and

$$\frac{\partial u}{\partial t} = \frac{1}{2}\sigma^2\frac{\partial^2 u}{\partial x^2} - \frac{\partial}{\partial x}[x(c + 2x^2 - x^4)u] \tag{A17}$$

in the super- and subcritical cases respectively.

A.3.1 Stationary Solutions.

It is straightforward to show that the stationary solution (A13) to the Fokker-Planck equation (A12) is given by

$$f_*(x) = K_1 e^{\beta x^2(2c - x^2)/4c} \tag{A18}$$

for the supercritical system, where $\beta = 2c/\sigma^2$, and by

$$f_*(x) = K_2 e^{\beta x^2(3c+3x^2-x^4)/6c} \tag{A19}$$

for the subcritical system. It is easy to show that the normalization constants K_1 and K_2 always exist and thus the $f_*(x)$ defined by (A18) and (A19) are stationary densities.

In Figure A.1a we show the stationary density given in equation (A18) for the supercritical system as a function of the parameter c. As might be expected on intuitive grounds, for $c < 0$ the stationary density $f_*(x)$ has a single maximum centered at $x = 0$, the location of the globally stable steady state of the unperturbed system (A2). Once $c > 0$, the stationary density $f_*(x)$ shows two maxima centered at $x = \pm\sqrt{c}$, the locally stable steady states of (A2), and a local minimum at the unstable steady state $x = 0$.

Figure A.1b shows the stationary density for the subcritical system, again as a function of c, given in equation (A19). For $c < -1$, the stationary density $f_*(x)$ has a single maximum located at $x = 0$, the globally stable steady state of the unperturbed system (A4). For $-1 < c < 0$, where the tristable behaviour of (A4) occurs, the stationary densities still have an absolute maximum at $x = 0$ but also display maxima at $x = \pm\sqrt{1+\sqrt{1+c}}$ that become progressively more prominent as c increases. Finally, for $c > 0$ the stationary density has absolute maxima located at $x = \pm\sqrt{1+\sqrt{1+c}}$ and a local minimum at $x = 0$.

A.3.2 Asymptotic Stability of the Stationary Solutions.

We now turn to a consideration of the stability of the stationary densities determined in the previous section.

We first define the property of stability by saying that equation (A8) is ***globally asymptotically stable*** if

$$\lim_{t\to\infty} u(t,x) = \lim_{t\to\infty} P_t f(x) = f_*(x)$$

for *all* initial densities $f(x)$, i.e. $P_t f$ converges to f_* in L^1 norm[13]. We will alternately say that f_* is *globally asymptotically stable* under this circumstance.

For parabolic equations whose solutions are given by an integral operator with a sufficiently smooth kernel, it is possible to prove their global asymptotic stability *via* a Liapunov function approach. Both Fokker-Planck equations (A16) and (A17)

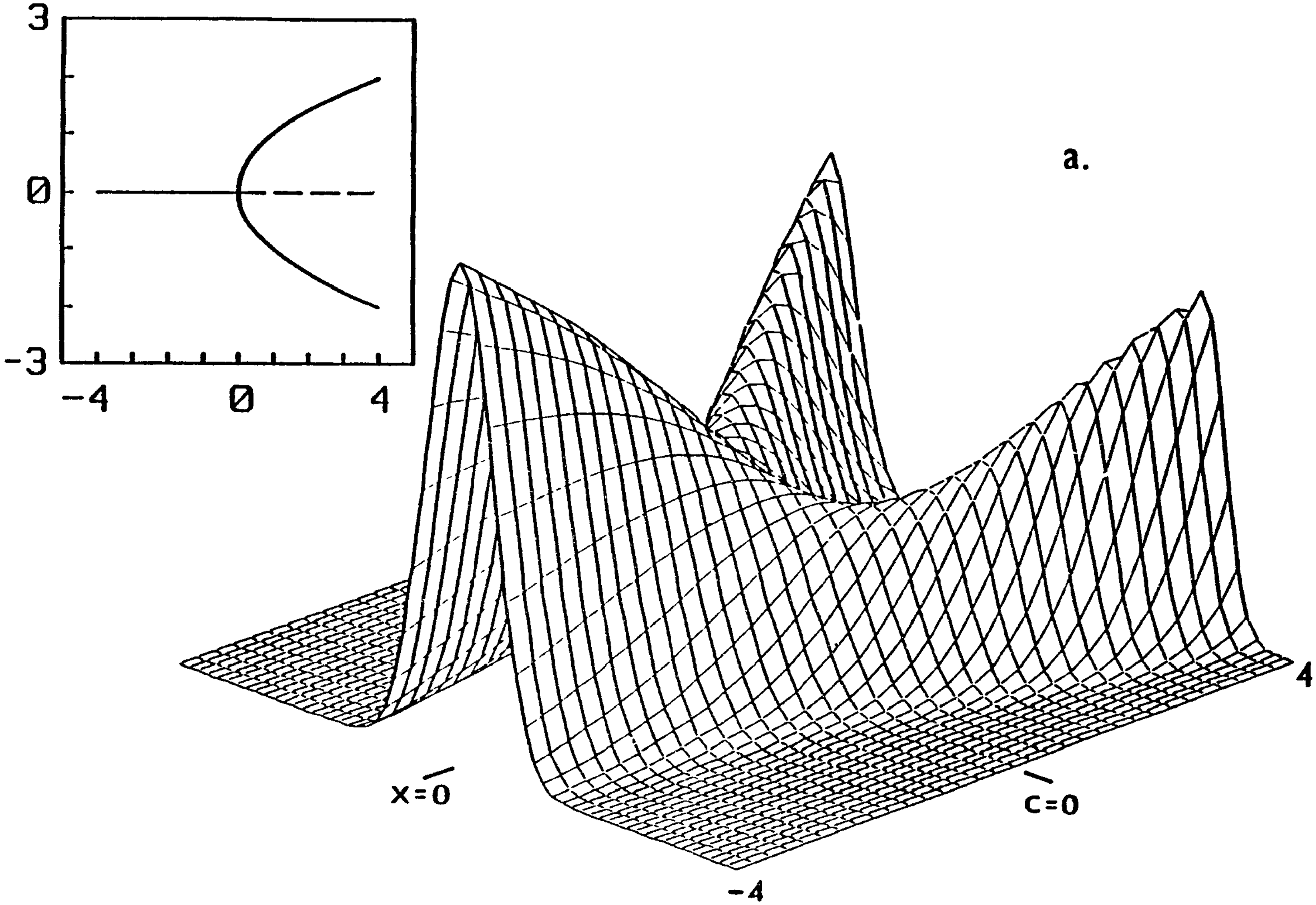

Figure A.1 Globally stable stationary densities in the presence of additive noise, as functions of x and the parameter c, for (a) the supercritical system (A2) and (b) the subcritical system (A4). To aid in visualization, in each the insert shows the location of the maxima in the stationary density as a solid line in the (c, x) plane. The dashed line in the insert of (b) corresponds to the minimum in the density.

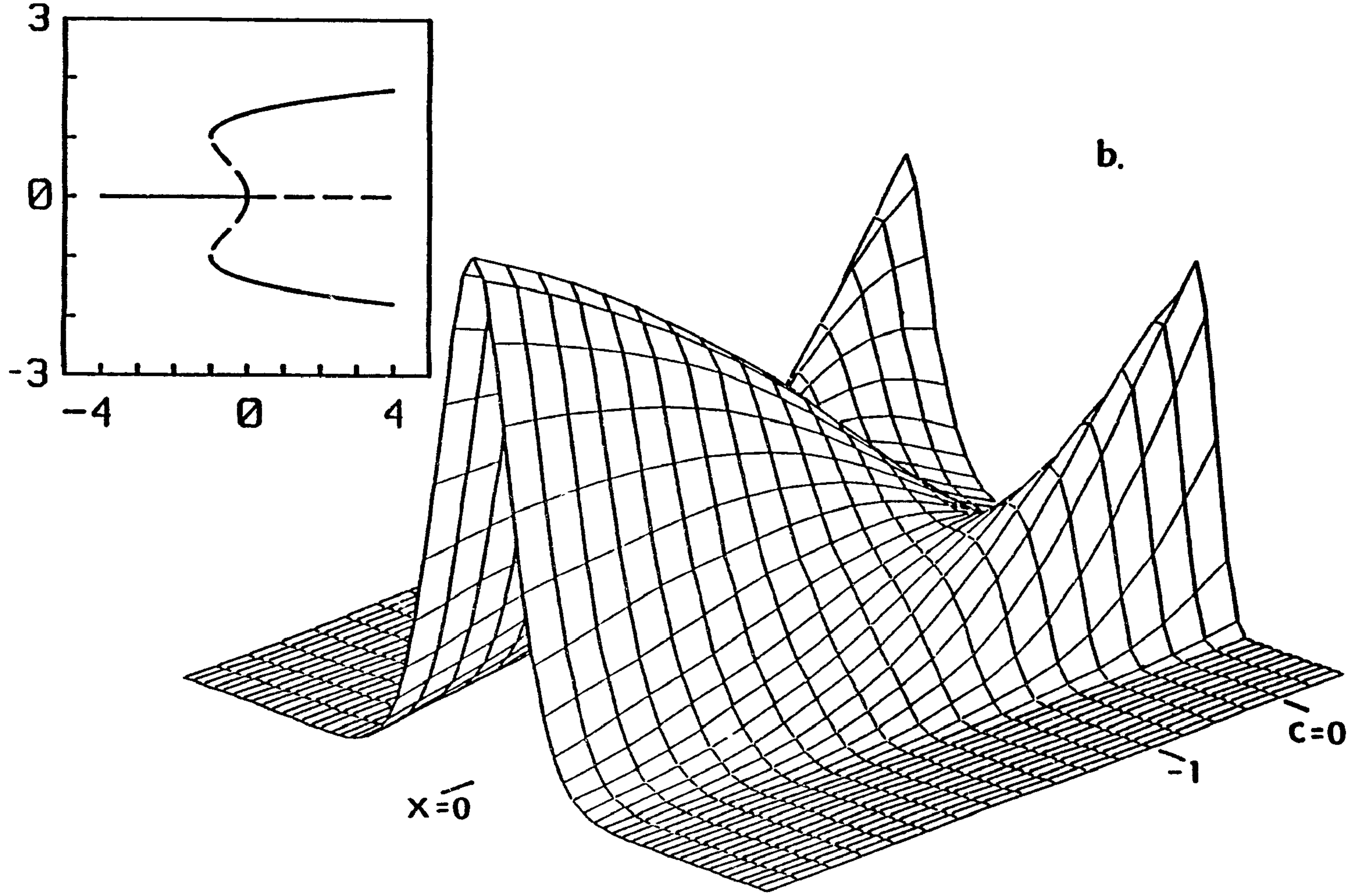

Figure A.1b

are quite regular from this point of view since they are uniformly parabolic (σ^2 is a positive constant) and $xg(x) < 0$ for sufficiently large x. These properties ensure that the solutions of equations (A16) and (A17) will decay at least exponentially as $x \to \pm\infty$.

We define a *Liapunov function* $V : R \to R$ as a C^2 function with the following properties:

1) $V(x) \geq 0$ for all x;
2) $\lim_{x\to\pm\infty} V(x) = \infty$; and
3) $V(x) \leq \rho e^{\delta|x|}$ and $|dV/dx| \leq \rho e^{\delta|x|}$ for some positive constants ρ and δ.

It has been shown[13] that the existence of a Liapunov function V satisfying

$$\sigma^2 \frac{\partial^2 V}{\partial x^2} + g(x)\frac{\partial V}{\partial x} \leq -\alpha V(x) + \beta, \tag{A20}$$

where α and β are positive constants, implies that the Fokker-Planck equation (A8) is globally asymptotically stable.

Let $V(x) = x^2$ so V is a Liapunov function, and consider the supercritical system with additive noise. Inequality (A20) becomes, in this case,

$$2\sigma^2 + (2c+\alpha)x^2 - 2x^4 \leq \beta. \tag{A21}$$

This is clearly satisfied for arbitrary fixed $\alpha > 0$ and sufficiently large $\beta > 0$, thus proving the global asymptotic stability of the Fokker-Planck equation (A16) for additive noise applied to the supercritical system (A2).

Retain $V(x) = x^2$ for the subcritical system (A4) with additive noise. An entirely analogous argument suffices to show that positive constants α and β can be found such that inequality (A20) is satisfied, thus establishing the global asymptotic stability of equation (A17).

Hence, the entrance of white noise perturbations to either the supercritical or subcritical systems (A2) and (A4) in an additive fashion always leads to globally asymptotically stable behaviour.

A.4. Parametric Noise.

Both the supercritical and subcritical systems contain a single parameter c, and in this section we investigate the effects of noise in this parameter by replacing c with

$$c + \sigma\xi,$$

where $\sigma > 0$ is a constant. As a result of this assumption, the stochastic differential equation (A7) takes the form

$$\frac{dx}{dt} = g(x) + \sigma x \xi, \tag{A22}$$

where $g(x)$ is given by equation (A15). From equation (A22) in conjunction with (A15) it is clear that $x(t) = 0$ is always a solution. Therefore, for any $x_0 > 0$ the solution $x(t)$ will always be positive. For $x_0 < 0$ we will have $x(t) < 0$. Thus in contrast to the situation with additive noise, in the presence of parametric noise we need only consider $-\infty < x \leq 0$ or $0 \leq x < \infty$. As the results are symmetric, we take $0 \leq x < \infty$.

With parametric noise, it is no longer the case that the Fokker-Planck equation corresponding to (A22) will be the same for the Ito and Stratonovich interpretations[21]. Hence, assume first that we are using the Ito calculus, and replace c by c_I to denote this distinction. Then, using (A8) and (A9a) the corresponding Fokker-Planck equations are

$$\frac{\partial u}{\partial t} = \frac{1}{2}\sigma^2 \frac{\partial^2 [x^2 u]}{\partial x^2} - \frac{\partial}{\partial x}[x(c_I - x^2)u], \qquad \text{supercritical} \tag{A23}$$

and

$$\frac{\partial u}{\partial t} = \frac{1}{2}\sigma^2 \frac{\partial^2 [x^2 u]}{\partial x^2} - \frac{\partial}{\partial x}[x(c_I + 2x^2 - x^4)u], \qquad \text{subcritical.} \tag{A24}$$

A.4.1 Stationary Solutions.

Supercritical System.

For parametric noise in the supercritical system it is a straightforward application of equation (13) to show that the stationary solution $f_*(x)$ of the Fokker-Planck equation (23) is given by

$$f_*(x) = K x^{\gamma} e^{-x^2/\sigma^2}, \tag{A25}$$

where $\gamma = (2c_I/\sigma^2) - 2$.

With parametric noise, a stationary density will not exist for some parameter values. In order that f_* is a density, it must be integrable on R^+, and from (25) this is only possible if $\gamma > -1$, or

$$c_I > \frac{1}{2}\sigma^2. \tag{A26}$$

Thus, in sharp contrast to the results for additive noise, for parametric noise a stationary density $f_*(x)$ in the supercritical case exists for only a limited range of values of the parameter c_I as defined by inequality (A26).

In Figure A.2 we show the graph of the stationary densities $f_*(x)$ given by equation (A25) for the range of c_I values for which it exists. For $(\sigma^2/2) < c_I < \sigma^2$ the density has a single maximum at $x = 0$. However, once $c_I > \sigma^2$, the stationary density $f_*(x)$ has a local minimum at $x = 0$ and a maximum at $x = \sqrt{c_I - \sigma^2}$. Thus, with parametric noise there is not only a shift in the value of the parameter c_I at which there is a transition between the stationary density having a maximum at $x = 0$ and a nonzero value of x, but there is also a shift in the nonzero location of the maximum in the stationary density below that of the globally stable steady state in the absence of noise ($x = \sqrt{c_I}$) toward zero. It is only as c_I becomes large that the location of the density maximum starts to approximate $\sqrt{c_I}$.

All of these calculations and conclusions are precisely the same if the Stratonovich interpretation is used in place of the Ito formulation. One must only replace c_I everywhere by $c_S = c_I + (\sigma^2/2)$ for the formulae and conclusions to be applicable to the Stratonovich case.

Subcritical System.

As in the previous section it is an elementary consequence of equation (A13) that the stationary solution of the (Ito) Fokker-Planck equation for the subcritical case with parametric noise is given by

$$f_*(x) = Kx^{\gamma}e^{x^2(4-x^2)/2\sigma^2}, \qquad \text{(A27)}$$

where γ is as before. For the $f_*(x)$ defined in (A27) to be a stationary density, precisely the same conditions must hold as for the supercritical system of the previous section. Namely, $f_*(x)$ will be a stationary density of the Fokker-Planck equation if and only if inequality (A26) is satisfied.

Figure A.3 graphically presents the stationary density given by (A27) for the range of c_I for which inequality (A26) is satisfied. The density for the subcritical system in the presence of parametric noise has two qualitatively different behaviours as the parameter c_I is varied. The appearance of either of these behaviours depends on the noise amplitude, σ.

For noise amplitudes satisfying $0 < \sigma^2 < 2$, a new feature unobserved in the supercritical system appears as shown in Figure A.3a. Namely, for f_* defined by (A27) and this range of σ, as c_I is increased past $\sigma^2/2$, f_* may be normalized, and the resulting stationary density has a maximum located at

$$x = \sqrt{1 + \sqrt{1 + c_I - \sigma^2}} \qquad \text{(A28)}$$

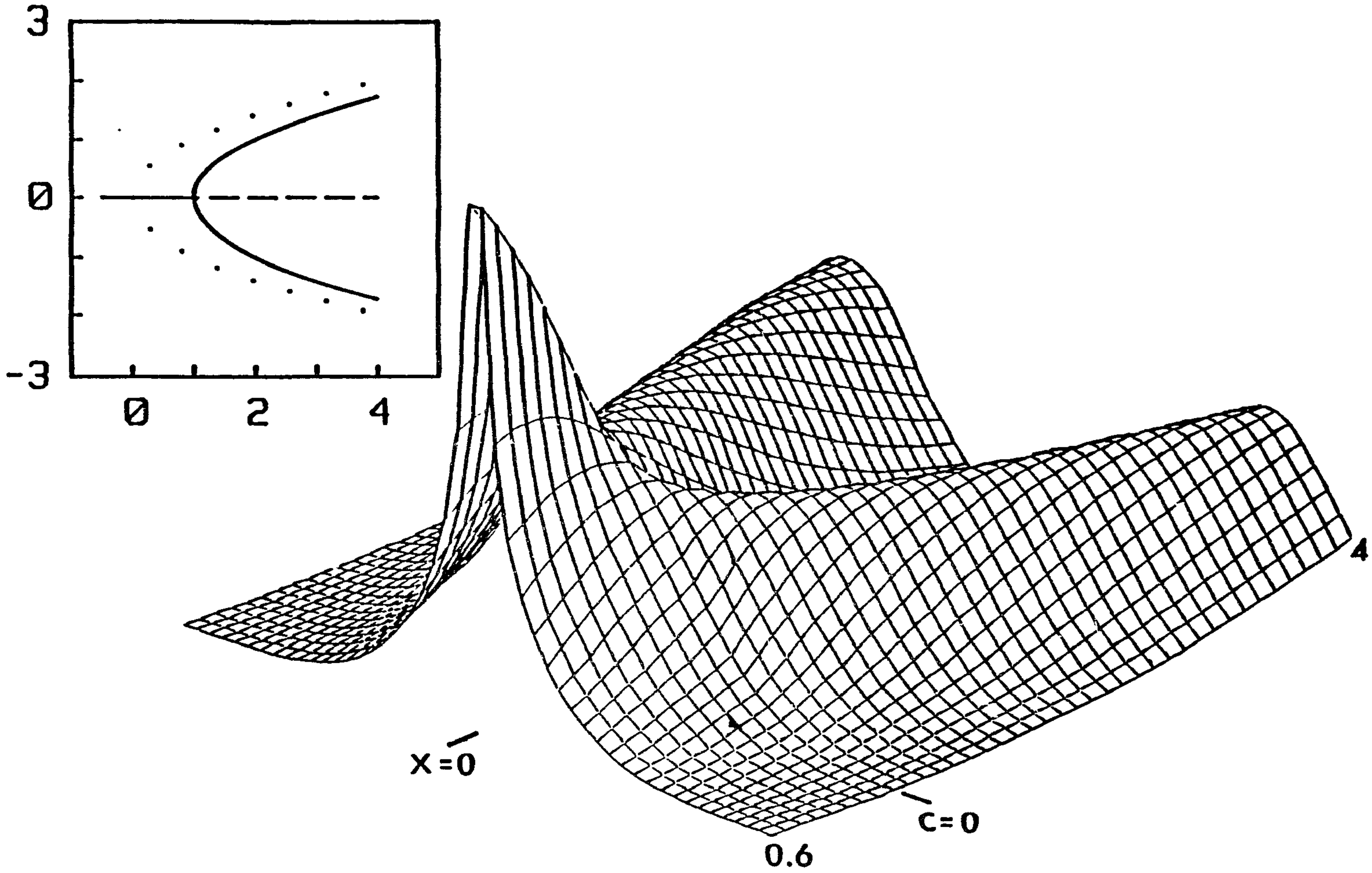

Figure A.2 Globally stable stationary densities for the supercritical system (A2) with parametric noise under the Ito interpretation. For clearer viewing, the density for $0 \leq x$ is reflected as a mirror image to $x < 0$ and also displayed. The inset shows the location of the maxima (solid line) and minima (dashed line) of the densities in the (c_I, x) plane, and the location of the globally stable steady states (dotted line) in the absence of noise.

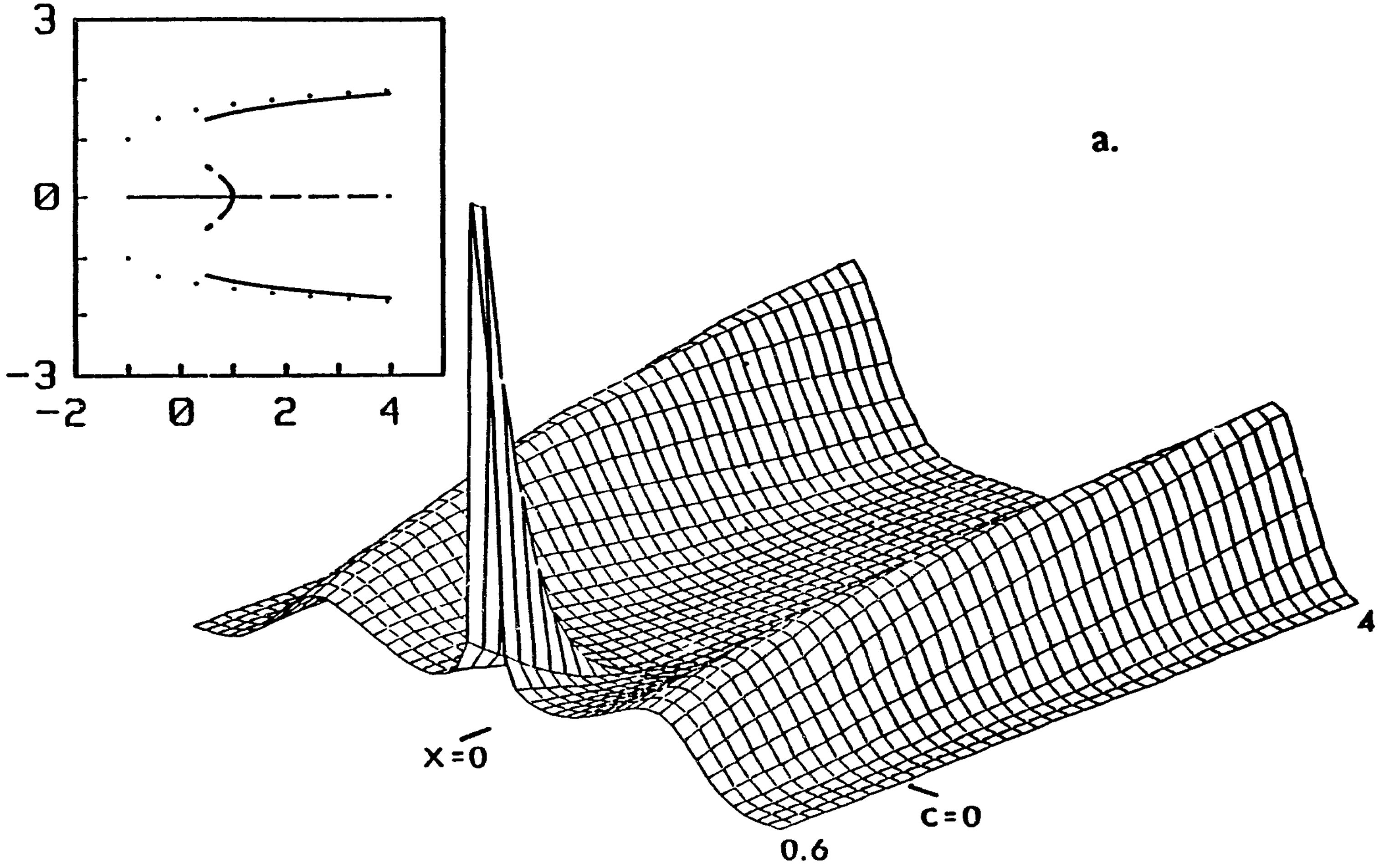

Figure A.3 Globally stable stationary densities for the subcritical system (A4) in the presence of parametric noise (Ito interpretation), reflected across the x axis as in Figure A.2. In (a) the qualitative situation for $0 < \sigma^2 < 2$ is depicted using $\sigma^2 = 1$, while (b), with $\sigma^2 = 3$, illustrates the qualitative features found when $2 < \sigma^2$. In both (a) and (b), the line types in the inserts have the same meaning as in Figure A.2.

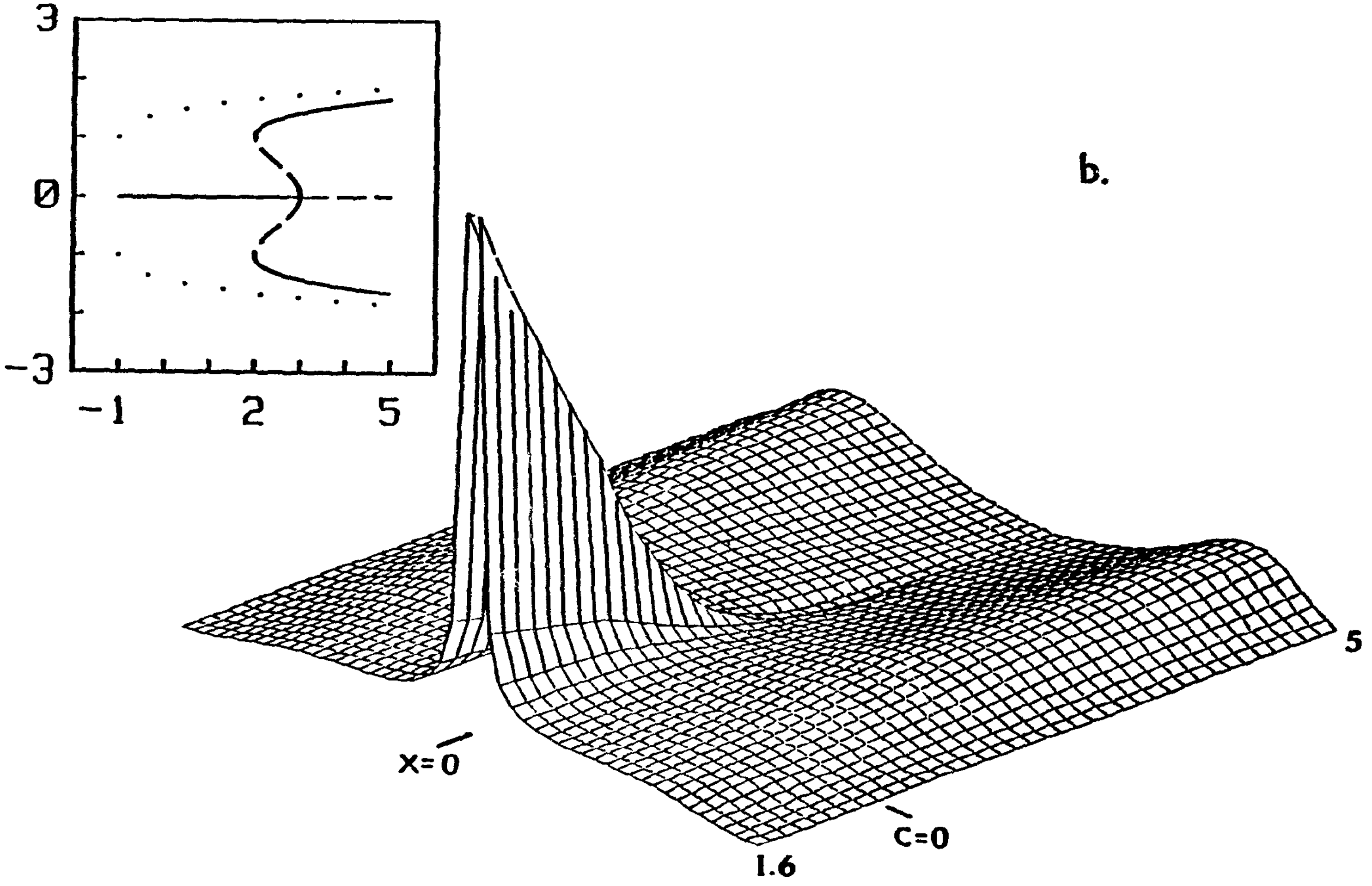

Figure A.3b

and a singularity at $x = 0$ which only exists for $(\sigma^2/2) < c_I < \sigma^2$. (The condition $0 < \sigma^2 < 2$ may seem dimensionally incorrect at first glance. However, it is simply a consequence of the choice of parameters in equations A3.)

However, as illustrated in Figure A.3b, for higher noise amplitudes such that $\sigma^2 > 2$, for $(\sigma^2/2) < c_I < \sigma^2 - 1$ the density f_* has a single maximum located at $x = 0$. As c_I is increased, once $\sigma^2 - 1 < c_I$ then f_* has a relative maximum at $x = 0$ and a second maximum located at the same location (see equation A28) as for $\sigma^2 < 2$. For all values of σ^2, as c_I is increased the location of this maximum tends toward the value of the nonzero steady state $x = \sqrt{1 + \sqrt{1 + c_I}}$ of the unperturbed system (A4).

As before, one need only replace c_I by c_S to obtain the corresponding Stratonovich results.

A.4.2 Asymptotic Stability with Parametric Noise.

In trying to prove that the stationary densities induced by parametric noise are globally asymptotically stable, we no longer have immediately available the Liapunov function technique that we were able to apply so easily in the case of additive noise. This is because with parametric noise, the coefficient $(\sigma^2 x^2/2)$ vanishes at $x = 0$ and the uniform parabolicity condition is violated at $x = 0$. This fact is crucial.

However, by a straightforward change of variables, we may transform the Fokker-Planck equations (A23) and (A24) to circumvent this problem, and then again apply the Liapunov function argument.

Define a new variable $y = \ln x$ and a new density $\tilde{u}$ by

$$\tilde{u}(t, y) = e^{2y} u(t, e^y). \tag{A29}$$

With these changes, the Fokker-Planck equations (A23) and (A24) take the form

$$\frac{\partial \tilde{u}}{\partial t} = \frac{1}{2}\sigma^2 \frac{\partial^2 \tilde{u}}{\partial y^2} - \frac{\partial}{\partial y}[\tilde{g}(y)\tilde{u}], \tag{A30}$$

where

$$\tilde{g}(y) = \begin{cases} c_I - \frac{1}{2}\sigma^2 - e^{2y}, & \text{supercritical} \\ c_I - \frac{1}{2}\sigma^2 + 2e^{2y} - e^{4y}, & \text{subcritical.} \end{cases} \tag{A31}$$

As in the case of additive noise, the uniform parabolicity condition is now satisfied and further $y\tilde{g}(y) < 0$ for sufficiently large y whenever $c_I > \sigma^2/2$, which is the range of concern here. Thus if we are able to find a Liapunov function V which satisfies (A20), the asymptotic stability of equation (A30) will be demonstrated.

Set $q = 2\alpha/(c_I - \sigma^2/2)$, where $\alpha > 0$ is the same as in inequality (A20). Clearly $c_I > \sigma^2/2$ whenever a stationary density of (A30) exists, so take $q > 0$. It is evident that

$$V(y) = cosh\,(qy)$$

is a Liapunov function. It is easy to show by a straightforward calculation that there are $\alpha > 0$ and $\beta > 0$ such that (A20) is satisfied in the new variable y when $g(x)$ is replaced by $\tilde{g}(y)$ as defined in equation (A31). Thus we know the stationary solution of (A30) is globally asymptotically stable which, by the change of variables (A29), in turn implies the global asymptotic stability of the stationary solutions of (A23) and (A24). The same conclusions hold for the Stratonovich interpretation.

A.4.3 Behaviour in the Absence of Asymptotic Stability.

The results of the previous section give no insight into the effects of parametric noise for values of the parameter c_I when globally stable stationary densities do not exist, i.e. when

$$c_I < \frac{1}{2}\sigma^2. \tag{A32}$$

It is the purpose of this section to explore this behaviour for values of the parameter c_I satisfying inequality (A32).

We start by defining a function

$$E_\rho(t) = \int_0^\infty x^\rho u(t,x)\,dx \tag{A33}$$

where $\rho > 0$ is a constant. It is clear that $E_\rho(t) \geq 0$. Observe from (A33) that

$$E_\rho(t) \geq \int_\epsilon^\infty x^\rho u(t,x)\,dx \geq \epsilon^\rho \int_\epsilon^\infty u(t,x)\,dx.$$

If we can demonstrate that $E_\rho(t) \to 0$ as $t \to \infty$, then we will know that for arbitrarily small $\epsilon > 0$ the density $u(t,x)$ is concentrated on $(0,\epsilon)$, i.e. $u(t,x)$ approaches an asymmetric Dirac delta function $\delta(x)$ as $t \to 0$.

Differentiation of $E_\rho(t)$ with respect to t, and using equation (A10) gives

$$\frac{dE_\rho}{dt} = \rho \int_0^\infty x^{\rho-1} S(t,x)\,dx \tag{A34}$$

after integration by parts under the assumption that $x^\rho S(t,x) \to 0$ for $x \to 0$ and $x \to \infty$. If we now insert equation (A11) for the probability current S into (A34) and again integrate by parts we have

$$\frac{dE_\rho}{dt} = \rho(\rho-1)\frac{\sigma^2}{2}E_\rho + \rho \int_0^\infty x^{\rho-1} g(x) u(t,x)\,dx \tag{A35}$$

whenever $x^{\rho+1}u \to 0$ as $x \to 0$ and $x \to \infty$. Equation (A35) is the fundamental relation we will use in examining the behaviour of the supercritical and subcritical systems in the presence of parametric noise when globally asymptotically stable stationary densities do not exist, i.e. when inequality (A32) holds.

Supercritical system. In this case we have explicitly from (A15) and (A35) that

$$\frac{dE_\rho}{dt} = \kappa\rho E_\rho - \rho E_{\rho+2} \tag{A36}$$

where

$$\kappa = (\rho - 1)\frac{\sigma^2}{2} + c_I. \tag{A37}$$

Since $E_{\rho+2} \geq 0$ and $\rho > 0$, equation (A36) immediately gives the differential inequality

$$\frac{dE_\rho}{dt} \leq \kappa\rho E_\rho. \tag{A38}$$

From (A38) it is immediate that for $\kappa < 0$ we have $E_\rho(t) \to 0$ for $\rho > 0$. The conditions $\kappa < 0$ and $\rho > 0$ are equivalent to

$$c_I < -(\rho - 1)\frac{\sigma^2}{2} < \frac{\sigma^2}{2}, \tag{A39}$$

and since ρ may be chosen arbitrarily small, inequality (A39) may always be satisfied by some ρ when (A32) holds.

Therefore $E_\rho(t) \to 0$ as $t \to \infty$, which completes the demonstration that for the supercritical system with parametric noise satisfying inequality (A32), the densities $u(t,x)$ converge to a Dirac delta function. The Stratonovich case is again covered by replacing c_I in (A39) by c_S.

Subcritical System. For the subcritical system with parametric noise, combining equations (A15) and (A35) gives

$$\frac{dE_\rho}{dt} = \kappa\rho E_\rho + \rho[2E_{\rho+2} - E_{\rho+4}]. \tag{A40}$$

Noting that $2x^2 - x^4 \leq 1$ for all $x \geq 0$ it is immediate that $2E_{\rho+2} - E_{\rho+4} \leq E_\rho$. As a consequence we may use (A40) to give the differential inequality

$$\frac{dE_\rho}{dt} \leq (\kappa + 1)\rho E_\rho.$$

Using the same method as in the previous case we may easily verify that, with $\rho > 0$, $E_\rho \to 0$ as $t \to \infty$ whenever $\kappa < -1$. This, in turn, is equivalent to

$$c_I < -1 + (\rho - 1)\frac{\sigma^2}{2} < -1 + \frac{\sigma^2}{2}$$

which is always satisfied for some $\rho > 0$ if

$$c_I < -1 + \frac{\sigma^2}{2}. \tag{A41}$$

A.5. Numerical Simulations.

The condition in inequality (A41) is disappointing in the sense that we do not have a complete analytic picture of the behaviour of the subcritical system in the presence of parametric noise, i.e. for values of c_I satisfying

$$-1 + \frac{\sigma^2}{2} \leq c_I < \frac{\sigma^2}{2}. \tag{A42}$$

Using an Euler integration algorithm with an integration time step of $\Delta = 0.01$, we have carried out a variety of numerical studies extending our analytic results for parametric noise when inequality (A42) is satisfied, or an analogous result for the Stratonovich case. In the Ito case we used

$$x(t + \Delta) = x(t) + \sigma\xi x(t)\sqrt{\Delta} + g(x)\Delta + \mathcal{O}(\Delta^{\frac{3}{2}}) \tag{A43}$$

while

$$x(t + \Delta) = x(t) + \sigma\xi x(t)\sqrt{\Delta} + g(x)\Delta + \frac{1}{2}x(t)\sigma^2\xi^2\Delta \tag{A44}$$

was used for the Stratonovich calculations[144,150]. To test the veracity of our numerical methods, we assured ourselves that the numerical solution had reached an asymptotic regime by discarding an initial transient and then constructed the numerical density from the iterates $x(t)$ for values of the parameter c_I (or c_S) satisfying inequality (A26). For both the supercritical and subcritical systems, the numerically constructed density coincided exactly with the analytically determined globally asymptotically stable densities (given by equations A25 and A27 respectively) in both the Ito and Stratonovich formulations.

Following this, extensive numerical simulations at a variety of noise amplitudes σ for values of the parameter c_I satisfying inequality (A 42) indicates that for this entire range the densities $u(t, x)$ do converge to a Dirac delta function as $t \to \infty$ in the sense that for every $\epsilon > 0$ the ratio of the time spent by $x(t)$ in the interval (ϵ, ∞) to that spent in the interval $[0, \epsilon]$ approaches 0 as $t \to \infty$. Thus we feel confident in asserting that for the subcritical system in the presence of parametric noise, $E_p \to 0$ as $t \to \infty$ whenever

$$c_I < \frac{\sigma^2}{2}.$$

A.6. Summary and Conclusion.

In this paper we have shown analytically that additive and parametric (multiplicative) noise, interpreted in either the Ito or Stratonovich formalism, induce global asymptotic stability in two systems, one of which has received attention as the Landau equation.

In both systems without noise, variation of the parameter c leads to a switching between a single globally stable steady state and multiple locally stable steady states. With additive noise this switching is mirrored in the behaviour of the extrema of globally stable probability densities at the same value of c. However, parametric noise causes a noise amplitude dependent shift (postponement) in the value of c at which the switching occurs.

Under suitable restrictions these results can be extended to more general polynomial forms $g(x)$ in which there are multiple bifurcations in the absence of noise. Further, it will be interesting to examine the situation where colored noise is used, as opposed to the white noise considered here.

Irregular Pupil Cycling as a Characteristic Abnormality in Patients With Demyelinative Optic Neuropathy

John G. Milton, M.D., Andre Longtin, M.Sc., Trevor H. Kirkham, M.D.,
and Gordon S. Francis, M.D.

We used an infrared videopupillometer combined with an electronic circuit that regulated the retinal light level as a function of pupil area to assess the regularity of pupil cycling in normal subjects and in patients with known abnormalities in the pupil light reflex pathways. The light stimulus was turned on whenever pupil area exceeded a preset value Two types of abnormalities were observed for patients with demyelinative optic neuropathy· a failure of the pupil to cycle despite a preserved pupillary response to a single light pulse; and, for those patients in whom cycling was possible, a characteristic intermittent irregularity in the amplitude of pupil cycling. These abnormalities were not seen in normal subjects or in patients with ischemic optic neuropathy, surgical lesions involving the optic chiasm, Adie's syndrome, or Horner's syndrome.

OSCILLATIONS in the diameter of the pupil can be induced by focusing a small beam of light at the pupillary margin [1,2] The average period of these oscillations has been referred to as the pupil cycle time Measurement of the pupil cycle time has been used as a clinical method to detect dysfunction in the pupil light reflex pathways [1-6] Although the oscillations in pupil diameter are usually regular, in some patients it can be quite irregular [7,8] It is uncertain whether these irregularities are a result of technical difficulties in maintaining the light beam correctly focused at the pupillary margin or reflect intrinsic abnormalities in the pupil light reflex pathways Consequently, little attention has been given to the possibility that irregularities in pupil cycling may be of diagnostic significance

We developed an automated method for obtaining pupil cycling[9] by combining an infrared videopupillometer[10] with an electronic circuit that regulates the retinal light level as a function of pupil area, the light is turned on whenever pupil area exceeds a preset area threshold This approach makes it easy for the patient to cooperate, is insensitive to small eye movements and the shading effects on the retina of the iris, since the light beam is focused down the center of the pupil under open loop conditions of the pupil light reflex, is not affected by segmental abnormalities in the movement of the iris, as occur in Adie's syndrome[11], and the changes in pupil area can be recorded quantitatively as a function of time

We used this method to examine the regularity of pupil cycling in patients with a variety of abnormalities in the pupil light reflex pathways

Subjects and Methods

We examined 21 healthy volunteers, aged 11 to 60 years, who were free of both ocular disease and disorders known to affect autonomic function We also examined 17 patients with abnormalities in the pupil light reflex pathways Of these 17 patients, 13 had an afferent pupillary defect including ten with clinically definite multiple sclerosis according to the criteria of Poser and associates,[12] two with ischemic optic neuropathy, and one with

---

Accepted for publication Jan 26, 1988

From the Departments of Neurology (Drs Milton and Francis) and Neuro-ophthalmology (Dr Kirkham), Montreal Neurological Institute and the Departments of Physiology (Dr Milton) and Physics (Mr Longtin), McGill University, Montreal, Canada This study was supported in part by Natural Science and Engineering Research Council grant A-0091 Mr Longtin received a Natural Science and Engineering Research Council postgraduate scholarship

Reprint requests to John G Milton, M D , Department of Physiology, McGill University, McIntyre Medical Sciences Bldg , 3655 Drummond St , Montreal, Quebec, Canada H3G 1Y6

a surgical lesion of the optic chiasm after resection of an intracranial tumor The remaining four patients had disorders affecting the autonomic nerve supply of the pupil three patients had Adie's syndrome and one patient had unilateral Horner's syndrome after surgical ablation of the ipsilateral superior cervical ganglion

All measurements were performed in subjects who had been dark adapted for at least 15 minutes in a room lit only by a dim red light During pupillary measurements, the subjects were instructed to refrain from blinking as much as possible and to fix their gaze on a target (a dim green asterisk) that appeared on a viewing screen inside the pupillometer

Measurements of pupil area were made with an infrared videopupillometer [10] The videocameras were a charge coupled device and their output was analyzed by a frame grabber that counted the number of pixels above a slice level (gray level) adjusted by the experimenter to discriminate between pupil and iris The output of the frame grabber was an analogue voltage, which was proportional to the pupil area (sampling rate, 60 Hz) Light-emitting diodes provided the light source (peak wavelength, 605 nm)

Pupil cycling measurements were performed as follows [9] The stimulating light beam of the pupillometer (diameter, 1 2 mm) was focused on the center of the pupil (diameter, 6 to 8 mm) under open loop, that is, maxwellian view, conditions. Under these conditions the iris does not alter the beam of light falling on the retina, however, we used the measured pupil area to control the timing and duration of the light pulses falling on the retina [9,13] This was accomplished by comparing the analogue output of the pupillometer to an adjustable area threshold by using operational amplifier circuitry [14] The output logic level goes high when the pupil area is greater than the area threshold and goes low otherwise The high level drives the light on and illuminates the retina in open loop In all experiments the pupil being stimulated was also the one being measured Pupil area and the output of the photodiode were recorded as a function of time on separate channels of a chart recorder

All measurements were performed separately on both eyes of each subject and pupil cycling was studied for at least four values of the area threshold setting to cover a pupil cycling period range of 1 5 to 5 seconds For each threshold setting, a minimum of ten pupil cycles were obtained corresponding to 50 seconds' observation for the longest period measured The latency time for the pupil light reflex was determined as the time between the onset of the light pulse and the onset of the pupillary constriction using a computer program incorporated in the videopupillometer A minimum of three measurements were made for each eye

Results

When the area threshold was set at a value larger than the initial pupil area, no regular oscillations in pupil area were seen (Fig 1, top) However, when the area threshold was set at a value lower than the initial pupil area, repetitive constrictions and dilations in pupil area were observed (Fig 1, middle and bottom) The light was turned on approximately 100 msec after the pupil area exceeded the area threshold This delay represents the electronic delay in our apparatus The onset of constriction occurred 296 ± 24 msec after the light was turned on (mean ± 1 S D for 21 subjects) This delay is the pupil latency time Once pupil area constricted to a value less than the area threshold, the light was turned off after the machine delay The pupil continued to constrict for the duration of the neural delay, after which it began to dilate

The period and amplitude of the oscillations in pupil area depend on the value of the area threshold relative to the initial pupil area (Fig 1, middle and bottom) This distinguishes our method from the pupil cycle time measurement [16] The changes in the period and amplitude of pupil cycling as a function of the area threshold can be used to determine the rates of constriction and dilation of the pupil (unpublished data) In the present study we focused on the regularity of the amplitude of the pupil cycling

In normal subjects, and patients with ischemic and surgical optic neuropathy and with autonomic nerve dysfunction, regular pupil cycling was obtained (Table and Fig 2) In each case, the area threshold was adjusted to give similar values of the period of pupil cycling There were small cycle-to-cycle variations in the amplitudes and intervals between successive constrictions, which were typically larger for patients with Adie's syndrome Conversely, regular pupil cycling was not observed in

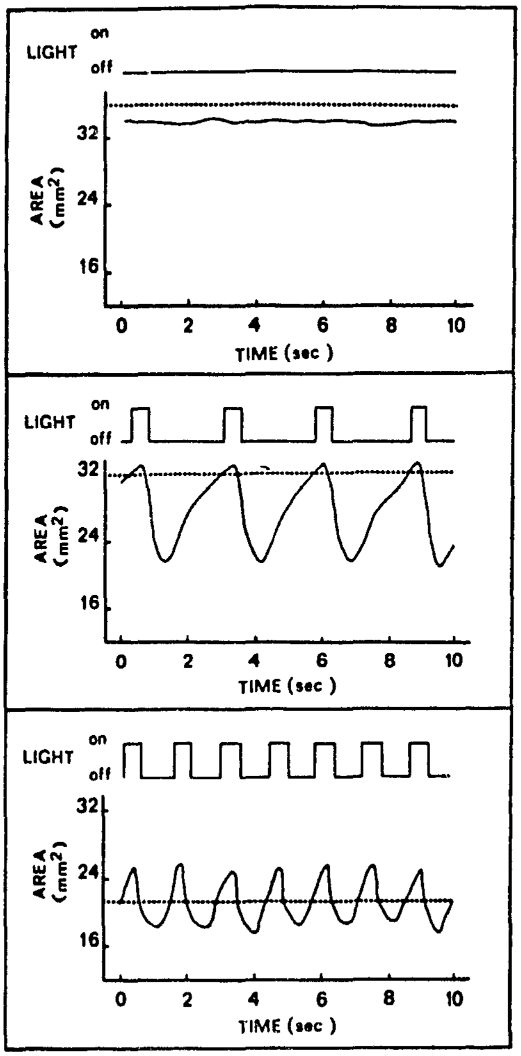

Fig. 1 (Milton and associates) Pupil cycling in a normal subject for three different values of the area threshold (dotted line) The sequence of light pulses is shown above the changes in pupil area (solid line) The pupil area before cycling was the same in all cases (approximately 34 mm^2) The initial transient changes in pupil area that occur immediately after adjustment of the area threshold are not shown (middle and bottom) They persist for the equivalent of two to three cycles

patients with demyelinative optic neuropathy There were two distinct types of abnormalities seen only when the light was presented to the affected eye Of 20 eyes (ten patients) with multiple sclerosis, 16 had evidence of optic neuritis (Fig 2) In nine of the 16 affected eyes, pupil cycling was punctuated by short segments of irregular amplitude (Patient 17, Fig 2) These irregular segments lasted for at least the equivalent of two cycles and were characterized by their abrupt onset and offset and a marked decrease in amplitude

We were unable to obtain pupil cycling in the remaining affected eyes In some cases, for example, Patient 12, this was clearly because of the much reduced response of the pupil to light In other patients, however, we were unable to maintain pupil cycling even though there was a good constriction to a single light pulse The pupil would undergo one to two constrictions and then no further response would be seen (Patient 10, Fig 2) A similar phenomenon occurred in some normal subjects when the area threshold was set too close to the minimum pupil area obtained in response to the light stimulus In these cases regular cycling was restored by increasing the area threshold However, this maneuver did not restore pupil cycling in patients with demyelinative optic neuropathy

The latency of the pupil light reflex was prolonged for patients with demyelinative optic neuropathy (341 ± 9 msec for eight patients) compared to normal subjects (296 ± 24 msec for 17 subjects) (Student's *t*-test, $P < 05$)

Discussion

Our observations indicate that the time course for pupil cycling in patients with demyelinative optic neuropathy differs from that seen in normal subjects, patients with ischemic optic neuropathy, and patients with autonomic nerve dysfunction There are two types of abnormalities that were observed only when light was presented to the affected eye failure of the pupil to cycle despite a pupillary response to a single light pulse, and, for those patients in whom cycling was possible, a characteristic irregularity in the amplitude of the cycling

Increased difficulties in obtaining sustained pupil cycling in patients with multiple sclerosis have been reported previously by several investigators using the pupil cycle time measurement[3,7] However, it must be noted that with the use of the slit lamp to obtain pupil cycling, up to 7% of normal pupils do not cycle[15] We experienced no difficulty in obtaining pupil cycling in normal subjects In particular, we

TABLE
PUPIL RESPONSES IN PATIENTS WITH LESIONS IN THE PUPIL LIGHT REFLEX PATHWAYS

PATIENT NO., AGE (YRS) SEX	SINGLE LIGHT PULSE[*] (MM²)		PUPIL CYCLING[†]		CLINICAL HISTORY
	RIGHT	LEFT	RIGHT	LEFT	
Normal subjects	12	13	Regular	Regular	—
Range	(6–20)	(6–20)			
Ischemic optic neuropathy					
1, 34, M	10	15	Regular	Regular	Right afferent pupillary defect, fat embolism, right inferior altitudinal defect
2, 55, M	7	12	Regular	Regular	Right afferent pupillary defect, temporal arteritis, right inferior arcuate defect
Optic chiasm lesion					
3, 42, F	7	10	Regular	Regular	Right afferent pupillary defect, partial resection of suprasellar meningioma, right temporal hemianopia
Horner's syndrome					
4, 14, F	10	16	Regular	Regular	Right Horner's syndrome after surgical procedure in neck
Adie's syndrome					
5, 38, F	1	8	Absent	Regular	Right Adie's pupil
6, 29, F	2	12	Regular	Regular	Right Adie's pupil
7, 36, F	6	10	Regular	Regular	Bilateral Adie's pupil, right worse than left
Demyelinative optic neuropathy[‡]					
8, 31, M	10	10	Regular	Irregular	Left afferent pupillary defect
9, 29, F	7	9	Irregular	Irregular	Right afferent pupillary defect, bilateral visual blurring
10, 33, F	4	7	Absent	Absent	Left afferent pupillary defect, bilateral visual blurring
11, 64, M	4	3	Irregular	Irregular	Left afferent pupillary defect, right visual blurring
12, 35, F	1	6	Absent	—	Right afferent pupillary defect
13, 19, F	3	5	Absent	Absent	Right afferent pupillary defect, visual evoked response showing bilateral slowing
14, 29, F	13	12	Regular	Irregular	Left afferent pupillary defect
15, 33, F	9	11	Irregular	Irregular	Left afferent pupillary defect, bilateral visual loss
16, 41, M	3	7	Absent	Regular	Right afferent pupillary defect
17, 29, F	9	9	Irregular	—	Right afferent pupillary defect, visual evoked response showing bilateral slowing

[*] Change in pupil area in response to a single 0.5-second light pulse. The intensity of the light pulse was the same for all subjects.

[†] Regular, pupil cycling as seen for normal eyes (see Fig. 1), irregular, irregular pupil cycling (see Patient 17, Fig. 2), absent, unable to cycle (see Patient 10, Fig. 2).

[‡] The clinical history gives the side of the afferent pupillary defect that was first detected clinically (range, one month to 15 years before our examination). In some patients the afferent pupillary defect was no longer detectable and in others it had switched sides, thereby indicating the presence of a new lesion.

easily elicited normal pupil cycling in two normal subjects in whom cycling could not be initiated by use of a slit lamp. Two previous studies have noted intermittent irregularities in pupil cycling of patients with multiple sclerosis[7,8]; however, the possibility that this may be specific for demyelinative lesions of the optic nerve was not recognized.

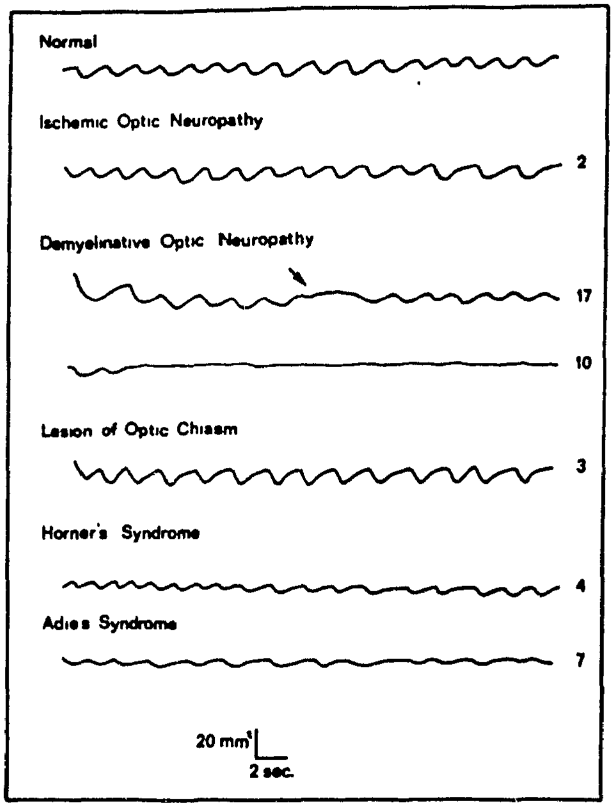

Fig. 2 (Milton and associates) Comparison of pupil cycling in a normal subject to that in patients with ischemic optic neuropathy, demyelinative optic neuropathy, Adie's syndrome, Horner's syndrome, and a patient with a surgical lesion of the optic chiasm The numbers at the right-hand side of the figure identify the patient. The irregularity observed in pupil cycling for the patient with demyelinative optic neuropathy is indicated by the arrow

The mechanism for the irregularities in pupil cycling in patients with demyelinative optic neuropathy is uncertain It is unlikely that these irregularities represent pupillary fatigue, habituation, or escape,[15] since the progressive diminution of the amplitude of the pupil light reflex associated with these phenomena is not present. Additionally, pupillary fatigue typically occurs after 60 seconds,[2,15,16] whereas the irregularity in pupil cycling observed in patients with demyelinative optic neuropathy occurred within 20 seconds.

It is more likely that these irregularities are related to the prolonged latency of the pupil reflex and time-dependent afferent pupillary defects. During pupil cycling, the optic nerve transmits a repetitive train of synchronous afferent impulses as the light pulse intermittently reaches the retina. Partially demyelinated nerve fibers have difficulties in transmitting trains of impulses and undergo intermittent conduction block,[17,18] which is believed to be related to the prolongation of the refractory period for transmission.[19] Partial demyelination of even a small proportion of the optic nerve fibers may be sufficient to desynchronize the train of afferent nerve impulses[17] to the point that pupil cycling is interrupted Conversely, in a partially infarcted optic nerve only the intact nerve fibers can conduct impulses Since the intact fibers appear to be normally myelinated[20,21] in a partially infarcted nerve, this desynchronization should not occur and cycling should be regular Thus, our observation that irregularities in pupil cycling are seen in optic nerves with demyelinated lesions but not in those with ischemic lesions is consistent with known differences in nerve conduction of repetitive impulses between myelinated and unmyelinated nerve fibers

Quantitation of pupillary changes has typically been disappointing as a method for enhancing clinical acumen. For example, the demonstration of an afferent pupillary defect at the bedside is well known to be a more sensitive indicator of optic nerve dysfunction than previously reported pupillographic methods.[22] This preliminary study suggests that precise measurements of pupil cycling under well-defined conditions may be useful for identifying the origin of an optic neuropathy, irregular cycling favors demyelination, whereas regular cycling favors ischemic or surgical lesions This task is not easily accomplished by other methods [22-24] Our method also appears to be useful for detecting whether there is bilateral optic nerve dysfunction in a patient with a relative afferent pupillary defect Clearly, more studies involving larger numbers of patients in different stages of evolution of their disease and with comparison to other diagnostic techniques of optic nerve dysfunction, for example, visual evoked potentials, will be necessary before it will be known whether this method also has a role in detecting the presence of subclinical dysfunction in an optic nerve

ACKNOWLEDGMENT

Hamamatsu Photonics Systems, Inc., Hamamatsu, Japan and Waltham, Massachusetts, provided the Binocular Iriscorder Model C-2515

References

1 Stern, H J A simple method for the early diagnosis of abnormality of the pupillary reaction Br J Ophthalmol 28 275, 1944

2 Campbell, F W , and Whiteside, T C D Induced pupillary oscillations Br J Ophthalmol 34 180, 1950

3 Miller, S D , and Thompson, H S Pupil cycle time in optic neuritis Am J Ophthalmol 85 635, 1978.

4 ——— Edge-light pupil cycle time Br J Ophthalmol 92 396, 1978

5 Martyn, C N , and Ewing, D J Pupil cycle time A simple way of measuring an autonomic reflex J Neurol Neurosurg Psychiatry 49 771, 1986

6. Kirkham, T H , Coupland, S G , Blanchet, L.-M., and Nelson, D E Effect of timolol maleate on intraocular pressure and pupil cycle time in normal eyes Can J Ophthalmol 16 132, 1981

7 Wybar, K C The ocular manifestations of disseminated sclerosis Proc R Soc Med 45 315, 1952

8. Ukai, K , Higashi, J , and Ishikawa, S Edge-light pupil oscillation of optic neuritis Neuro-ophthalmology 1.33, 1980

9. Longtin, A , and Milton, J G Complex oscillations in the human pupil light reflex with 'mixed' and delayed feedback Mathematical Biosci In press.

10 Ishikawa, S , Naito, M , and Inabe, K A new videopupillography. Ophthalmologica 160 248, 1970

11 Thompson, H S Segmental palsy of the iris sphincter in Adie's syndrome Arch Ophthalmol 96 1615, 1978

12. Poser, C M , Paty, D , Scheinberg, L , McDonald, W. I , Davis, F A , Ebers, G C , Johnson, K P , Sibley, W A , Silberberg, D H , and Tourtellotte, W W . New diagnostic criteria for multiple sclerosis Guidelines for research protocols Ann Neurol 13.227, 1983

13 Stark, L Environmental clamping of biological systems Pupil servomechanism J Opt Soc Am 52 925, 1962

14 Horowitz, P , and Hill, W The Art of Electronics. New York, Cambridge University Press, 1986, pp 92–142

15 Safran, A B , Walser, A , Roth, A , and Gauthier, G Pupil cycle induction test A way of evaluating the pupillary light reflex Ophthalmologica 183 205, 1981

16 Lowenstein, O , Feinberg, R , and Loewenfeld, I. E Pupillary movements during acute and chronic fatigue Invest Ophthalmol Vis Sci 2 138, 1963

17 MacDonald, W I Pathophysiology in multiple sclerosis Brain 97 179, 1974

18 Daley, M L , Swank, R L , and Ellison, C M . Flicker fusion thresholds in multiple sclerosis A functional measure of neurological damage Arch Neurol 36 292, 1979

19 Rasminsky, M , and Sears, T A Internodal conduction in undissected demyelinated nerve fibres J Physiol 227 323, 1972

20 Ellenberger, C , and Netsky, M G Infarction in the optic nerve J Neurol Neurosurg Psychiatry 31 606, 1968

21 Henkind, P , Charles, N C , and Pearson, J Histopathology of ischemic optic neuropathy Am J Ophthalmol 69 78, 1970

22 Cox, T A , Thompson, H S , Hayreh, S S , and Snyder, J E Visual evoked potential and pupillary signs A comparison in optic nerve disease Arch Ophthalmol 100 1603, 1982

23 Wilson, W B Visual-evoked response differentiation of ischemic optic neuritis from the optic neuritis of multiple sclerosis Am J Ophthalmol 86 530, 1978

24 Alexandritis, E , Argyropoulos, T , and Krastel, H The latent period of the pupil light reflex in lesions of the optic nerve Ophthalmologica 182.211, 1981

APPENDIX C

FITTING THE SINGLE PULSE RESPONSE OF THE PUPIL

This appendix describes the functions used to fit the response of the pupil to a light pulse of duration T seconds, as well as the algorithms used to perform the fit. This pupillary response consists in a constriction followed by a dilation.

There are 4 different programs. Each program is a subroutine containing the function to be fitted to the data, and the partial derivatives of this function with respect to the parameters. The main program to which the subroutines are appended is the **Basic Statistics and Regression Analysis Program** by Hewlett-Packard, running on a Hewlett-Packard 9816 computer. It uses a Marquardt algorithm to search for a local minimum of the χ^2 function in parameter space starting from user specified initial guesses. This method combines the best features of the gradient search (which follows the steepest descent of the χ^2 function) with the method of linearization of the fitting function (see e.g. Bevington[185]).

1. The first subroutine is SPF12ORD. The constriction phase is modelled by one exponential process. The dilation process takes over from the constriction process at time $t = T$, and is modelled by two exponential processes. The fit is constrained by the condition that the solution and its derivative be continuous at time T. Time $t = 0$ is chosen as the onset of constriction. An extra constraint is the initial pupil area at time $t = 0$.

Denoting pupil area during the constriction phase by $x_c(t)$ and during the dilation phase by $x_d(t)$, this model takes the form

$$x_c(t) = Ae^{-\alpha_c t} + B \qquad 0 \leq t \leq T \qquad \textit{(constriction)} \tag{C1}$$

$$x_d(t) = Ce^{-\alpha_d(t-T)} + De^{-\beta_d(t-T)} + E \qquad t > T \qquad \textit{(dilation)} \tag{C2}$$

This model has 8 parameters : {A,B,C,D,E,α_c,α_d,β_d;T}, the parameter T being fixed prior to the fit. Imposing continuity of the solution and its first derivative at $t = T$ yields:

$$Ae^{-\alpha_c T} + B = C + D + E \tag{C3}$$

$$-\alpha_c Ae^{-\alpha_c T} = -\alpha_d C - \beta_d D \tag{C4}$$

The initial condition gives

$$x_c(0) \equiv x_o = A + B\,. \tag{C5}$$

These constraints can be used to eliminate 3 parameters, leaving 5 free parameters for the fit. When the parameters {B,D,E} are expressed as a function of {A,C,α_c,α_d,β_d}, then B is obtained from (C5), and

$$D = -\frac{\alpha_d}{\beta_d} C + \frac{\alpha_c}{\beta_d} A e^{-\alpha_c T} \tag{C6}$$

$$E = x_o + A(e^{-\alpha_c T} - 1) - C + \frac{\alpha_d}{\beta_d} C - \frac{\alpha_c}{\beta_d} A e^{-\alpha_c T} . \tag{C7}$$

2. SPFC1D2 is a variation of SPF12ORD. This program has 4 free parameters because the final asymptotic value $E = A_{off}$ is imposed on the solution. The value of A_{off} used is the one obtained from the parameter estimation scheme for the first order model (Section 3.2.3). Expressed in terms of the free parameters {A,α_c,α_d,β_d}, the fitting equations are :

$$x_c(t) = x_o + A(e^{-\alpha_c t} - 1) \tag{C8}$$

and

$$x_d(t) = Ce^{-\alpha_d(t-T)} - \frac{\alpha_d}{\beta_d} Ce^{-\beta_d(t-T)} + \frac{\alpha_c A}{\beta_d} e^{-\alpha_c T - \beta_d(t-T)} + A_{off} , \tag{C9}$$

where

$$C = \frac{\beta_d}{\beta_d - \alpha_d} \{Ae^{-\alpha_c T}[1 - \frac{\alpha_c}{\beta_d}] - A + x_o - A_{off}\}. \tag{C10}$$

3. The subroutine CYCLFIT5 has five constraints. Besides the 4 constraints of SPFC1D2, it fixes the lower asymptote, i.e. $B = A_{on}$. The value of A_{on} used is also obtained from the first order model (Section 3.2.3). There are 3 free parameters {α_c,α_d,β_d} and the data are fitted to the functions :

$$x_c(t) = (x_o - A_{on})e^{-\alpha_c t} + A_{on} \tag{C11}$$

and

$$x_d(t) = Ce^{-\alpha_d(t-T)} - \frac{\alpha_d}{\beta_d} Ce^{-\beta_d(t-T)} + \frac{\alpha_c}{\beta_d}(x_o - B)e^{-\alpha_c T - \beta_d(t-T)} + A_{off} , \tag{C12}$$

where

$$C = \frac{\beta_d}{\beta_d - \alpha_d} \{e^{-\alpha_c T}(x_o - B)(1 - \frac{\alpha_c}{\beta_d}) + B - A_{off}\}. \tag{C13}$$

4. Finally, the subroutine SPF2ORD describes a model where both constriction and dilation are described by the solutions of a second order differential equations :

$$x_c(t) = Ae^{-\alpha_c t} + Be^{-\beta_c t} + K_c \qquad 0 \leq t \leq T \tag{C14}$$

$$x_d(t) = Ce^{-\alpha_d(t-T)} + De^{-\beta_d(t-T)} + K_d \qquad t > T \tag{C15}$$

This model has been studied with three constraints : 1) continuity of the solution at time T; 2) continuity of the derivative at time T; and 3) $x(0) = x_o$. When the parameters $\{\mathrm{B},\mathrm{D},K_d\}$ are expressed in terms of the 7 free parameters $\{\mathrm{A},K_c,\mathrm{C},\alpha_c,\beta_c,\alpha_d,\beta_d\}$,

$$D = \left[-\alpha_d C + \alpha_c A e^{-\alpha_c T} + \beta_c(x_o - A - K_c)e^{-\beta_c T}\right](\beta_d)^{-1}\ , \tag{C16}$$

and

$$K_d = Ae^{-\alpha_c T} + (x_o - A - K_c)e^{-\beta_c T} + K_c - C - D \tag{C17}$$

result, and B is again obtained from (C5).

These routines were used to fit single pulse responses that are either isolated (Sections 3.2 and 3.3) or which occur as part of pupil cycling (Section 3.4.5). These two pulse responses are distinguished by the different conditions under which they occur. In pupil cycling, the pulses occur in succession and their duration is observed to fluctuate from one cycle to the next. For the isolated single pulse response, the constriction and dilation time courses can be fit separately (see Figures 3.2.6a and 3.2.6b of Section 3.2). The solution has a slope discontinuity at the light offset, because the single exponential process neglects higher order dynamics of the iris muscles. As seen in Figure 3.2.6a the pupil continues on constricting before dilating, even though the light is off. In Figure 3.2.6c the parameters estimated from pupil cycling (C1D1: see Section 3.2.3) provide a better fit to the isolated single pulse response than the method used in Figures 3.2.6a and 3.2.6b.

An excellent fit to the isolated pulse response is obtained when SPF12ORD (Figure 3.2.6d) or SPFC1D2 (Figure 3.4.6a) is used. The SPF2ORD model (10 parameters, 3 constraints)was found to have many local minima when applied to the isolated single pulse (data not shown). Thus, the fit obtained was not very robust even though it minimized the χ^2 very well. In fact, certain initial guesses led to negative rate constants.

In Section 3.4.5, successive constriction-dilation cycles were fitted using SPFC1D2, A_{off} being fixed to the value obtained using the cycling parameter estimation scheme (for C1D1). SPFC1D2 was found to give more consistent results than SPF12ORD and CYCLFIT5. The parameters were then used in the program C1D2SOL (Appendix D) which numerically integrates the C1D2 model (see Section 3.4.5 for PCNF and Appendix II of Section 3.2 for single pulse response). The damping and frequency are related to the rate constants of the fit : $\delta = \alpha_d + \beta_d$ and

$\omega^2 = \alpha_d \beta_d$. This equivalence simply follows from the relation between the coefficients and the roots of the characteristic equation of a second order linear differential equation. The forcing constants in the differential equations are obtained by equating the asymptotic values predicted by these equations with those from the fit : $\frac{C_{for}}{\alpha_c} = x_o - A \equiv A_{on}$ and $\frac{D_{for}}{\omega^2} = E \equiv A_{off}$.

All our fits were repeated a number of times starting with different initial guesses for the parameters. Reasonable parameter guesses for the more complicated C1D2 fits could be obtained from the simpler C1D1 fits in Section 3.2. In all cases except for SPF2ORD, the fits were found to be robust, and thus there were no problems caused by the presence of other local minima of the χ^2 function in parameter space. Further, the χ^2 was slightly lower when values of the light pulse duration T used in the fitting subroutines were made slightly larger than those used in the experiment (e.g. 600 msec instead of 500 msec for the single pulse responses). This corresponds to making the offset delay larger than the onset delay. However, in Section 3.2 the first order model was shown to give better agreement between the predicted and observed period of pupil area oscillations when the delays were equal (see Figure 3.2.4). Based on this and the fact that our physiological model in Section 2.2 assumes that these delays are equal (see Section 3.2), all the fits were finally done using the real duration of the light pulse.

APPENDIX D
PROGRAMS

```
      program rkcnad1
c
c     rkcnad1 : Runge Kutta Colored Noise Additive Noise
c     Language : Fortran 77
c     Computer : VAX 3200
c
c     This program integrates a nonlinear delay-differential equation
c     which is a model for smooth negative feedback oscillations in
c     the pupil light reflex.
c     Either the deterministic or the stochastic version of this
c     equation can be numerically integrated with double precision
c     accuracy.
c     The program computes the density of the solution as well as the
c     period and amplitude distribution for additive or multiplicative
c     Gaussian colored noise.
c
c     The basic numerical integration algorithm is a fourth order
c     Runge-Kutta scheme with linear interpolation for the delay.
c     It appears in subroutine RK4.
c     The integration time step is given as a fraction (DELT) of the
c     delay (TAU).
c     The program uses a delay buffer XDEL(DELDIV+1), where
c     DELDIV=1/DELT, to continuously store the solution from
c     (REALT-TAU) to (REALT), REALT being the present integration
c     time (in seconds).
c     The initial condition (taken to be a constant = XTINIT in our
c     simulations) is stored in the delay buffer.
c     The program computes the solution X for (NTAUMAX) delays, and
c     for each delay the index K runs from 1 to DELDIV.
c     It further constructs the density from the time solution.
c     The binning of the iterates into the (BN=500) bins of the
c     solution histogram RHO(BN) occurs only for  NTAU > NTAUMIN,
c     in order to allow for transients to decay (this is important
c     for the determination of the invariant density).
c     The values of the solution between XMIN and XMAX are linearly
c     mapped into a bin number between 0 and BN.
c     Values of the solution at which the derivative changes sign
c     are stored in order to calculate the amplitude and period
c     at each cycle. The amplitude is computed as the difference
c     between two such successive values of the solution (i.e. from
c     peak to trough), while the period is computed from peak to peak.
c     The amplitude histogram is RHOA(BINS), and the period histogram
c     RHOP(BINS), and their bounds are fixed between AMPMIN and AMPMAX
c     and PERMIN and PERMAX.
c     If 2 successive changes in the derivative sign occur too close in
c     time, they are neglected (the parameter FLUKE controls this).
c     This is because such rapid changes are not measurable in the
c     pupil data we have analyzed. Also, since very small amplitudes
c     escape detection, we neglect the contents of the first
c     JZERO bins of RHOA (the total number of neglected values is
c     given by CORNITA).
c
c     The program calculates the solution, amplitude and period
c     densities for different values of the parameter  U(2)  ( n in
c     the Hill-type feedback function) around the Hopf bifurcation.
```

```
c     The noise can affect any parameter U(*) in the equation which
c     appears in the subroutine DERIVS. When the noise affects U(5),
c     it is additive. Close to the bifurcation, the rate of relaxation
c     onto the limit cycle is very slow. The solution is first allowed
c     to relax onto the limit cycle for NZMIN=2500 delays. When
c     NTAU > NZMIN, noise is applied, and we allow another NTAUMIN=2500
c     delays for a steady-state to be reached. The integration proceeds
c     until time NTAUMAX*TAU.
c     The intensity of the Gaussian noise is given by SIGMA, and its
c     correlation time by TCOR.
c     The integration time step for the noise is the same as that for
c     the deterministic component handled by the RK4 routine.
c     The noise satisfies an Ornstein-Uhlenbeck process which is
c     integrated using an integral Euler method as suggested by Fox
c     (see section 5.2 for more details). The uniformly distributed
c     random numbers are generated by the RAN1 subroutine taken from
c     Numerical Recipes.
c
      real*8 xdel(101),gausx,u5bar,fluke,pi
      real*8 x,dxdt,xh,delt,tau,xmin,xmax,x1tau,u(5),xtinit
      real*8 nksi,ksi1,ksi2,sigma,realt,tnext,tcor,sig
      real*8 ampmin,ampmax,permin,permax,ampl,per,ampli,peri
      real*8 xlast,tlast,sgnlast,e,bige,difft
      integer bn,bins,binnumb,deldiv,delpr,rho(500),idum
      integer ntau,ntaumin,ntaumax,rhoa(200),rhop(200)
      integer jmin,jmax,stepj
      integer aflag,flag,bnumba,bnumbp,cornita,jzero,nzmin
      integer nit,nita,nitp,nitapr
      real*4 robar,robara,robarp,varrho,varroa,varrop
      real*4 xsumsq,asumsq,psumsq,xofi
      real*4 sigro,sigroa,sigrop
      real*4 fnit,fnita,fnitp
      common/eqparam/u,xdel,delt,tau
      common/deloop/k
      open(5,file='rk2ad7.01')
      rewind 5
      idum=-5813
      pi=3.141592653589793
      bins=200
      bn=500
      u(1)=3.21d0
      u(3)=50.0d0
      u(4)=200.0d0
      u5bar=0.0d0
      tau=0.3d0
      delt=0.01d0
      deldiv=100
      xtinit=40.0d0
      nzmin=2500
      ntaumin=5000
      ntaumax=25000
      xmin=10.0d0
      xmax=75.0d0
      ampmin=0.0d0
      ampmax=40.0d0
```

```
    permin=0.5d0
    permax=1.5d0
    fluke=20.0d0*delt*tau
    jzero=3
    nit=(ntaumax-ntaumin)*deldiv
    tcor=1.0d0
    sig=7.0d0
    sigma=sig*tcor
    bige=dexp(-delt*tau/tcor)
    jmin=818
    jmax=830
    stepj=2
    goto 45
55  continue
    jmin=84
    jmax=120
    stepj=2
45  continue
    do 20 j=jmin,jmax,stepj
       if(jmin.eq.818) then
          u(2)=dble(j)/100.0d0
       else
          u(2)=dble(j)/10.0d0
       end if
       write(5,002) u(2),sigma
002 format(' ','u(2)= ',d19.14,3x,'sigma= ',d19.14)
    do 10 i=1,bn
       rho(i)=0
 10 continue
    do 11 i=1,bins
       rhoa(i)=0
       rhop(i)=0
 11 continue
    delpr=deldiv+1
    do 30 k=1,delpr
       xdel(k)=xtinit
 30 continue
    cornita=0
    nita=0
    nitp=0
    xlast=xtinit
    tlast=0.0d0
    sgnlast=1.0d0
    ksi1=ran1(idum)
    ksi2=ran1(idum)
    nksi=dsqrt(-2*dlog(ksi1))*dcos(2*pi*ksi2)
    e=dsqrt(1/(2*tcor))*sigma*nksi
    eh=e
    flag=0
    aflag=0
    do 100 ntau=1,ntaumax
       x=xdel(deldiv+1)
       do 101 k=1,deldiv
          tnext=(ntau-1+k*delt)*tau
          realt=tnext-delt*tau
```

```
          x1tau=xdel(k)
          if(ntau.gt.nzmin) then
             u(5)=u5bar+e
             ksi1=ran1(idum)
             ksi2=ran1(idum)
             nksi=dsqrt(-2*dlog(ksi1))*dcos(2*pi*ksi2)
             gausx=nksi*sigma*dsqrt((1-bige**2)/(2*tcor))
             eh=e*bige+gausx
          else
             u(5)=u5bar
          end if
          call derivs(realt,x,dxdt,x1tau)
          if(ntau.gt.ntaumin) then
             difft=realt-tlast
             if((dsign(1.0d0,dxdt).ne.sgnlast) .and. (difft.gt.fluke
   +)) then
                ampl=abs((x-xlast))
                if(aflag.eq.0) then
                   aflag=1
                   goto 35
                end if
                bnumba=idint((ampl-ampmin)*dble(bins)/(ampmax-ampmin
   +))+1
                if((bnumba.gt.0) .and. (bnumba.le.bins)) then
                   rhoa(bnumba)=rhoa(bnumba)+1
                   nita=nita+1
                end if
 35             continue
                if(flag.eq.0) then
                   per=realt-tlast
                   bnumbp=idint((per-permin)*dble(bins)/(permax-permin
   +))+1
                   if((bnumbp.gt.0) .and. (bnumbp.le.bins)) then
                      rhop(bnumbp)=rhop(bnumbp)+1
                      nitp=nitp+1
                   end if
                   tlast=realt
                end if
                flag=1-flag
                xlast=x
                sgnlast=-sgnlast
             end if
          end if
          call rk4(x,dxdt,realt,xh)
          if(ntau.gt.ntaumin) then
             binnumb=idint((xh-xmin)*dble(bn)/(xmax-xmin))+1
             if((binnumb.ge.1) .and. (binnumb.le.bn)) then
                rho(binnumb)=rho(binnumb)+1
             end if
          end if
          xdel(k)=x
          x=xh
          e=eh
101    continue
       xdel(deldiv+1)=xh
```

```
  100 continue
c
c   STATISTICS
c
      do 60 l=1,jzero
         cornita=cornita+rhoa(l)
         rhoa(l)=0
   60 continue
      robar=0.0
      robara=0.0
      robarp=0.0
      xsumsq=0.0
      asumsq=0.0
      psumsq=0.0
      do 61 i=1,bn
         xofi=i*(xmax-xmin)/float(bn)+xmin
         robar=robar+rho(i)*xofi
         xsumsq=xsumsq+rho(i)*(xofi**2)
   61 continue
      fnit=float(nit)
      robar=robar/fnit
      varrho=xsumsq/(fnit-1)-fnit/(fnit-1)*(robar**2)
      if(varrho.gt.0.0) then
         sigro=sqrt(varrho)
      end if
      do 62 i=1,bins
         ampli=i*(ampmax-ampmin)/float(bins)+ampmin
         peri=i*(permax-permin)/float(bins)+permin
         robara=robara+rhoa(i)*ampli
         robarp=robarp+rhop(i)*peri
         asumsq=asumsq+rhoa(i)*(ampli**2)
         psumsq=psumsq+rhop(i)*(peri**2)
   62 continue
      nitapr=nita-cornita
      fnita=float(nitapr)
      if(nitapr.le.1) then
         robara=0.
         sigroa=0.
      else
         robara=robara/fnita
         varroa=asumsq/(fnita-1)-fnita/(fnita-1)*(robara**2)
         if(varroa.le.0.0) then
            sigroa=0.0
         else
            sigroa=sqrt(varroa)
         end if
      end if
      fnitp=float(nitp)
      if(nitp.le.1) then
         robarp=0.
         sigrop=0.
      else
         robarp=robarp/fnitp
         varrop=psumsq/(fnitp-1)-fnitp/(fnitp-1)*(robarp**2)
         if(varrop.le.0.0) then
```

```
            sigrop=0.0
         else
            sigrop=sqrt(varrop)
         end if
      end if
      write(5,003) xsumsq,asumsq,psumsq
      write(5,003) robar,robara,robarp
      write(5,003) sigro,sigroa,sigrop
      write(5,004) nita,nitp,cornita
  003 format(' ',3e15.4)
  004 format(' ',3i10)
      write (5,001) (i,rho(i),i=1,bn)
  001 format(' ',2i10)
   20 continue
      if(jmin.eq.818) then
         goto 55
      end if
      close(5)
      stop
      end
      subroutine derivs(realt,x,dxdt,x1tau)
      double precision u(5),x1tau,x,dxdt,xdel(101),delt,tau,realt
      common/eqparam/u,xdel,delt,tau
      dxdt=-u(1)*x+u(4)/(1+(x1tau/u(3))**u(2))+u(5)
      return
      end
      function ran1(idum)
      real*8 r(97),rm1,rm2
      integer idum
      parameter (m1=259200,ia1=7141,ic1=54773)
      parameter (m2=134456,ia2=8121,ic2=28411)
      parameter (m3=243000,ia3=4561,ic3=51349)
      rm1=1./m1
      rm2=1./m2
      data iff /0/
      if ((idum.lt.0) .or. (iff.eq.0)) then
      iff=1
      ix1=mod(ic1-idum,m1)
      ix1=mod(ia1*ix1+ic1,m1)
      ix2=mod(ix1,m2)
      ix1=mod(ia1*ix1+ic1,m1)
      ix3=mod(ix1,m3)
      do 11 j=1,97
         ix1=mod(ia1*ix1+ic1,m1)
         ix2=mod(ia2*ix2+ic2,m2)
         r(j)=(dble(ix1)+dble(ix2)*rm2)*rm1
   11 continue
      idum=1
      endif
      assign 12 to ilabel
   12 continue
      ix1=mod(ia1*ix1+ic1,m1)
      ix2=mod(ia2*ix2+ic2,m2)
      ix3=mod(ia3*ix3+ic3,m3)
      j=1+(97*ix3)/m3
```

```
if((j.gt.97) .or. (j.lt.1)) then
   goto ilabel
endif
ran1=r(j)
r(j)=(dble(ix1)+dble(ix2)*rm2)*rm1
return
end
subroutine rk4(x,dxdt,realt,xh)
double precision u(5),x,dxdt,xh,xdel(101),realt,delt,tau
double precision ksi,xt,dxt,dxm,hh,h6,th,tprime,x1tau
common/eqparam/u,xdel,delt,tau
common/deloop/k
hh=delt*tau/2
h6=hh/3
th=realt+hh
xt=x+hh*dxdt
x1tau=(xdel(k)+xdel(k+1))/2
call derivs(th,xt,dxt,x1tau)
xt=x+hh*dxt
call derivs(th,xt,dxm,x1tau)
xt=x+delt*tau*dxm
dxm=dxt+dxm
x1tau=xdel(k+1)
tprime=realt+delt*tau
call derivs(tprime,xt,dxt,x1tau)
xh=x+h6*(dxdt+dxt+2*dxm)
return
end
```

```
10      !  THIS IS PROGRAM HUMPFMAP
20      !
30      !  LANGUAGE : HEWLETT - PACKARD  BASIC 3.0
40      !  COMPUTER : HEWLETT - PACKARD 9816  WITH MATHEMATICAL COPROCESSOR
50      !
60      !  THIS PROGRAM CALCULATES THE EXACT SOLUTION TO THE FIRST ORDER
70      !  DELAY-DIFFERENTIAL EQUATION WITH PIECEWISE CONSTANT MIXED FEEDBACK:
80      !  DX/DT = -ALPHA * X(T) + F [X(T-TAU)]    WHERE
90      !  F=D1     IF X(T-TAU) < THR1            (REGION 1)
100     !  F=C      IF THR1 < X(T-TAU) < THR2     (REGION 2)
110     !  F=D3     IF X(T-TAU) > THR2            (REGION 3)
120     !
130     !  THE PROGRAM EITHER CALCULATES AND PLOTS THE SOLUTION,
140     !  OR (LINES 4100-4160  & 4270-4330) COMPUTES AND DISPLAYS A POINCARE
150     !  MAP  X(N+1) VS X(N)  (SAMPLING INTERVAL IS GIVEN BY "SAMSTEP"),
160     !  OR (LINES 3520-3900) COMPUTES AND DISPLAYS A POINCARE MAP OF CROSSING
170     !  TIME INTERVALS  (CROSSINGS WITH THRESHOLD 1  OR THRESHOLD 2).
180     !  THE LATTER PLOT IS AT THE BASIS OF THE ANALYSIS OF THIS EQUATION
190     !  (BY UWE AN DER HEIDEN AND MICHAEL MACKEY); WE USED IT TO TRY TO
200     !  GET MORE INSIGHT INTO THE DYNAMICS OF SIMPLE AND COMPLEX SOLUTIONS,
210     !  ESPECIALLY THOSE FOR WHICH NO THEORY EXISTS.
220     !  THE PROGRAM FINDS THE CROSSING TIMES WITH THE THRESHOLDS.
230     !  TAU-SECONDS AFTER A CROSSING, THERE WILL BE AN EXTREMA IN THE SOLUTION
240     !  SINCE AT THIS POINT THE DERIVATIVE CHANGES ABRUPTLY.
250     !  THE PROGRAM SEWS THE EXTREMA TOGETHER USING INCREASING OR DECREASING
260     !  EXPONENTIALS.
270     !  THE RATE CONSTANT ALPHA CAN TAKE ON A DIFFERENT VALUE FOR DX/DT<0 OR
280     !  DX/DT>0. ALSO THE DELAY CAN TAKE ON TWO DIFFERENT VALUES, DEPENDING
290     !  ON WHETHER THE CROSSING OCCURRED FROM REGIONS 1 OR 3 INTO REGION 2
300     !  OR THE OPPOSITE.
310     !  THE PROGRAM ALLOWS FOR 2 DIFFERENT KINDS OF INITIAL CONDITIONS.  THE
320     !  FIRST IS REFERRED TO AS "NORMAL" AND CORRESPONDS TO
330     !  THR1 < X(T) <THR2   FOR T IN (-TAU,0)  WITH X(0)=THR2.
340     !  THE SECOND ALLOWS FOR A THRESHOLD CROSSING IN THE INTERVAL (-TAU,0)
350     !  AT T = -TAU + W, WHERE W BELONGS TO (0,TAU). THE INITIAL CONDITION IS
360     !  THR1 < X(T) < THR2, T IN (-TAU,-TAU+W); X(T) < THR1, T IN (-TAU+W,0)
370     !  AND X(0)=THR1.
380     !  BY VARYING W, KEEPING ALL OTHER PARAMETERS FIXED, ONE CAN EXPLORE
390     !  A SUBSET OF THE INITIAL CONDITIONS.
400     !
410     !  THE CALCULATION PROCEEDS UNTIL N THRESHOLD CROSSINGS HAVE BEEN DETERMI
NED.
420     !  THE VECTOR T CONTAINS THE CROSSING TIMES.
430     !  THE VECTOR XPRIM CONTANS THE VALUES OF THE EXTREMA OF THE SOLUTION.
440     !  THE INDEX M  (M2) COUNTS THE NUMBER OF CROSSINGS WITH THR1  (THR2).
450     !  THE INDEX I COUNTS THE TOTAL NUMBER OF CROSSINGS THAT HAVE OCCURRED.
460     !  TTHR1(M) CONTAINS THE VALUE OF THE INDEX I AT WHICH THE M'TH CROSSING
470     !  OCCURRED (LIKEWISE FOR TTHR2(M2)).
480     !  THE INDEX J COUNTS THE NUMBER OF THRESHOLD CROSSINGS UP TO WHICH THE
490     !  THE SOLUTION HAS BEEN PLOTTED.
500     !  AT EACH ITERATION OF THE J-LOOP (LINE 1930-3270) THE SIGN OF THE
510     !  DERIVATIVE CHANGES.  WHEN PAR=0, DX/DT < 0, AND PAR=1 WHEN DX/DT > 0.
520     !
530     !  FOR EACH J, THE PROGRAM FIRST DETERMINES WHETHER THE CROSSING TIME T(J
)
540     !  IS KNOWN (LINE 2010).  IF IT IS, THE PROGRAM COMPUTES THE ASSOCIATED
550     !  EXTREMUM AND FINDS WHETHER ANY OTHER THRESHOLD CROSSINGS WILL OCCUR ON
560     !  THE WAY FROM XPRIM(J-1) TO XPRIM(J) (LINES 2050-2260). IF THERE ARE NO
```

```
570     !  MORE CROSSINGS. IT PLOTS THE INCREASING OR DECREASING EXPONENTIAL
580     !  BETWEEN XPRIM(J-1) AND XPRIM(J).  IF THERE ARE MORE CROSSINGS,
590     !  THE PROGRAM DETERMINES THEM IN LINES 2470-2840 (PAR=0) OR IN LINES
600     !  2880-3230 (PAR=1).
610     !  THERE CAN ONLY BE ONE OR TWO MORE CROSSINGS DEPENDING ON XPRIM(J-1)
620     !  AND XPRIM(J).  THE PROGRAM SIMPLY EXPLORES THE DIFFERENT POSSIBILITIES
.
630     !
640     !  NOTE THAT THE CROSSING TIMES ARE DETERMINED EXACTLY, SINCE THEY ARE FO
UND
650     !  BY SOLVING FOR THE INTERSECTION OF AN EXPONENTIAL (+ CONSTANT) WITH
660     !  ONE OF THE THRESHOLDS. IF WE WERE DEALING WITH A SECOND ORDER ODE,
670     !  WE WOULD HAVE TO SOLVE FOR THE CROSSING TIMES NUMERICALLY.
680     !
690     !  FINALLY, IN LINES 3310-3450 THE PROGRAM COMPUTES THE PERIOD OF THE
700     !  SOLUTION IN SECONDS AND THE NUMBER OF PULSES PER PERIOD (I.E. THE
710     !  NUMBER OF TIMES THE SOLUTION ENTERS REGION 2 PER PERIOD).
720     !
730     !
740     INTEGER Par,Flag(6),M,Tthr1(1000),Tthr2(1000)
750     REAL T(2000),Xprim(2000)
760     COM /Params/ Alph1,Alph2,C,Amax,Tmax,Ymax,D(0:1000),L,D1,D3,Yesplot,Yespc
map,First,Sampstep,Counter
770     Alph1=3
780     Alph2=Alph1
790     Tau0=1
800     Dtau=0
810     Tau1=Tau0+Dtau
820     N=1000
830     Mc1=N/2-10
840     Accur=.0000000001
850     Tmin=0
860     Tmax=2.5
870     Ymax=2
880     C=2*Alph1
890     Gamma=C/Alph1
900     D1=0
910     D3=0
920     W=.12
930     Thr1=1
940     Thr2=2.9
950     Istart=120
960     Samper=1
970     Sampstep=INT(Samper/.01)
980     Counter=0
990     Yespcmap=0
1000    Yesplot=0
1010    Yescross=0
1020    GINIT
1030    PLOTTER IS 3,"INTERNAL"
1040!   PLOTTER IS 705,"HPGL"
1050    GRAPHICS ON
1060    GINIT
1070!   OUTPUT 705;"VSS"
1080    DISP "IS A PLOT OF THE SOLUTION DESIRED?   [YES:1   ,  NO:0]"
1090    WAIT 1
1100    INPUT Yesplot
1110    IF Yesplot=0 THEN GOTO 1390
1120    VIEWPORT 0,130,0,100
1130    WINDOW -Tau0,Tmax,0,Ymax
1140    FRAME
1150    AXES 1.0,1.0,0,0,5,1
1160    MOVE -Tau0,Thr1
1170    LINE TYPE 5
1180    DRAW Tmax,Thr1
1190    MOVE Tmax,Thr2
```

```
1200   DRAW -Tau0,Thr2
1210   LINE TYPE 4
1220   MOVE Tau0,0
1230   DRAW Tau0,Ymax
1240   !   LINE TYPE 4
1250   !   MOVE W,0
1260   !   DRAW W,Ymax
1270   !   MOVE 1,Ymax
1280   !   DRAW 1,0
1290   !   MOVE 2,0
1300   !   DRAW 2,Ymax
1310   !   MOVE 0,Thr1
1320   LINE TYPE 1
1330   MOVE -Tau0,(Thr1+Thr2)/2
1340   DRAW -Tau0+W,1
1350   DRAW -Tau0+.9,.5
1360   DRAW 0,1
1370   PENUP
1380   GOTO 1570
1390   DISP "IS A POINCARE MAP OF THE SOLUTION DESIRED ?    [YES:1;NO:0]"
1400   WAIT 1
1410   INPUT Yespcmap
1420   IF Yespcmap=1 THEN
1430       VIEWPORT 10,100,10,100
1440       IF B>Gamma THEN
1450           Xmax=B
1460       ELSE
1470           Xmax=Gamma
1480       END IF
1490       WINDOW 0,Xmax,0,Xmax
1500       AXES .2,.2,0,0,5,5
1510       FRAME
1520       LINE TYPE 4
1530       MOVE 0,0
1540       DRAW Xmax,Xmax
1550       PENUP
1560   END IF
1570   LINE TYPE 1
1580   L=0
1590   !
1600   !     INITIAL CONDITIONS
1610   !
1620   DISP "NORMAL I.C.: 1    ;    I.C. SPECIFIED BY  W : 0"
1630   WAIT 1
1640   INPUT Icnormal
1650   IF Icnormal=1 THEN
1660       !  NORMAL INITIAL CONDITION: 1<X(T)<B  FOR T IN (-TAU,0)
1670       First=Thr2
1680       T(1)=0
1690       Tprim1=Tau1
1700       Xprim(1)=(Thr2-C/Alph1)*EXP(-Alph1*Tprim1)+C/Alph1
1710       CALL Plotexp(Thr2,0,Tprim1,1)
1720       K=1
1730   ELSE
1740       !  INITIAL CONDITION SPECIFIED BY  W  (W IS IN (0,1))
1750       First=Thr1
1760       T(1)=-Tau+W
1770       T(2)=0
1780       Tprim1=W
1790       Xprim(1)=(Thr1-C/Alph1)*EXP(-Alph1*Tprim1)+C/Alph1
1800       CALL Plotexp(Thr1,0,Tprim1,1)
1810       K=2
1820       IF Xprim(1)>Thr2 THEN
1830           T(3)=1/Alph1*LOG((Gamma-Thr1)/(Gamma-Thr2))
1840           K=3
1850       END IF
```

```
1860   END IF
1870   M=1
1880   M2=1
1890   D(0)=D3
1900   !
1910   !       SOLUTION FOR  T > 0
1920   !
1930   FOR J=2 TO N STEP 1
1940        Par=J MOD 2
1950        Tau=Tau1
1960        IF Par=0 THEN
1970             L=(J-2)/2
1980             Tau=Tau0
1990        END IF
2000        Xpr=Xprim(J-1)
2010        IF T(J)>0 OR (J=2 AND Icnormal=0) THEN
2020 !
2030 !          CROSSING TIME T(J) IS KNOWN
2040 !
2050             Flags=1
2060             Tprim2=T(J)+Tau
2070             IF Par=0 THEN
2080                  Xprim(J)=(Xprim(J-1)-D(L)/Alph2)*EXP(-Alph2*(Tprim2-Tprim1))+
D(L)/Alph2
2090             ELSE
2100                  Xprim(J)=(Xprim(J-1)-C/Alph1)*EXP(-Alph1*(Tprim2-Tprim1))+C/A
lph1
2110             END IF
2120 !
2130 !    IF THE LAST 2 EXTREMA  XPRIM(J-1) AND XPRIM(J) ARE IN THE SAME
2140 !    REGION, NO MORE CROSSING TIMES HAVE TO BE COMPUTED.
2150 !    SOLUTION IS SIMPLY PLOTTED, AND PROGRAM GOES ON TO NEXT J.
2160 !    IF NOT , FURTHER CROSSINGS TIMES HAVE TO BE DETERMINED,
2170 !    STARTING AT LINE 2240 IF PAR=0, OR 2620 IF PAR=1.
2180 !
2190             FOR Mm=1 TO 6 STEP 1
2200                  Flag(Mm)=0
2210             NEXT Mm
2220             IF Xprim(J)>Thr2 AND Xprim(J-1)>Thr2 THEN Flag(1)=1
2230             IF Xprim(J)<Thr2 AND Xprim(J-1)<Thr2 THEN Flag(2)=1
2240             IF Xprim(J)>Thr1 AND Xprim(J-1)>Thr1 THEN Flag(3)=1
2250             IF Xprim(J)<Thr1 AND Xprim(J-1)<Thr1 THEN Flag(4)=1
2260             Flag(5)=Flag(3) AND Flag(2)
2270             IF Flag(1) OR Flag(4) OR Flag(5) THEN
2280                  CALL Plotexp(Xpr,Tprim1,Tprim2,Par)
2290                  GOTO 3260
2300             ELSE
2310                  I=K+1
2320                  IF Par=0 THEN GOTO 2470
2330                  IF Par=1 THEN GOTO 2880
2340             END IF
2350        ELSE
2360 !
2370 !    CROSSING TIME T(J) IS NOT KNOWN
2380 !    FLAGS=1 IF T(J) IS ALREADY KNOWN
2390 !    FLAGS=0 IF T(J) IS NOT KNOWN
2400 !
2410             Flags=0
2420             I=J
2430             IF Par=1 THEN GOTO 2880
2440 !
2450 !    DETERMINE CROSSINGS WHEN  DX/DT < 0  (PAR=0)
2460 !
2470             IF Xprim(J-1)>Thr2 THEN
2480                  T(I)=Tprim1-1/Alph2*LOG((Thr2-D(L)/Alph2)/(Xprim(J-1)-D(L)/Al
ph2))
```

```
2490                Tthr2(M2)=I
2500                M2=M2+1
2510                IF Flags=1 THEN GOTO 2540
2520                Tprim2=T(I)+Tau
2530                Xprim(J)=(Thr2-D(L)/Alph2)*EXP(-Alph2*Tau)+D(L)/Alph2
2540                IF Xprim(J)<Thr2 AND Xprim(J)>Thr1 THEN
2550                     CALL Plotexp(Xpr,Tprim1,Tprim2,0)
2560                ELSE
2570                     T(I+1)=Tprim1-1/Alph2*LOG((Thr1-D(L)/Alph2)/(Xprim(J-1)-D
(L)/Alph2))
2580                     D(I/2)=D1
2590                     Tthr1(M)=I+1
2600                     M=M+1
2610                     K=K+1
2620                     CALL Plotexp(Xpr,Tprim1,Tprim2,0)
2630                END IF
2640                GOTO 3250
2650           ELSE
2660                IF Xprim(J-1)<Thr1 THEN
2670                     PRINT "EQUILIBRIUM REACHED: SOLUTION GOES TO ZERO"
2680                     CALL Plotexp(Xpr,Tprim1,Tmax,0)
2690                     GOTO 3970
2700                END IF
2710                IF Thr1<(D(L)/Alph2) THEN
2720                     Tprim2=Tmax
2730                     GOTO 2820
2740                END IF
2750                T(I)=Tprim1-1/Alph2*LOG((Thr1-D(L)/Alph2)/(Xprim(J-1)-D(L)/Al
ph2))
2760                D((I-1)/2)=D1
2770                Tthr1(M)=I
2780                M=M+1
2790                IF Flags=1 THEN GOTO 2820
2800                Tprim2=T(I)+Tau
2810                Xprim(J)=(Thr1-D(L)/Alph2)*EXP(-Alph2*Tau)+D(L)/Alph2
2820                CALL Plotexp(Xpr,Tprim1,Tprim2,0)
2830           END IF
2840           GOTO 3250
2850 !
2860 !     DETERMINE CROSSNGS WHEN DX/DT > 0  (PAR=1)
2870 !
2880           IF Xprim(J-1)<Thr1 THEN
2890                T(I)=Tprim1-1/Alph1*LOG((Thr1-C/Alph1)/(Xprim(J-1)-C/Alph1))
2900                Tthr1(M)=I
2910                M=M+1
2920                IF Flags=1 THEN GOTO 2950
2930                Tprim2=T(I)+Tau
2940                Xprim(J)=(Thr1-C/Alph1)*EXP(-Alph1*Tau)+C/Alph1
2950                IF Xprim(J)<Thr2 AND Xprim(J)>Thr1 THEN
2960                     CALL Plotexp(Xpr,Tprim1,Tprim2,1)
2970                ELSE
2980                     T(I+1)=Tprim1-1/Alph1*LOG((Thr2-C/Alph1)/(Xprim(J-1)-C/Al
ph1))
2990                     Tthr2(M2)=I+1
3000                     M2=M2+1
3010                     D(I/2)=D3
3020                     K=K+1
3030                     CALL Plotexp(Xpr,Tprim1,Tprim2,1)
3040                END IF
3050                GOTO 3250
3060           ELSE
3070                IF Xprim(J-1)>Thr2 THEN
3080                     PRINT "EQUILIBRIUM REACHED: SOLUTION GOES TO GAMMA"
3090                     GOTO 3970
3100                END IF
3110                IF Thr2>(C/Alph1) THEN
```

```
3120                Tprim2=Tmax
3130                GOTO 3220
3140            END IF
3150            T(I)=Tprim1-1/Alph1*LOG((Thr2-C/Alph1)/(Xprim(J-1)-C/Alph1))
3160            Tthr2(M2)=I
3170            M2=M2+1
3180            D((I-1)/2)=D3
3190            IF Flags=1 THEN GOTO 3220
3200            Tprim2=T(I)+Tau
3210            Xprim(J)=(Thr2-C/Alph1)*EXP(-Alph1*Tau)+C/Alph1
3220            CALL Plotexp(Xpr,Tprim1,Tprim2,1)
3230        END IF
3240    END IF
3250    K=K+1
3260    Tprim1=Tprim2
3270 NEXT J
3280 !
3290 !  DETERMINE PERIOD AND NUMBER OF PULSES PER PERIOD
3300 !
3310 Mm=N-1
3320 FOR I=2 TO Mcl STEP 2
3330     Delta1=T(N)-T(N-I)
3340     Delta2=T(N-I)-T(N-2*I)
3350     Diff1=ABS(Delta2-Delta1)
3360     Delta3=T(Mm)-T(Mm-I)
3370     Delta4=T(Mm-I)-T(Mm-2*I)
3380     Diff2=ABS(Delta3-Delta4)
3390     IF Diff1<Accur AND Diff2<Accur THEN
3400         PRINT "PERIOD IS",Delta1
3410         PRINT "NUMBER OF PULSES PER PERIOD IS",I/2
3420         GOTO 3460
3430     END IF
3440 NEXT I
3450 PRINT "PERIOD DOESN'T CONVERGE FOR N=",N,"AND MCL=",Mcl
3460 IF Yespcmap=1 THEN GOTO 3970
3470 !
3480 !
3490 !  PLOTS OF CROSSING TIME INTERVALS
3500 !
3510 !
3520 DISP "IS PLOT OF THE CROSSING TIMES DESIRED?    [ YES: 1    ;   NO : 0 ]"
3530 WAIT 1
3540 INPUT Yescross
3550 DISP "CROSSINGS WITH THR1  (1)  OR  THR2  (2)  ? "
3560 WAIT 2
3570 DISP "ENTER 0 FOR GRAPHICS DUMP,   -1 FOR NEITHER, GOTO END"
3580 WAIT 1
3590 INPUT Cross12
3600 IF Cross12=-1 THEN GOTO 3970
3610 IF Cross12=0 THEN GOTO 3920
3620 IF Yescross=1 THEN
3630     PLOTTER IS 3,"INTERNAL"
3640     GRAPHICS ON
3650     GINIT
3660     VIEWPORT 10,100,10,100
3670     WINDOW 0,1.5,0,1.5
3680     AXES .1,.1,0,0,5,5
3690     FRAME
3700     IF Cross12=1 THEN
3710         FOR I=Istart TO M/2-2 STEP 1
3720             Deltatpr=T(Tthr1(2*I+2))-T(Tthr1(2*I+1))
3730             Deltat=T(Tthr1(2*I))-T(Tthr1(2*I-1))
3740             !            PENUP
3750             PLOT Deltat,Deltatpr
3760             !            PENUP
3770         NEXT I
```

```
3780            PENUP
3790        ELSE
3800            FOR I=Istart TO M2/2-2 STEP 1
3810                Deltatpr=T(Tthr2(2*I+2))-T(Tthr2(2*I+1))
3820                Deltat=T(Tthr2(2*I))-T(Tthr2(2*I-1))
3830                !               PENUP
3840                PLOT Deltat,Deltatpr
3850                !               PENUP
3860            NEXT I
3870            PENUP
3880        END IF
3890        PENUP
3900    END IF
3910    GOTO 3550
3920    PRINTER IS 701
3930    PRINT "ALPH=",Alph1,"C=",C,"TAU=",Tau,"THR1=",Thr1
3940    PRINT "THR2=",Thr2,"N=",N,"W=",W,"D3=",D3
3950    CALL Gdump
3960    GOTO 3550
3970    end
3980    sub Plotexp(Xprim,Tprim1,Tprim2,INTEGER Par)
3990        COM /Params/ Alph1,Alph2,C,Amax,Tmax,Ymax,D(0:1000),L,D1,D3,Yesplot,Y
espcmap,First,Sampstep,Counter
4000        IF Yesplot=0 AND Yespcmap=0 THEN GOTO 4370
4010        N=(Tprim2-Tprim1) DIV .01
4020        IF Par=0 THEN
4030            FOR M=0 TO N STEP 1
4040                Tpr=M*.01
4050                Y=(Xprim-D(L)/Alph2)*EXP(-Alph2*Tpr)+D(L)/Alph2
4060                Ampl=Y
4070                IF Yesplot=1 THEN
4080                    PLOT Tprim1+Tpr,Ampl,-1
4090                ELSE
4100                    Counter=Counter+1
4110                    IF (Counter MOD Sampstep)=0 THEN
4120                        PENUP
4130                        PLOT First,Ampl
4140                        PENUP
4150                        First=Ampl
4160                    END IF
4170                END IF
4180            NEXT M
4190        ELSE
4200            FOR M=0 TO N STEP 1
4210                Tpr=M*.01
4220                Y=(Xprim-C/Alph1)*EXP(-Alph1*Tpr)+C/Alph1
4230                Ampl=Y
4240                IF Yesplot=1 THEN
4250                    PLOT Tprim1+Tpr,Ampl,-1
4260                ELSE
4270                    Counter=Counter+1
4280                    IF (Counter MOD Sampstep)=0 THEN
4290                        PENUP
4300                        PLOT First,Ampl
4310                        PENUP
4320                        First=Ampl
4330                    END IF
4340                END IF
4350            NEXT M
4360        END IF
4370    SUBEND
```

```
10    ! PROGRAM C1D2SOL
20    !
30    !  THIS PROGRAM INTEGRATES THE PUPIL DELAY-DIFFERENTIAL EQUATION
40    !  WITH IS FIRST ORDER FOR CONSTRICTION AND SECOND ORDER FOR DILATION.
50    !  IT INTEGRATES THE EQUATION UNTIL EITHER THE MAXIMUM NUMBER OF
60    !  CROSSING TIMES HAS BEEN REACHED, OR FOR A  MAXIMUM NUMBER OF
70    !  TIME DELAYS, WHICH EVER COMES FIRST.
80    !  THE PROGRAM THEN PROCEDES TO FIND THE PERIOD OF THE SOLUTION
90    !  (IN SECONDS) AS WELL AS THE NUMBER OF PULSES PER PERIOD.
100   !  THE SOLUTION IS DISPLAYED ON THE SCREEN OR ON THE PLOTTER.
110   !
120   !  X(1) IS THE STATE VARIABLE (PUPIL AREA)
130   !  DXDT(1) IS THE TIME DERIVATIVE OF PUPIL AREA
140   !  XH(1) AND DXDTH(1) ARE THE VALUES OF X(1) AND DXDT(1) AT THE END
150   !  OF THE INTEGRATION TIME STEP.
160   !  X1TAU IS X(1) AT TIME (T-TAU) WHERE TAU IS THE DELAY.
170   !  THR1 (THR2) IS THE LOWER (UPPER) THRESHOLD.
180   !  THE UPPER (LOWER) ASYMPTOTE IS Aoff (Aon).
190   !  THE FORCING SWITCHES BETWEEN "DFOR" AND "CFOR" DEPENDING ON THE
200   !  POSITION  OF X1TAU WITH PESPECT OT THE THRESHOLDS.
210   !
220   !  FOR CONSTRICTION PUPIL AREA OBEYS :
230   !       DXDT = -ALPHC*X+CFOR
240   !  FOR DILATION PUPIL AREA OBEYS :
250   !       D(DXDT)/DT=-DELTA*DXDT-(W^2)*X+DFOR
260   !
270   !  THESE DIFFERENTIAL EQUATIONS ARE NUMERICALLY INTEGRATED USING
280   !  AN EULER METHOD. THE INTEGRATION STEP IS DELT*TAU.
290   !  ACCUR IS THE ACCURACY OF PERIOD DETERMINATION.
300   !  THE PERIOD IS COMPUTED FROM THE SEQUENCE OF THRESHOLD CROSSINGS
310   !  TIMES STORED IN T(N) (CROSSINGS ARE DETECTED BY THE CHANGES IN
311   !  THE FLAGS WHICH LABEL THE 3 REGIONS OF THE FEEDBACK FUNCTION).
320   !
330   Delt=.01
340   Deldiv=1/Delt
350   ALLOCATE Xdel(0:Deldiv)
360   COM /Vect/ X1tau,Sigma(1),Tau
370   COM /Param/ Thr1,Thr2,C
380   COM INTEGER K
390   DIM Dxdt(1),X(1),Xh(1),Dxdth(1)
400   N=100                 ! MAXIMUM NUMBER OF THRESHOLD CROSSINGS
410   ALLOCATE T(N)
420   Ntaumax=200          ! INTEGRATE TILL TIME (NTAUMAX*TAU)
430   Mm=N-1
440   Mcl=N/2-1            ! MAXIMUM CYCLE LENGTH
450   Accur=.0001
460   !
470   !    SYSTEM PARAMETERS
480   !
490   Tau=.411
500   Thr1=21.5
510   Thr2=30
520   !
530   ! ENTER PARAMETERS FROM THE C1-D2 FIT OF THE SINGLE PULSE RESPONSE
540   !
550   Aoff=34.2
560   Xnod=21.5
570   A=4.39
580   Aon=Xnod-A
590   Alphc=7.91
```

```
600   Alphd=1.68
610   Betad=.587
620   Cfor=Alphc*Aon
630   Delta=Alphd+Betad
640   W=Alphd*Betad
650   Dfor=Aoff*(W^2)
660   !
670   !   GRAPHICS
680   !
690 ! Xtinit=(Thr1+Thr2)/2
700   Xtinit=22.5
710   Tmin=0
720   Tmax=7
730   Xmin=16
740   Xmax=24
750 ! PLOTTER IS 705,"HPGL"
760   PLOTTER IS 3,"INTERNAL"
770 ! OUTPUT 705;"VS5"
780   GRAPHICS ON
790   GINIT
800   VIEWPORT 10,100,10,70
810   WINDOW -Tau,Tmax,Xmin,Xmax
820   FRAME
830   AXES  2,1,Tmin,Xmin,5,5
840   LINE TYPE 4
850   MOVE -Tau,Thr1
860   DRAW Tmax,Thr1
870   MOVE Tmax,Thr2
880   DRAW -Tau,Thr2
890   LINE TYPE 1
900   MOVE -Tau,0
910   !
920   !  INITIALIZE FUNCTION ON [-TAU,0]
930   !
940   FOR K=0 TO Deldiv STEP 1
950     Xdel(K)=Xtinit
960     PLOT (K-Deldiv)*Delt*Tau,Xdel(K)
970   NEXT K
980   IF Xtinit<=Thr2 AND Xtinit>=Thr1 THEN
990      Lastflag=2
1000  ELSE
1010     IF Xtinit<Thr1 THEN
1020        Lastflag=1
1030     ELSE
1040        Lastflag=3
1050     END IF
1060  END IF
1070  !
1080  !   NUMERICAL INTEGRATION BEGINS HERE;  INTEGRATION STEP IS DELT,
1090  !   DELAY BUFFER IS USED.
1100  !
1110  I=1
1120  FOR Ntau=1 TO Ntaumax STEP 1
1130    X(1)=Xdel(Deldiv)
1140    FOR K=1 TO Deldiv STEP 1
1150      Tnext=(Ntau-1+K*Delt)*Tau
1160      Realt=Tnext-Delt*Tau
1170      X1tau=Xdel(K-1)
1180      IF X1tau<Thr1 OR X1tau>Thr2 THEN
1190         Xh(1)=Delt*Tau*Dxdt(1)+X(1)
1200         Dxdth(1)=(-(W^2)*X(1)-Delta*Dxdt(1)+Dfor)*Delt*Tau+Dxdt(1)
1210      ELSE
1220         Xh(1)=(Cfor-Alphc*X(1))*Delt*Tau+X(1)
1230         Dxdth(1)=Cfor-Alphc*X(1)
1240      END IF
1250      PLOT Tnext,Xh(1)
```

```
1260      IF Xh(1)<=Thr2 AND Xh(1)>=Thr1 THEN
1270         Flag=2
1280      ELSE
1290         IF Xh(1)<Thr1 THEN
1300            Flag=1
1310         ELSE
1320            Flag=3
1330         END IF
1340      END IF
1350      IF Lastflag<>Flag THEN
1360         T(I)=Realt
1370         I=I+1
1380         Lastflag=Flag
1390         IF I>N THEN GOTO 1510
1400      END IF
1410      Xdel(K-1)=X(1)
1420        X(1)=Xh(1)
1430        Dxdt(1)=Dxdth(1)
1440    NEXT K
1450    Xdel(Deldiv)=Xh(1)
1460  NEXT Ntau
1470  BEEP
1480  !
1490  !   DETERMINATION OF PERIOD
1500  !
1510  FOR J=2 TO Mcl STEP 2
1520     Delta1=T(N)-T(N-J)
1530     Delta2=T(N-J)-T(N-2*J)
1540     Diff1=ABS(Delta2-Delta1)
1550     Delta3=T(Mm)-T(Mm-J)
1560     Delta4=T(Mm-J)-T(Mm-2*J)
1570     Diff2=ABS(Delta4-Delta3)
1580     IF Diff1<Accur AND Diff2<Accur THEN
1590        PRINT "PERIOD IS",Delta1
1600        PRINT "NUMBER OF PULSES PER PERIOD IS ",J/2
1610        GOTO 1650
1620     END IF
1630  NEXT J
1640  PRINT "PERIOD IS UNDETERMINED"
1650  DISP "DUMP GRAPHICS ?   [YES:1 , NO:0]"
1660  WAIT 2
1670  INPUT Flag
1680  IF Flag=1 THEN
1690    PRINTER IS 701
1700    PRINT "INITIAL CONDITION ON (-TAU,0) IS  X=",Xtinit
1710    PRINT "XMIN=",Xmin,"XMAX=",Xmax,"TMAX=",Tmax
1720    PRINT "DELT=",Delt,"TAU=",Tau
1730    DUMP GRAPHICS
1740    PRINTER IS 1
1750  END IF
1760  end
```

APPENDIX E

CONTRIBUTIONS OF THE AUTHOR TO THE MANUSCRIPTS

SECTION 2.2 : Modelling autonomous oscillations in the human pupil light reflex using nonlinear delay-differential equations.
AUTHORS : André Longtin and John G. Milton. *Bulletin of Mathematical Biology* 51, 605-624 (1989).

1- Theory.
2- Numerical calculations and associated figures (2,3,4).
3- Literature review for anatomy and physiology of this reflex.

SECTION 2.3 : Insight into the transfer function, gain, and oscillation onset for the pupil light reflex using nonlinear delay-differential equations.
AUTHORS : André Longtin and John G. Milton. *Biological Cybernetics* 61, 51-58 (1989).

1- Theory.
2- Numerical calculations and associated figures (1,2,3,4).
3- Literature review of control system's approach applied to biological systems and to pupil light reflex in particular.

SECTION 3.2 : Evaluation of pupil constriction and dilation from cycling measurements.
AUTHORS : John G. Milton and André Longtin. *Vision Research*, in press.

1- Design and setup of experimental apparatus.
2- Experiments.
3- Model for pupil cycling.
4- Computer algorithm to integrate model equation (see Appendix D) and produce phase plots.
5- Smooth fit to single pulse response (Figure 6d) (see Appendix C).

SECTION 3.3 : Complex oscillations in the human pupil light reflex with "mixed" and delayed feedback.
AUTHORS : André Longtin and John G. Milton. *Mathematical Biosciences* 90, 183-199 (1988).

1- Design and setup of experimental apparatus.
2- Experiments.
3- Phenomenological model.
4- Algorithm to integrate model equation and produce bifurcation diagrams.
5- Part of literature review and data analysis.

The data for the next manuscript was obtained from the same kind of piecewise constant feedback experiments as in Sections 3.2 and 3.3.

SECTION 5.3 : Noise and critical behavior of the pupil light reflex at oscillation onset.
AUTHORS : André Longtin, John G. Milton, Jelte Bos and Michael C. Mackey. *Physical Review A*, to be submitted (October 1989).

1- Literature review.
2- Theory.
3- Numerical integration of stochastic DDE (see Appendix D).
4- Fast Fourier Transforms for PCNF.

APPENDIX A : Noise induced global asymptotic stability.
AUTHORS : Michael C. Mackey, André Longtin and Andrzej Lasota. *Journal of Statistical Physics*, in press.

1- Literature review.
2- Numerical integration of stochastic ODE's.
3- Numerical computations for and production of the figures.

APPENDIX B : Irregular pupil cycling as a characteristic abnormality in patients with demyelinative optic neuropathy.
AUTHORS : John G. Milton, André Longtin, Trevor Kirkham and Gordon S. Francis. *American Journal of Ophthalmology* 105, 402-407 (1988).

1- Design and setup of experimental apparatus.
2- Experiments on patients.

REFERENCES

1) L. Stark, "Environmental clamping of biological systems:pupil servomechanism", J. Opt. Soc. Amer. **52**, 925 (1962).

2) H. Poincaré, "Sur les équations de la dynamique et le problème de trois corps", Acta. Math. **13**,1 (1890).

3) A.J. Lotka, *"Elements of Mathematical Biology"* (Dover, New York, 1956).

4) V. Volterra, *"Leçons sur la Théorie Mathématique de la Lutte pour la Vie"* (Gauthiers-Villars, Paris, 1931).

5) N. Raschevsky, *"Mathematical Biophysics. Physico-Mathematical Foundations of Biology"* (Dover, New York, 1960).

6) B. van der Pol, "Forced oscillations in a circuit with nonlinear resistance (receptance with reactive triode)", London, Edinburgh and Dublin Phil. Mag. **3**, 65 (1927).

7) T.Y. Li and J.A. Yorke, "Ergodic maps on [0,1] and nonlinear pseudo-random number generators", Nonlin. Anal. **2**, 473 (1978).

8) H.G. Schuster, *"Deterministic Chaos : an Introduction"* (Physik-Verlag, Weinheim, 1984).

9) R.L. Devaney, *"An Introduction to Chaotic Dynamical Systems"* (Benjamin/ Cummings, Menlo Park, 1986).

10) J. Guckenheimer and P. Holmes, *"Nonlinear Oscillations, Dynamical Systems, and Bifurcations of Vector Fields"* (Springer, New York, 1983).

11) J.D. Farmer, "Chaotic attractors of infinite-dimensional dynamical systems", Physica **4D**, 366 (1982).

12) J.D. Farmer, E. Ott and J.A. Yorke, "The dimension of chaotic attractors", Physica **7D**, 153 (1983).

13) A. Lasota and M.C. Mackey, *"Probabilistic Properties of Deterministic Systems"* (Cambridge University Press, Cambridge, 1985).

14) B.-L. Hao, *"Chaos"* (World Scientific, Singapore, 1984).

15) P. Cvitanović, *"Universality in Chaos"* (Adam Hilger, Bristol, 1986).

16) A.V. Holden, *"Chaos"* (Princeton University Press, Princeton, 1986).

17) G. Mayer-Kress, *"Dimensions and Entropies in Chaotic Systems"* (Springer, Berlin, 1986).

18) A. Ben-Mizrachi, I. Procaccia and P. Grassberger, "Characterization of experimental (noisy) strange attractors", Phys. Rev. A **29**, 975 (1984).

19) G. Mayer-Kress and J. Holzfuss, "Analysis of the human electro-encephalogram

with methods from nonlinear dynamics", in *"Temporal Disorder in Human Oscillatory Systems"*, L. Rensing, U. an der Heiden and M.C. Mackey, eds., pp.57-68 (Springer, New York, 1987).

20) J.M. Milton, A. Longtin, A. Beuter, M.C. Mackey and L. Glass, "Complex dynamics and bifurcations in neurology", J. Theor. Biol. **138**, 129 (1989).

21) W. Horsthemke and R. Lefever, *"Noise-Induced Transitions. Theory and Applications in Physics, Chemistry and Biology"* (Springer, Berlin, 1984).

22) J.P. Crutchfield, J.D. Farmer and B.A. Huberman, "Fluctuations and simple chaotic dynamics", Phys. Rep. **92**, 45 (1982).

23) K. Matsumoto and I. Tsuda, "Noise-Induced Order", J. Stat. Phys. **31**, 87 (1983).

24) M.C. Mackey and L. Glass, "Oscillation and chaos in physiological control systems", Science **197**, 287 (1977).

25) L. Glass and M.C. Mackey, "Pathological conditions resulting from instabilities in physiological control systems", Ann. N. Y. Acad. Sci. **316**, 214 (1979).

26) L. Glass and M.C. Mackey, *"From Clocks to Chaos : The Rhythms of Life"* (Princeton University Press, Princeton, 1988).

27) H. Degn, A.V. Holden and L.F. Olsen, *"Chaos in Biological Systems"* (Plenum, New York, 1987).

28) M.R. Guevara, L. Glass and A. Shrier, "Phase-locking, period-doubling bifurcations and irregular dynamics in periodically stimulated cardiac cells", Science **214**, 1350 (1981).

29) D.R. Chialvo and J. Jalife, "Non-linear dynamics of cardiac excitation and impulse propagation", Nature **330**, 749 (1987).

30) H. Hayashi and S. Ishizuka, "Chaos in molluscan neuron", in *"Chaos in Biological Systems"*, H. Degn, A.V. Holden and L.F. Olsen, eds., pp.157-166 (Plenum, New York, 1987).

31) L. Stark and P.M. Sherman, "A servoanalytic study of consensual pupil reflex to light", J. Neurophysiol. **20**, 17 (1957).

32) L. Stark, "The pupil as a paradigm for neurological control systems", IEEE Trans. **BME-31**, 919 (1984).

33) A.C. Guyton, *"Basic Human Neurophysiology"*, 3^{rd} ed. (Saunders, Philadelphia, 1981).

34) I.E. Loewenfeld, "Mechanisms of reflex dilation of the pupil: Historical review and experimental analysis", Doc. Ophthalmol. **12**, 185 (1958).

35) J.J.B. Jack, D. Noble and R.W. Tsien, *"Electric Current Flow in Excitable Cells"* (Oxford University Press, Oxford, 1983).

36) B. Pansky and D.J. Allen, *"Review of Neuroscience"* (Macmillan, New York, 1980).

37) N.R. Miller, Ed., *"Walsh and Hoyt's Clinical Neuro-Ophthalmology"* (Williams and Wilkins, Baltimore, 1985), **Vol. 2**.

38) J.D. Smith, G.A. Masek, L.Y. Ichinose, T. Watanabe and L. Stark, "Single neuron activity in the pupillary system", Brain Res. **24**, 219 (1970).

39) T. Inoue and T. Kiribuchi, "Cortical and subcortical pathways for pupillary reactions in rabbits", Jpn. J. Ophthalmol. **29**, 63 (1985).

40) E. Alexandridis, *"The Pupil"* (Springer, New York, 1985).

41) A.M. Sillito and A.W. Zbrożyna, "The localization of pupilloconstrictor function within the midbrain of the cat", J. Physiol. **211**, 461 (1970a).

42) A.M. Sillito and A.W. Zbrożyna, "The activity characteristics of the preganglionic pupilloconstrictor neurones", J. Physiol. **211**, 767 (1970b).

43) M.S. Bonvallet and A.W. Zbrożyna, "Les commandes réticulaires du système autonome et en particulier de l'innervation sympathique et parasympathique de la pupille", Arch. Biol. Ital. **101**, 174 (1963).

44) R.W. Rodieck, "Maintained activity of cat retinal ganglion cells", J. Neurophysiol. **30**, 1043 (1967)

45) D.A. Johnson and D. Purves, "Tonic and reflex synaptic activity recorded in ciliary ganglion cells of anaesthetized rabbits", J. Physiol. **339**, 599 (1983).

46) L. Stark, "Stability, oscillations, and noise in the human pupil servomechanism", Proc. **IRE 47**, 1925 (1959).

47) S.F. Stanten and L. Stark, "A statistical analysis of pupil noise", IEEE Trans. **BME-13**, 140 (1966).

48) T. Muramatsu, F. Okuyama and T. Tokoro, "Studies on fluctuation of accommodation and pupil size", Proceedings of the "15th International Pupil Colloquium", Hamamatsu City, Japan, June 16-18, 1986.

49) J. Semmlow and D. Chen, "A simulation model of the human pupil light reflex", Math. Biol. **33**, 5 (1977).

50) R.E. Yoss, N.J. Moyer and R.W. Hollenhorst, "Hippus and other spontaneous rhythmic pupillary waves", Am. J. Ophthalmol. **70**, 935 (1970).

51) H. Bouma and L.C.J. Baghuis, "Hippus of the pupil : periods of slow oscillations of unknown origin", Vision Res. **11**, 1345 (1971).

52) E. Henneman, "Recruitment of motoneurons : the size principle", in *"Motor Unit Types, Recruitment and Plasticity in Health and Disease"*, J.E. Desmedt, ed., pp.26-60 (Karger, Basel, 1981).

53) S. Usui and L. Stark, "Sensory and motor mechanisms interact to control am-

plitude of pupil noise", Vision Res. **18**, 505 (1978).

54) M.C. Mackey and J.G. Milton, "Dynamical diseases", Ann. N. Y. Acad. Sci. **504**, 16 (1987).

55) M.R. Guevara, L. Glass, M.C. Mackey and A. Shrier, "Chaos in neurobiology", IEEE Trans. **SMC-13**, 790 (1983).

56) R. King, J.D. Barchas and B.A. Huberman, "Chaotic behaviour in dopamine neurodynamics", Proc. Nat. Acad. Sci. USA **81**, 1244 (1984).

57) M.C. Mackey and U. an der Heiden, "The dynamics of recurrent inhibition", J Math. Biol. **19**, 211 (1982).

58) F.W. Campbell and T.C.D. Whiteside, "Induced pupillary oscillations", Br. J. Ophthalmol. **34**, 180 (1950).

59) H.J. Stern, "A simple method for the early diagnosis of abnormality of the pupillary reaction", Br. J. Ophthalmol. **28**, 275 (1944).

60) C.N. Martyn and D.L. Ewing, "Pupil cycle time. A simple way of measuring an autonomic reflex", J. Neurol. Neurosurg. Psychiatry **49**, 771 (1986).

61) S.D. Miller and H.S. Thompson, "Edge-light pupil cycle time", Br. J. Ophthalmol. **62**, 495 (1978).

62) J.G. Milton, A. Longtin, T.H. Kirkham and G.S. Francis, "Irregular pupil cycling as a characteristic abnormality in patients with demyelinative optic neuropathy", Amer. J. Ophthalmol. **105**, 402 (1988). (Appendix B of this thesis)

63) K. Ukai, J. Higashi and S. Ishikawa, "Edge-light pupil oscillation of optic neuritis", Neuro-ophthalmology **1**, 33 (1980).

64) A. Longtin and J.G. Milton, "Complex oscillations in the pupil light reflex with 'mixed' and delayed feedback", Math. Biosci. **90**, 183 (1988). (Section 3.3 of this thesis)

65) J.P.H. Reulen, J.T. Marcus, M.J. van Gilst, D. Koops, J.E. Bos, G. Tiesinga, F.R. de Vries and K. Boshuizen, "Stimulation and recording of dynamic pupillary reflex: the IRIS technique. Part 2.", Med. Biol. Eng. Comp. **26**, 27 (1988).

66) U. an der Heiden and M.C. Mackey,"The dynamics of production and destruction: Analytic insight into complex behaviour", J. Math. Biol. **16**, 75 (1982).

67) L. Stark and T.N. Cornsweet, "Testing a servoanalytic hypothesis for pupil oscillations", Science **127**, 588 (1958).

68) C.J.K. Ellis, "The pupillary light reflex in normal subjects", Br. J. Ophthalmol. **65**, 754 (1981).

69) I.E. Loewenfeld, "Pupillary movements associated with light and near vision: An experimental review of the literature", in *"Recent Developments in Vision Research"*, M. Whitcomb, ed.,pp.17-105 (National Research Council, No. 1272, Washington, 1966).

70) T.N. Cornsweet *"Visual Perception"* (Academic Press, New York,1967).

71) J.G. Webster, "Pupillary light reflex: Development of teaching models", IEEE Trans. **BME-18**, 187 (1971).

72) L.D. Partridge and L.A. Benton, "Muscle, the motor", in *"Handbook of Physiology, Motor Control"*, V. Brooks, ed., pp. 43-106 (American Physiological Society, Washington, 1981), **Vol. 2**.

73) J. Terdiman, J.D. Smith and L. Stark, "Dynamic analysis of the pupil with light and electrical stimulation", IEEE Trans. **SMC-1**, 239 (1971).

74) S. Usui and L. Stark, "A model for nonlinear stochastic behaviour of the pupil", Biol. Cybern. **45**, 13 (1982).

75) O. Lowenstein and E.D. Friedman, "Pupillographic studies. I. Present state of pupillography; its method and diagnostic significance", Arch. Ophthalmol. **27**, 969 (1942).

76) N.D. Hayes, "Roots of the trancendental equation associated with a certain difference differential equation", J. Lond. Math. Soc. **25**, 226 (1950).

77) M.C. Mackey, "A unified hypothesis for the origin of aplastic anemia and periodic haematopoiesis", Blood **51**, 941 (1978).

78) H.W. Stech, "Hopf bifurcation calculations for functional differential equations", J. Math. Anal. Appl. **109**, 472 (1985).

79) V. Sirkus, *"Hopf bifurcation for delay-differential equations"*, M. Sc. Thesis, McGill University, Montréal (1975).

80) M.S. Arkin and R.F. Miller, "Bipolar origin of synaptic inputs to sustained OFF-ganglion cells in the mudpuppy retina", J. Neurophys. **60**, 1122 (1988).

81) R.J. Clarke and H. Ikeda, "Luminance and darkness detectors in the olivary and posterior pretectal nuclei and their relationship to the pupillary light reflex in the rat. I. Studies with steady lumiance levels", Exp. Brain Res. **57**, 224 (1985).

82) I. Nisida, H. Okada and O. Nakano, "Electrical activity of the pretectal region of the cat to visual stimulus", Yonago Acta Medica 4, 7 (1959).

83) P.H. Schiller, "The connections of the retinal ON and OFF pathways to the lateral geniculate nucleus of the monkey", Vision Res. **24**, 923 (1984).

84) A. Longtin and J.G. Milton, "Insight into the transfer function, gain, and oscillation onset for the pupil light reflex using nonlinear delay-differential equations", Biol. Cybern. **61**, 51 (1989). (Section 2.3 of this thesis)

85) F. Sun, W.C. Krenz and L. Stark, "A systems model for the pupil size effect. I. Transient data", Biol. Cybern. **48**, 101 (1983).

86) M.C. Mackey, "Periodic auto-immune hemolytic anemia: An induced dynamical disease", Bull. Math. Biol. **41**, 829 (1979).

87) M.C. Mackey, "Commodity price fluctuations: Price dependent delays and nonlinearities as explanatory factors", J. Econ. Theory **48**, 497 (1989). (In press)

88) L. Stark, F.W. Campbell and J. Atwood, "Pupil unrest: An example of noise in a biological servomechanism", Nature **182**, 857 (1958).

89) J.G. Milton and A. Longtin, "Evaluation of pupil constriction and dilation from cycling measurements", Vision Res. (in press) (Section 3.2 of this thesis)

90) M. Clynes, "Unidirectional rate sensitivity: A biocybernetic law of reflex and humoral systems as physiologic channels of control and communication", Ann. N. Y. Acad. Sci. **92**, 949 (1968).

91) D. Tranchina, J. Gordon and R. Shapley, "Retinal light adaptation - evidence for a feedback mechanism", Nature **310**, 314 (1984).

92) N. Wiener, *"Cybernetics: or Control and Communication in the Animal and the Machine"* (MIT Press, Cambridge, 1948).

93) S.M. Shinner, *"Modern Control System Theory and Application"*, 2nd ed. (Addison-Wesley, Reading, 1978).

94) N. Wiener, *"Nonlinear Problems in Random Theory"* (Wiley, New York, 1958).

95) A. Sandberg and L. Stark, "Wiener G-function analysis as an approach to nonlinear characteristics of human pupil light reflex", Brain Res. **11**, 194 (1968).

96) N. Minorsky, *"Nonlinear Oscillations"* (Van Nostrand, Princeton, 1962).

97) H. Nyquist, "Regeneration theory", Bell System Tech. J. **11**, 126 (1932).

98) W. Krenz and L. Stark, "Neuronal population model for the pupil size effect", Math. Biosci. **68**, 247 (1984).

99) A. Longtin and J.G. Milton, "Modelling autonomous oscillations in the human pupil light reflex using nonlinear delay-differential equations", Bull. Math. Biol. **51**, 605 (1989). (Section 2.2 of this thesis)

100) R. Pallu de la Barrière, *"Optimal Control Theory"* (Dover, New York, 1967).

101) P. Nardone, P. Mandel and R. Kapral, "Analysis of a delay-differential equation in optical bistability", Phys. Rev. A **33**, 2465 (1986).

102) D.J. Allwright, "Harmonic balance and the Hopf bifurcation", Math. Proc. Camb. Phil. Soc. **82**, 453 (1977).

103) A.I. Mees and D.J. Allwright, "Using characteristic loci in the Hopf bifurcation", Proc. IEE **126**, 628 (1979).

104) F. Sun, P. Tauchi and L. Stark, "Binocular alternating pulse stimuli: Experimental and modelling studies of the pupil reflex to light", Math. Biosci. **67**, 225 (1983).

105) F. Sun and L. Stark, "Pupillary escape intensified by large pupillary size", Vision

Res. **23**, 611 (1983).

106) S. Ishikawa, M. Naito and K. Inabe, "A new videopupillography", Ophthalmologica **160**, 248 (1970).

107) U. an der Heiden, "Delays in physiological systems", J. Math. Biol. **8**, 345 (1979).

108) M.C. Mackey and U. an der Heiden, "Dynamical diseases and bifurcations: understanding functional disorders in physiological systems", Funkt. Biol. Med. **1**, 156 (1982).

109) R.M. Noyes, "The interface between mathematical chaos and experimental chemistry", in *"Stochastic Phenomena and Chaotic Behavior in Complex Systems"*, P. Schuster, ed., pp.106-115 (Springer, Berlin, 1984).

110) R.H. Simoyi, A. Wolf and H.L. Swinney, "One-dimensional dynamics in a multicomponent chemical reaction", Phys. Rev. Lett. **49**, 245 (1982).

111) L. Stark, *"Neurological Control Systems: Studies in Bioengineering"* (Plenum, New York, 1969).

112) R. Vallée, C. Delisle and J. Chrostowski, "Noise versus chaos in acousto-optic bistability", Phys. Rev. A **30**, 336 (1984).

113) H.M. Gibbs, F.A. Hopf, D.L. Kapana and R.L. Shoemaker, "Observation of chaos in optical bistability", Phys. Rev. Lett. **46**, 474 (1981).

114) U. an der Heiden, "Stochastic properties of simple differential-delay equations", in *"Delay Equations, Approximation and Application"*, G. Meinardus and G. Nürnberger, eds., Internat. Ser. Num. Math., (Birkhäuser, Basel, 1985), **Vol.74**.

115) W. Horsthemke and D.K. Kondepudi (eds.), *"Fluctuations and Sensitivity in Nonequilibrium Systems"* (Springer, New York, 1984).

116) A. Libchaber, C. Laroche and S. Fauve, "Period doubling cascade in mercury, a quantitative measurement", Phys. Lett. **43**, 211 (1982).

117) N. MacDonald, *"Time Lags in Biological Models"*, Lecture Notes in Biomathematics **27** (Springer, Berlin, 1978).

118) N. Ohba and M. Alpern, "Adaptation of the pupil light reflex", Vision Res. **12**, 953 (1972).

119) A. Lasota and M.C. Mackey, "Noise and statistical periodicity", Physica **22D**, 143 (1987).

120) M.J. Feigenbaum and B. Hasslacher, "Irrational decimations and path integrals for external noise", Phys. Rev. Lett. **49**, 605 (1982).

121) G. Mayer-Kress and H. Haken, "The influence of noise on the logistic model", J. Stat. Phys. **26**, 149 (1981).

122) J. Hale, *"Theory of Functional Differential Equations"* (Springer, New York, 1977).

123) S.-E. A. Mohammed, *"Stochastic Functional Differential Equations"* (Pitman, London, 1984).

124) T.L. Saaty, *"Modern Nonlinear Equations"* (Dover, New York, 1981).

125) J. Mallet-Paret and R.D. Nussbaum, "A bifurcation gap for a singularly perturbed delay equation", in *"Chaotic Dynamics and Fractals"*, M.F. Barnsley and S.G. Demko, eds., pp.263-286 (Academic Press, Orlando, 1986).

126) D. Fargue, "Réductibilité des systèmes héréditaires à des systèmes dynamiques (régis par des équations différentielles ou aux dérivées partielles)", C. R. Acad. Sc. Paris, **T.277, No. 17** (Série B, 2^e semestre) (1973).

127) H.T. Banks, "Delay systems in biological models : approximation techniques", in *"Nonlinear Analysis and Applications"*, pp.21-38 (Academic Press, New York, 1977).

128) N. MacDonald, *"Time lags in Biological Models"*, Lecture Notes in Biomathematics **27** (Springer, Berlin,1978).

129) R. Vallée and C. Marriott, "Analysis of an N^{th}-order nonlinear differential-delay equation", Phys. Rev. A **39**, 197 (1989).

130) K. Ikeda, "Multiple-valued stationary state and its instability of the transmitted light by a ring cavity system", Optics Comm. **30**, 257 (1979).

131) H.-O. Walther, "Homoclinic solution and chaos in $\dot{x}(t) = f(x(t-1))$ ", Nonlin. Anal. **5**, 775 (1981).

132) U. an der Heiden and H.-O. Walther, "Existence of chaos in control systems with delayed feedback", J. Diff. Equations **47**, 273 (1983).

133) T.Y. Li and J.A. Yorke, "Period three implies chaos", Am. Math. Monthly **82**, 985 (1975).

134) S.N. Chow and D. Green, "Some results on singular delay-differential equations", in *"Chaos, Fractals and Dynamics"*, P. Fischer and W.R. Smith, eds., pp.161-182 (Dekker, New York, 1985).

135) H.-J. Zhang, J.-H. Dai, P.-Y. Wang, F.-L. Zhang, G. Xu and S.-P. Yang, "Chaos in liquid crystal optical bistability", in *"Directions in Chaos"*, Hao Bai-Lin ed. (World Scientific, Singapore, 1988), **Vol. 2**.

136) R.F. Fox, I.R. Gatland, R. Roy and G. Vemuri, "Fast, accurate algorithm for numerical simulation of exponentially correlated colored noise", Phys. Rev. A. **38**, 5938 (1988).

137) E. Hopf, "Abzweigung einer periodischen Lösung von einer stationären Lösung eines Differentials-Systems", Ber. Math.-Phys.Kl. Sächs. Acad. Wiss. Leipzig **94**, 1 (1942) and Ber. Verh. Sächs. Acad. Wiss. Leipzig Math.-Nat. Kl. **95**, 3 (1942).

138) J. Bélair and M.C. Mackey, "Consumer memory and price fluctuations in commodity markets : an integrodifferential model", J. Dynam. Diff. Eq. **1**, 299 (1989).

139) J.Y. Gao, J.M. Yuan and L.M. Narducci, "Instabilities and chaotic behavior in a hybrid bistable system with a short delay", Optics Comm. **44**, 201 (1983).

140) G. Nicolis and I. Prigogine, *"Self-Organization in Nonequilibrium Systems. From Dissipative Structures to Order through Fluctuations"* (Wiley, New York, 1977).

141) H. Risken, *"The Fokker-Planck Equation"* (Springer, Berlin, 1984).

142) E. Helfand, "Numerical integration of stochastic differential equations", Bell Syst. Tech. J. **58**, 2289 (1979).

143) W. Rümelin, "Numerical treatment of stochastic differential equations", SIAM J. Numer. Anal. **19**, 604 (1982).

144) J.M. Sancho, M. San Miguel, S.L. Katz and J.D. Gunton, "Analytical and numerical studies of multiplicative noise", Phys. Rev. A. **26**, 1589 (1982).

145) R.F. Fox, "Stochastic calculus in physics", J. Stat. Phys. **46**, 1145 (1987).

146) D.E. Knuth, *"The Art of Computer Programming"* (Addison-Wesley, Reading (MA), 1969), **Vol. 2**.

147) W.H. Press, B.P. Flannery, S.A. Teukolsky and W.T. Vetterling, *"Numerical Recipes. The Art of Scientific Computing"* (Cambridge University Press, Cambridge, 1987).

148) L.Fronzoni, R Mannella, P.V.E. McClintock and F. Moss, "Postponement of Hopf bifurcations by multiplicative colored noise", Phys.Rev. A **36**, 834 (1987).

149) G. Iooss and D.D. Joseph, *"Elementary Stability and Bifurcation Theory"* (Springer, New York, 1980).

150) C.W. Gardiner, *"Handbook of Stochastic Methods for Physics, Chemistry and the Natural Sciences"* (Springer, Berlin, 1985).

151) P.E. Rapp, A.I. Mees and C.T. Sparrow, "Frequency encoded biochemical regulation is more accurate than amplitude dependent control", J.Theor.Biol. **90**, 531 (1981).

152) R. Lefever and J.W. Turner, "Sensitivity of a Hopf bifurcation to multiplicative colored noise", Phys. Rev. Lett. **56**, 1631 (1986).

153) S. Kabashima and T. Kawakubo, "Observation of a noise-induced phase transition in a parametric oscillator", Phys. Lett. A **70**, 375 (1979).

154) L. Schimansky-Geier, A.V. Tolstopjatenko and W. Ebeling, "Noise induced transitions due to external additive noise", Phys.Lett. A **108**, 329 (1985)

155) S.J. Linz and M. Lücke, "Effect of additive and multiplicative noise on the first bifurcations of the logistic model", Phys.Rev. A **33**, 2694 (1986).

156) J.Y. Gao, L.M. Narducci, L.S. Schulman, M. Squicciarini and J.M. Yuan, "Routes to chaos in a hybrid bistable system with delay", Phys.Rev. A **28**, 2910 (1983).

157) J.Y. Gao, L.M. Narducci, H. Sadiky, M. Squicciarini and J.M. Yuan, "Higher-order bifurcations in a bistable system with delay", Phys.Rev. A **30**, 901 (1984).

158) A. Longtin and M.C. Mackey, in preparation.

159) L. Fronzoni, F. Moss and P.V.E. McClintock, "Swept-parameter-induced postponements and noise on the Hopf bifurcation", Phys.Rev. A **36**, 1492 (1987).

160) S.M. Baer, T. Erneux and J. Rinzel, "The slow passage through a Hopf bifurcation: delay, memory effects, and resonance", Siam.J.Appl.Math. **49**, 55 (1989).

161) P.C. Martin, in *"Melting, Localization and Chaos"*, R.K. Kalia and P. Vashishta, eds., p.179 (North-Holland, Amsterdam, 1982).

162) M. San Miguel and S. Chaturvedi, "Limit cycles and detailed balance in Fokker-Planck equations", Z. Phys. B **40**, 167 (1980).

163) M.W. Derstine, H.M. Gibbs, F.A. Hopf and D.L. Kaplan, "Bifurcation gap in hybrid optically bistable system", Phys.Rev. A **26**, 3720 (1982).

164) R. Kapral, E. Celarier, P. Mandel and P. Nardone, "Noisy delay-differential equations in optical bistability", SPIE *Optical Chaos*, Vol. 667, 175 (1986).

165) C. Stevens, "Principles and applications of fluctuation analysis: a nonmathematical introduction", in *"Membranes, Ions and Impulses"*, J.W. Moore, ed. (Plenum, New York, 1975).

166) G. Matsumoto, I. Tasaki and I. Inoue, "Oscillatory subthreshold responses and potential fluctuation observed in squid giant axons ", J.Phys.Soc. Japan **44**, 351 (1978).

167) G. Matsumoto and T. Kunisawa, "Critical slowing down near the transition region from the resting to time-ordered states in squid giant axons", J.Phys.Soc. Japan **44**, 1047 (1978).

168) H. Haken, J.A.S. Kelso and H. Bunz, "A theoretical model of phase transitions in human bimanual coordination", Biol. Cybern. **51**, 347 (1985).

169) K. Wiesenfeld, "Noisy precursors of nonlinear instabilities", J. Stat. Phys. **38**, 1071 (1985).

170) H. Haken, *"Advanced Synergetics"* (Springer, Berlin, 1983).

171) P. Borgdorff, "Respiratory fluctuations in pupil size", Am. J. Physiol. **228**, 1094 (1975).

172) K. Ohtsuka, K. Asakura, H. Kawasaki and M. Sawa, "Respiratory fluctuations of the human pupil", Exp. Brain Res. **71**, 215 (1988).

173) S. Toulmin, cited by R. Pool, in "Chaos theory: How big an advance?", Science **245**, 26 (1989).

174) J.P. Eckmann and D. Ruelle, "Ergodic theory of chaos and strange attractors", Rev. Mod. Phys. **57**, 617 (1985).

175) S. Wolfram, "Origins of randomness in physical systems", Phys. Rev. Lett. **55**, 449 (1985).

176) M.C. Mackey, "The dynamic origin of increasing entropy", Rev. Mod. Phys. (in press, to appear Jan. 1990).

177) C. Nicolis and G. Nicolis, "Normal form analysis of stochastically forced dynamical systems", Dynam. Stab. Syst. **1**, 249 (1986).

178) R.J. MacGregor and E.R. Lewis, *"Neural Modeling. Electric Signal Processing in the Nervous System"* (Plenum, New York, 1977).

179) F. Baras, M.M. Mansour and C. Van den Broeck, "Asymptotic properties of coupled nonlinear Langevin equations in the limit of weak noise. II: Transition to a limit cycle", J. Stat. Phys. **28**, 577 (1982).

180) R. Graham, "Hopf bifurcation with fluctuating control parameter", Phys. Rev. A **25**, 3234 (1982).

181) M. Schumaker, "Center manifold reduction and normal form transformations in systems with additive noise", Phys. Lett. A **122**, 317 (1987).

182) H. Engel-Herbert, W. Ebeling and H. Herzel, "The influence of fluctuations on sustained oscillations", in *"Temporal Order"*, L. Rensing and N.I. Jaeger, eds. (Springer, Berlin, 1984).

183) R. Lefever and J.W. Turner, "Sensitivity of a Hopf bifurcation to external multiplicative noise",in *"Fluctuations and Sensitivity in Nonequilibrium Systems"*, W. Horsthemke and D.K. Kondepudi, eds. (Springer, Berlin, 1984).

184) E. Knobloch and K.A. Wiesenfeld, "Bifurcations in fluctuating systems: the center-manifold approach", J. Stat. Phys. **33**, 611 (1983).

185) P.R. Bevington, *"Data Reduction and Error Analysis for the Physical Sciences"* (McGraw-Hill, New York, 1969).